

**Hierarchical clustering-based segmentation (HCS) aided
diagstic image interpretation monitoring.**

SELVAN, A.D. Arul Nirai.

Available from Sheffield Hallam University Research Archive (SHURA) at:

<http://shura.shu.ac.uk/20342/>

This document is the author deposited version. You are advised to consult the publisher's version if you wish to cite from it.

Published version

SELVAN, A.D. Arul Nirai. (2007). Hierarchical clustering-based segmentation (HCS) aided diagstic image interpretation monitoring. Doctoral, Sheffield Hallam University (United Kingdom)..

Copyright and re-use policy

See <http://shura.shu.ac.uk/information.html>

Sheffield Hallam University
/ Learning *m o* information Services
s Adsetts Centre, City Campus
Sheffield S11WD

ProQuest Number: 10700988

All rights reserved

INFORMATION TO ALL USERS

The quality of this reproduction is dependent upon the quality of the copy submitted.

In the unlikely event that the author did not send a complete manuscript and there are missing pages, these will be noted. Also, if material had to be removed, a note will indicate the deletion.

uest

ProQuest 10700988

Published by ProQuest LLC(2017). Copyright of the Dissertation is held by the Author.

All rights reserved.

This work is protected against unauthorized copying under Title 17, United States Code
Microform Edition © ProQuest LLC.

ProQuest LLC.
789 East Eisenhower Parkway
P.O. Box 1346
Ann Arbor, MI 48106- 1346

Hierarchical Clustering-based Segmentation (HCS) Aided Diagnostic Image Interpretation and Monitoring

A.D. Arul Nirai Selvan

**A thesis submitted in partial fulfilment of the requirements of
Sheffield Hallam University
for the award of Doctor of Philosophy**

February 2012

Declaration

This is to certify that I am responsible for the work submitted in the thesis, that the original work is my own except in acknowledgements, and that neither the thesis nor the original work contained therein has been submitted to this or any institution for a higher degree.

Signature :

Name : A.D. Arul Nirai Selvan

Date : 10 February 2012

Abstract

Hierarchical Clustering-based Segmentation (HCS) Aided Diagnostic Image Interpretation and Monitoring

Machines are good at operations which require precision and computing objective measures. In contrast, humans are good at generalisation and making decisions based on their past experience and heuristics. Hence, to solve any problem with a solution involving human-machine interaction, it is imperative that the tasks are shared appropriately. However, the boundary which divides these two different set of tasks is not well defined in domains such as medical image interpretation. Therefore, one needs a versatile tool which is flexible enough to accommodate the varied requirements of the user. The aim of this study is to design and implement such a software tool to aid the radiologists in the interpretation of diagnostic images.

Tissue abnormality in a medical image is usually related to a dissimilar part of an otherwise homogeneous image. The dissimilarity may be subtle or strong depending on the medical modality and the type of abnormal tissue. Hierarchical Clustering-based Segmentation (HCS) process is a dissimilarity highlighting process that yields a hierarchy of segmentation results. In this study, the HCS process was investigated for offering the user a versatile and flexible environment to perceive the varied dissimilarities that might be present in diagnostic images. Consequently, the user derives the maximum benefit from the computational capability (perception) of the machine and at the same time incorporate their own decision process (interpretation) at the appropriate places.

As a result of the above investigation, this study demonstrates how HCS process can be used to aid radiologists in their interpretive tasks. Specifically this study has designed the following HCS process aided diagnostic image interpretation applications :

- interpretation of computed tomography (CT) images of the lungs to quantitatively measure the dimensions of the airways and the accompanying blood vessels.
- interpretation of X-ray mammograms to quantitatively differentiate benign from malignant abnormalities.

One of the major contribution of this study is to demonstrate how the above HCS process aided interpretation of diagnostic images can be used to monitor disease conditions. This thesis details the development and evaluation of the novel computer aided monitoring (CAM) system. The designed CAM system is used to objectively measure the properties of suspected abnormal areas in the CT images of the lungs and in X-ray mammogram. Thus, the CAM system can be used to assist the clinician to objectively monitor the abnormality. For instance, its response to treatment and consequently its prognosis. The implemented CAM system to monitor abnormalities in X-ray mammograms is briefly described below.

Using the approximate location and size of the abnormality, obtained from the user, the HCS process automatically identifies the more appropriate boundaries of the different regions within a region of interest (ROI), centred at the approximate location. From the set of, HCS process segmented, regions the user identifies the regions which most likely represent the abnormality and the healthy areas. Subsequently, the CAM system compares the characteristics of the user identified abnormal region with that of the healthy region; to differentiate malignant from benign abnormality. In processing sixteen mammograms, the designed CAM system demonstrated the possibility of successfully differentiating malignant from benign abnormalities.

Acknowledgements

I wish to thank my supervisory team, Dr. Reza Saatchi, and Dr. Christine M. Ferris, for all their kind support and encouragement throughout this work.

Publications

1. Selvan, A. N., Saatchi, R. and Ferris, C. M. "Improving Medical Image Perception by Hierarchical Clustering based Segmentation". *In: 9th International Conference on Information Technology and Applications in Biomedicine*, Larnaka, Cyprus, 4-7 November, 2009.
2. Selvan, A. N., Saatchi, R. and Ferris, C. M. "Computer Aided Monitoring of Breast Abnormalities in X-ray Mammograms". *In Medical Image Understanding and Analysis Conference*, London, 14-15 July, 2011.
3. Selvan, A. N., "Boundary Extraction in Images Using Hierarchical Clustering-based Segmentation" *British Machine Vision Conference (Student workshop)*, Dundee, UK, Sept. 2011.

Table of Contents

Declaration.....	i
Abstract.....	ii
Acknowledgements.....	iii
Publication.....	iv
Table of Contents.....	v
List of Figures.....	ix
List of Tables.....	xv
List of Equations.....	xvii
List of Abbreviations.....	xviii

Chapter 1 Introduction and Objective of this Study.....	1
1.1 Aim.....	1
1.2 Background.....	1
1.3. Objective and Purpose of this Study	1
1.3.1. User Decision based Medical Image Processing and HCS Process Aided Image Interpretation	2
1.3.1.1. User-Decision based CT Image Processing.....	3
1.3.1.2. User Decision based Mammogram Image Processing.....	4
1.3.2. Computer Aided (disease) Monitoring (CAM).....	5
1.3.2.1. Computer Aided (disease) Monitoring of Cystic Fibrosis.....	5
1.3.2.2. Computer Aided (disease) Monitoring of Breast Abnormalities	5
1.3.3. Uniqueness and Novelty of the Developed Medical Image Processing Methods.....	6
1.4. Contribution of the Study.....	6
1.5.Thesis Structure.....	8

Chapter 2 Background and Relevant Studies Review.....	10
2.1 Introduction.....	10
2.2 Digital Image Segmentation.....	10
2.2.1 Medical Image Segmentation.....	17
2.3 Cystic Fibrosis.....	18
2.3.1 Measurement of Airways and Blood Vessel Dimensions in CT Images.....	20
2.4 Computer Aided Detection and Diagnosis of Breast Abnormalities in X-ray Mammograms.....	23
2.4.1 Segmentation and Detection of Abnormalities in X-ray Mammographic Images	30
2.5. Studies Most Relevant to the Current Study	33
2.6 Summary.....	36

Chapter 3 Hierarchical Clustering Based Segmentation (HCS).....	37
3.1 Introduction.....	37
3.2. Overview of the HCS Process	37
3.2.1.Border Pixel Re-Classification.....	43
3.3. HCS Process Performance.....	46
3.3.1. Performance of the HCS Process in Processing Diagnostic Images of Different Modalities.....	46
3.3.1.1. Performance of the HCS Process in Highlighting Infarct in Magnetic Resonance Imaging (MRI) T2 Weighted Images.....	47
3.3.1.2. Performance of the HCS Process in Segmenting Different Regions in CT Images.....	49

3.3.1.3. Performance of the HCS Process in Segmenting Different Regions in Ultrasound (US) Images.....	50
3.3.1.4. Performance of the HCS Process in Segmenting Different Regions in X-ray Mammogram Images.....	51
3.4. Objective evaluation of the performance of the HCS process.....	53
3.4.1. HCS Process Evaluation and Benchmarking Experimental Results.....	54
3.4.2. Critical Evaluation of the HCS Process's Experimental Results.....	60
3.5. HCS as a Perceptual Aid for Radiologists.....	63
3.5.1.HCS as a Perceptual Aid by Augmenting the Information Provided by CAD Prompts in Mammograms.....	67
3.6. Summary.....	82
Chapter 4 HCS Process Aided Interpretation of CT Images of the Lungs to Monitor Cystic Fibrosis.....	83
4.1. Introduction	83
4.2. User Decision Incorporated Processing of Diagnostic Images for Highlighting Dissimilarities in Medical Images.....	83
4.2.1. The Use of HCS Output to Incorporate User Decision in Processing Diagnostic Images	84
4.2.2. Graphical User Interface (GUI) Facility for Displaying HCS Process Output	84
4.3. User Decision Incorporated Processing of CT Images of the Lungs	87
4.3.1. Motivation Behind the Study.....	87
4.3.2. CT Image of the Airway.....	87
4.3.3.CT Image Data.....	89
4.3.4. Unsupervised Segmentation of the CT Image Data of the Lungs Using HCS.....	94
4.3.4.1. Additional criteria incorporated, within the HCS process, to improve segmentation.....	96
4.3.4.2. Unsupervised segmentation of the remapped CT image grey scale data.....	99
4.3.5. Incorporating user knowledge to aid segmentation.....	101
4.3.5.1. Passing user knowledge, based on the HCS process initial unsupervised segmentation output.....	103
4.3.5.2. Passing user knowledge, by making use of initial user tagged information.....	106
4.3.5.3. Segmentation, of the remapped CT image grey scale data, making use of initial user tagged information.....	108
4.3.6. Synopsis of the Different Approaches Adopted to Segment the Boundaries of the Air-Way and the Accompanying Blood Vessel.....	111
4.3.7. Improving the output of the user guided HCS process and the estimation of the properties of airways and the accompanying blood vessels.....	113
4.3.7.1. Fitting an ellipse to the boundaries of the airway and the accompanying blood vessel.....	114
4.3.7.2. Quantitative Measurements of the Airways and the Accompanying Blood Vessels.....	116
4.3.8. Synopsis of the User Guided HCS process Based Estimation of the Properties of the Airways and the Accompanying Blood Vessels.....	117
4.3.9. Critical Evaluation of the Implemented User Guided HCS Process Based Procedure to Estimate the Dimensions of the Air-Way and Artery.....	117
4.3.9.1.Critical Discussion on Making Use of User Input.....	119
4.3.10. Segmentation of Airway and the accompanying Blood Vessel making use of the user tagged boundary locations around the individual anatomy.....	120

4.3.10.1. Marking the approximate boundaries around the Blood Vessel and the Airway-wall.....	122
4.3.10.2. Fitting cubic splines to connect the user given discrete locations and form a continuous closed curve.....	122
4.3.10.3. HCS process based segmentation of the part of the image enclosed by the continuous curves.....	123
4.3.10.4. Reducing the misclassification by specifying pixel value range to restrict merging of regions across the Airway-Wall.....	125
4.3.10.5. Estimating the Dimensions of the Blood vessel, Airway-wall and Airway-lumen.....	126
4.4. Summary.....	127
Chapter 5 HCS Process Aided Interpretation of X-ray Mammograms.....	128
5.1 Introduction.....	128
5.2. User Decision Incorporated Processing of X-ray Mammograms.....	128
5.2.1. Mammogram Image Data	129
5.2.1.1. mini-MIAS Database of Mammograms.....	130
5.2.2. Preliminary Investigation of the HCS Process Based Analysis of the X-ray Mammograms.....	131
5.2.2.1. HCS Process Analysis of a Benign Abnormality.....	131
5.2.2.2. HCS process analysis of a malignant abnormality.....	137
5.2.2.3. Overall Discussion of the HCS Process Analysis of the Benign and Malignant Abnormalities.....	143
5.2.3. Differentiating Benign from Malignant Abnormalities; a Possibility.....	143
5.2.3.1. Differentiating Benign from Malignant Abnormalities; a Hypothesis.....	144
5.2.4. Design and Implementation of an Objective Measure to Differentiate Benign from Malignant Abnormalities.....	145
5.2.4.1. More Appropriate Delineation of the Boundary of the Abnormalities.....	146
5.2.4.2. Identifying the Region of the Image Comprising of the Healthy Part.....	153
5.2.4.2.1. Using the User Provided Approximate Boundary of the Abnormality To Identify the Healthy Part of the Image.....	154
5.2.4.2.2. Making use of the HCS Process Output.....	155
5.2.4.3. Measuring Dissimilarity Between Regions Containing the Abnormality and the Healthy Tissue.....	159
5.2.4.3.1. Dissimilarity Between Clusters within the Abnormality and the Healthy Regions.....	160
5.2.4.3.2. Dissimilarity Between the Primary Clusters within the Abnormality Region and the Clusters Within the Healthy Region	160
5.2.4.3.3. Dissimilarity Between the Cluster Containing the User Tagged Location Within the Abnormality Region and the Clusters Within the Healthy Region.....	161
5.2.4.3.4. The Choice of the Dissimilarity Measure Between Regions Containing the Abnormality and the Healthy Tissue.....	163
5.2.5. Differentiating Benign from Malignant Abnormalities by Making Use of the Objective Measure.....	163
5.2.5.1. Classifying Malignant Abnormality Using the Objective Measure.....	168
5.2.5.2. Classifying Benign Abnormality Using the Objective Measure.....	172
5.2.6. Necessity for the User Identified Healthy Region for the Correct Estimate of the Objective Measure.....	177
5.2.6.1. Benign Case Getting Misclassified as Malignant.....	178
5.2.6.2. Malignant Case Getting Correctly Classified for All Wrong Reasons.....	187
5.3. Summary.....	195

Chapter 6 HCS Process Aided Disease Monitoring.....	196
6.1. Background.....	196
6.2. Computer Aided Monitoring of the Dimensions of the Airway and the Accompanying Blood Vessel.....	198
6.2.1. HCS Process Based Quantitative Measure of the Airway and the Accompanying Blood Vessel Dimensions for Cases of Known Diagnosis.....	199
6.2.1.1. HCS Process Based Quantitative Measure of the Airway and the Accompanying Blood Vessel Dimensions for a Healthy Case.....	199
6.2.1.2. HCS Process Based Quantitative Measure of the Airway and the Accompanying Blood Vessel Dimensions for a CF Case.....	202
6.2.1.3. Critical Evaluation of the Processing of the CT image data for the Healthy Case and that Diagnosed Cystic Fibrosis.....	204
6.2.2. Correlating the HCS Process Based Objective Measurements with that of an Expert's.....	206
6.2.2.1. HCS Process Based Objective Measure of the Dimensions of the Airway and the Accompanying Blood-Vessel for the Test Cases.....	207
6.2.2.2. Comparing HCS Process based Objective Measure with that of the Radiologist's Manual Measure.....	212
6.2.2.3. Critical evaluation of the Results.....	213
6.3. Computer Aided Monitoring of Abnormalities in X-ray Mammograms.....	216
6.3.1. Details of the Computer Aided Monitoring of the Abnormalities in X-ray Mammograms for Sixteen Test Cases	218
6.3.2. Overall Results Obtained through the CAM Process.....	234
6.3.3. Diagnosis of an Expert Radiologist.....	235
6.3.4. Comparing HCS Process based Objective Measure with that of the Radiologist's Manual Measure.....	237
6.3.5. Possible Usage of the CAM Process of Abnormalities in X-ray Mammograms	239
6.4. Summary.....	240
Chapter 7 Study Contribution, Possibilities and Further Work.....	242
7.1 Introduction.....	242
7.2. Contribution and Possible Application of the Current Study.....	243
7.2.1.Possible Application of the Computer Aided Monitoring of CF.....	243
7.2.2.Possible Application of Computer Aided Monitoring of Breast Abnormalities... ..	246
7.3.Further Work.....	247
7.3.1. Proposed Further Work on HCS Process.....	247
7.3.2. Proposed Further Work on the CAM process to monitor CF.....	249
7.3.3.Proposed Further Work on CAM process to monitor Breast Abnormalities...	249
7.4 Conclusion.....	250
Appendix 1.....	251
Appendix 2.....	257
Appendix 3.....	259
Appendix 4.....	261
Appendix 5.....	264
Appendix 6.....	265
References.....	266

List of Figures

Figure 2.1 - Image acquired using MDCT	22
Figure 2.2 - Radiologist scrutinizing mammograms using a magnifying glass.....	24
Figure 2.3 - CAD marking of micro-calcification.....	26
Figure 2.4 - MED-SEG processing of mammograms.....	36
Figure 3.1-A Flow chart illustrating the different operations of the HCS process (Image courtesy Selvan 2007).....	40
Figure 3.1-B Pixel-values distribution feature representation for a grey tone image (Image courtesy Selvan 2007).....	41
Figure 3.2 - Processing of a CT image by HSEG	44
Figure 3.3 - Segmentation of a CT image by HCS with and without border pixel reclassification.....	45
Figure 3.4 - HCS process Segmentation of a MRI image.....	48
Figure 3.5 HCS process Segmentation of a CT image.....	49
Figure 3.6 HCS process Segmentation of a US image.....	51
Figure 3.7 HCS process Segmentation of a X-ray mammogram image	52
Figure 3.8 A natural scene from the Berkley database (Image ID 42049).....	55
Figure 3.9 - HCS process Segmentation of a natural scene.....	56
Figure 3.10: HCS process segmented boundaries of a natural scene.....	58
Figure 3.11 Precession and Recall plot for 228 levels of HCS process.....	60
Figure 3.12 Boundary output and the P-R curve for the segmentation method "Boosted Edge Learning"	61
Figure 3.13 Boundary output and the P-R curve for the segmentation method "Segmentation induced by Scale Invariance".....	62
Figure 3.14 - HCS process segmentation output highlighting the subtle dissimilarities in the natural scene.....	62
Figure 3.15 - CT image of a section of the brain showing the infarct affected area marked in white by the expert.....	64
Figure 3.16 - The location and the size of the ROI enclosing the infarct affected area..	64
Figure 3.17 - The regions during an intermediate stage of the HCS process.....	65
Figure 3.18 - Borders of the regions during an intermediate stage of the HCS process.	65
Figure 3.19 - Infarct outlined by the expert after evaluating the HCS process results..	66
Figure 3.20 - Borders of the regions during an intermediate stage of the HCS process superimposed on the expert newly outlined image.....	66
Figure 3.21 - Three of the pixel locations which were correctly classified, by the HCS process (marked in Green) and three of the pixel locations which were misclassified (marked in Yellow).....	67
Figure 3.22-A - Computer Aided Detection (CAD) through prompting.....	68
Figure 3.22-B - Effect of Prompting based CAD on Human Decision.....	69
Figure 3.23 - T2 weighted MRI Image (Image courtesy Selvan 2007).....	71
Figure 3.24 - The distribution of the pixel values in the T2 weighted MRI Image shown in Figure 3.23.....	72
Figure 3.25 - The linear mapping of the actual pixel values in the T2 weighted MRI Image (Figure 3.24), to 256 gray levels.....	72
Figure 3.26 - Equal-probability quantizing [Haralick et al., 1973] mapping of the actual pixel values in the T2 weighted MRI Image (Figure 3.24), to 256 gray levels.....	73
Figure 3.27 - T2 weighted MRI Image data (Figure 3.24) mapped to 256levels making use of the equal-probability quantizing [Haralick et al., 1973] method.....	74

Figure 3.28 - Diffusion weighted MRI Image showing the location of the abnormality (arrow head).....	74
Figure 3.29 - Quantised images of X-ray mammograms.....	76
Figure 3.30 - Composite quantised image of X-ray mammograms.....	77
Figure 3.31 GUI display of the HCS process output (right canvas) and the quantised image quantised to the narrow grey scale range of 200 to 224 (left canvas).....	78
Figure 3.32 GUI display of the properties of the region coloured red in the right canvas of the GUI in Figure 3.31.....	78
Figure 3.33 Histogram (black) of the pixel values within the ROI of the mammogram shown in Figure 3.29 (a).....	79
Figure 3.34 Histogram (Brown) of the pixel values within the ROI of the mammogram shown in Figure 3.30 (a).....	80
Figure 3.35 mini-MIAS Mammogram image (Image-ID mdb005) showing the approximate location of the circumscribed mass (a, b). HCS process segmented regions (c) and their boundaries (d) when there were 10 regions yet to be merged.....	81
Figure 3.36 - Histogram (black) of the pixel values within the ROI of the mammogram shown in Figure 3.35 (a). The coloured plots shows the histograms of the pixel values within the four major regions identified by the HCS process (Figure 3.35 b).....	81
Figure 4.1 - Annotated screen captured image of the GUI, to visualize HCS process output.....	86
Figure 4.2 - Dimensions of the airway lumen, airway wall, and accompanying pulmonary artery (Image courtesy de Jong 2005).	88
Figure 4.3 - Annotated CT Image showing two locations of airway and accompanying pulmonary artery.....	90
Figure 4.4 - Graphical user interface facility [Selvan, 2007] to view DICOM images and to choose the appropriate windowing parameters.....	92
Figure 4.5 - Region 1 part of the CT image (Figure 4.3) displayed using appropriate windowing parameters to highlight either only the blood vessel (a) or the blood vessel and the airway (b).....	92
Figure 4.6 - Manually segmented and colour coded four different classes of regions, namely Blood-Vessel (Red), airway-wall (Green), Lumen (Blue) and Lung Parenchyma at the background (Black) as perceived by a radiologist.....	93
Figure 4.7 - Distribution of the Pixel Values based on the Ground Truth.....	93
Figure 4.8 - Segmentation of a CT image using HCS.....	95
Figure 4.9 - The HCS process unsupervised segmentation output.....	95
Figure 4.10 - HCS unsupervised segmentation, when the additional criteria of pixel euclidean distance factor is taken into account for merging.....	98
Figure 4.11 - The HCS process unsupervised segmentation, when only adjacent clusters were merged.....	99
Figure 4.12 - Remapped CT image data and its segmentation by the HCS process	100
Figure 4.13 - The segmentation output of the HCS process based unsupervised segmentation of the ROI shown in Figure 4.6.....	104
Figure 4.14 - Passing user knowledge based on the HCS process initial segmentation.....	105
Figure 4.15 - Passing user knowledge, by tagging locations within the major anatomies.....	107
Figure 4.16 - Images illustrating how the user initial tagging information influences the final segmentation.....	108
Figure 4.17 - User tagged locations on the remapped CT image data.....	109
Figure 4.18 - Segmentation of the remapped CT image grey scale data making use of user tagged information of Figure 4.17 (b).....	110

Figure 4.19 - Segmentation of the original CT image data making use of user tagged information of Figure 4.17 (b).....	111
Figure 4.20 - Boundary locations of the segmented anatomies.....	115
Figure 4.21 Minor and Major axis of the fitted ellipse to the boundary of the Blood Vessel (a), Airway-Wall (b) and Airway Lumen (c).....	115
Figure 4.22 Minor and Major axis of the fitted ellipse to the Blood Vessel (a), Airway-Wall (b) and Airway Lumen (c).....	115
Figure 4.23 - Locations marked by the user just outside and around the Blood Vessel (Red) and the Airway-Wall of the CT image of Figure 4.6.....	122
Figure 4.24 - Cubic spline interpolated locations of the locations marked by the user just outside and around the Blood Vessel (Red) and the Airway-Wall of the CT image of Figure 4.6.....	123
Figure 4.25 - HCS process based segmentation of the blood vessel (Red), Airway-Wall and Airway-Lumen.....	124
Figure 4.26 - HCS process based segmentation of the Blood Vessel (Red), Airway-Wall and Airway-Lumen.....	126
Figure 4.27 - Minor and Major axis of the fitted ellipse to the Blood Vessel (a), Airway-Wall (b) and Airway-Lumen (c).....	126
Figure 5.1 - Digitised X-ray Mammogram image data mini-MIAS mdb097.....	131
Figure 5.2 - Intermediate segmented image showing the five regions and their boundaries.....	133
Figure 5.3 - Intermediate segmented image showing the four regions and their boundaries.....	134
Figure 5.4 - Intermediate segmented image showing the three regions and their boundaries	135
Figure 5.5 - Intermediate segmented image showing the two regions and their boundaries.....	136
Figure 5.6 - Digitised X-ray Mammogram image data mini-MIAS mdb102.....	137
Figure 5.7 - Intermediate segmented image showing the six regions and their boundaries	139
Figure 5.8 - Intermediate segmented image showing the four regions and their boundaries	140
Figure 5.9 - Intermediate segmented image showing the three regions and their boundaries	141
Figure 5.10 - Intermediate segmented image showing the two regions and their boundaries	142
Figure 5.11 - For the mini-MIAS mammogram (Image ID mdb095), images showing the difference between the boundary of the abnormality as suggested by mini-MIAS (Red circle) and by another different radiologist (Black curve).....	148
Figure 5.12 - HCS processing of mini-MIAS mdb095.....	149
Figure 5.13 - For the mini-MIAS image ID mdb102 (a). Figure showing the region chosen as the abnormality region (b) extending beyond the user given approximate boundary (c) (d).....	152
Figure 5.14 - HCS processing of mini-MIAS mdb090.....	153
Figure 5.15 - Abnormal and Healthy regions considered for mini-MIAS mdb095.....	155
Figure 5.16 - Abnormal and Healthy regions considered for mini-MIAS mdb090.....	156
Figure 5.17 - HCS process intermediate output for mammogram image mdb090.....	158
Figure 5.18 - Abnormal and Healthy regions considered for mini-MIAS mdb090.....	159
Figure 5.19 – Segmentation of mini-MIAS Mammogram image mdb102.....	162
Figure 5.20 – Segmentation of mini-MIAS Mammogram image mdb028.....	166
Figure 5.21 - Segmentation of mini-MIAS Mammogram image mdb213.....	167

Figure 5.23 - For mini-MIAS Mammogram image (Image-ID mdb102) graph showing the dissimilarity amongst the clusters within the abnormality area and the healthy area and between the clusters within the abnormality and healthy areas.....	171
Figure 5.24 - For mini-MIAS Mammogram image (Image-ID mdb102) graph showing the dissimilarity between the cluster having the user tagged location and other clusters belonging to the abnormality area and the healthy area.....	171
Figure 5.25 - HCS processing of mini-MIAS mammogram (Image-ID mdb097).....	173
Figure 5.26 - HCS processing of mdb097.....	174
Figure 5.27 - For mini-MIAS Mammogram image (Image-ID mdb097) graph showing the dissimilarity amongst the clusters within the abnormality area and the healthy area and between the clusters within the abnormality and healthy areas.....	176
Figure 5.28 - For mini-MIAS Mammogram image (Image-ID mdb097) graph showing the dissimilarity between the cluster having the user tagged location and other clusters belonging to the abnormality area and the healthy area.....	176
Figure 5.29 - HCS processing of mini-MIAS mammogram mdb083.....	179
Figure 5.30 - For mini-MIAS Mammogram image (Image-ID mdb083) graph showing the dissimilarity amongst the clusters within the abnormality area and the healthy area and between the clusters within the abnormality and healthy areas.....	182
Figure 5.31 - For mini-MIAS Mammogram image (Image-ID mdb083) graph showing the dissimilarity between the cluster having the user tagged location and other clusters belonging to the abnormality area and the healthy area.....	182
Figure 5.32 - HCS processing of mini-MIAS mammogram mdb083.....	183
Figure 5.33 - HCS processing of mini-MIAS mammogram mdb083.....	185
Figure 5.34 - For Image-ID mdb083 graph showing the dissimilarity amongst the clusters within the abnormality area, within the user identified healthy area and between the clusters within the abnormality and the user identified healthy areas.....	186
Figure 5.35 - For Image-ID mdb083 graph showing the dissimilarity between the cluster having the user tagged location and other clusters belonging to the abnormality area and the user identified healthy area.....	186
Figure 5.36 - HCS processing of mini-MIAS mammogram mdb090	188
Figure 5.37 - For Image-ID mdb090 graph showing the dissimilarity amongst the clusters within the abnormality area and the user identified healthy area and between the clusters within the abnormality and the healthy areas.....	190
Figure 5.38 - For Image-ID mdb090 graph showing the dissimilarity between the cluster having the user tagged location and other clusters belonging to the abnormality area and the healthy area.....	190
Figure 5.39 - HCS processing of mini-MIAS mammogram image mdb090.....	191
Figure 5.40 - Abnormal and healthy region for mini-MIAS mammogram mdb090.....	193
Figure 5.41 - For Image-ID mdb090 graph showing the dissimilarity amongst the clusters within the abnormality area and the user identified healthy area and between the clusters within the abnormality and the user identified healthy areas.....	194
Figure 5.42 - For Image-ID mdb090 graph showing the dissimilarity between the cluster having the user tagged location and other clusters belonging to the abnormality area and the user identified healthy area.....	194
Figure 6.1 - CT Image data for the healthy case.....	200
Figure 6.2 - Processing details of the ROI on the left lung	200
Figure 6.3 - Minor and Major axis of the fitted ellipses to the Blood-Vessel (a), Airway-Wall (b) and Airway-Lumen (c).....	201

Figure 6.4 - HCS process based segmentation details within the hand drawn boundary on the right lung	202
Figure 6.5 - Minor and Major axis of the fitted ellipse to the Blood-Vessel (a), Airway-Wall (b) and Airway-Lumen (c).....	202
Figure 6.6 - CT Image data for the Cystic Fibrosis diagnosed case	203
Figure 6.7 - CT image data within the ROI (18x12) marked in the left lungs of Figure 6.6.	203
Figure 6.8 - Minor and Major axis of the fitted ellipse to the Blood-Vessel (a), Airway-Wall (b) and Airway-Lumen (c).....	204
Figure 6.9 - Screen capture of the GUI similar to one used by the radiologist to manually measure the dimensions of the Airway and the accompanying Blood-Vessel	207
Figure 6.10 (A) - Images showing the part of the image within the ROI surrounding an Airway and the adjoining Blood Vessel and the user tagged locations identifying background (Yellow) Airway Lumen (Blue), Airway Wall (Green) and Blood Vessel (Red).....	208
Figure 6.10 (B) - Images showing the part of the image within the ROI surrounding an Airway and the adjoining Blood Vessel and the user tagged locations identifying background (Yellow) Airway Lumen (Blue), Airway Wall (Green) and Blood Vessel (Red).....	209
Figure 6.11 (A) - Images showing the major and minor axes of the ellipses fitted around Blood Vessel (Red), Airway Lumen (Blue) and Airway Wall (Green).....	210
Figure 6.11 (B) - Images showing the major and minor axes of the ellipses fitted around Blood Vessel (Red), Airway Lumen (Blue) and Airway Wall (Green).....	211
Figure 6.12 - Image showing the 3D plot of the Airway Wall Thickness (AWT), Airway Lumen Diameter (ALD) and the ratio ALD:VD where VD is the blood vessel diameter	215
Figure 6.13 (A) - Images showing the approximate size and location of the abnormality and the ROI surrounding it	220
Figure 6.13 (B) - Images showing the approximate size and location of the abnormality and the ROI surrounding it	221
Figure 6.13 (C) - Images showing the approximate size and location of the abnormality and the ROI surrounding it.....	222
Figure 6.13 (D) - Images showing the approximate size and location of the abnormality and the ROI surrounding it	223
Figure 6.14 (A) - Images showing the abnormality and the ROI surrounding it (Column 2). For the HCS process segmentation, chosen by the user, the regions (Column 3) and their boundaries (Column 4)	224
Figure 6.14 (B) - Images showing the abnormality and the ROI surrounding it (Column 2). For the HCS process segmentation, chosen by the user, the regions (Column 3) and their boundaries (Column 4)	225
Figure 6.14 (C) - Images showing the abnormality and the ROI surrounding it (Column 2). For the HCS process segmentation, chosen by the user, the regions (Column 3) and their boundaries (Column 4)	226
Figure 6.14 (D) - Images showing the abnormality and the ROI surrounding it (Column 2). For the HCS process segmentation, chosen by the user, the regions (Column 3) and their boundaries (Column 4)	227
Figure 6.15 (A) - Images showing the Region (Column 1) and Boundaries (Column 2) of the abnormality and the healthy region surrounding it chosen by the user.	230
Figure 6.15 (B) - Images showing the Region (Column 1) and Boundaries (Column 2) of the abnormality and the healthy region surrounding it chosen by the user.....	231

Figure 6.15 (C) - Images showing the Region (Column 1) and Boundaries (Column 2) of the abnormality and the healthy region surrounding it chosen by the user.....	232
Figure 6.15 (D) - Images showing the Region (Column 1) and Boundaries (Column 2) of the abnormality and the healthy region surrounding it chosen by the user.....	233
Figure 6.16 - Invasive carcinoma of the right breast. The irregular mass with stellate borders is a strong indicator of malignancy.....	238
Figure A2.1 – Airway wall measurement using the full-width at half maximum algorithm.....	258
Figure A4.1 – Thin slice CT scan showing regions of gas trapping.....	262
Figure A6.1 – Radiologist's diagnosis of the sixteen mini-MIAS cases.....	265

Note : Unless specified otherwise all figures, graphs, tables of values and images are created for this study by the author.

List of Tables

Table 3.1 - Coordinates of three of the pixels located inside and outside the expert marked boundary of the infarct and their pixel values.....	66
Table 3.2 - Details of the pixel values in the MRI image shown in Figure 3.23	71
Table 3.3 - Details of the four regions in the intermediate HCS process segmentation output shown in Figure 3.29	76
Table 3.4 - Details of the four regions in the intermediate HCS process segmentation output shown in Figure 3.30	77
Table-4.1 Hounsfield values of the pixel locations within the different anatomical regions.....	94
Table-4.2 - X-ray attenuation of the pixels within the airway lumen region (Blue) and lung parenchyma region (Yellow), miss-classified as airway lumen (Figure 4.9 b).....	96
Table-4.3 - X-ray attenuation of the pixels within the airway lumen region (Blue) and lung parenchyma region (Yellow), miss-classified as airway lumen (Figure 4.10 b).....	98
Table-4.4 Properties of the different anatomical regions (Figure 4.14 c).....	105
Table-4.5 - Details of the user tagged locations in Figure 4.15 b.....	106
Table-4.6 Properties of the different anatomical regions (Figure 4.15 c).....	107
Table-4.7 - Details of the user tagged locations in Figure 4.16 b.....	108
Table-4.8 - Details of the user tagged locations in Figure 4.17 b.....	109
Table-4.9 - Minor and Major axis (Figure 4.22) dimensions (in pixels) of the fitted ellipse to the boundary of the Blood vessel, Airway wall and Airway lumen shown in Figure 4.20 a	115
Table-4.10 - Linear measurements of the airway and the accompanying blood vessel of Figure 4.22.....	116
Table-4.11 - Ratios of the various linear dimensions of the airway and the accompanying blood vessel of Figure 4.22.....	116
Table-4.12 - Area related dimensions of the airway and the accompanying blood vessel of Figure 4.22.....	117
Table-4.13 - Ratios of Area related dimensions of the airway and the accompanying blood vessel of Figure 4.22.....	117
Table-4.14 - Minor and Major axis dimensions (in pixels) of the fitted ellipse to the boundary of the Blood vessel, Airway wall and Airway lumen (Figure 4.27).....	126
Table-4.15 - The difference between the Minor and Major axis dimensions (in pixels) of the fitted ellipse to the boundary of the Blood vessel, Airway wall and Airway lumen (Figure 4.22) (Table 4.9) and (Figure 4.27) (Table 4.14)	127
Table 5.1 - Details of the intermediate segmented results shown in Figures 5.2 to 5.5	132
Table 5.2 - Details of the five regions in the intermediate segmentation result shown in Figure 5.2.	133
Table 5.3 - Details of the four regions in the intermediate segmentation result shown in Figure 5.3..	134
Table 5.4 - Details of the three regions in the intermediate segmentation result shown in Figure 5.4.....	135
Table 5.5 - Details of the two regions in the intermediate segmentation result shown in Figure 5.5.....	136
Table 5.6 - Details of the intermediate segmented results shown in Figure 5.7 to 5.10....	138

Table 5.7 - Details of the six regions in the intermediate segmentation result shown in Figure 5.7	139
Table 5.8 - Details of the four regions in the intermediate segmentation result shown in Figure 5.8	140
Table 5.9 - Details of the three regions in the intermediate segmentation result shown in Figure 5.9.....	141
Table 5.10 - Details of the two regions in the intermediate segmentation result shown in Figure 5.10.....	142
Table 5.11 - Details of the breast tissue type, classes of abnormalities and severity of abnormality considered, for evaluating the objective measure.....	168
Table-6.1 - Minor and Major axis dimensions (in pixels) of the fitted ellipse to the boundary of the Blood-Vessel, Airway-Wall and Airway-Lumen.....	201
Table-6.2 - Minor and Major axis dimensions (in pixels) of the fitted ellipse to the boundary of the Blood-Vessel, Airway-Wall and Airway-Lumen (Figure 6.4)	202
Table-6.3 - Minor and Major axis dimensions (in pixels) of the fitted ellipse to the boundary of the Blood-Vessel, Airway-Wall and Airway-Lumen (Figure 6.8).....	204
Table-6.4 - The relative measures for the two cases.....	205
Table-6.5 - HCS process based objective measure of the dimensions of the anatomies in pixels.....	212
Table-6.6 - Measurements by the expert in millimetre.....	212
Table-6.7 - The measures for the three cases of known diagnosis.....	214
Table 6.8 - The measures for the seven cases of unknown diagnosis.....	214
Table 6.9 - Performance of the CAM process in differentiating malignant from benign abnormalities.....	235
Table 6.10 - Breast Imaging Reporting and Data System (BIRADS) score.....	236
Table 6.11 - Performance of the expert in differentiating malignant from benign abnormalities.....	237

Note : Unless specified otherwise all figures, graphs, tables of values and images are created for this study by the author.

List of Equations

$$Precision = \frac{t_p}{t_p + f_p} \quad [2.1] \dots\dots\dots 16$$

$$Recall = \frac{t_p}{t_p + f_n} \quad [2.2] \dots\dots\dots 16$$

$$F = \frac{(Precision \times Recall)}{((1 - \alpha) \times Precision + \alpha \times Recall)} \quad [2.3] \dots\dots\dots 16$$

$$Number\ of\ combinations = \frac{N \times (N - 1)}{2} \quad [3.1] \dots\dots\dots 40$$

$$\chi^2 = \sum \frac{(R_i - S_i)^2}{R_i + S_i} \quad [3.2] \dots\dots\dots 41$$

$$Q(\chi^2 | \nu) = Q\left(\frac{\nu}{2}, \frac{\chi^2}{2}\right) = \text{gammap}\left(\frac{\nu}{2}, \frac{\chi^2}{2}\right) \quad [3.3] \dots\dots\dots 42$$

$$F = \frac{(Precision \times Recall)}{((1 - \alpha) \times Precision + \alpha \times Recall)} \quad [3.4] \dots\dots\dots 54$$

$$P_1 \ (2 \leq N(p_0) \leq 6) \ \&\& \ (T(p_0) = 1) \ \&\& \ (p_1 \cdot p_3 \cdot p_5 = 0) \ \&\& \ (p_3 \cdot p_5 \cdot p_7 = 0) \quad [3.5] \dots\dots\dots 57$$

$$P_2 \ (2 \leq N(p_0) \leq 6) \ \&\& \ (T(p_0) = 1) \ \&\& \ (p_1 \cdot p_3 \cdot p_7 = 0) \ \&\& \ (p_1 \cdot p_5 \cdot p_7 = 0) \quad [3.6] \dots\dots\dots 57$$

$$HU = mx + b \quad [4.1] \dots\dots\dots 89$$

$$Region_Dissimilarity_Measure = Pixel_Dissimilarity_Measure + \dots\dots\dots Pixel_Spatial_Distance \quad [4.2] \dots\dots\dots 97$$

$$I_o = \{I(m, n) : I(m, n) > T\} \quad [A\ 1.1] \dots\dots\dots 251$$

$$I_b = \{I(m, n) : I(m, n) \leq T\} \quad [A\ 1.2] \dots\dots\dots 251$$

List of Abbreviations

ACR	American College of Radiology
AW	Airway
AWT	Airway Wall Thickness
BIRADS	Breast Imaging Reporting and Data System
BODE	Body mass index, Obstruction, Dyspnea, Exercise
CAD	Computer Aided Diagnostic
CAD(e)	Computer Aided Detection
CAD(i/x)	Computer Aided Diagnosis
CAM	Computer Aided Monitoring
CBF	Cerebral Blood Flow
CBV	Cerebral Blood Volume
CF	Cystic Fibrosis
COPD	Chronic Obstructive Pulmonary Disease
CPU	Central Processing Unit
CSF	Cerebrospinal Fluid
CT	Computed Tomography
DICOM	Digital Imaging and Communications
DWI	Diffusion Weighted Images
FDA	Food and Drug Administration (USA)
FROC	Free-Response Receiver Operating Characteristics
GP-GPU	General Purpose Graphical Processing Unit
GUI	Graphical User Interface
HCS	Hierarchical Clustering based Segmentation
HRCT	High Resolution CT
HSEG	Hierarchical Segmentation
HU	Hounsfield Unit
IPF	Idiopathic Pulmonary Fibrosis
MCCs	Microcalcification Clusters
MDCT	Multi-Detector row CT
MIAS	Mammographic Image Analysis Society
MR	Magnetic Resonance
MRF	Markov Random Field
MRI	Magnetic Resonance Imaging
NASA	National Aeronautics and Space Administration
NHS	National Health Services (UK)

NIH	National Institutes of Health (USA)
PET	Positron Emission Tomography
PWI	Perfusion Weighted Imaging
RAM	Random Access Memory
RHSEG	Recursive Hierarchical Segmentation
ROC	Receiver Operating Characteristics
ROI	Region of Interest
T2-WI	T2 Weighted Images
UIP	Usual Interstitial Pneumonitis
UK or U.K.	United Kingdom
US	Ultrasound or Ultrasonogram
U.S. or U.S.A or USA	United States of America

Chapter 1 Introduction and Objectives of the Research

1.1. Aim

The aim of this study is to explore the possibility of adopting image processing techniques to assist medical imaging professionals in perceiving diagnostic images and thus improve diagnostic capability. Specifically, the Hierarchical Clustering based Segmentation (HCS) process [Selvan 2007] is investigated for its ability to augment the diagnostic information present in Computed Tomography (CT) images for cystic fibrosis (CF) diagnosis and digitised X-ray mammograms, to differentiate malignant from benign abnormalities.

1.2. Background

Radiologists' expertise in reading diagnostic images calls for a combination of perceptual skills to find what may be faint and small features in a complex visual environment, and interpretive skills to rate their (the features') significance [Tabar and Dean, 1985]. Computing systems are more consistent in their perceiving ability but they cannot match human interpretive skills. Drawing a line so as to limit the system's interpretive function has the virtue of achieving a complementary synthesis of system and radiologists' strengths [Claridge 1997]. However, in practice the question of where to draw the line in computer aided detection/diagnostic systems between perception and interpretation is problematic [Hartswood *et al.* 1997]. Hence, one needs a versatile tool which is flexible enough to accommodate the varied requirements of the user.

1.3. Objective and Purpose of this Study

The objective of this study is to investigate the effectiveness of two paradigm shifting approaches in the usage of computers to assist and/or aid medical image processing and subsequent interpretation. This paradigm shift is based on two methods which will be tested for validity and effectiveness :

- User decision based medical image processing and HCS process aided Image Interpretation
- Computer aided (disease) monitoring

The above two new approaches use the decision making skills of the users (medical imaging professional) and thus maximise the effectiveness and efficiencies of the image processing techniques. These two new approaches are discussed in detail in the following two sections.

1.3.1. User Decision based Medical Image Processing and HCS Process Aided

Image Interpretation

In the area of medical image processing it has so far been a normal practice to offer a solution for the user under a 'take it or leave it' condition. Moreover, it is usual that the process is treated as a "black box" by the user who has minimal knowledge of what happens within the process and how and why it came to a particular solution. Hence, the user does not have a full understanding of the logic the process made use of to arrive upon the solution. This lack of knowledge on the part of the user has led to situations where the software tools have been used inappropriately by the user. For example, Alberdi *et al* [Alberdi *et al* 2005] have suggested that X-ray mammogram readers were using computer aided detection (CAD) software as a decision making tool instead of a prompting aid. They conclude that "incorrect CAD can have a detrimental effect on human decisions" [Alberdi *et al* 2005].

Current prompting based Computer aided diagnosis (CADx) software makes their own decision regarding the existence of some abnormality at a location and places a prompt at that location [Alberdi *et al* 2005]. The user is left with the choice of either accepting the prompting software decision or rejecting it. The prompting software does not indicate how and why that location was prompted. Hartwood *et al.* [1997] in their study note that radiologists tried to make sense of the system's behaviour from the evidence of the features it had prompted. In their study they had observed the following responses of the radiologists towards the prompting software's behaviour [Hartwood 1997]:

- the radiologists had misunderstood the extent of the system's capabilities and were confused because of apparent inconsistencies in its behaviour.
- the radiologists were unable to accurately place the system's operational scope: *i.e.*, the types of feature it is capable of detecting.
- the radiologists had problems with understanding how the system interprets micro- calcification clusters
- the radiologists indicated that they had not seen anything of significance in the areas prompted.

In the application developed to improve users' perception, HCS process highlights the dissimilar regions. Unlike the prompting, the highlighting process aids the user to evaluate the significance of the differences highlighted by the HCS process. Hence

the HCS process is more suitable for drawing the attention of the user and thus aiding in the process of the diagnosis.

Moreover, in the developed solutions in this study, the user makes decisions at key stages in the process. Such that in the medical image processing solutions developed in this study, while the computer does its work the user still has full control of the process and makes key decisions at crucial stages. Thus the solution pathway is traversed by both the man and machine hand in hand. Hence the user is well aware of how and why the process arrived upon a solution.

Thus, a new paradigm of “user-decision based image processing” is introduced. It should be noted that this solution pathway is subtly different from currently existing closely related supervised (i.e. user-guided) methods.

The following two applications developed in this study will explain this new and novel user-decision based image processing approach.

1.3.1.1. User-Decision based CT Image Processing

An application area to demonstrate the developed image processing scheme is to segment blood vessel, airway wall and lumen, in the CT images of the lungs. One of the developed methods is fully automated i.e. unsupervised and completely data driven. Specifying a region of interest by the user, the method does not need any further assistance from the user to do the initial segmentation. However, the method yields a set of solutions and the role of the user is to decide and choose the best segmentation. Subsequently, making use of the user decided segmentation output, the developed method automatically fits the best fitting ellipse and estimates the dimensions of blood vessels, airway walls and corresponding lumen.

The above outlined method, cannot be categorised as supervised because the method carries out the initial segmentation fully automatically without any kind of intervention from the user. This means that the entire segmentation process is totally unsupervised.

However, the process as a whole cannot be termed as automatic or unsupervised, that is, the method as a whole is not fully automatic. This is because once the

unsupervised segmentation stage is performed; the user makes the decision of choosing the best segmentation most suitable for their use. As per the users' decision, the method proceeds to the next stage and carries it out without any further intervention from the user.

1.3.1.2. User Decision based Mammogram Image Processing

Another image processing application, developed in this study, is to differentiate benign from malignant abnormalities, by processing X-ray mammograms. The developed method first does an automatic unsupervised segmentation of the boundary of the abnormality. But, since the method yields a set of segmentation solutions, it is left for the user to decide and choose the best segmentation which defines the boundary of the abnormality most appropriately.

It is practically impossible for the user to precisely delineate the complex boundaries of the different regions in the image. However, the user is the best judge to choose the most appropriate segmentation from a set of segmentations (yielded by the HCS process) such that the segmented abnormality and the healthy parts of the image are isolated as unique regions. This decision making process includes the user rather than designing an automated procedure that removes the user from the solution pathway. Once the correct segmentation which captures the best shape and size of the abnormality has been decided by the user, subsequent objective measure to differentiate benign from malignant abnormalities is performed by the machine.

In a similar manner to the CT segmentation method, the mammogram segmentation developed in this study is not supervised because the method does the segmentation fully automatically without any type of intervention or parameters tuning by the user. Thus, the whole segmentation process is fully unsupervised, that is, purely data driven. The process still needs the decision of the user to decide which segmentation is best suited for the subsequent objective measure, i.e. the method as a whole is not fully automatic. This is because once the unsupervised segmentation stage is performed, the user makes the decision of choosing the best segmentation most suitable for their use. As per their decision, the method proceeds to the next stage and carries on without any further intervention from the user. Thus, this method can neither be categorised as supervised (i.e. user guided) nor unsupervised but rather as “user-decision” driven based.

1.3.2. Computer Aided (disease) Monitoring (CAM)

In the domain of computers aiding medical image interpretation, so far computers have been used for Computer Aided Detection (CAD) and/or Computer Aided Diagnosis (CADx). Computer aided detection (CADE) systems address the problem that radiologists often miss signs of cancers that are retrospectively visible in mammograms. Furthermore, computer aided diagnosis (CADx) systems assist the radiologist in the classification of mammographic lesions as benign or malignant [Elter and Horsch 2009].

In contrast to the above listed current practices, making use of the developed methods in this study, computers can aid users to "monitor" the progress and/or prognosis of disease. Thus, we introduce a new process named Computer Aided disease Monitoring (CAM) a new paradigm for solution pathway.

The following two applications, for which CAM methods have been developed in this study, will explain this new and novel approach :

- Computer aided Monitoring of Cystic Fibrosis
- Computer aided Monitoring of breast abnormalities

1.3.2.1. Computer Aided (disease) Monitoring of Cystic Fibrosis

Cystic Fibrosis is normally diagnosed through gene detection. CT images of the lungs can give visual indications or clue of the presence of the disease. Hence, strictly speaking medical image processing techniques are neither needed for CAD nor are they needed for CADx. However, the morphological changes like variation of the dimensions of the blood vessels and airways over time cannot be easily visualised. Hence, the method developed in the current study helps the radiologists to "monitor" the CF condition's progress and/or prognosis.

1.3.2.2. Computer Aided (disease) Monitoring of Breast Abnormalities

Yet another application which was developed in this study is to differentiate benign from malignant abnormalities by processing X-ray mammograms. In the method hereby developed, the approximate location of the abnormality is given by the user. Hence, the developed method is not a CAD solution. The severity of the abnormality (i.e. whether the abnormality is benign or malignant) will also be subsequently confirmed by other means such as taking an Ultrasound guided needle biopsy

[Osanai *et al.* 2000]. Hence the developed method in this study is not a CADx method either. However, the developed method delineates the boundary of the abnormality and also differentiates whether that part of the abnormality is benign or malignant. This is useful to subsequently monitor the size of the abnormality as well as the response of the abnormality to treatment. Thus, the developed method can be used as an aid for monitoring the abnormality. Hence, the developed method is neither CAD nor CADx but rather “CAM”.

1.3.3.Uniqueness and Novelty of the Developed Medical Image Processing Methods

The following are other aspects in which the medical image processing methods, developed for this study, are unique and novel when compared to current existing methods :

- the methods developed in this study need no prior training. The developed methods find the dissimilarity within the same image. Hence, the input data can be made use of without any kind of data pre-processing like normalization.
- the unsupervised, that is, the autonomous components of the method can be applied to any medical modality image data without any modifications whatsoever.

For instance, the same HCS process which was made use of to find the boundaries of the natural scenes (please see Chapter 3 Section 3.4) was used, without any modifications or parameter tuning, to find the boundaries of the abnormalities in X-ray mammograms (please see Chapter 5 Section 5.2). For the segmentation of blood vessels and airway in CT images (please see Chapter 4 Section 4.3) the only additional parameter considered was the spatial distance between the cluster (please see Chapter 4 Section 4.3.4.1).

1.4. Contribution of the Study

Machines are good at operations which require precision and computing objective measures. In contrast, humans are good at generalisation and making decisions based on their past experience and heuristics. So, to solve any problem with a solution involving human-machine interaction, it is imperative that the tasks are shared appropriately. However the boundary which divides these two different set of tasks is not well defined in medical image interpretation. Hence one needs a versatile tool which is flexible enough to accommodate the varied requirements of the user. In this

study, the HCS process is investigated for offering the user such a versatile and flexible environment.

Tissue abnormality in a medical image is usually related to a dissimilar part of an otherwise homogeneous image. The dissimilarity may be subtle or strong depending on the medical modality and the type of abnormal tissue. HCS is a dissimilarity highlighting process that yields a hierarchy of segmentation results. In this study, the HCS process was investigated for offering the user a versatile and flexible environment to perceive the varied dissimilarities that might be present in diagnostic images. Consequently, the user derives the maximum benefit from the computational capability (perception) of the machine and at the same time incorporate their own decision process (interpretation) at the appropriate places.

As a result of the above investigation this study demonstrates how HCS process can be used to aid radiologists in their interpretive tasks. Specifically, this study has designed the following HCS aided diagnostic image interpretation applications :

- interpretation of CT images of the lungs to quantitatively measure the dimensions of the airways and the accompanying blood vessels.
- interpretation of X-ray mammograms to quantitatively differentiate benign from malignant abnormalities.

One of the major contribution of this study is to demonstrate how the above HCS aided interpretation of diagnostic images can be used to monitor disease conditions. This thesis details the development and evaluation of the novel computer aided monitoring (CAM) system. The designed CAM system is used to objectively measure the properties of suspected abnormal areas in the CT images of the lungs and in X-ray mammogram. Thus, the CAM system can be used to assist the clinician to objectively monitor the abnormality. For instance its response to treatment and consequently its prognosis. The implemented CAM system to monitor abnormalities in X-ray mammograms is briefly described below.

Using the approximate location and size of the abnormality, obtained from the user, the HCS process automatically identifies the more appropriate boundaries of the different regions within a region of interest (ROI), centred at the approximate location. From the set of, HCS process segmented, regions the user identifies the

regions which most likely represent the abnormality and the healthy areas. Subsequently the CAM system compares the characteristics of the user identified abnormal region with that of the healthy region; to differentiate malignant from benign abnormality. In processing sixteen mammograms, the designed CAM system demonstrated the possibility of successfully differentiating malignant from benign abnormalities.

1.5.Thesis Structure

The rest of this thesis is structured as follows :

- Chapter 2 : Background and Literature review

Background information related to the following areas of investigation will be discussed :

- Image segmentation and clustering.
- Diagnostic image perception and interpretation.
- Computer aided detection and computer aided diagnosis.
- Cystic fibrosis.
- Breast cancer detection and diagnosis.

- Chapter 3 : Hierarchical Clustering based Segmentation (HCS)

A brief but complete discussion about the functioning, performance and suitability of Hierarchical Clustering based Segmentation process.

- Chapter 4 : HCS Process Aided Interpretation of CT Images of the Lungs to Monitor Cystic Fibrosis

Chapter 4 discusses how the HCS process can be used to aid users in the interpretation of diagnostic images. Specifically, details are given about how the HCS process can be used to aid users to interpret CT images of the lungs to quantitatively measure the dimensions of the airways and the accompanying blood vessels.

- Chapter 5 : HCS Process Aided Interpretation of X-ray Mammograms

This chapter discusses how the HCS process can be used to aid users in the interpretation of diagnostic images. Specifically, details are given about how the HCS process can be used to aid users to interpret X-ray mammograms to quantitatively differentiate benign from malignant abnormalities.

- Chapter 6.: HCS process aided disease monitoring

This chapter discusses how the HCS process can be used to aid the user in the monitoring of the following diseases :

- to monitor cystic fibrosis by processing CT images of the lungs.
 - to monitor abnormalities of the breast by processing X-ray mammograms.
- Chapter 7 :HCS process possibilities and proposals
- This chapter discusses how the capabilities of the HCS process developed in this study can be further explored in the following areas of diagnostic imaging perception and interpretation :
- diagnostic image interpretation of the CT images of the lungs to monitor cystic fibrosis.
 - diagnostic image interpretation of the X-ray mammograms to monitor breast abnormalities.

2.1. Introduction

The main focus of the current study is to explore the possibility of incorporating the experts' decision process within a diagnostic image processing environment to elicit objective measures for monitoring diseases. The following are the specific diagnostic applications for which the above possibility was explored :

- Quantitative measure of the airways and the accompanying blood vessels' dimensions, by processing CT images of the lungs.
- Quantitative differentiation of malignant from benign abnormalities, by processing X-ray mammograms.

In this chapter background information from published literature related to the following relevant topics is discussed :

- Digital image processing, specifically, segmentation of regions in digital images.
- Diagnosis of Cystic Fibrosis
- Computer Aided Detection and Diagnosis in the context of the abnormalities of the breast.

Many of the references discussed in this chapter are referred to in the main body of the thesis in the relevant chapters. The purpose of this chapter is to collate the literature which informs the study and present it in a unified form.

2.2. Digital Image Segmentation

Image segmentation is an essential processing step for many image analysis applications. There are indications that there is no general method suitable for all image analysis applications [Yang and Jiang, 2002].

In one of their publications Yang and Jiang [2002] list the different types of segmentation techniques. Available segmentation techniques include thresholding [Sahoo *et al.*, 1988], region growing [Udupa and Samarasekera, 1996], clustering [Coleman and Andrews, 1979], classifier [Bezdek *et al.*, 1993], neural network-based approaches [Vilarino *et al.*, 1998], deformable models [Caselles *et al.*, 1997], and Markov random field (MRF) model based approaches [Andrey and Tarroux, 1998]. Appendix 1 gives a synopsis of the above listed different types of segmentation techniques.

Thresholding does not take into account the spatial aspects of an image. This makes it sensitive to noise. The primary disadvantage of region growing is that it requires manual interaction to obtain the seed point. Clustering algorithms do not require training data, but they do require an initial segmentation. Classifier methods are pattern recognition techniques to partition a feature space derived from the image using data with known labels. Neural network represents a paradigm for machine learning and can be used in a variety of ways for image segmentation. Deformable models are physically motivated, model-based techniques for delineating region boundaries using closed parametric curves or surfaces that deform under the influence of internal and external forces [Yang and Jiang, 2002].

MRF modelling itself is not a segmentation method but a statistical model which can be used within segmentation methods. MRFs model spatial interactions between neighbouring or nearby pixels. These local correlations provide a mechanism for modelling a variety of image properties [Li, 1985]. In medical imaging, they are typically used to take into account the fact that most pixels belong to the same class as their neighbouring pixels. In physical terms, this implies that any anatomical structure that consists of only one pixel has a very low probability of occurring under a MRF assumption [Pham *et al.*, 2000].

The methodology of using MRF models to the problem of segmentation has emerged later and has created a lot of interest. Markov random fields have been, and are increasingly being used to model a prior beliefs about the continuity of image features such as region labels, textures, edges and so on [Lu and Jiang, 2001]. The main disadvantage of MRF-based methods is that the objective function associated with most nontrivial MRF problems is extremely non-convex and as such the minimization problem is computationally very taxing. To reduce the computational burden, some approaches based on multiresolution techniques have been reported [Sarkar *et al.*, 2000], [Kim and Yang *et al.*, 1994]. The essence of the MRF framework on multi-resolution is that it starts processing images at a coarse resolution, and then progressively refine them to finer resolution [Yang and Jiang, 2002].

Hierarchical organization is one of the main characteristics of human segmentation. A human subject segments a natural image by identifying physical objects and marking their boundaries up to a certain level of detail. If we suppose that different subjects segmenting a single image perceive the same objects then, up to variations in the exact localization of boundaries, the intersection of their segments determines the finest level of detail considered [Arbelaez, 2006].

Segmentation can be thought of as a process of grouping visual information, where the details are grouped into objects, objects into classes of objects, etc. Thus, starting from the composite segmentation, the perceptual organization of the image can be represented by a tree of regions, ordered by inclusion. The root of the tree is the entire scene, the leaves are the finest details and each region represents an object at a certain scale of observation [Arbelaez, 2006].

Since the early days of computer vision, the hierarchical structure of visual perception has motivated clustering techniques to segmentation [Ohlander *et al.*, 1978], where connected regions of the image domain are classified according to an inter-region dissimilarity measure. The traditional approach for clustering is a bottom-up approach, also called agglomerative clustering, where the regions of an initial partition are iteratively merged [Nadler and Smith, 1993].

In one of his publication, Arbelaez [2006] studied the segmentation problem in the framework of data classification, where the notions of tree of regions and scale are formalized by the structure of indexed hierarchy or, equivalently, by the definition of an ultrametric distance on the image domain. He presents a formulation of the problem in terms of contours that allows to represent an indexed hierarchy of regions as a soft boundary image called ultrametric contour map.

From a theoretical point of view, topological feature clustering is a precise and powerful partitioning technique. However, designing efficient algorithms is a non-trivial task, primarily with respect to the processing sequence of the neighbouring pixels. An implemented algorithm can process pixel vectors only sequentially. Initializing a merge process means selecting one pixel at a time and computing the Euclidean distance to its neighbours. Consequently, there is always a preference for the first neighbour. This fundamental problem underlies all clustering algorithms.

Two effects occur depending on the counter strategy. Either some large regions consume all the others without visual significance or restrictive rules leave too many small regions leading to an over-segmentation. Both problems can be dampened using heuristic convergence criteria [Tilton, 2000] but the dependency on initial processing direction remains. A brute force approach, where only those regions with the smallest overall distance are merged in each step is the only solution to overcome this effect. This is necessary to achieve independence with respect to rotation and translation of the image objects [Thies *et al.*, 2003].

The spectral clustering algorithm is based on the concept of similarity between locations in an image [Shi and Malik, 1997] [Kannan *et al.*, 2000], [Ng *et al.*, 2001]. Weiss [1999] presents a comparative analysis of various clustering algorithms based on spectral methods in his publication.

Nearly three quarters of a century ago, Wertheimer [1938] pointed out the importance of perceptual grouping and organization in vision and listed several key factors, such as similarity, proximity, and good continuation, which lead to visual grouping. However, even to this day, many of the computational issues of perceptual grouping remain unresolved [Shi and Malik, 1997] [Han, *et al.* 2006].

Since there are many possible partitions of the domain of an image into subsets, how do we pick the “right” one? Following are two aspects to be considered here :

- The first is that there may not be a single correct answer. A Bayesian view is appropriate as there are several possible interpretations in the context of prior world knowledge. Bayesian techniques use prior knowledge regarding the statistical distribution of pixel values from known samples to estimate the probabilities that an individual pixel value belongs to each of the component objects in the image.

The difficulty, of course, is in specifying the prior world knowledge. Some of it is low level, such as coherence of brightness, colour, texture, or motion, but equally important is mid- or high-level knowledge about symmetries of objects or object models. [Shi and Malik, 1997].

- The second aspect is that the partitioning is inherently hierarchical. Therefore, it is more appropriate to think of returning a tree structure corresponding to a hierarchical partition instead of a single “flat” partition [Shi and Malik, 1997].

This suggests that image segmentation based on low-level cues cannot and should not aim to produce a complete final “correct” segmentation. The objective should instead be to use the low-level coherence of brightness, colour, texture, or motion attributes to sequentially come up with hierarchical partitions. Mid- and high-level knowledge can be used to either confirm these groups or select some for further attention. This attention could result in further repartitioning or grouping. Prior literature on the related problems of clustering, grouping and image segmentation is huge. The clustering community [Jain and Dubes, 1988] has offered agglomerative and divisive algorithms; in image segmentation, there are region-based merge and split algorithms [Shi and Malik, 1997].

Hierarchical Clustering-based Segmentation (HCS) [Selvan 2007] implements the traditional agglomerative clustering. The HCS procedure automatically generates a hierarchy of segmented images. The hierarchy of segmented images is generated by partitioning an image into its constituent regions at hierarchical levels of allowable dissimilarity between its different regions. At any particular level in the hierarchy, the segmentation process cluster the pixels and/or regions which have dissimilarity among them less than or equal to the dissimilarity allowed for that level. Thus Hierarchical clustering based segmentation (HCS) process mimics the capability of human vision [Selvan 2007].

The hierarchy of segmented images generated by the HCS process represents the continuous merging of similar, spatially adjacent or disjoint, regions as the allowable threshold value of dissimilarity between regions, for merging, is gradually increased. Other similar Agglomerative hierarchical clustering or bottom-up methods suffer from a distorting phenomena, in which the cluster structures depend on the order in which the regions are considered for merging [Nadler, 1993]. The brute force approach, followed by the HCS process, where only those regions with the smallest overall dissimilarity are merged in each step, is the only solution to overcome this effect [Thies, 2003].

HCS process is unsupervised and is completely data driven. This ensures that the segmentation process can be applied to any image, without any prior information about the image data and without any need for prior training of the segmentation process with the relevant image data [Selvan 2007].

Unsupervised image segmentation is an important component in many image understanding algorithms and practical vision systems. However, evaluation of segmentation algorithms thus far has been largely subjective, leaving a system designer to judge the effectiveness of a technique based only on intuition and results in the form of a few example segmented images. This is largely due to image segmentation being an ill-defined problem-there is no unique ground-truth segmentation of an image against which the output of an algorithm may be compared. Unnikrishnan *et al.* [2007] in their paper demonstrate how a recently proposed measure of similarity, the Normalized Probabilistic Rand (NPR) index, can be used to perform a quantitative comparison between image segmentation algorithms using a hand-labelled set of ground-truth segmentations. They showed that the measure allows principled comparisons between segmentations created by different algorithms, as well as segmentations on different images. They outline a procedure for algorithm evaluation through an example evaluation of some familiar algorithms. Results are presented on the 300 images in the publicly available Berkeley Segmentation Data Set [Unnikrishnan *et al.* 2007].

Martin *et al.* [2002] [2004] designed the Berkeley segmentation dataset and benchmark system. The goal of their work is to provide an empirical basis for research on image segmentation and boundary detection. To this end, they have collected 12,000 hand-labelled segmentations of 1,000 Corel dataset images from 30 human subjects. Half of the segmentations were obtained from presenting the subject with a colour image; the other half from presenting a grayscale image. The public benchmark based on this data consists of all of the grayscale and color segmentations for 300 images. The images are divided into a training set of 200 images, and a test set of 100 images. The goal of the benchmark is to produce a score for an algorithm's boundaries for the following two reasons:

- so that different algorithms can be compared to each other
- so that progress toward human-level performance can be tracked over time.

Any boundary marked by a human subject is considered to be valid. Thus the human segmented images provide the ground truth boundaries. Since they have multiple segmentations of each image by different subjects, it is the collection of these human-marked boundaries that constitutes the ground truth. Presented the

segmentation (boundary) output of some algorithm for an image. The boundary map of the algorithm is compared with the ground truth boundaries at many levels. At each level, two quantities -- precision and recall -- are computed and in this manner a precision-recall curve for the algorithm is produced. Precision and recall are similar to, but different from the axes of ROC curves. Precision is the probability that a machine-generated boundary pixel is a true boundary (ground truth) pixel (Equation 2.1). Recall is the probability that a true boundary (ground truth) pixel is detected (Equation 2.2). Martin *et al.* [2002] [2004] consider these axes to be sensible and intuitive. Precision is a measure of how much noise is in the output of the detector. Recall is a measure of how much of the ground truth is detected. The curve shows the inherent trade-off between these two quantities -- the trade-off between misses and false positives -- as the detector threshold changes. The performance of the algorithm is found by the following summary statistic : The F-measure is found at all points on the precision-recall curve (Equation 2.3). The maximum F-measure value across an algorithm's precision-recall curve is its summary statistic.

$$Precision = \frac{t_p}{t_p + f_p} \quad [2.1]$$

$$Recall = \frac{t_p}{t_p + f_n} \quad [2.2]$$

$$F = \frac{(Precision \times Recall)}{((1 - \alpha) \times Precision + \alpha \times Recall)} \quad [2.3]$$

Where :

t_p is True positive

f_p is False positive

f_n is False negative

Value of α is set to 0.5 [Martin *et al.* 2002]

The above detailed benchmarking process was used to evaluate the performance of the HCS process [Selvan, 2007], which is made use of in this study (For further details please see Chapter.3 Section 3.4).

2.2.1. Medical Image Segmentation

Diagnostic imaging is an invaluable tool in medicine today. Magnetic resonance imaging (MRI), CT, digital X-ray mammography, and other imaging modalities (like Ultrasound etc.) provide an effective means for non-invasively mapping the anatomy of a subject. These technologies have greatly increased knowledge of normal and diseased anatomy for medical research and are a critical component in diagnosis and treatment planning [Pham *et al.*, 2000].

With the increasing resolution and number of medical images, the use of computers in facilitating their processing and analysis has become necessary. In particular, computer algorithms for the delineation of anatomical structures and other regions of interest are a key component in assisting and automating specific radiological tasks. These algorithms, called image segmentation algorithms, play a vital role in numerous biomedical imaging applications such as the quantification of tissue volumes [Laric and Abukmeil, 1999], diagnosis [Taylor, 1995], localization of pathology [Zijdenbos and Dawant, 1994], study of anatomical structure [Worth *et al.*, 1997], treatment planning [Khoo *et al.*, 1997], partial volume correction of functional imaging data [Muller-Gartner *et al.*, 1992], and computer integrated surgery [Ayache *et al.*, 1996] [Grimson *et al.*, 1997]. Additional surveys on image segmentation specifically for medical images have also appeared [Chaney and Pizer, 1992] [Bezdek *et al.*, 1993] [Suetens *et al.*, 1993] [Zijdenbos and Dawant, 1994] [Clarke *et al.*, 1995] [Ayache *et al.*, 1996] [Pham *et al.*, 2000].

The methods employed for medical image segmentation can be divided into the following different categories, *viz.* thresholding approaches, region growing approaches, classifiers, clustering approaches, Markov random field models, artificial neural networks, deformable models, atlas-guided approaches, model-fitting and watershed algorithm [Pham *et al.*, 2000].

A short critical synopsis of each of the above different segmentation methods and their corresponding advantages and disadvantages, as outlined by Pham *et al.* [2000], in their survey on the methods in medical image segmentation can be found in Appendix 1.

2.3. Cystic Fibrosis

Cystic Fibrosis (CF) is a recessive genetic condition. It is the most common autosomal recessive genetic disorder among the Caucasian population. CF is caused by one or more mutations involving the CF transmembrane conductance regulator (CFTR) gene located on chromosome 7. These mutations generally affect ion transport within epithelia-primarily chloride and sodium transport. As a result, there is dehydration and production of thick secretions in many affected organs, most notably the lungs. In the lung, the presence of highly viscous secretions from chronic infection and inflammation causes airway obstruction and subsequent vasoconstriction of the vessels in the microcirculation. This, in turn, causes perfusion defects, altering lung function and ultimately leads to a poor prognosis [NIH Publication-No.-95-3650]

The first step towards improving both life expectancy and the quality of life for patients with CF is to diagnose and monitor the condition. Radiologic technology plays a key role in these processes. Computed tomography, especially the high-resolution CT (HRCT) scan, has become the preferred imaging test to detect early pulmonary disease, before symptoms develop.

CF results in inflammation, hence thickening of airway (AW) walls. It has been demonstrated that AW inflammation begins early in life producing structural AW damage. Because this damage can be present in patients who are relatively asymptomatic, lung disease can progress insidiously. High-resolution computed tomographic imaging has also shown that the AWs of infants and young children with CF have thicker walls and are more dilated than those of normal children. [Mumcuoglu, *et al.*, 2009]

Long *et al.*, [2004] conducted a study to determine whether the airway structure of infants and young children with CF differs from that of normal children by using HRCT imaging. Full-inflation, controlled ventilation HRCT images of the lungs were obtained at four anatomic levels in 34 infants with CF (age, 2.4 \pm 1.4 years) and 20 control infants (age, 1.8 \pm 1.4 years). Short axis diameters of all clearly identifiable, round airway/vessel pairs were measured to obtain airway wall thickness (AWT), airway lumen diameter (ALD), and vessel diameter (VD). They found that in infants with CF, mean AWT (\pm SD) was 0.58 \pm 0.13 mm, ALD was 1.31 \pm 0.56

mm, and VD was 1.62 \pm 0.58 mm. In control infants, mean AWT was 0.49 \pm 0.13 mm, ALD was 1.07 \pm 0.42 mm, and VD was 1.86 \pm 0.64 mm. Mean AWT and ALD were greater in children with CF than in normal subjects ($P < .001$). ALD:VD ratios increased with age in patients with CF compared with control subjects ($P = .026$). They concluded that the airways of infants and young children with CF have thicker walls and are more dilated than those of normal infants [Long *et al.*, 2004].

de Jong *et al.* [2005 (July)] carried out a study to quantify airway wall thickening and lumen dilatation in children with CF over a 2-year interval. Children with CF ($n = 23$) who had two CT scans (CTcf1 and CTcf2) combined with pulmonary function tests (PFTs), with a 2-year interval between measurements, were compared with control subjects ($n = 21$) who had one CT (CTcontrols). On cross-sectional cut airway-artery pairs, airway wall area (WA), airway lumen area (LA) and perimeter, and arterial area (AA) were quantified. LA/AA (= marker of bronchiectasis), airway wall thickness (AWT), and WA/AA (= markers of wall thickness) were calculated. CT scans were scored using four different scoring systems. PFTs were expressed as percent predicted. They found that Airway WA-to-AA ratio was 1.45 ($P < 0.001$) and airway LA-to-AA ratio was 1.92 times higher ($P < 0.001$) in children with CF compared with age-matched control subjects. LA/AA and WA/AA remained unchanged from CTcf1 to CTcf2 and did not increase with age. AWT as a function of airway size increased from CTcf1 to CTcf2 by 2% (0.03 mm; $P = 0.02$). The change in AWT was inversely related to the change in forced expiratory flow between 25 and 75% of expiratory VC ($P = 0.002$). They concluded that in CF, quantitative measurements of airways on CT scans show an increased ratio between airway LA and AA and progressive airway wall thickening. Scoring systems show progression of bronchiectasis but unchanged AWT. PFTs remained stable.

In the above discussion P value is the probability that the observation occurred by chance. Lower the P value higher the confidence one will have about the observation.

In a study involving 22 male and female patients by Dodd *et al.* [2006], the correlation between exercise limitation and HRCT was stronger than it was between pulmonary function testing or body mass index. Zavalett *et al.* [2007] performed a study which demonstrated that computer aided analysis of CT images can be used towards quantification of various pathologies present in lungs with UIP/IPF. (UIP - Usual Interstitial Pneumonitis) (IPF - Idiopathic Pulmonary Fibrosis).

2.3.1. Measurement of Airways and Blood Vessel Dimensions in CT Images

Ever since the site and nature of airflow obstruction in chronic obstructive pulmonary disease was described by Hogg, Thurlbeck, and Macklem, investigators have been looking for methods to noninvasively measure the airway wall dimensions. Recent advances in CT technology and new computer algorithms have made it possible to visualize and measure the airway wall and lumen [Coxson and Lam, 2009].

In general, CT has been found to be more sensitive to early changes in CF lung disease, often preceding any change in lung function [de Jong, 2004], [Brody, 2004], [Helbich, 1999]. Accurate segmentation is essential for making measurements that can be made on CT images of airways and the blood vessels. The advantages to use computer methodologies to quantify peripheral airway disease include reproducible visualization methods to display the location, severity, and the extent of airway dilatation, bronchial wall thickening, and the presence of mucoid impacted airways. [Kiraly, 2008].

de Jong *et al.* [2005] have carried out a detailed review of the earlier studies which had attempted to quantitatively assess the dimensions of airways through CT images of the lungs. In that review they have mentioned that Saba *et al.* [2003] have developed an alternate technique for measuring airways that are not cut in cross-section. This method involves fitting an ellipse to the airway lumen and wall, and shows great promise in correcting the errors in measurement of obliquely cut airways. They also note that these techniques claim to be more accurate than the more commonly used techniques, but have not been generally applied, presumably because of the limited availability of the complex algorithms involved. An excerpt from de Jong *et al.* [2005] review can be found in Appendix 2.

The HCS process based method of segmentation of airways and the accompanying blood vessels, developed in the present study, approximates their boundary by fitting an ellipse (please refer Chapter 4 Section 4.3.7).

Coxson and Lam [2009] in their publication have critically reviewed the progression of computer techniques to qualitatively assess the Airway wall using CT. Relevant material extracted from their publication can be found in Appendix 3.

From Coxson and Lam [2009] publication the following chronology of publications, related to computer techniques developed to qualitatively assess the Airway wall using CT, can be seen :

- 1992 – 1994 : publications on how to best trace the airway wall to produce the best images [McNamara *et al.* 1992], [Seneterre *et al.*, 1994], [Okazawa *et al.*, 1996].
- 1996 : realisation that quantitative measurements of airway structure were very dependent on the display parameters of the image [Bankier *et al.*, 1996].
- 1997 – 2002 : early very simple approaches using threshold techniques to find the lumen [McNitt-Gray *et al.*, 1997] and simple algorithms like the full-width at half maximum to assess the wall area [Nakano *et al.*, 2002], [Nakano *et al.*, 2002].
- 1997 – 2003 : More complex algorithms using model-based approaches to provide more reliable measurements were developed [Reinhardt *et al.*, 1997], [King *et al.*, 2000], [Saba *et al.*, 2003], [Leader *et al.*, 2003], [San *et al.*, 2008].
- 2005 – 2008 : Correlation between airway wall measurements obtained using CT and those obtained using histology [Nakano *et al.*, 2005] and subjects with symptoms of chronic bronchitis have more airway wall thickening than those with airflow limitation but no symptoms [Orlandi *et al.*, 2005], [Patel *et al.*, 2008].

Most of the studies listed above were performed using traditional HRCT scans. During this time period, CT imaging took a leap forward in complexity with the introduction of the multi-detector row CT (MDCT) scanner. MDCT scanners have allowed the acquisition of sub-millimeter thickness images of the entire chest within a single breath-hold of 5 to 15 seconds. These new images can have the same resolution in the X, Y, and Z dimensions (isometric voxels), allowing images to be reconstructed in any orientation without loss of spatial resolution. This has greatly facilitated the visualization of airways and vessels that are oriented in a radial pattern around pulmonary hila (Figure 2.1) [Coxson and Lam 2009] .

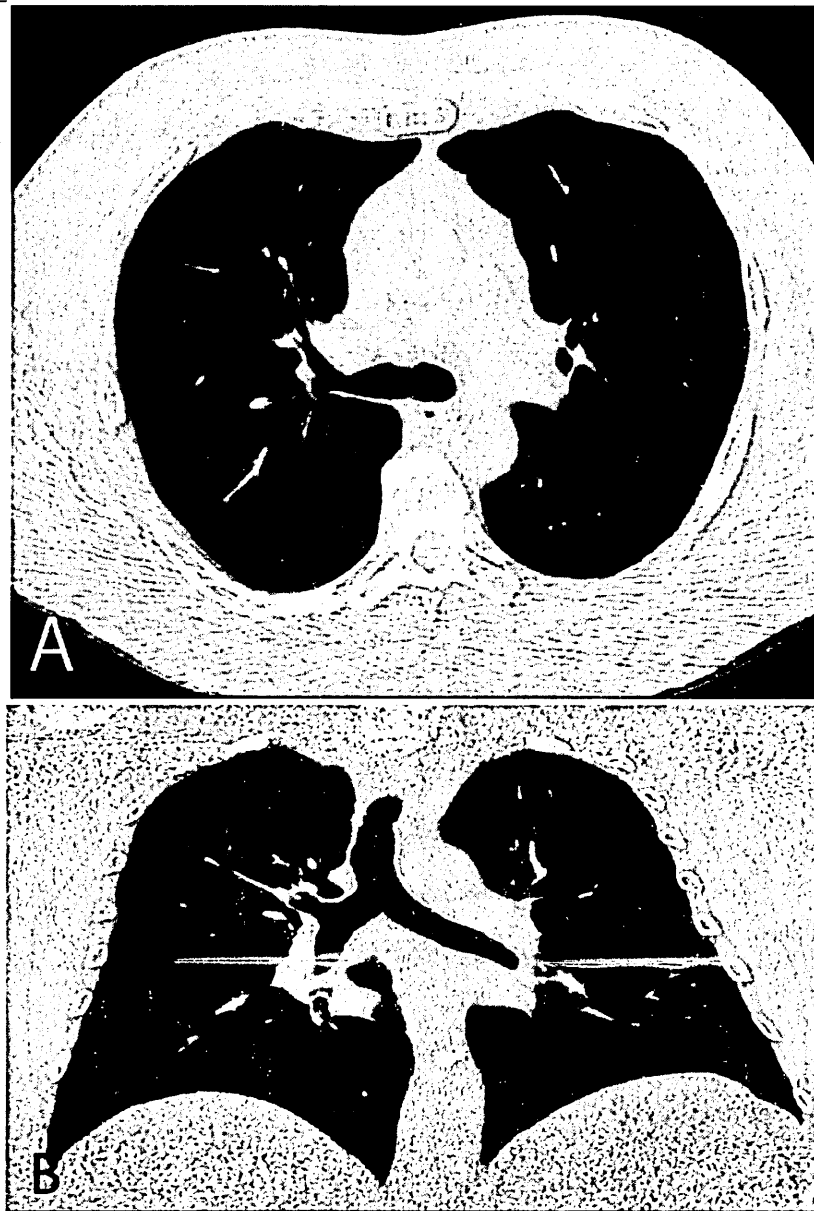


Figure 2.1 – Image acquired using MDCT.

This figure shows a thin slice (1-mm slice thickness) computed tomography (CT) scan acquired using a multi-detector CT scanner (A) in the traditional transverse plane and reformatted into (B) the coronal plane (Image and caption courtesy Coxson and Lam, 2009).

In a more recent study Mumcuoglu, *et al.*, [2009] have developed a computerized method which allows rapid, efficient and accurate assessment of computed tomographic airway wall (AW) and vessel (V) dimensions from axial CT lung images. Here they developed a full-width-half-max [Reinhardt *et al.*, 1997] based automatic AW and V size measurement method. In their method the only user input required was the approximate centre marking of AW and V by an expert. They evaluated their method on a patient population of 4 infants and 4 children with different stages of mild CF related lung disease. Their automated method for

assessing early AW disease in infants and children with CF represents a potentially useful outcome measure for future intervention trials [Mumcuoglu *et al.*, 2009].

Following are the limitations, identified by Coxson and Lam [Coxson and Lam, 2009], in the use of CT scanning to measure airways : (The material extracted from their publication can be found in Appendix 4)

- limitation in the resolution of the CT scanner. In the usual clinical CT scanning, the field of view limits the pixel size to approximately 0.5 mm in the X and Y dimension. This means that the airways that are responsible for airflow limitation are below the resolution of the CT scanner.
- there is no definitive data on the best algorithm to measure the airway wall. Whilst a great deal of research has gone into airway wall algorithms [Reinhardt *et al.*, 1997], [Saba *et al.*, 2003], [Nakano *et al.*, 2000], [Hasegawa *et al.*, 2006], [Brown *et al.*, 2000], [King *et al.*, 1999], [Montaudon *et al.*, 2007], [Aykan *et al.*, 2003], [Tschirren *et al.*, 2005], there is no clear indication that one algorithm provides more useful data than another one.
- the analysis of airways using three-dimensional algorithms is still in its infancy, these analyses have a long way to go before they become practical in the clinical setting. As such they remain in the research domain and are limited in their applicability

2.4. Computer Aided Detection and Diagnosis of Breast Abnormalities in X-ray

Mammograms

Breast cancer is one of the leading causes of death in women. Studies have indicated that cure rates dramatically increase if the breast lesion can be detected at a size less than 1 centimetre, which is too small for the lesion to be palpable. The only way a lesion this small can be detected is through screening mammography.

Mammographic interpretation is one of the most difficult tasks in all of radiology. Reading mammograms can be more of an art than a science. Breast parenchymal patterns are not stable between patients, between left and right breasts, and even within the same breast from year to year in the same patient. Positioning, particularly in the mediolateral oblique projection, and the amount of compression applied are variable from examination to examination. Breast cancer has a varied appearance on mammograms, from the obvious spiculated masses, to very subtle asymmetries noted

Figure 2.2 - Radiologist scrutinizing mammograms using a magnifying glass. (Stock Image).

on only one view, to faint calcifications seen only with full digital resolution or a magnifying glass (Figure 2.2). Task repetition and fatigue combine to make missing the subtle signs of breast cancer a very real possibility, but one that can have serious consequences [Liane E. and Philpotts, MD, 2009].

Given these difficulties, it is not surprising that approximately 20% of cancers are known to be missed at mammography [Warren Burhenne *et al*, 2002] [Brem *et al.*, 2003] [Birdwell *et al.*, 2001]. Some of these are because of the reduced sensitivity of mammography in the detection of lesions in dense breast tissues. But even if a lesion is visible on the images, the combination of the variable presentation of breast cancer on mammograms, as stated above, as well as the interpreting radiologist's threshold for both detecting and deciding to act on (i.e., recall) such lesions, affects the reading. Accuracy in mammographic interpretation depends on many factors, of which experience and volume of studies read play a large role. Having a good tool to help the radiologist in the difficult task of mammographic interpretation would be an advantage [Liane and Philpotts, 2009].

Having a good tool to help the radiologist in the difficult task of mammographic interpretation would be an advantage. CAD has been developed for that very purpose. It seems obvious that this difficult task could likely be made less error prone with the help of computer programs. However, how much is art and how much is science? How can a computer be expected to operate in a very imperfect system (i.e.,

variable mammograms and differing breast cancer patterns) at a level that would be clinically relevant (i.e., not missing any or many cancers) without causing more problems (eg, many false-positive results)? It is a lot to ask, even of a computer. [Liane E. and Philpotts, MD, 2009]

CAD tools use software to analyse digital or digitized images to find features associated with the target disease. The objective of CAD is to mark suspicious findings on the monitor and/or on a print of the image to help radiologists detect lesions (Figure 2.3). CAD algorithms work by identifying areas of signal in images that may contain a cancer. The standard approach is to use thresholding algorithms to identify as many true signals and as few false signals as possible. Signal data are separated from the background in a process known as segmentation. The signals are then subjected to a probabilistic analysis to assess the likelihood that the structure on the image contains malignancy-induced abnormalities [Nishikawa and Vyborny, 2007]. The final result is a CAD prompt if the probability of cancer being present is sufficiently high. All CAD systems must also be trained on a database of real cases before they are used in clinical practice. These cases should ideally be proven by biopsy or, if not, by follow-up of at least two years. The incidence and type of disease should mirror that expected in the target population [Bazzocchi *et al.*, 2007]. A basic method for assessing CAD performance during the training period is to plot the free-response receiver operating characteristic (FROC). This represents the sensitivity of the system in detecting cancer as a function of the averaged number of false-positive marks on each image. The best performing CAD systems will have a low false-positive rate as well as high sensitivity [Nishikawa and Vyborny, 2007].

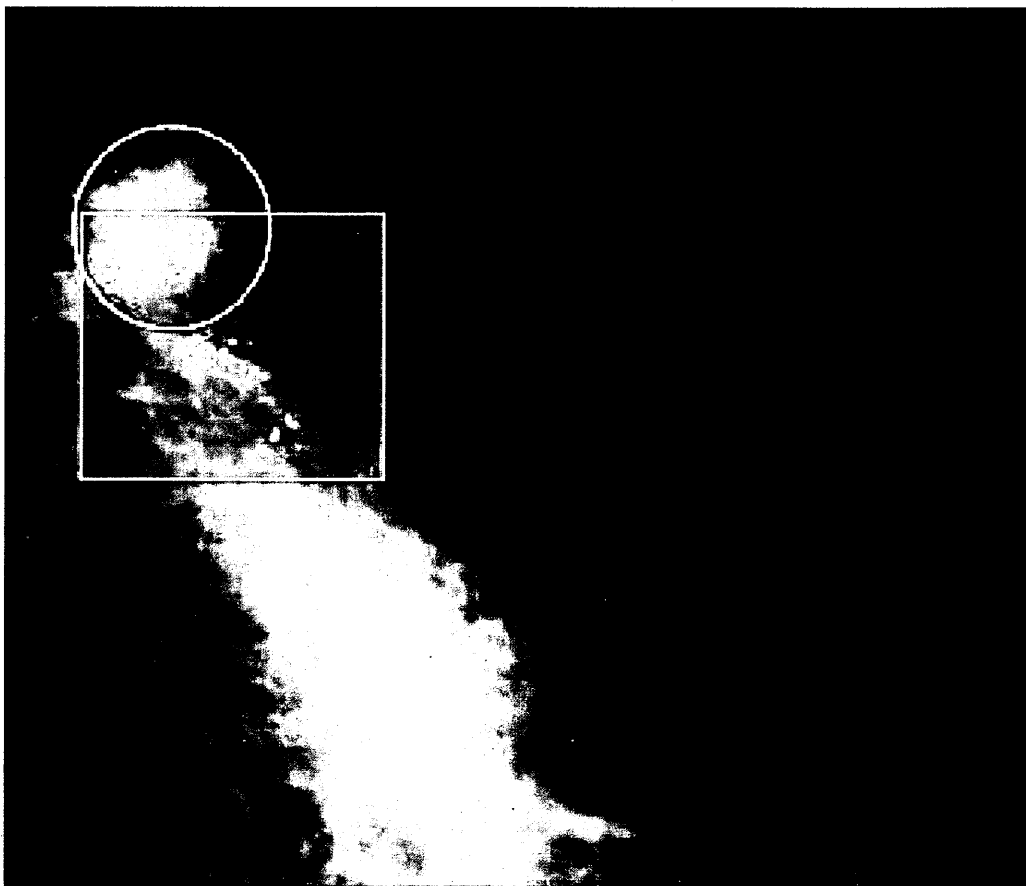


Figure 2.3 - CAD marking of micro-calcification.
Digital mammogram (cranio-caudal view) of 57-year-old woman. CAD correctly marked cluster of micro-calcification (square mark) and mass (round mark). Percutaneous biopsy targeted on mass revealed invasive ductal carcinoma. (Image and caption courtesy Bazzocchi *et al.* 2007).

The concept of computer-aided detection (CADE) was introduced more than 50 years ago; however, only in the last 20 years there have been serious and successful attempts at developing CADE for mammography [Nishikawa and Vyborny, 2007]. The introduction of systems for automated reading in mammography has been proposed to improve the sensitivity [computer-aided detection (CADE) systems] and, more recently, the specificity [computer-aided diagnosis (CADi) systems] of the test. Only CADE systems have been approved by the U.S. Food and Drug Administration (FDA) and are used in current practice [Bazzocchi *et al.*, 2007]. The first CAD tools were approved by the U.S. FDA for clinical use in 1998. Several commercial and non-commercial CAD systems have since become available [Girometti *et al.*, 2010].

These systems are still under investigation. Several studies have demonstrated that they are beneficial to inexperienced readers and that, through comparison with the computer, radiologists see an improvement in their performance. There is still

considerable variation among different studies in the level of benefit deriving from CAD. Therefore, the role of these systems in clinical practice is still debated, and their real contribution to the overall management of the diagnostic process is not yet clear [Bazzocchi, *et al.*, 2007].

Ciatto *et al.* [2006] evaluated the role of CAD in cancers undergoing double reading and detected by one reader only. A series of 33 cancers, originally missed by the first reader and detected by the second reader, and 75 negative controls were processed to assess CAD sensitivity, and were read with the help of CAD printouts by the six radiologists who originally missed the cancers. Their findings were, CAD case-based sensitivity, specificity and positive predictive value were 51.5%, 18.6% and 21.7%, respectively. Average sensitivity of all radiologists in all cancers in the series was 74.7%, being higher for CAD+ (86.2%) than for CAD- (62.5%) cancers ($P < 0.01$). When reading cancer cases that they had originally missed, radiologists had a sensitivity of 75.8%, which was higher for CAD+ (100.0%) than for CAD- (58.3%) cancers. They also found that the average recall rate was 14.2%, the majority of recalls (45 out of 64) occurring for lesions marked by CAD. Their conclusion was CAD may help in detecting at most half of cancers missed at a single reading but detected by a second reader.

Onega *et al.* [2010] examined radiologists' use and perceptions of CAD and double reading for screening mammography interpretation. They did a mailed survey of 257 community radiologists participating in the national Breast Cancer Surveillance Consortium (USA) to assess perceptions and practices related to CAD and double reading. They classified radiologists' overall perceptions of CAD and double reading on the basis of their agreement or disagreement with specific statements about CAD and double reading. The results of their survey were that most radiologists (64%) reported using CAD for more than half the screening mammograms they interpreted, but only <5% reported double reading that much. More radiologists perceived that double reading improved cancer detection rates compared to CAD (74% vs 55% reported), whereas fewer radiologists thought that double reading decreased recall rates compared to CAD (50% vs 65% reported). Radiologists with the most favourable perceptions of CAD were more likely to think that CAD improved cancer detection rates without taking too much time compared to radiologists with the most unfavourable overall perceptions. In latent class analysis, an overall favourable

perception of CAD was significantly associated with the use of CAD (81%), a higher percentage of workload in screening mammography (80%), academic affiliation (71%), and fellowship training (58%). Perceptions of double reading that were most favourable were associated with academic affiliation (98%). They concluded radiologists' perceptions were more favourable toward double reading by a second clinician than by a computer, although fewer used double reading in their own practice. The majority of radiologists perceived both CAD and double reading at least somewhat favourably, although for largely different reasons [Onega *et al.* 2010].

One method of helping radiologists screen mammograms for signs of cancer is prompting, in which computer based algorithms are used to detect potential abnormalities in digital images and to draw attention to the corresponding regions in the original films. Prompting aims to improve radiologists' performance by reducing the number of false negative errors, i.e. cases in which a mammogram containing a significant abnormality is classified as normal. Alberdi *et al.* [2005] examined the effects of CAD prompts on performance, comparing the negative effect of no prompt on a cancer case with prompts on a normal case. They showed that no prompt on a cancer case can have a detrimental effect on reader sensitivity and that the reader performs worse than if the reader was not using CAD. This became particularly apparent when difficult cases were being read. They suggested that the readers were using CAD as a decision making tool instead of a prompting aid. They conclude that "incorrect CAD can have a detrimental effect on human decisions" [Alberdi *et al.*, 2005]. The goal of a CAD system is to reduce errors by drawing radiologists' attention to possible abnormalities. CAD is not intended to be used as a computer-aided diagnosis tool, i.e. the decision as to whether a feature is of clinical significance remains with the radiologist. In practice, however, the distinction between detection and diagnosis may be blurred. One study has indicated that, for subtle microcalcification clusters, subjects' confidence that a cluster was present was increased if the cluster was prompted, and decreased if the cluster was unprompted [Chan *et al.*, 1990]. Another study reported that prompting can entail an increase in false positive decisions without necessarily having an overall effect on confidence levels [Mugglestone *et al.*, 1996]. The first study would seem to indicate that radiologists' confidence with respect to the detection task is affected by prompting, but that their diagnostic decision making remains largely unaffected. The second

study, however, raises doubts regarding the latter conclusion [Hartswood *et al.*, 1998].

The gold standard of symptomatic breast diagnosis for more than a decade has been triple assessment by clinical examination, needle biopsy and X-ray mammography [The Breast Surgeons Group of the British Association of Surgical Oncology, 1995]. Recently, Ultrasound is used increasingly for symptomatic cases. Moss *et al.* [1999] analysed the role of ultrasound, freely used, to supplement X-ray mammography, and showed that the resultant sensitivity is extremely high. but that it must be used in conjunction with needle biopsy to achieve satisfactory specificity and avoid unnecessary benign surgical biopsies. Their study of 559 biopsied symptomatic cases showed that targeted ultrasound, used liberally as an adjunct to X-ray mammography, increased their cancer detection rate by almost 15%. but at the expense of reduced specificity. Their study illustrated the limitations of X-ray mammography in a symptomatic population, but showed that ultrasound covers the shortfall in most cases, with only one cancer near the nipple not detected by either imaging test (0.4% of cancers). They therefore recommended performing ultrasound in all women in whom there is a clinical suspicion of malignancy even if the X-ray mammogram is normal. Importantly, there were 11 cancers (4.3% of cancers in the study) in patients in whom an abnormality was seen in the area of clinical concern on one or both investigations but categorized as benign. This underlines the necessity that any focal X-ray mammographic or ultrasound abnormality should undergo needle biopsy [Moss *et al.* 1999].

Rahbar *et al.* [1996] in their study of one hundred and sixty-two consecutive solid masses with a tissue diagnosis found that the US features that most reliably characterize masses as benign were a round or oval shape (67 of 71 [94%] were benign), circumscribed margins (95 of 104 [91%] were benign), and a width-to-anteroposterior (AP) dimension ratio greater than 1.4 (82 of 92 [89%] were benign). Features that characterize masses as malignant included irregular shape (19 of 31 [61%] were malignant), microlobulated (four of six [67%] were malignant) or spiculated (two of three [67%] were malignant) margins, and width-to-AP dimension ratio of 1.4 or less (28 of 70 [40%] were malignant). They also investigated the general applicability and interobserver variability of US features in differentiating benign from malignant solid breast masses. They found that if the three most reliable

criteria had been strictly applied by each radiologist, the overall cancer biopsy yield would have increased (from 23% to 39%) by 16%. When US images and mammograms were available, the increase in biopsy yield contributed by US was not statistically significant (2%, $P = .73$). They concluded that certain US features can help differentiate benign from malignant masses. However, practice and interpreter variability require further exploration before these criteria are generally applied to defer biopsy of solid masses.

Surgeons are frequently faced with the question of whether to biopsy those palpable abnormalities in the setting of normal radiographic studies. One might propose that such lesions could be safely observed rather than immediately biopsied. Bayer and Moonka [2002] investigated the relationship of non biopsy to how many cancers would escape detection? To address this issue, a population of patients with known, palpable breast cancer was retrospectively examined to determine the frequency of normal or benign findings on both mammography and ultrasonography. The results of their study indicated that nearly 4% of women with breast cancer who present with palpable lumps will have normal or benign findings on both mammography and ultrasonography. Their data supported prior studies of similar false negative rates.

2.4.1. Segmentation and Detection of Abnormalities in X-ray Mammographic Images

Pham *et al.* [2000] in their survey, on methods employed for medical image segmentation, have identified the following processes and procedures (For an extract from their publication please refer Appendix 5)

In delineating suspicious masses for mammography, segmentation methods are typically employed in one of two ways.

- In the first approach, the mammogram is initially segmented into candidate regions which are then labelled as being suspicious or normal [Polakowski *et al.*, 1997], [Li *et al.*, 1995], [Ibrahim *et al.*, 1997], [Karssemeijer, 1997].
- In the second approach, the image is first processed to detect for the presence of pathology and a segmentation is performed as a final step to determine its precise location [Cheng *et al.*, 1998], [Kupinski and Giger, 1998] [Gupta and Undrill, 1995], [Chen and Lee, 1995].

Thresholding and its variations are the most often used segmentation technique in X-ray mammography [Polakowski *et al.*, 1997], [Strickland and Hahn, 1996], [Cheng *et al.*, 1998], [Gupta and Undrill, 1995], [Ibrahim *et Mon Jan 30 21:36:26 GMT 2012al.*, 1997], although extensions of region growing methods have also been proposed [Kupinski and Giger, 1998], [Pohlman *et al.*, 1996]. A comparison of thresholding and region growing was presented in [Kallergi *et al.*, 1992].

Because pathological areas often possess different textural properties in mammograms, Markov random field methods have also been successfully employed [Li *et al.*, 1995], [Chen and Lee, 1995].

It is widely accepted in the medical community that breast tissue density is an important risk factor for the development of breast cancer [Oliver *et al.* 2006]. Thus, the development of reliable automatic methods for classification of breast tissue is justified and necessary. Although different approaches in this area have been proposed in recent years, only a few are based on the Breast Imaging Reporting and Data System (BIRADS) classification standard. Oliver *et al.* [2006] reviewed different strategies for extracting features in tissue classification systems, and demonstrated, not only the feasibility of estimating breast density using automatic computer vision techniques, but also the benefits of segmentation of the breast based on internal tissue information. Their evaluation was based on the full Mammographic Image Analysis Society (MIAS) [Suckling *et al.*, 1994].digital mammogram database classified according to BIRADS categories, and agreement between automatic and manual classification of 82% was obtained. Adel *et al.* [2007] in their study explored the possibility of the segmentation of breast anatomical regions, pectoral muscle, fatty and fibroglandular regions, using a Bayesian approach. The developed method was tested on 50 digitized mammograms of the mini-MIAS database [Suckling *et al.*, 1994]. Computer segmentation was compared to manual one made by a radiologist. They report that a good agreement was obtained on 68% of the mini-MIAS X-ray mammographic image database used in their study [Adel *et al.*, 2007].

CADe systems address the problem that radiologists may miss signs of cancers that are retrospectively visible in mammograms. Furthermore, computer-aided diagnosis (CADx) systems have been proposed that assist the radiologist in the classification of mammographic lesions as benign or malignant. Elter and Horsch [2009] present a

review of the state of the art of CADx approaches. Their survey is restricted to the two most important types of mammographic lesions: masses and clustered microcalcifications. Furthermore, it focuses on articles published in international journals.

Oliver *et al.*, [2010] reviewed the performance of methods designed to automatically detect and diagnose masses in X-ray mammographic images.

The important sign for the breast cancer detection is the presence of lesions such as microcalcification clusters (MCCs). For MCCs, the interpretations of their presence are very difficult because of their morphological features. For example, the sizes of MCCs are typically in the range of 0.1mm-1.0mm and the average is about 0.3mm, implying it can easily be overlooked by a radiologist. While in some dense tissues, and/ or skin thickening, MCCs areas are almost invisible to be seen by examining radiologist. The dense tissues especially in younger women may easily be misinterpreted as MCCs due to film emulsion error, digitization artifacts or anatomical structures such as fibrous strands, breast borders or hypertrophied lobules that are almost similar to MCCs. Other factors that contribute to the difficulty of MCCs detection are due to their fuzzy nature, low contrast and low distinguishability from their surroundings [Chang and Cui, 2004]. Yusof *et al.* [2007] in their publications have reviewed the computer-aided detection and diagnosis systems for microcalcifications.

Liu *et al.* [2001] discussed their multiresolution scheme for the detection of spiculated lesions in digital mammograms. In their first approach first, a multiresolution representation of the original mammogram was obtained using a linear phase nonseparable two-dimensional (2-D) wavelet transform. A set of features was extracted at each resolution in the wavelet pyramid for every pixel. Their approach addresses the difficulty of predetermining the neighborhood size for feature extraction to characterize objects that may appear in different sizes. Detection was performed from the coarsest resolution to the finest resolution using a binary tree classifier. Their top-down approach required less computation by starting with the least amount of data and propagating detection results to finer resolutions. To evaluate the computer diagnosis results, they adopted the criteria suggested by Kegelmeyer *et al.* [1994] by which a computer finding is considered as a true

positive detection if its area is overlapped by at least 50% of a true lesion as indicated by an expert radiologist; a computer finding that does not so overlap a true lesion is considered as false positive; and a true lesion that is not overlapped by any computer finding is considered as false negative. By these criteria, the diagnostic accuracy performance of their algorithm on the MIAS [Suckling *et al.* 1994] database was 84.2% true positive detection at less than 1 false positive per image and 100% true positive detection at 2.2 false positive per image.

2.5. Studies Most Relevant to the Current Study

In the following chapters it will be detailed how the author's Hierarchical Clustering-based Segmentation process was used :

- to segment regions in digital images (specifically medical images Chapter 3)
- to combine machines' power of perceiving details, in images, with the human interpretive skills to design quantitative measures to monitor abnormalities in diagnostic images (specifically CF Chapter 4 and breast abnormalities Chapter 5)

To successfully implement the above applications the current study made use of the following methodologies :

- Hierarchical clustering-based process to segment images
- Incorporating users' interpretive knowledge within a computer aided diagnoses process.

Given below are the studies which are of relevance to the above methodologies adopted by the current study.

In relevance to hierarchical segmentation of images :

Shi and Malik are one of the very few researchers who insist that a single segmentation solution is not appropriate and that only hierarchical segmentation output should be produced. Their strong recommendation "*...image segmentation based on low-level cues cannot and should not aim to produce a complete final "correct" segmentation. The objective should instead be to use the low-level coherence of brightness, colour, texture, or motion attributes to sequentially come up with hierarchical partitions*" [Shi and Malik, 1997]. They also recommend that higher level knowledge (user knowledge ?) should be used to finalize the most appropriate segmentation. Their recommendation is "*Mid- and*

high-level knowledge can be used to either confirm these groups or select some for further attention. This attention could result in further repartitioning or grouping” [Shi and Malik, 1997].

Researchers Martin *et al*, [Martin *et al*, 2002] [Martin *et al*, 2004] have specifically designed a benchmarking process to objectively evaluate the performance of methods which yields multiple segmentation output. In their discussion of their benchmarking algorithm they specifically advocate against thresholding of boundary maps, as follows : *“Traditionally, one would “binarize” the boundary map by choosing some threshold. There are two problems with thresholding a boundary map: (1) The optimal threshold depends on the application, and (2) Thresholding a low-level feature like boundaries is likely to be a bad idea for most applications, since it destroys much information. For these reasons, our benchmark operates on a non-thresholded boundary map” [Arbelaez et al., 2007].*

The following researchers are one of the very few who have specifically made use of hierarchical segmentation output as a tool for medical image related applications :

Thies *et al*. [Thies *et al.*, 2003] have used the information for retrieving images from a image database. Their description of the retrieval process *“Due to varying medical context and questions, data structures for image description must provide all visually perceivable regions and their topological relationships, which poses one of the major problems for content extraction. In medical applications main criteria for segmenting images are local features such as texture, shape, intensity extrema, or gray values. For this new approach, these features are computed pixel-based and neighbouring pixels are merged if the Euclidean distance of corresponding feature vectors is below a threshold. Thus, the planar adjacency of clusters representing connected image partitions is preserved. A cluster hierarchy is obtained by iterating and recording the adjacency merging. The resulting inclusion and neighbourhood relations of the regions form a hierarchical region adjacency graph. This graph represents a multiscale image decomposition and therefore an extensive content description. It is examined with respect to application in daily routine by testing invariance against transformation, run time behaviour, and visual quality For retrieval purposes, a graph can be matched with graphs of other images, where the*

quality of the matching describes the similarity of the images." [Thies *et al.*, 2003]

The Hierarchical Segmentation Software (HSEG) — developed by NASA's Goddard Space Flight Center Computer Engineer James C. Tilton, [Tilton, 2000], [Tilton, 2003] forms the core of a commercial medical segmentation program MED-SEG. MED-SEG is developed by Barton Medical Imaging Inc. a USA based company [<http://www.bartron.ws/>]. The FDA recently cleared the system to be used by trained professionals to process images. These images can be used in radiologist's reports and communications as well as other uses, but the processed images should not be used for primary image diagnosis. In the future, Dr. Molly Brewer, a professor with the Division of Gynecologic Oncology, University of Connecticut Health Center, would like to do clinical trials with the MED-SEG system. The goal, she said, would be improving mammography as a diagnostic tool for detecting breast cancer. ***"The MED-SEG processes the image allowing a doctor to see a lot more detail in a more quantitative way."*** (Figure 2.4). [<http://www.nasa.gov/topics/nasalife/features/medical-imagerv.html>]

In segmenting medical images the performance of HSEG has been compared with that of HCS (Chapter 3 Section 3.2.1).

The following study is relevant in making use of the radiologists' interpretive skills to approximately locate the abnormality to aid the computer for its subsequent objective evaluation of the abnormality :

Researchers at the University of Chicago have developed a computer technique that "learns" how benign and malignant breast calcifications appear on digital mammograms. Radiologists read the mammograms and electronically put a box around the suspicious calcifications. The computer then automatically detected the calcifications within the box, analysed them and calculated the probability of cancer. The system proved to consistently achieve performance comparable to the radiologists in classifying malignant and benign calcifications, regardless of who was using it. One technique for rating the computer's effectiveness is to give it one malignant case and one benign case and then test its ability to determine which is which. Using this technique, the radiologist had a 72% chance of making the correct diagnosis, and the computer had a 79% chance.

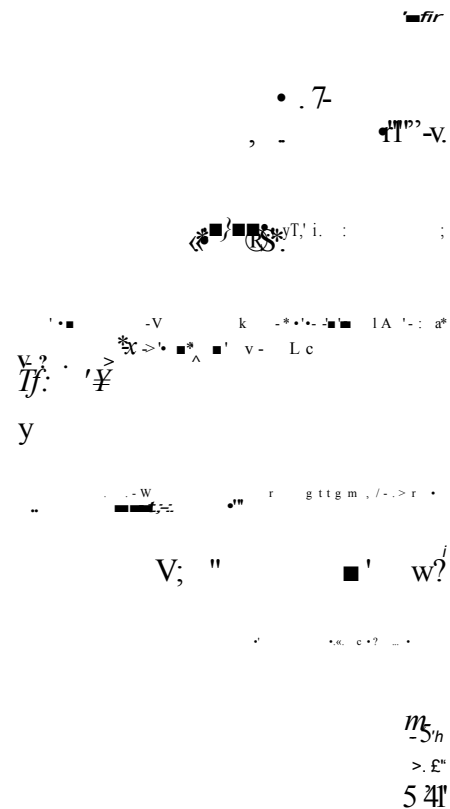


Figure 2.4 - MED-SEG processing of mammograms.
 The left image shows an original mammogram before MED-SEG processing. The image on the right, with region of interest (white) labeled, shows a mammogram after MED-SEG processing.
 (Image and caption credit: Barton Medical Imaging)

The computer aided monitoring process designed in the current study follows a very similar approach as above to differentiate malignant from benign abnormalities (See Chapter 5 Section 5.2.4).

2.6.Summary

This chapter outlined the studies by researchers related to the following areas of investigation:

- Segmentation of regions in digital images specifically medical images.

- Computer aided diagnosis and monitoring of CF by measuring airway dimensions in the CT images of the lungs

- Computer aided Detection and Diagnosis of abnormalities in mammograms

After studying the existing research it can be inferred that only a few studies have used hierarchical segmentation for processing medical images.

Chapter 3. Hierarchical Clustering Based Segmentation (HCS)

3.1. Introduction

The main aim of this study is to design and implement image processing techniques to assist medical professionals in perceiving diagnostic images and thus improve their diagnostic capabilities. To achieve the above objective the Hierarchical Clustering based Segmentation (HCS) based process [Selvan 2007] was investigated. Specifically, HCS was investigated for its ability to augment the diagnostic information present in CT images for CF diagnosis and X-ray mammograms to differentiate malignant from benign abnormalities.

This chapter discusses the HCS process in detail and is covered under the following headings :

- overview of the HCS process
- reasons for choosing the HCS process to augment diagnostic information present in medical images.
- objective evaluation of the performance of the HCS process.
- use of the HCS process output as a perceptual aid.

3.2. Overview of the HCS Process

Hierarchical organization is one of the main characteristics of human segmentation. A human subject segments a natural image by identifying physical objects and marking their boundaries up to a certain level of detail [Arbelaez, 2006]. For example, given an anatomical image of the cross-section of a skull, at a coarse level a radiologist can classify the image as regions belonging to soft tissues and the skull bone. At a fine level different types of soft tissues are also identified. At a still finer level, the radiologist will also be able to distinguish the regions which might be dissimilar, due to some pathological condition, within the same tissue type.

Segmentation can be thought as a process of grouping visual information, where the details are grouped into objects, objects into classes of objects and classes of objects as scenes. Thus, starting from the composite segmentation, the perceptual organization of the image can be represented by a tree of regions, ordered by inclusion. The root of the tree is the entire scene, the leaves are the finest details and each region represents an object at a certain scale of observation [Arbelaez, 2006].

Since the early days of computer vision, the hierarchical structure of visual perception has motivated clustering techniques to segmentation [Ohlander *et al.* 1978], where connected regions of the image domain are classified according to an inter-region dissimilarity measure. Hierarchical Clustering-based Segmentation (HCS) implements the traditional bottom-up approach, also called agglomerative clustering [Nadler and Smith 1993], where the regions of an initial partition are iteratively merged. HCS procedure automatically generates a hierarchy of segmented images. The hierarchy of segmented images is generated by partitioning an image into its constituent regions at hierarchical levels of allowable dissimilarity between its different regions. At any particular level in the hierarchy, the segmentation process will cluster together all the pixels and/or regions which have dissimilarity among them less than or equal to the dissimilarity allowed for that level. Thus, the HCS process mimics the capability of human vision.

The HCS process automatically generates a hierarchy of segmented images. The hierarchy represents the continuous merging of similar, spatially adjacent or disjoint, regions as the allowable threshold value of dissimilarity between regions, for merging, is gradually increased. HCS process is unsupervised and is completely data driven. This ensures that the segmentation process can be applied to any image, without any prior information about the image data and without any need for prior training of the segmentation process with the relevant image data.

The following is a high-level description of the HCS process [Selvan 2007] (See Figure 3.1-A for a flow chart representation) :

- i. Give each pixel in the image a region label as follows.
 If an initial segmentation of the image is available, label each pixel according to this pre-segmentation. The initial segmentation can be obtained by prior class information for e.g. based on the user information.
 If no initial segmentation is available, label each pixel as a separate region.
 Set the current dissimilarity allowed between regions, *dissimilarity_allowed*, equal to zero.
- ii. Calculate the dissimilarity value, (*dissimilarity_value*), between all pairs of regions in the image.
 Set *threshold_value* equal to the smallest *dissimilarity_value*.

- iii. If the *threshold_value* found, in step (ii), is less than or equal to the current *dissimilarity_allowed* value, then merge all those regions having *dissimilarity_value*, between them, less than or equal to the *threshold_value*. Otherwise go to step (vi).
- iv. If the number of regions merged in Step iii is greater than 0, then reclassify the pixels on the border of the merged regions with the rest of the regions until no more reclassification is possible. After all the possible border pixels are reclassified, among the merged regions, store the region information for this iteration as an intermediate segmentation and go to step (ii).
Otherwise, if the number of regions merged in step (iii) is equal to 0 then, go to step (v).
- v. If the current number of regions in the image is less than the pre-set value, *check_no_regions*, then go to step (vii). Otherwise, go to step (vi).
Normally the value of *check_no_regions* is set as 1.
- vi. If the current value of *dissimilarity_allowed* is less than the maximum possible value then increase the *dissimilarity_allowed* value by an incremental value,
$$dissimilarity_allowed = dissimilarity_allowed + dissimilarity_increment,$$
 and go to step (ii).
Otherwise go to step (vii).
- vii. Save the region information from the current iteration as the coarsest instance of the final hierarchical segmentation result and stop.

The above steps ensure that the segmentation of the image into its constituent regions is always unique irrespective of the order in which the image regions are processed. Other similar Agglomerative hierarchical clustering or bottom-up methods suffer from a distorting phenomena, in which the cluster structures depend on the order in which the regions are considered for merging [Nadler, 1993]. The brute force approach, followed by the HCS process, where only those regions with the smallest overall dissimilarity are merged in each step, is the only solution to overcome this effect [Thies, 2003].

Merging only those regions with the smallest overall dissimilarity requires the comparison of all the possible combinations of the locations or regions present in a image. This is a combinatorial problem and the complexity of the solution

exponentially increases with the number of locations (regions) in the image as given by the expression in equation 3.1.

$$\text{Number of combinations} = \frac{N \times (N-1)}{2} \quad [3.1]$$

Where N is the number of locations or regions in the image

The feature measure used by the HCS process, to estimate the similarity between locations within a image, is the actual distribution of the pixel values in a region surrounding the locations. This technique may be considered to work in a way similar to the human visual system where features for texture (region) segmentation are not consciously computed [Bhattacharya, 1997].

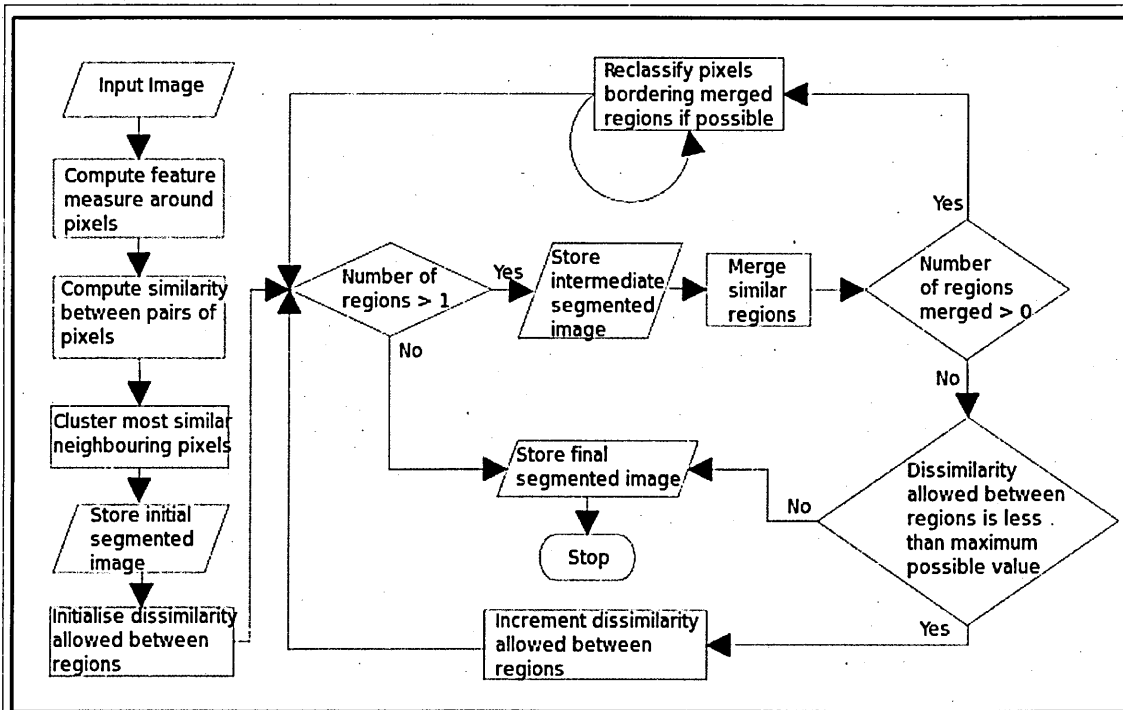


Figure 3.1-A - Flow chart illustrating the different operations of the HCS process (Image courtesy Selvan 2007).

The pixel-values distribution feature was found as follows. A small mask of fixed size is placed around the pixel of interest. The pixel-values within the mask, moving from the top left corner of the mask to the bottom right corner of the mask, were taken as the distribution of the pixel-values feature for the pixel. Figure 3.1-B illustrates the method.

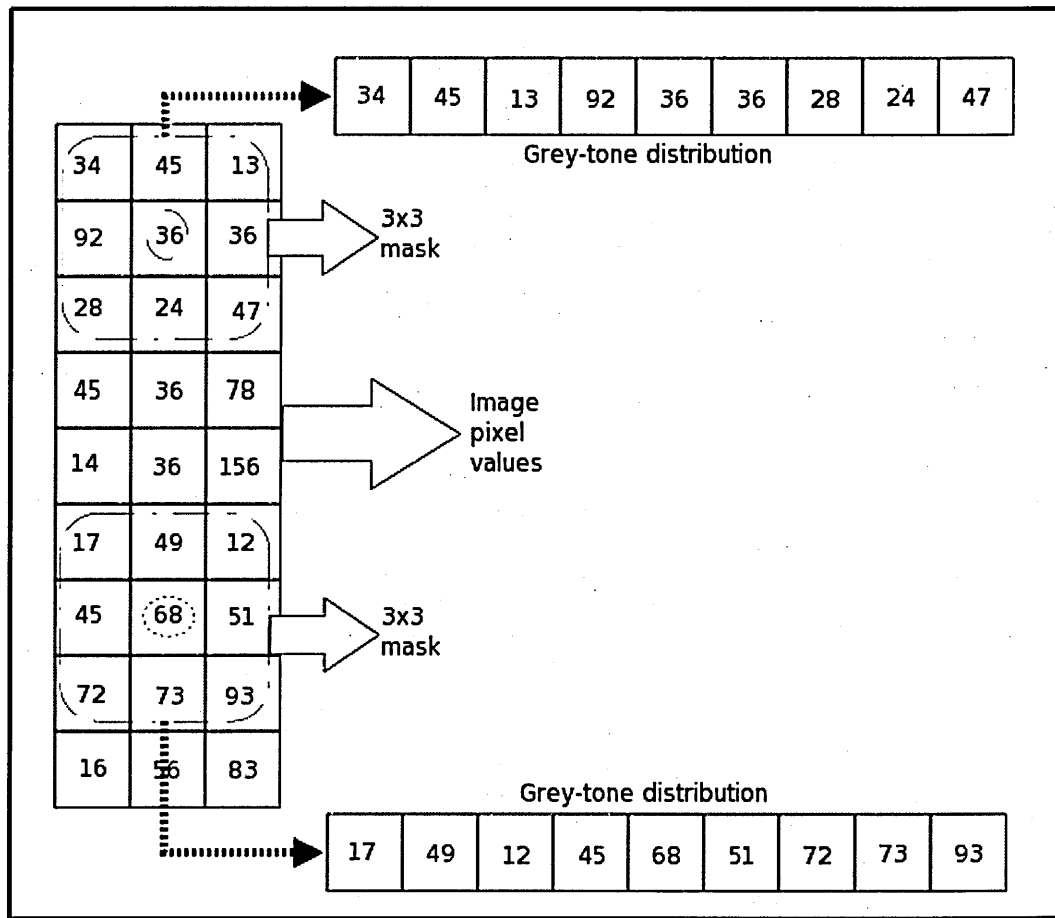


Figure 3.1-B - Pixel-values distribution feature representation for a grey tone image
(Image courtesy Selvan 2007)

Given the observations of the pixel-values from two different locations in the image and a certain level of significance, the aim was to determine whether they belonged to the same distribution. The commonly used test for difference between binned distributions is the Chi-Squared test [Press *et al.*, 2002]. To compare the two binned data sets the chi-square statistic is found as given by the expression 3.2

$$\chi^2 = \sum \frac{(R_i - S_i)^2}{R_i + S_i} \quad [3.2]$$

Where

the sum is over all the bins i

R_i is the number of events in bin i for the first data set

S_i is the number of events in the same bin bin i for the second data set

A large value of χ^2 (Equation 3.2) indicates that the null hypothesis (that the two distributions belonged to the same distribution) is rather unlikely [Press *et al.*, 2002].

$Q(\chi^2|\nu)$ is the probability that the observed chi-square will exceed the value by chance even for a correct model. ν is an integer, the number of degrees of freedom. The *chi-square probability function* $Q(\chi^2|\nu)$ has the limiting values $Q(0|\nu)=1$ and $Q(\infty|\nu)=0$ and is estimated as an incomplete gamma function as expressed in the equation 3.3 [Press *et al.*, 2002].

$$Q(\chi^2|\nu)=Q\left(\frac{\nu}{2}, \frac{\chi^2}{2}\right)=\text{gammapq}\left(\frac{\nu}{2}, \frac{\chi^2}{2}\right) \quad [3.3]$$

A range of images were processed, using HCS, including the diagnostic images of different modalities MRI, CT, X-ray and Ultrasound and images of natural scenes. They were all processed using the same feature mentioned above and with the same set of parameters without any prior training. The HCS process is not aware of the source of the digital image data. The digital data could be of the brain (MRI Section 3.3.1.1) (CT Section 3.3.1.2) or abdomen (US Section 3.3.1.3) or of a breast (X-ray Mammograms Section 3.3.1.4) or of a bird (natural scene Section 3.4.1). For the HCS process it is the same, and treats them all as an array of two byte numbers and are all processed in the same manner without any prior training on that data set.

It should also be noted that the HCS process is different from the Hierarchical image segmentation methods discussed, for example, by Schroeter and Bigün [1995]. The term hierarchy in the study by Schroeter and Bigün [1995] refers to the multi-resolution hierarchy in scale space. Also, the HCS process, unlike other segmentation methods, such as those by Cheng and Ying [2000] Jeon *et al.* [2005] and Zhou *et al.* [2009], is not an iterative optimization process. Instead at each level the HCS process yields an optimized segmentation output related to the dissimilarity allowed for that level.

The HCS process yields a merge tree. Based on the merge tree, a graphical user interface (GUI) can display the hierarchy of merges. The algorithmic diagram, shown in Figure 3.1-A [Selvan, 2007], illustrates the overall operation of HCS.

3.2.1.Border Pixel Re-Classification

One of the unique features of the HCS process is the border pixel re-classification (Figure 3.1-A). Border pixel re-classification is one of the main reasons behind HCS process's ability to attain smooth segmentation of the regions in the image. This section will discuss in detail HCS's process border pixel re-classification feature.

After the merging of similar regions, the border pixels of the regions that had merged and their bordering regions were further evaluated to allocate them to the most suitable region (Figure 3.1-A). Border pixel reclassification is necessary because the merging process starts with individual pixels which are merged to form regions and subsequently regions are merged to form bigger regions and so on. During the initial merging of neighbouring pixels and neighbouring small regions, pixels belonging to different regions may be merged. This could happen, for example, when comparing pixels over a small neighbourhood, where the dissimilarity between pixels belonging to different regions might be smaller than the dissimilarity between pixels belonging to the same region because of the local in-homogeneity (arising due to inadequate scaling factor in measuring the repetitive pattern constituting the texture). However as the regions grow those pixels which have been merged as a result of comparison with neighbouring pixels may subsequently be reclassified by adequately comparing them with the rest of the pixels from a larger neighbourhood.

Border pixel reclassification was considered only for those pixels on the boundary of the clusters which had been merged with other clusters. These boundary pixels were removed one at a time from their original clusters. The pixel removed was considered as a region of its own and the similarity between the one pixel region and the regions bordering it (which included the original cluster to which it belonged) were found and the single pixel region was merged with the most similar bordering region. During this process the pixel could possibly be re-classified to one of the neighbouring regions rather than the region to which it originally belonged [Selvan 2007].

Figure 3.2 (a) shows a CT image of a section of the brain. The image area within the region of interest (rectangular area outlined in black) is made up of three different types of regions viz. Grey matter, White matter and the stroke affected area. The approximate boundary of the stroke affected area has been outlined in white by an

expert. The purpose of the segmentation process is to estimate more appropriate boundary of the stroke affected region.

Figure 3.2 (b) shows the segmentation result obtained by Hierarchical Segmentation (HSEG) [Tilton 2003]. Figure 3.2 (b) illustrates the difficulties faced by the segmentation process to segment medical images. Although the image pixels within the region of interest (ROI), have been segmented into three classes colour coded as Red (the diseased area), Green (white matter) and blue (Grey matter) it has misclassified some of the pixels not belonging to the diseased area as being diseased as well. This can be seen by the presence of red coloured pixels at the other end of the ROI i.e. outside the area outlined by the expert.

m %

Figure 3.2 - Processing of a CT image by HSEG [Tilton 2003].

CT image showing the suspected area outlined in white by a neuroradiologist (a). Segmentation of the Grey matter, White matter and Stroke affected regions and their boundaries by HSEG [Tilton 2003] (b) (Image courtesy Selvan 2007).

The HCS process does not have a stopping criteria and hence it iterates until there are no more regions yet to be merged. Figure 3.3 (a) shows an intermediate segmentation of the CT image (Figure 3.2 (a)) by the HCS process, when there are three regions yet to be merged. It can be seen that the HCS process has successfully delineated the three different types of regions viz. Grey matter, White matter and the stroke affected area. Comparing the segmentation results of HCS Figure 3.3 (a) and that of HSEG

Figure 3.2 (b), it can be seen that the HSEG process segmentation (Figure 3.2 (b)) is suboptimal while the HCS process is able to achieve a smooth segmentation as can be seen in Figure 3.3 (a).

Figure 3.3 (b) shows the intermediate segmentation results of the HCS process, performed without border pixels reclassification. In Figure 3.3 (b) the pixels belonging to the larger clusters of the major classes White Matter and the infarct are coloured as Green and Red. Pixels clustered as belonging to the Grey matter class are not coloured.

From Figure 3.3 (b) it can be seen that the cluster belonging to the major class infarct has misclassified pixels on the other part of the image. Comparing the segmentation output of the HSEG (Figure 3.2 (b)) with that obtained by HCS without border pixel reclassification (Figure 3.3 (b)), it can be seen that they are almost the same. Since the similarity measures adopted by the HCS and the HSEG processes may or may not be the same it can be safely assumed that border pixel reclassification plays a crucial role in obtaining a smooth segmentation.

a

Figure 3.3 - Segmentation of a CT image by HCS with and without border pixel reclassification.

Segmentation of the Grey matter, White matter and Stroke affected regions and their boundaries by HCS with border pixel reclassification (a).

Segmentation of the Grey matter, White matter and Stroke affected regions by HCS without border pixels reclassification, where misclassification had occurred (b). (Image courtesy Selvan, 2007)

Although only one example was shown to compare the performance of the HSEG with that of HCS. It is also shown how HCS process output is very similar to that of HSEG when HCS process does not perform border-pixel reclassification. From this it can be inferred that the HCS process with border-pixel-reclassification will always give a better segmentation output when compared to HSEG.

3.3. HCS Process Performance

The following section outlines the main reasons why the HCS process was adopted to augment the diagnostic information present in medical images.

- Hierarchical clustering based segmentation process is unsupervised and is completely data driven. This ensures that the segmentation process can be applied to any medical image modality, with equal success, without any prior information about the image data and without any need to train the segmentation process with the relevant image data.

The above mentioned claim had been successfully verified earlier by the successful processing of images of different modalities with the same set of parameters and with the same set of procedural steps [Selvan 2007].

- Hierarchical clustering based segmentation process can automatically generate a hierarchy of segmentation results.
- Hierarchical clustering based merging (*i.e.* clustering) of the most similar regions does not depend on the order in which the regions are evaluated for merging [Selvan 2007].
- Hierarchical clustering based segmentation process is a modular framework and any similarity measure can be used. The operation of the HCS process is independent of the type of similarity measure used to compare the different regions in the image.
- Hierarchical clustering based merging process is capable of merging spatially adjacent or disjoint similar regions.
- Hierarchical clustering based segmentation process yields smooth border delineation between the regions.

3.3.1. Performance of the HCS Process in Processing Diagnostic Images of Different Modalities

The performance of the HCS process can be gauged by its ability to process medical images of different modalities. The following examples demonstrate how the HCS process has been used successfully to process Magnetic Resonance Images (MRI), CT images, X-ray images (Mammogram) and Ultrasound images. It should be noted that the processing of the images from different modalities is carried out unsupervised with the same set of parameters. That is, the HCS process was neither modified nor had its parameters tuned in anyway to handle any specific modality.

In each of the following examples the HCS process was applied within a ROI. The ROI was chosen in such a way as to encompass that part of the image which has been identified by an expert as having some pathological condition. The HCS process performance was evaluated based upon its ability to delineate a more appropriate boundary of the pathological condition.

3.3.1.1. Performance of the HCS Process in Highlighting Infarct in Magnetic Resonance Imaging (MRI) T2 Weighted Images

HCS process dissimilarity-highlighting feature was successfully used for highlighting infarct in MRI T2-weighted images that are hard to visualise. Figures 3.4 (a) and 3.4 (b) are the Diffusion weighted and T2 weighted MR images of a stroke patient, respectively. The Diffusion-weighted image clearly shows the area in the brain, affected by the stroke, in white (pointed by a black arrow). Figure 3.4 (c) displays the different dissimilar regions, segmented by the HCS process, in the T2 weighted image, for a specific dissimilarity level. Figure 3.4 (d) shows a region, that was dissimilar from the rest of the image, which has been isolated and highlighted. The isolated dissimilar region corresponds to the stroke affected area that is clearly visible in the diffusion-weighted MRI image (Shown in Figure 3.4 (a)) [Selvan 2007].

The results shown in Figure 3.4 were presented to a neuroradiologist for evaluation. His opinion regarding the effectiveness of the HCS process is reproduced below :

Quote *“I have been going through all the processed images. My preliminary assessment is that the programme is able to pick up the abnormal area correctly on the T2 weighted scan (confirmed by the diffusion weighted scans). I would also like to mention that the signal changes seen on the T2 weighted scan, would be missed by most physicians and possibly neuroradiologists”* End Quote [Selvan 2007].

Figure 3.4 - HCS process Segmentation of a MRI image.
Diffusion weighted MRI, arrow pointing to an infarct (a).
T2 weighted MRI with a ROI placed around the suspected area (b)
Different dissimilar regions, segmented by the HCS process, for a specific
dissimilarity level (c).
One of the dissimilar regions, isolated by the HCS process, for a specific dissimilarity
level (d). (Image courtesy Selvan 2007).

3.3.I.2. Performance of the HCS Process in Segmenting Different Regions in CT Images

Figure 3.5 (a) shows a CT image of a section of the brain. The image area within the region of interest (rectangular area outlined in black) is made up of three different types of regions viz. Grey matter, White matter and the stroke affected area. The stroke affected area has been outlined in white by an expert. Figure 3.5 (b) shows the segmentation result given by the HCS process. It can be seen from the output that the HCS process has successfully delineated the three different types of anatomical regions viz. Grey matter, White matter and the stroke affected area. It can also be seen that the HCS process delineation of the stroke affected area is much more precise than that marked by an expert through visual inspection [Selvan 2007].

JSIK arw M rlc?

b

Figure 3.5 - HCS process Segmentation of a CT image.
CT image showing the suspected area outlined in white by an expert(a).
Segmentation of the Grey matter, White matter and Stroke affected regions and their boundaries by the HCS process (b). (Image courtesy Selvan 2007).

3.3.1.3. Performance of the HCS Process in Segmenting Different Regions in Ultrasound (US) Images

Figure 3.6 (a) shows an Ultrasound longitudinal section of the uterus. The image shows the diseased area outlined in white by the sonologist. As shown in the image a ROI was marked to enclose the diseased area and the HCS process was applied within the ROI. Figure 3.6 (b) shows the clusters identified by the HCS process during an intermediate stage. There are three clusters coloured as Green, Blue and Yellow as shown in the Figure 3.6 (b). The cluster coloured as Blue contains the pixels from the area outlined as diseased by the sonologist. The Figure 3.6 (b) also shows the boundaries of the three clusters and the diseased area outlined in Red. The segmentation results, shown in Figures 3.6 (b) were sent to the sonologist for critical comments. A synopsis of the sonologist's observation follows : [Selvan 2007]

- Looking at the original image only an expert sonologist would be able to identify this abnormality.
- The program had delineated the diseased area very clearly as a separate region coloured Blue. As for the pixels outside the diseased area coloured Blue it could be differentiated by the physician as non diseased area as they were in the border of the Uterus. Therefore, the program will be useful to differentiate diseased area in the case of border line pathology, where the sonologist will not be very sure of the diseased area.
- The region marked as Yellow within the diseased area gave the additional information that the area has got the core of the disease, and it was spreading out from that location.

Figure 3.6 - HCS process Segmentation of a US image.
 An Ultrasound image section. Diseased area outlined in white and the ROI marked in black (a).
 Regions segmented (and their Boundaries) by the HCS process during an intermediate stage (b) (Image courtesy Selvan 2007).

3.3.1.4. Performance of the HCS Process in Segmenting Different Regions in X-ray Mammogram Images

Figure 3.7 (a) shows a X-ray mammogram image (Image ID mdb102) from the mini-MIAS database [Suckling 1994]. The mammogram image data mdb102 (Figure 3.7 a) has a dense-glandular background tissue with an abnormality of malignant asymmetric density. The approximate boundary of the abnormality, based on the suggestion by the mini-MIAS database, is shown as a circle in Red (Figure 3.7 a).

b

c

d

Figure 3.7 - HCS process Segmentation of a X-ray mammogram image.
A X-ray mammogram from mini-MIAS database (Image ID mdb102) the approximate boundary of the abnormality outlined in Red (a).
HCS process segmentation output, regions (b), region boundaries (c).
Boundary of one of the regions (Red) superimposed on top of the approximate boundary of the abnormality (Green) (d). (Image courtesy Selvan *et al*, 2011).

The HCS process was applied within a ROI, shown as a rectangle in Green (Figure 3.7 a). Figure 3.7 (b) and (c) illustrates the results of HCS applied to the mammogram image data, within the ROI. Figure 3.7 (d) shows the boundary of a region which is dissimilar from the rest superimposed on the approximate boundary given by the mini-MIAS database.

3.4. Objective evaluation of the performance of the HCS process

The HCS process, developed by Selvan [Selvan, 2007] was developed in an ad hoc manner and was validated subjectively by segmenting medical images of different modalities. Hence, before being adapted as a probable Computer Aided Disease Monitoring (CAM) tool, HCS need to be evaluated objectively for its performance.

HCS yields a segmentation of regions and their boundaries at different levels of allowable dissimilarity between the constituent regions. To evaluate the performance of segmentation methods like HCS, which yields a hierarchy of boundaries, precision-recall curves, an alternative to Receiver Operating Characteristic (ROC) curve, is more suited. Precision-recall curve was suggested by at the university of Berkley to benchmark boundary detecting algorithms against their database of human segmented natural images [Martin *et. al* 2001].

The procedure to benchmark the performance of any boundary detecting algorithm, like HCS, is described as follows [Arbelaez, 2007]:

[<http://www.eecs.berkeley.edu/Research/Projects/CS/vision/bsds/>]

For each image a collection of human-marked boundaries, marked by different human subjects, constitutes the ground truth. The output of the boundary detecting algorithm, will be a boundary map with one pixel wide boundaries. The objective is to find out how well the algorithm's boundary map matches with that of the human subjects'. Traditionally, one would "binarize" the boundary map by choosing some threshold. Following are the two problems with thresholding a boundary map:

The optimal threshold depends on the application, and

Thresholding a low-level feature like boundaries is likely to be a bad idea for most applications, since it destroys much information.

For these reasons, the Berkley benchmark operates on a non-thresholded boundary map. Nevertheless, one needs to threshold the boundary map in order to compare it to the ground truth boundaries, but this is done at many levels. At each level, the two quantities precision (Chapter 2 Equation 2.1) and recall (Chapter 2 Equation 2.2) - are computed. In this manner the precision-recall curve for the boundary detecting algorithm is produced.

To distill the performance of an algorithm into a single number is possible to do in a meaningful way for algorithms whose curves do not intersect and are roughly parallel. When two precision-recall curves do not intersect, then the curve furthest from the origin dominates the other. The summary statistic that is used is a measure of this distance. It is the F-measure, which is the harmonic mean of precision and recall. The F-measure, combines precision and recall as given by the expression in the equation 3.4.

$$F = \frac{2 \times (Precision \times Recall)}{(1 + Precision + Recall)} \quad [3.4]$$

Where α is set to 0.5 [Martin *et al.* 2002]

The F-measure is defined at all points on the precision-recall curve. The maximum F-measure value across an algorithm's precision-recall curve is its summary statistic [Martin *et al.* 2001].

3.4.1. HCS Process Evaluation and Benchmarking Experimental Results

Figure 3.8 shows an image (of size 481x321) of a natural scene from the Berkley database [Martin *et al.* 2001] (Image ID 42049) and the boundaries as outlined by one of the human subjects.

The subset of the natural scene of the Berkley database [Martin *et al.* 2001] (Image ID 42049) was used to evaluate the performance of the HCS process, using the process outlined above (Section 3.4). Figure 3.9 (a) shows the subset (of size 111x191) of the whole scene (Figure 3.8). Figure 3.9 (b) and (c) show the HCS process output clusters and their respective boundaries when there were twenty two regions yet to be merged.

Figure 3.8 - A natural scene from the Berkley database (Image ID 42049) and the corresponding hand segmented boundary by one of the human subjects.

Since HCS process is a region segmentation process, the borders of the regions will be two pixels wide by design. This could be seen from the zoomed up part of the region and border images (3.9 (b) and (c)). Before the HCS process boundaries are compared with the human drawn boundaries the HCS process boundaries output need to be thinned to one pixel wide boundaries.

b c d

Figure 3.9 - HCS process Segmentation of a natural scene.
 A subset of the natural scene from the Berkley database (Image ID 42049) (a). HCS process segmentation output when there were 22 regions yet to be merged (b). The regions' two pixel wide boundaries (c). The corresponding one pixel wide thinned boundaries (d).

Thinning can be defined heuristically as a set of successive erosions of the outermost layers of a shape (border of a region), until a connected unit-width set of lines (skeleton) is obtained [Davies and Plummer, 1981]. Thus, thinning algorithms are iterative algorithms that 'peel off' border pixels. Connectivity is an important property that must be preserved in the thinned object. Therefore, border pixels are deleted in such a way that object connectivity is maintained. Thinning algorithms satisfy the following two constraints [Pitas, 2000] :

They maintain connectivity at each iteration. They do not remove border pixels that may cause discontinuities.

They do not shorten the end of thinned shape limbs.

An iterative algorithm [Zhang and Suen 1984] [Gonzalez and Wintz 1987] which

satisfies the above two constraints adopted from Pitas [Pitas 2000] was used to thin the borders output by the HCS process.

To flag border pixels for deletion the thinning algorithm applies locally in a 3x3 window the following two operations [Pitas 2000].

Step : 1 the logical rule P_1 is applied in a 3x3 neighbourhood and flags the border pixels *that can be deleted*

Step 2: the logical rule P_2 is applied in a 3x3 neighborhood and flags the border pixels *that will be deleted*.

The logical rules P_1 , P_2 used in the above the two steps have the forms given by the expressions 3.5 and 3.6

$$P_1 \ (2 \leq N(p_0) \leq 6) \ \&\& \ (T(p_0)=1) \ \&\& \ (p_1 \cdot p_3 \cdot p_5=0) \ \&\& \ (p_3 \cdot p_5 \cdot p_7=0) \quad [3.5]$$

$$P_2 \ (2 \leq N(p_0) \leq 6) \ \&\& \ (T(p_0)=1) \ \&\& \ (p_1 \cdot p_3 \cdot p_7=0) \ \&\& \ (p_1 \cdot p_5 \cdot p_7=0) \quad [3.6]$$

Where

$N(p_0) = \sum p_i$ denotes the number of object pixels ($p_i = 0, 1 \ i = 1, \dots, 8$) in the 3x3 window (excluding the central pixel)

$T(p_0)$ denote the number of $0 \rightarrow 1$ transitions in the pixel sequence $p_1 p_2 p_3 \dots p_8 p_1$.

The products of the form $(p_i \cdot p_j \cdot p_k=0)$ denote logical conjunctions of the corresponding pixels.

The first condition of both logical predicates states that the central pixel can be deleted if it possesses at least one and at most six 8-connected neighbours in a 3x3 window. If the central pixel has only one neighbour, it cannot be deleted, because the skeleton limb will be shortened. If the central pixel has more than six neighbours, central pixel deletion is not permitted because it will cause object erosion.

The second predicate $(T(p_0)=1)$ checks if the pixels of the perimeter of the 3x3 neighbourhood form only one connected component.

The third and fourth predicates $(p_1 \cdot p_3 \cdot p_5=0)$ and $(p_3 \cdot p_5 \cdot p_7=0)$ in P_1 are satisfied if $p_3=0$ or $p_5=0$, or if $(p_1=0 \text{ and } p_7=0)$

When the entire image has been scanned, the flagged pixels are deleted. This procedure is applied iteratively, until no more image thinning can be performed.

Figure 3.9 (d) shows the thinned boundaries of the HCS output when there were twenty two regions (Figure 3.9 (c)).

Figure 3.10 (b) shows the hand drawn boundaries by four of the human subjects' (Top row). Figure 3.10 (c) shows some of the HCS process intermediate segmentation thinned boundaries output (Bottom row) when there were twenty-two, fifteen, ten and six regions.



Figure 3.10 - HCS process segmented boundaries of a natural scene. A natural scene from the Berkley database (subset of Image ID 42049) (a). Top row of images are boundaries, marked by four different human subjects (b). Bottom row of thinned boundary images are the HCS process segmentation output when there were 22, 15, 10 and 6 regions (c). (Image courtesy Selvan Sept. 2011)

The segmentation output when there are fifteen, ten and six regions looks very similar. This is the case because of the following reason :

As the HCS process iterates the allowable dissimilarity between regions to be merged is increased. Hence, at later stages of the merging process the HCS process will merge regions which will be highly dissimilar. In images which are

more or less homogeneous the highly dissimilar regions will be a very small part of the image. In the scene depicted in the Figure 3.10 (a) the three main objects namely the sky, the bird and the branch are more or less homogeneous within themselves. Hence, once these three objects' boundaries have been delineated (when there were 15 regions Figure 3.10 c) subsequent merging of regions within the homogeneous areas are very small part of the image which are not very obvious in the later segmentation.

Given the list of segmentation output generated by the HCS process for the image of the Berkeley Segmentation Database (BSD) (Figure 3.10 (a)), the code by Estrada and Jepson [Estrada and Jepson 2009], was used to compute the precision and recall with regard to the human segmentations from the BSD (Figure 3.10 (b))

Figure 3.11 shows the precision and recall plot for two-hundred-and-twenty-eight segmentation levels of the HCS process. The maximum F-measure value across the precision-recall curve was found to be 0.82. which is the summary statistic [Martin *et. al.* 2001].

It should be noted that for this specific example the F-measure increased as the number of iterations of the HCS process increased until it reached the maximum value and there onwards it decreased. But this might not be the case for other examples because the way the HCS process segments the image might not exactly correlate with the way the humans segment the images. That is the reason why the F-measure values is found by making use of the precision-recall curve.

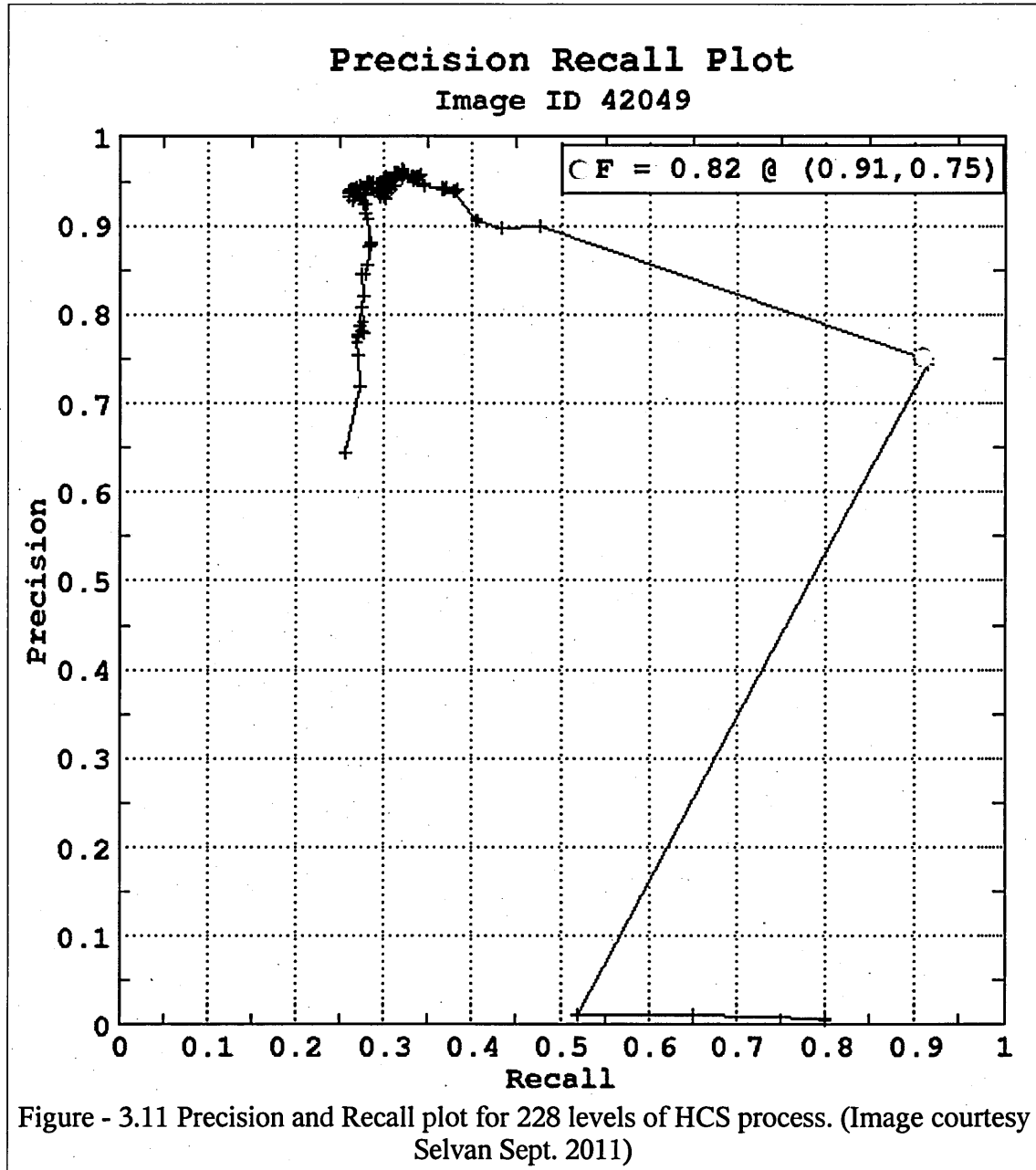


Figure - 3.11 Precision and Recall plot for 228 levels of HCS process. (Image courtesy Selvan Sept. 2011)

3.4.2. Critical Evaluation of the HCS Process's Experimental Results

The F measure (0.82) obtained by the HCS process (Figure 3.11) is among the top scores for this image. The corresponding scores for other segmentation algorithms ranges from 0.92 (Figure 3.12) [Dollar *et al.*, 2006] to 0.76 (Figure 3.13) [Yu, 2005], (See Arbelaez 2007). The “Boosted Edge Learning” algorithm which has got the highest score of 0.92 (Figure 3.12) is supervised [Dollar *et al.*, 2006] and was trained with training images before it was applied to the test images. In contrast the HCS process is unsupervised and needed no prior training to do the segmentation. The HCS process which is unsupervised has got a better score 0.82 (Figure 3.11) when compared with the score 0.76 (Figure 3.13) obtained by the unsupervised method “Segmentation induced by Scale Invariance” [Yu, 2005].

0 0,1 0.2 0.3 0.4 0.5 0.6 0.7 0.8 0.9 1
Recall

Figure 3.12 - Boundary output and the P-R curve for the segmentation method “Boosted Edge Learning” [Dollar, 2006] (Image courtesy Arbelaez 2007).

Moreover the human subjects' boundaries (Figure 3.10 b), with which the algorithms' output are compared, outline only the major structures in the scene. For example, none of the human subjects has outlined the border of the bird's legs. In contrast, the HCS process has not only outlined the legs of the bird but has also outlined the subtle difference in the chest plumage of the bird (Figure 3.14).

The subtle differences in the shades of grey in the chest plumage of the bird could be clearly observed once HCS process has outlined the borders (Figure 3.14). This outlining of subtle differences within an otherwise a homogeneous region is found to be very useful in highlighting dissimilarities in diagnostic images which aids the image perception. This due to the fact that tissue abnormalities in medical images are indicated by parts of the image being dissimilar from otherwise homogeneous areas representing healthy parts.

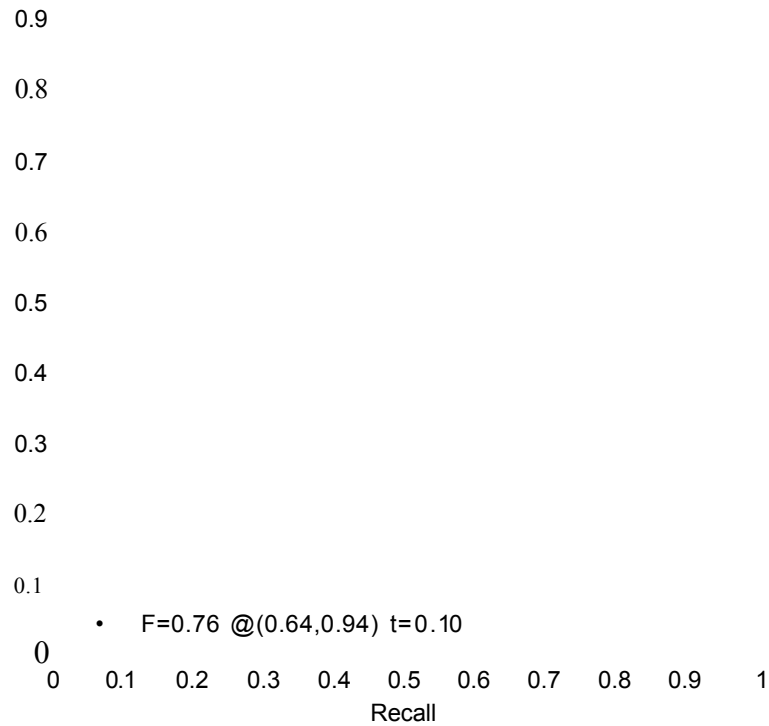


Figure 3.13 - Boundary output and the P-R curve for the segmentation method “Segmentation induced by Scale Invariance” [Yu, 2005] (Image courtesy Arbelaez 2007).

Figure 3.14 - HCS process segmentation output highlighting the subtle dissimilarities in the natural scene (Image courtesy Selvan Sept. 2011)

Hence, the performance of the HCS process based on correlating its segmentation output with human drawn boundaries serves only the purpose of an academic exercise [Selvan, Sept. 2011] with limited practical value.

3.5. HCS as a Perceptual Aid for Radiologists

Radiologists' expertise in reading diagnostic images calls for a combination of perceptual skills to find what may be faint and small features in a complex visual environment, and interpretive skills to rate their (the features') significance [Tabar and Dean 1985]. Computing systems are more consistent in their perceiving ability but they cannot match human interpretive skills. Drawing a line so as to limit the system's interpretive function has the virtue of achieving a complementary synthesis of system and radiologists' strengths [Claridge 1997]. However, in practice the question of where to draw the line in computer aided detection/diagnostic systems between perception and interpretation is problematic [Hartswood *et al.* 1997].

The HCS process may be able to address the above problem as follows :

- given a diagnostic image the HCS process can output a hierarchy of segmentation output which is the perception part of the overall solution.
- from the set of HCS process segmentation output, an experienced user can choose the most appropriate segmentation best suited for a specific application. This is the interpretation part of the overall solution.

The following example, from [Selvan, 2007], illustrates the above.

Figure 3.15 shows the infarct affected area (right side of the Pons) of the brain outlined in white by the expert. The image was processed within a ROI which enclosed the part of the image affected by the stroke. Figure 3.16 shows the location and size of the ROI chosen.

Figure 3.17 shows the four major clusters segmented within the ROI by the HCS process during an intermediate stage. Figure 3.18 shows the borders of the clusters. The cluster which includes the pixels from the area outlined by the expert is coloured red and the rest of the clusters are given other unique colours.

It can be seen from Figures 3.17 and 3.18 the red coloured cluster includes other pixels which were not within the expert outlined area. From the boundary outlined image shown in Figure 3.18 it can be seen that the area of the image within the red boundary has got visually very similar pixels.

Figure 3.15 - CT image of a section of the brain showing the infarct affected area marked in white by the expert. (Image courtesy Selvan 2007)

Figure 3.16 - The location and the size of the ROI enclosing the infarct affected area. (Image courtesy Selvan 2007)

When the segmentation, shown in the Figures 3.17 and 3.18, were given to the expert for their evaluation, the expert's response was that the segmentation had misclassified areas not belonging to the infarct as belonging to the infarct. This is indicated in Figure 3.19 where the expert has marked the true area of the infarct. Figure 3.20 shows the boundaries of the regions segmented by the HCS process superimposed on the image subsequently marked by the expert. The boundary of the cluster, which includes the pixels from the area outlined by the expert, is coloured red and the rest of the clusters' boundaries are given other unique colours.

Figure 3.17 - The regions during an intermediate stage of the HCS process (Image courtesy Selvan 2007)

Figure 3.18 - Borders of the regions during an intermediate stage of the HCS process (Image courtesy Selvan 2007)

On inspecting Figure 3.20, the following two observations were made :

HCS process did aid the expert in delineating the boundary of the infarct much more appropriately. This could be inferred when one compares the earlier outline of the infarct by the expert, shown in Figure 3.15, with the one outlined by the expert (see Figure 3.19) after inspecting the HCS process segmented regions. Thus HCS aids perception.

- When one compares the actual pixel values of some of the pixel locations within the infarct and the one outside the infarct, but identified as belonging to the infarct by the HCS process, it could be seen that they have exactly the same values.

Table 3.1 lists the some of the pixel locations and their values. In Figure 3.21 the pixel locations listed in Table 3.1 are marked. In Figure 3.21 the correctly classified pixel locations are in Green and misclassified pixel locations are in Yellow.

Thus, where the HCS process has failed the expert making use of his anatomical knowledge can do the interpretation better than HCS.

Figure 3.19 - Infarct outlined by the expert after evaluating the HCS process results, (Image courtesy Selvan 2007)

Figure 3.20 - Borders of the regions during an intermediate stage of the HCS process superimposed on the expert newly outlined image. (Image courtesy Selvan 2007)

Table 3.1 - Coordinates of three of the pixels located inside and outside the expert marked boundary of the infarct and their pixel values. (See Figure 3.21) [Selvan 2007]

Pixel Location	Pixel Coordinates	Pixel value
Within the expert marked	250, 284	1033
boundary of the infarct	249, 278	1036
(Pixels coloured in Green)	251,278	1038
Outside the expert marked	296, 297	1033
boundary of the infarct	289,313	1036
(Pixels coloured Yellow)	283,268	1038

Figure 3.21 - Three of the pixel locations which were correctly classified, by the HCS process (marked in Green) and three of the pixel locations which were misclassified (marked in Yellow). Refer Table 3.1 for details.(Image courtesy Selvan 2007)

3.5.1.HCS as a Perceptual Aid by Augmenting the Information Provided by CAD Prompts in Mammograms

Dense breasts contain more glandular and connective tissue. Less dense breasts are mainly made up of fat tissue. Breast cancer itself is made up of dense tissue. This means that on a mammogram, a tumour is harder to spot in dense tissue than in fatty tissue, because the tumour looks a lot like the tissue around it. An analogy is often used to describe the way cancer tissue looks on film, "It's like looking for a polar bear in a snow storm". Breast cancers are readily seen in fatty tissue with up to 98% sensitivity in film mammography. Breast density is one of the strongest—if not the strongest—predictors of mammography screening failure [Moon, 2000]. In a study of breast cancers that are missed by radiologists, Georger *et al.*[1997] found that missed cancers were significantly lower in density than detected cancers, and missed cancers were more often seen on only one of the two views.

One method of helping radiologists screen mammograms for signs of cancer is prompting, in which computer based algorithms are used to detect potential abnormalities in digital images and to draw attention to the corresponding regions in the original films (Figure 3.22-A). Prompting aims to improve radiologists' performance by reducing the number of false negative errors, i.e. cases in which a mammogram containing a significant abnormality is classified as normal.

The goal of the prompting based CAD system is to reduce errors by drawing radiologists' attention to possible abnormalities. CAD is not intended to be used as a

Figure 3.22-A - Computer Aided Detection (CAD) through prompting. (Stock Image)

computer-aided diagnosis tool: the decision as to whether a feature is of clinical significance remains with the radiologist. In practice, however, the distinction between detection and diagnosis may be blurred. One study has indicated that, for subtle microcalcification clusters, subjects' confidence that a cluster was present was increased if the cluster was prompted, and decreased if the cluster was unprompted [Chan *et al* 1990]. Another study reported that prompting can entail an increase in false positive decisions without necessarily having an overall effect on confidence levels [Muggleston *et al* 1996]. The first study would seem to indicate that radiologists' confidence with respect to the detection task is affected by prompting, but that their diagnostic decision making remains largely unaffected. The second study, however, raises doubts regarding the latter conclusion [Hartwood *et al* 1998]. Alberdi et al. [2005] in their study have argued that CAD had both beneficial and detrimental effects on readers' performance (Figure 3.22-B).

Gale *et al* [2006] have wondered whether there are better ways to present the CAD prompts and are there other image inputs that we can use than those simply visible to the human observer? Alberdi *et al* [2005] propose to explore how the CAD tool could provide explanations of its behaviour on demand. They anticipate that the challenge would be to produce the sorts of accounts that would be useful to a reader, which calls for an understanding of the sorts of explanations where confusion may arise. They have also questioned whether such exacting specifications could be

implemented reliably enough not to make the explanation facility a source of further problems.

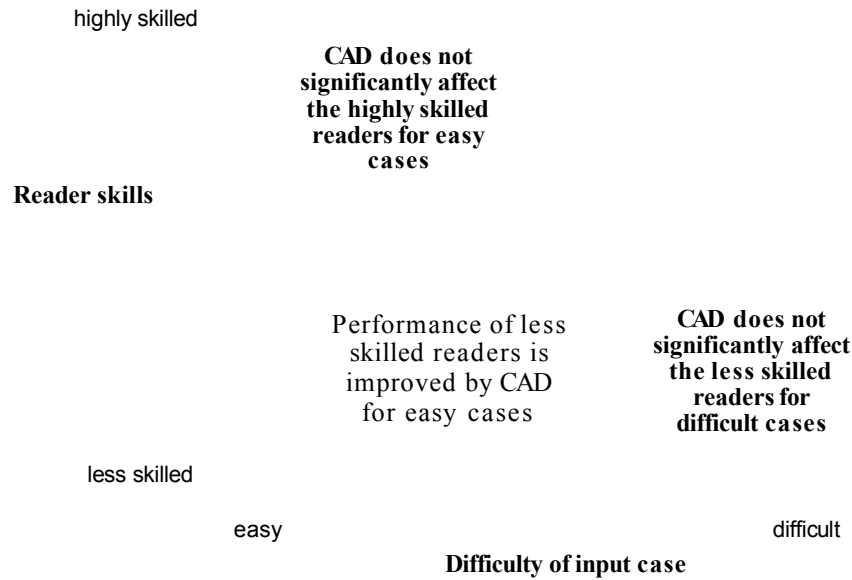


Figure 3.22-B - Effect of Prompting based CAD on Human Decision. [Image courtesy Alberdi, 2004]

Hierarchical Clustering-based Segmentation (HCS) process's segmentation output around the prompted area, could possibly serve as additional information which might augment the information provided by the prompts. This could be the case because HCS process output could possibly aid the reader to perceive the area around the prompt “better” and could possibly reduce the detrimental effects of the prompts [Selvan *et al.*, 2009]. This possibility is discussed below.

A computer monitor can display only 256 different shades of grey, at any one time. The technique of windowing is an electronic manipulation of the data to enable these 256 shades of grey to be used to represent a limited range, or window, of 16 bit medical image data. Until the last half-decade interpreting medical images was based solely on hard copies of the images. With the recent availability of powerful graphical workstations soft copy (electronic) evaluation of the images is replacing the role of hard copy interpretation [Johnson, 2003]. The possibility of directly interacting with the original 16 bit data gives the radiologists the freedom to set the window settings interactively. Studies have assessed the clinical significance of using variable window settings in soft copy interpretation [Fayad *et al.*, 2002].

In the medical imaging community the windowing parameters are referred to as 'window centre' (C) and the 'window width' (W) of an image. Narrowing the window or compressing the grey scale increases contrast for the purpose of visual perception. Conversely, widening the window will increase the range of pixel values displayed in a single shade of grey [Albertyn, 1996]. Lev *et al.* [1999] conducted a study to evaluate the advantage of viewing electronic copies of the CT image using variable window settings. They concluded that in non-enhanced CT of the head, detection of ischemic brain parenchyma is facilitated by soft-copy (electronic copy) review with variable window width and centre level settings to accentuate the contrast between normal and edematous tissue.

There had been previous studies to design an appropriate non-linear mapping function to optimally display a range of pixel values using the same window settings. For example, the pilot study by Fayad *et al.* [2002]. To fit a wide range of pixel values into 256 shades of gray, our study uses a technique known as equal-probability quantizing [Haralick, 1973]. Equal-probability quantising is an alternative technique that is particularly attractive for distributing the pixel values. The equal-probability quantising technique consists of computing the frequency of occurrence of all allowed pixel values (within a windowing parameter range). If pixel values in a certain range occur frequently, while others occur rarely, the quantisation levels are finely spaced in frequently occurring range and coarsely spaced outside it. In some literature equal-probability quantising method is sometimes referred as tapered quantisation [Gonsalez, 1992] or histogram equalisation [Yu *et al.*, 2001]. Advantages of making use of equal probability quantising method to optimally display medical images is demonstrated with an example.

Figure 3.23 shows a T2 weighted MRI image. Table 3.2 lists the properties of the pixels in the image. Although the image could possibly have 1349 different values there are actually only 1046 unique values within the image. Figure 3.24 shows the distribution of the different pixel values within the image.

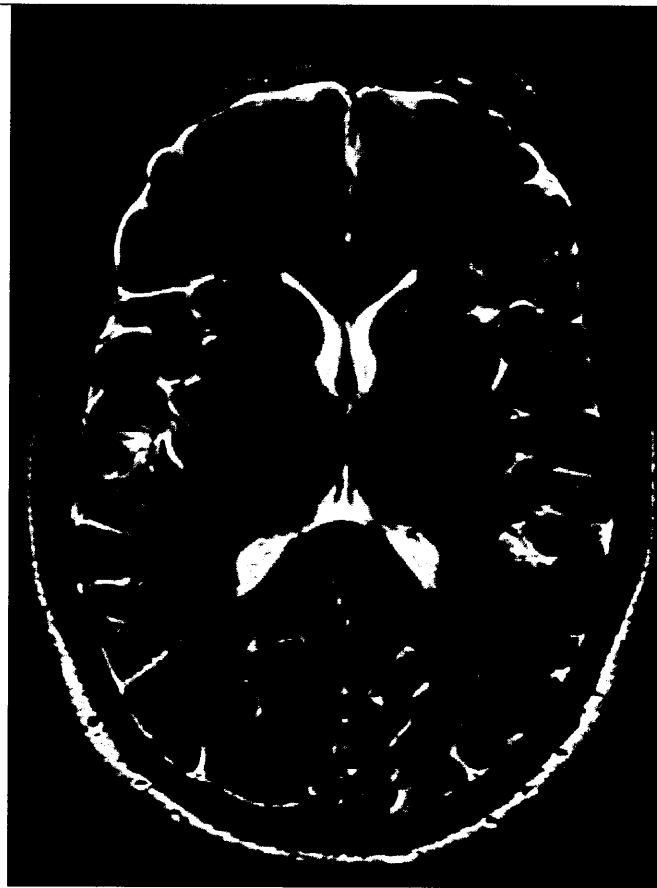


Figure 3.23 – T2 weighted MRI Image (Image courtesy Selvan 2007)

Table 3.2 - Details of the pixel values in the MRI image shown in Figure 3.23			
Pixel		Value	
Minimum	Maximum	Average	Standard Deviation
0	1348	241.3	172.6

Figure 3.25 shows the linear mapping of the whole range of pixel values present in the MRI image (Figure 3.24) to the available 256 levels for display. Figure 3.23 is the resulting image displayed using the linearly mapped 256 gray levels.

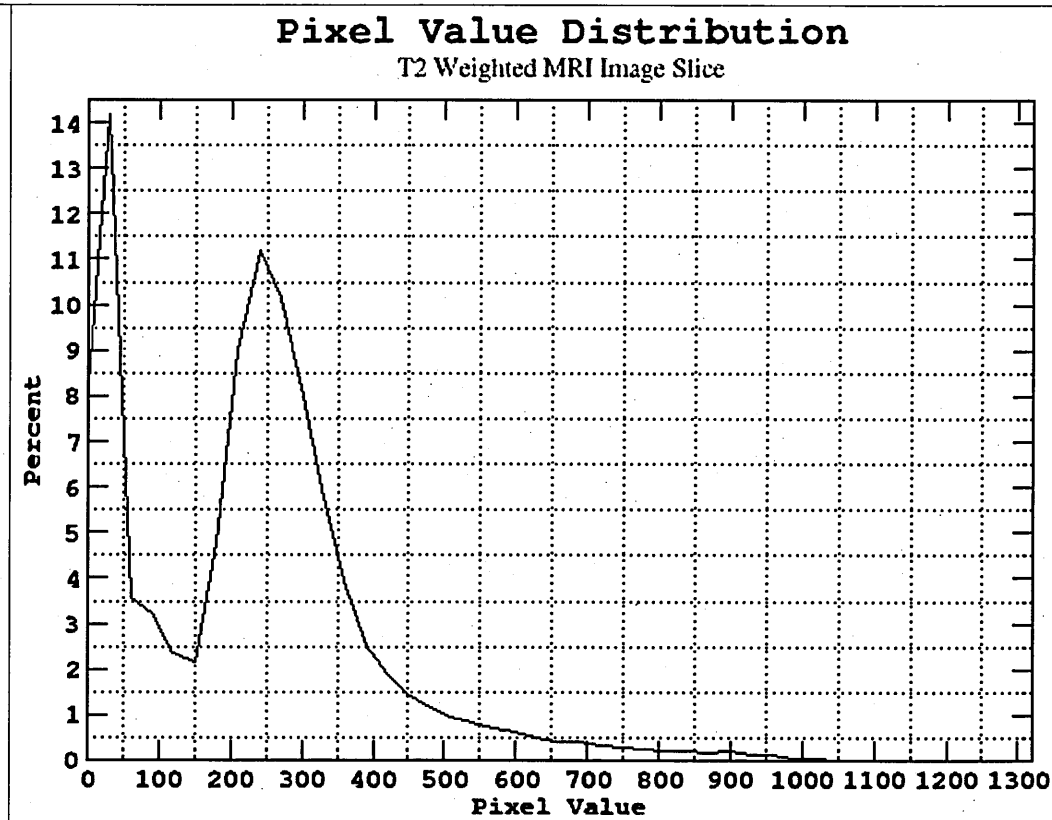


Figure 3.24 – The distribution of the pixel values in the T2 weighted MRI Image shown in Figure 3.23

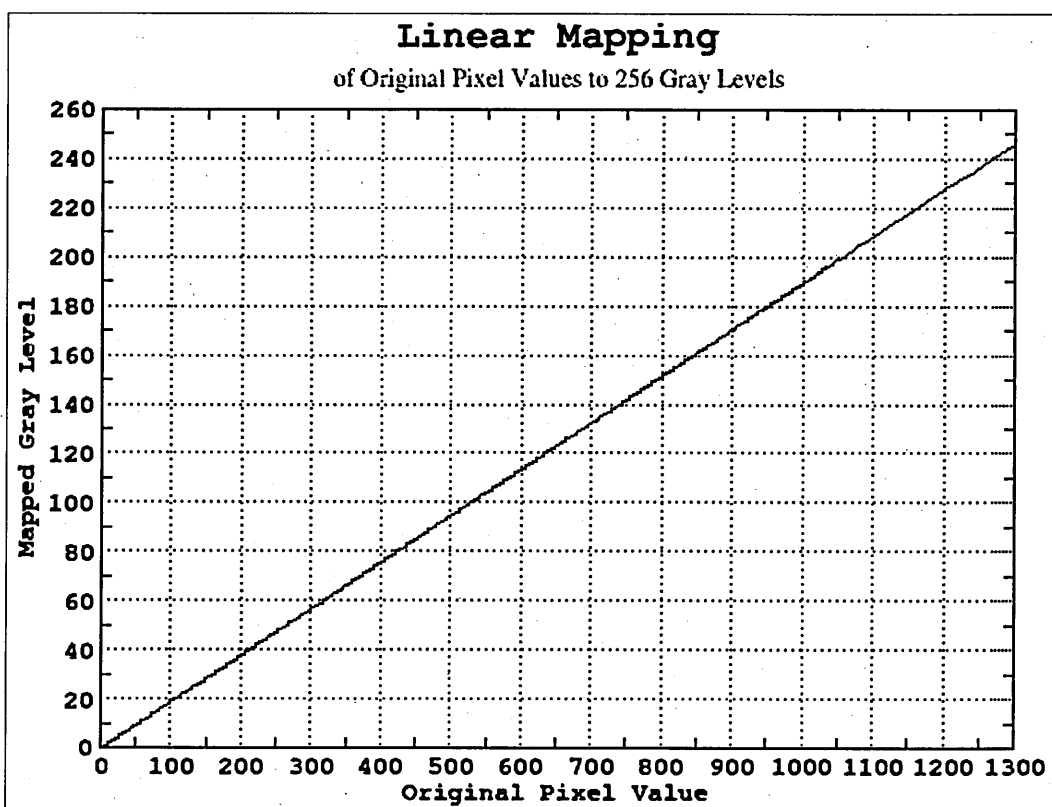


Figure 3.25 – The linear mapping of the actual pixel values in the T2 weighted MRI Image (Figure 3.24), to 256 gray levels.

Figure 3.26 shows the equal-probability quantizing [Haralick *et al.*, 1973] based mapping of the range of pixel values, shown in Figure 3.24, to 256 gray levels. Figure 3.27 is the resulting image displayed using the non-linearly mapped to 256 gray levels. In some literature equal-probability quantising method is sometimes referred as tapered quantisation [Gonzalez, 1992] or histogram equalisation [Yu *et al.*, 2001].

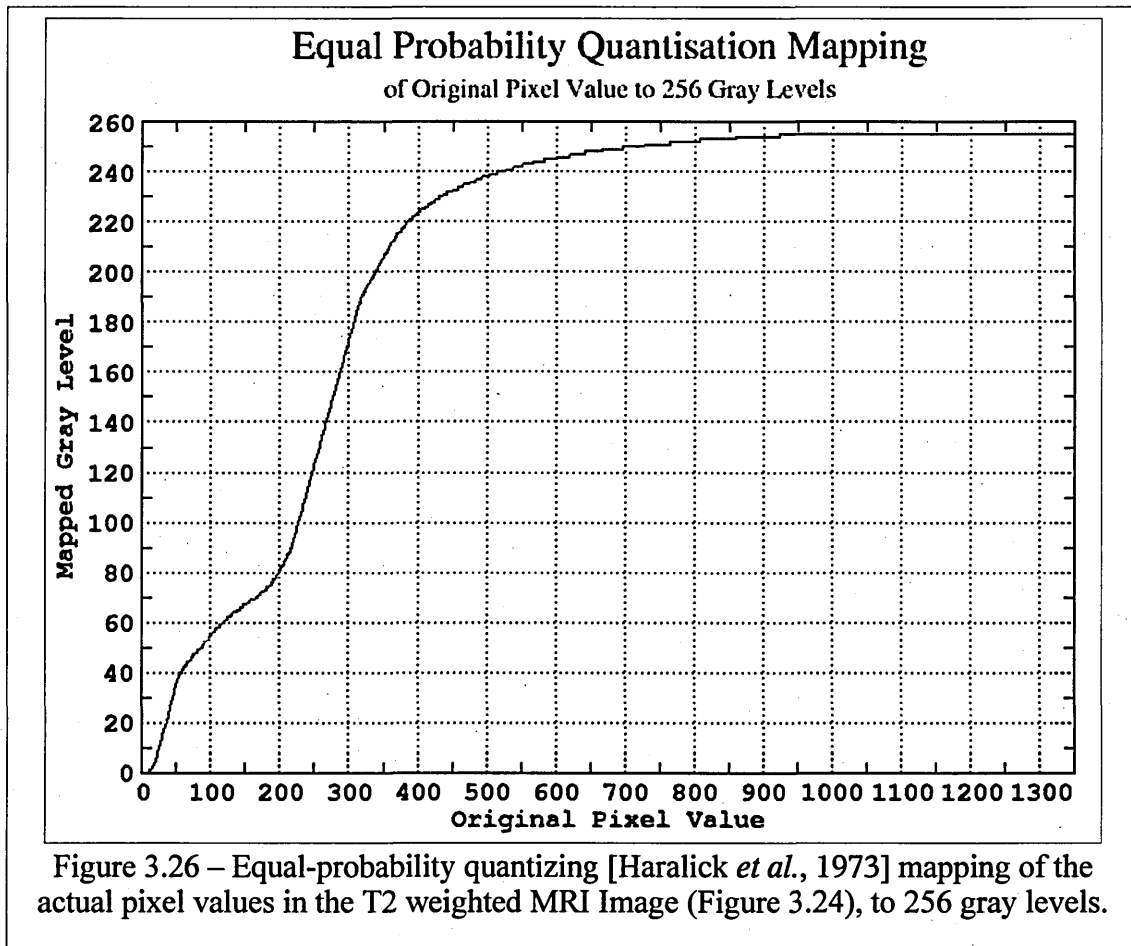


Figure 3.26 – Equal-probability quantizing [Haralick *et al.*, 1973] mapping of the actual pixel values in the T2 weighted MRI Image (Figure 3.24), to 256 gray levels.

Unlike CT Hounsfield values MRI images do not have specific ranges of values for the different anatomy. So choosing windowing parameters varies from image to image. Hence it will be very useful for the user if the image is displayed in the most optimised manner. For example Figure 3.28 shows the diffusion weighted image for the same patient where the location of the abnormality is quite obvious (arrow head). In the T2 weighted MRI image displayed making use of linear mapping (Figure 3.23) the corresponding location of the abnormality is not visible. But in the equal probability quantisation based mapped image (Figure 3.27) the corresponding location of the abnormality is clearly visible. When the original image data was processed by the HCS process this abnormal part of the image was confirmed to be dissimilar from the rest of the similar anatomy (Figure 3.4 d).

Figure 3.27 - T2 weighted MRI Image data (Figure 3.24) mapped to 256 levels making use of the equal-probability quantizing [Haralick *et al*, 1973] method (Figure 3.26).

Figure 3.28 - Diffusion weighted MRI Image showing the location of the abnormality (arrow head). (Image courtesy Selvan 2007)

From the foregoing discussion it can be gathered that knowing the right set of windowing parameters to display a specific image will greatly aid the visual perception of the diagnostic image and thus aid in the interpretation of the same. It will be shown with an example how HCS process can aid the estimation of these parameters.

Figure 3.29 (a) shows a mammogram (Image ID mdb028) from the mini-MIAS mammogram database [Suckling *et al.*, 1994]. The malignant abnormality, shown circled in Black, is of circumscribed mass class. The user has outlined the approximate location and boundary of an abnormality as perceived by him (Figure 3.29 a). When HCS process was applied within a ROI, around and centred at the abnormality, it produces a hierarchy of segmentations. Inspecting the HCS process produced hierarchy of segmentations the user can choose the segmentation which gives the most appropriate boundary of the abnormality (Figure 3.29 b).

Figure 3.29 (b) and (c) show the intermediate segmentation output of the HCS process when there were four regions yet to be merged. Table 3.3 tabulates the pixel properties within each of the four regions shown in the Figure 3.29 (b).

Once the pixel values range within different segmented regions is known it can be used as the windowing parameters to optimally view that part of the medical image.

Figure 3.29 (g) shows the quantised image, quantised (using equal probability quantising technique) within the narrow grey scale range of 185 to 218. The quantised image Figure 3.29 (g) shows the structure within the part of the image coloured red which is not visible in the normal scaled image Figures 3.29 (a) and (c).

Figure 3.29 - Quantised images of X-ray mammograms.
 mini-MIAS Mammogram image (Image-ID mdb028) showing the approximate
 location of the circumscribed mass (a). HCS process segmented regions (b) and their
 boundaries (c) when there were 4 regions yet to be merged.

Quantised images :

Quantised within the narrow range of 111 to 139 (d), 129 to 164 (e), 156 to 191 (f)
 and 185 to 218 (g)

**Table 3.3 - Details of the four regions in the intermediate HCS process segmentation
 output shown in Figure 3.29**

Region (shown in colour)	Minimum	Density Maximum	Value Average	Standard Deviation
Red	185	218	203	6.9
Yellow	156	191	173	8.2
Green	129	164	146	6.9
Blue	111	139	127	5.3

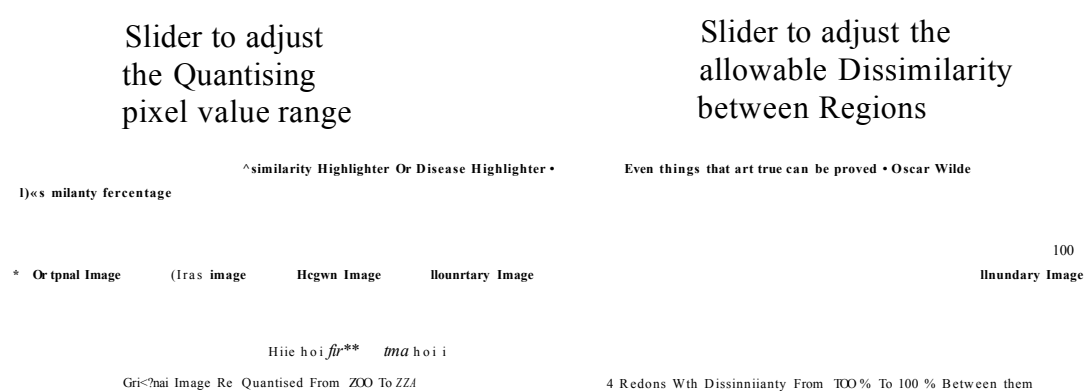
Figure 3.30 - Composite quantised image of X-ray mammograms. mini-MIAS Mammogram image (Image-ID mdb102) showing the approximate location of the circumscribed mass (a). HCS process segmented regions (b) and their boundaries (c) when there were 4 regions yet to be merged. The four regions, coloured Red, Green, Blue and Black (Table 3.4) are quantised within the narrow range of 200 to 224, 183 to 207, 162 to 194, and 133 to 171 respectively and the composite image is produced (d)

Table 3.4 - Details of the four regions in the intermediate HCS process segmentation output shown in Figure 3.30

Region (shown in colour)	Minimum	Density Maximum	Value Average	Standard Deviation
Red	200	224	212	5.1
Green	183	207	194	5.1
	162	194	177	5.9
	133	171	156	7.0

Figure 3.30 (d) shows the composite image generated by quantising the four regions, coloured Red, Green, Blue and Black (Table 3.4) quantised within the narrow range of 200 to 224, 183 to 207, 162 to 194, and 133 to 171 respectively and combining them in one image to generate the composite image (Figure 3.30 d).

The above described process of making use of the HCS process segmentation output to quantise the image for the purpose of better visualisation of the diagnostic image can be done interactively making use of the graphical user interface (GUI) [Selvan, 2007] designed to display the HCS process output (Figure 3.31).



Quantised Image	Density Value at Cursor Location	Cursor Location	Region Index at Cursor Location	Region Image
-----------------	----------------------------------	-----------------	---------------------------------	--------------

Figure 3.31 - GUI display of the HCS process output (right canvas) and the quantised image quantised to the narrow grey scale range of 200 to 224 (left canvas).

Total No Hxels	No_Of_Unique_Values	
Mirim Value	Maxm Value	AvgValue

Figure 3.32 = GUI display of the properties of the region coloured red in the right canvas of the GUI in Figure 3.31

Figure 3.31 (right canvas) shows the HCS process output of the mini-MIAS mammogram Image-ID mdb102. Figure 3.32 shows the GUI display of the properties of the region coloured red in Figure 3.31. The information of the grey value range got from the region properties display (Figure 3.32) was used to set the values for the quantising slider scale (Figure 3.31). The quantised image for the narrow grey scale value range of 200 to 224 is displayed on the left canvas (Figure 3.31).

Segmentation of the major structures in images can be to some extent done by the process of identifying the peaks and troughs in the histogram distribution of the pixel values in the image [Worth *et al.*, 1997] [Zhao *et al.* 2003].

Figures 3.33 and 3.34 illustrate how the histograms of the pixel values within the four different regions, segmented by the HCS process, correlates with the peaks and troughs of the overall histogram of the pixel values within the ROI, for the mammograms mdb028 (Figure 3.29) and mdb102 (Figure 3.30) respectively.

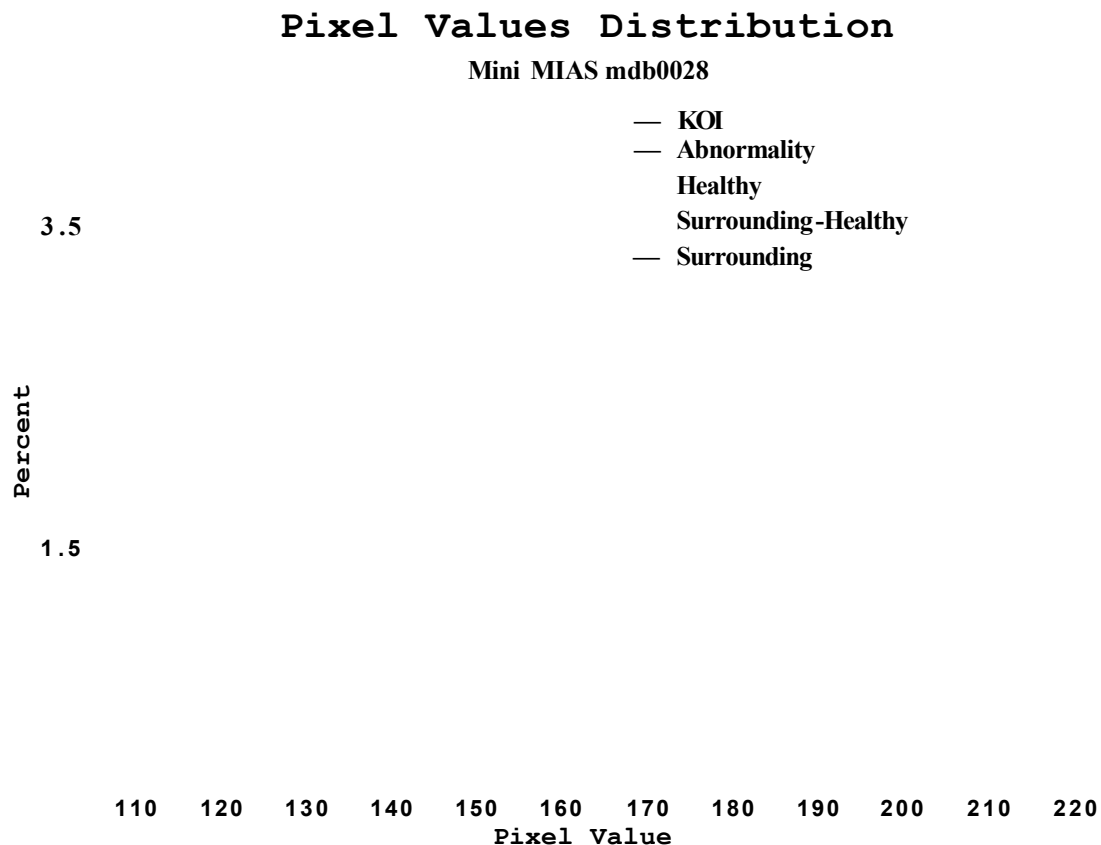


Figure 3.33 - Histogram (black) of the pixel values within the ROI of the mammogram shown in Figure 3.29 (a). The coloured plots show the histograms of the pixel values within the four regions identified by the HCS process (Figure 3.29 b).

Pixel Values Distribution

Mini MIAS mdb102

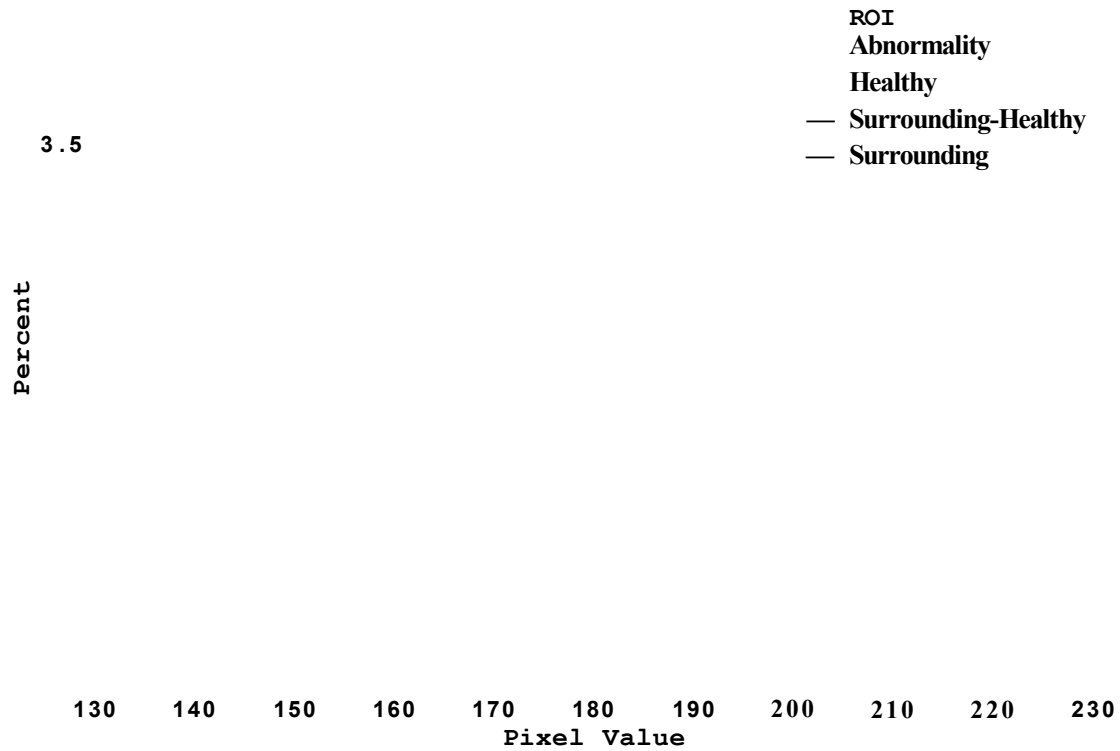


Figure 3.34 - Histogram (Brown) of the pixel values within the ROI of the mammogram shown in Figure 3.30 (a).

The Red, Green and Blue and Black coloured plots show the histograms of the pixel values within the four regions identified by the HCS process (Figure 3.30 b).

It should be noted that the histograms of the pixel values within the, HCS process segmented, different regions overlap. The reason being HCS process estimates the similarity between the different locations, in a image, by comparing the distribution of the pixel values within a small neighbourhood rather than compare just the individual pixel values [Selvan 2007].

Although the major regions within an image can possibly be segmented by identifying the corresponding peaks and troughs of the histogram plot of the pixel values in the image. Thresholding does not take into account the spatial characteristics of an image. This makes the method sensitive to noise [Yang and Jiang, 2002]. The difficulties faced by the method can be inferred from the Figures 3.35 and 3.36. Even for the histogram shown in Figure 3.33 it is not trivial to identify the threshold to segment the healthy region coloured Yellow (Figure 3.29).

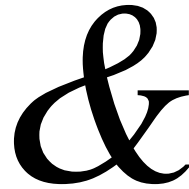


Figure 3.35 - mini-MIAS Mammogram image (Image-ID mdb005) showing the approximate location of the circumscribed mass (a, b). HCS process segmented regions (c) and their boundaries (d) when there were 10 regions yet to be merged.

Pixel Values Distribution

Mini-MIAS mdb005

- ROI
- Abnormality
- Healthy
- Surrounding Healthy
- Surrounding

50 60 70 80 90 100 110 120 130 140 150 160 170 180 190
Pixel Value

Figure 3.36 - Histogram (black) of the pixel values within the ROI of the mammogram shown in Figure 3.35 (a). Coloured plots shows the histograms of the pixel values within the four major regions identified by the HCS process (Fig 3.35 b).

From the above discussion it can be inferred that the HCS process can be used by the user to perceive diagnostic images more appropriately and subsequently interpret them. This process of making use of the HCS process to aid perceiving and subsequently interpret diagnostic images is discussed in more detail in the next two chapters titled HCS process aided interpretation of CT images of the lungs for Cystic Fibrosis (Chapter 4) and HCS process aided interpretation of X-ray mammogram (Chapter 5).

3.6. Summary

The Hierarchical Clustering based Segmentation (HCS) was introduced. An objective performance measure was obtained by evaluating the performance of the HCS process in segmenting natural scenes correlated with human subjects'. The suitability of the HCS process to aid medical image interpretation was investigated.

The suitability of the HCS process to aid in perceiving and subsequently interpreting diagnostic images was further investigated by developing the following two HCS process based diagnostic image interpretation applications :

- processing CT images of the lungs to segment the boundaries of the airway and the adjoining blood vessels (See Chapters 4 and 6).
- Computer Aided Monitoring (CAM) of breast abnormalities by processing X-ray mammograms [Selvan *et al.* 2011] (See Chapters 5 and 6).

Chapter 4 HCS Process Aided Interpretation of CT Images of the Lungs to Monitor Cystic Fibrosis

4.1. Introduction

One of the objectives of this study is to demonstrate how user decision incorporated image processing techniques can be used for processing diagnostic images and augment the information present in those images to aid the diagnosis process. In this chapter the implementation details of user decision incorporated CT image interpretation techniques for Cystic Fibrosis are discussed.

As discussed in Chapter 3, HCS is the process adopted in this study to augment diagnostic information in medical images. Hence, initially the use of HCS process to incorporate the users' decision, in the interpretation of diagnostic images, is discussed. Subsequently, the following application in which user decisions were incorporated during the processing of the CT image data, and thus augment their diagnostic information, is discussed in detail :

- user decision incorporated processing of CT images of the lungs.

4.2. User Decision Incorporated Processing of Diagnostic Images for Highlighting Dissimilarities in Medical Images

Tissue abnormalities in medical images are indicated by that part of the image being dissimilar from otherwise homogeneous areas representing healthy parts. The dissimilarity may be subtle or strong depending on the medical modality and the type of tissue abnormality. The goal of medical image segmentation is to separate the image into regions that are meaningful for a specific task. Medical image segmentation is a difficult task because of issues such as spatial resolution, poor contrast, ill-defined boundaries, noise, or acquisition artefacts [Sonka and Fitzpatrick, 2000].

Traditionally, segmentation algorithms highlight the boundaries between the different regions in an image by using some threshold. The two problems associated with the approach of thresholding to highlight boundaries are [Martin et al. 2001] are:

- the optimal threshold depends on the image data and the application.
- thresholding a low-level feature like boundaries is likely to be a bad idea for most applications, since it destroys much information.

For these reasons, the HCS process was adopted in this study to generate non-thresholded boundaries. The HCS process automatically generates a hierarchy of segmented images. The hierarchy represents the continuous merging of similar, spatially adjacent or disjoint, regions as the allowable threshold value of dissimilarity between the regions to be merged is gradually increased [Selvan *et. al* 2005] [Selvan 2007] [Selvan *et. al* 2009] [Selvan *et. al* 2011].

Nevertheless, we do need to identify the most relevant boundary map (segmentation) for subsequent processing. One of the capabilities of the human vision process when visualising images is its ability to visualise them at different levels of details. Since the HCS process mimics this capability of human vision, the user decision process is used of to choose the most appropriate segmentation.

4.2.1. The Use of HCS Output to Incorporate User Decision in Processing

Diagnostic Images

The details of how users can make use of HCS output to identify the most appropriate segmentation relevant to an application is application specific. Hence, the usage of HCS, for choosing the most appropriate segmentation, is discussed in detail, later in this chapter and the next, in relevance to the following applications :

- processing CT images of the lungs to segment the boundaries of the airway and the adjoining blood vessels (Section 4.3.5.1).
- processing X-ray mammograms to delineate the most appropriate boundaries of the abnormality (Section 5.2.4.1) and the healthy part of the image (Section 5.2.4.2.2).

4.2.2. Graphical User Interface (GUI) Facility for Displaying HCS Process Output

The HCS process generates a hierarchy of segmentation results, associated with a set of dissimilarity values. The segmentation results are stored at the end of the HCS processing. Subsequently, the GUI can be used to reproduce the resulting segmentation images associated with a dissimilarity value instantaneously. Making use of the GUI, the user can inspect how the merging process evolves. The user can interactively choose the dissimilarity level at which (s)he wants to view the segmentation results. At a low value of dissimilarity, the segmented image shows many varied regions similar to the original image. When choosing a high value of dissimilarity the image only shows regions which are significantly different. The

original image may be displayed alongside the processed image showing regions of dissimilarity. And a dual cursor facility provided by the GUI will allow the user to correlate the segmentation results with the original image data. This enables the clinician to improve their ability to identify regions having subtle differences or dissimilarities. The GUI also helps the user to differentiate dissimilarities in the image down to a single pixel level by providing the facility to highlight pixels belonging to the same region which might occur across the image. The GUI is designed in such a way as to make it easy for the user to view all the different solutions and select the most suitable. The easy viewing and scrutinization of segmentation results is achieved by the GUI by having the following facilities [Selvan 2007] :

- The different segmentation results can be viewed by using a slider bar giving the dissimilarity index.
- Individual region properties like the number of pixels, the lowest, highest and average pixel value and the distribution of the pixel values within the region can be scrutinized.
- The original image or another segmented image at a different level of dissimilarity can be compared with the segmented image by displaying them alongside each other and a dual cursor moves simultaneously on both the images.
- In order to allow the user to quickly display the segmented image the GUI provides a gallery of the set of segmented images. The user can click on any one of the thumb nail images to have it displayed on the main window.

The image of Figure 4.1 shows a screen captured image of the GUI and the user controls provided for the above listed facilities. The GUI facility will be useful for the user to choose the most appropriate segmentation for subsequent processing. For example, the GUI can be used to choose the most appropriate segmentation to identify the regions which correspond to the healthy and diseased part of the breast tissue in X-ray mammograms for subsequent processing to differentiate malignant from benign abnormalities (Please see Section 5.2.4.1).

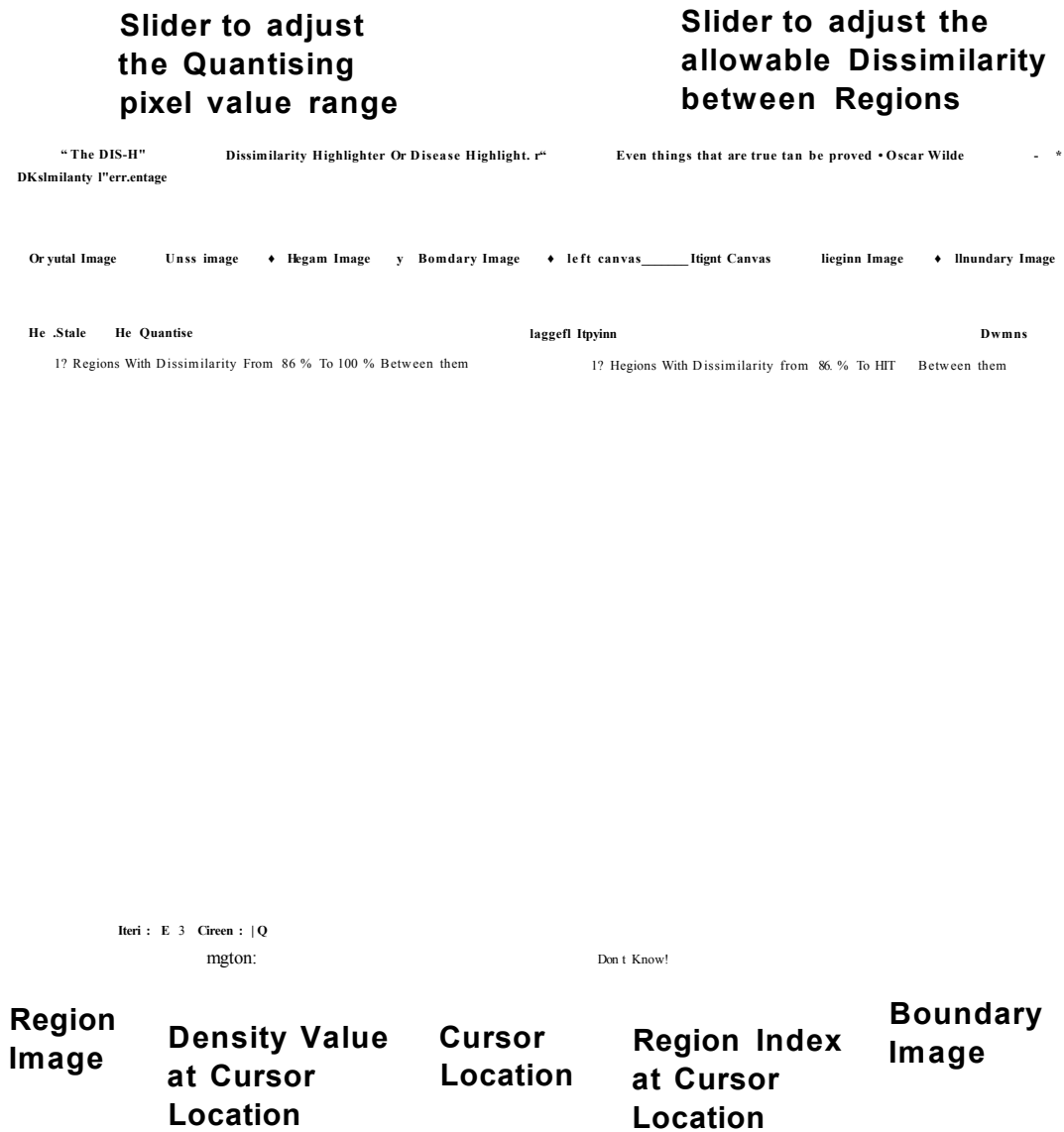


Figure 4.1 - Annotated screen captured image of the GUI, to visualize the HCS process output.

4.3. User Decision Incorporated Processing of CT Images of the Lungs

In this application, an investigation into the segmentation of airways and the accompanying blood vessels, in CT images, using the HCS process [Selvan 2007] was carried out.

Additional new methods such as ellipse fitting were also incorporated to the HCS process to quantify the dimensions of the segmented airways and blood vessels in the CT images. The developed methods were evaluated for their accuracy by segmenting and estimating the measurements of Blood Vessel and Airway in CT images of the lungs.

4.3.1. Motivation Behind the Study

Technical advances in CT allow an assessment of airway wall thickness and cross-sectional area *in vivo* that is comparable to histological examination. Quantitative assessments of airway dimensions have shown that there is an increase in airway wall thickness and lumen area (bronchitises) in Cystic Fibrosis (CF) infants and children compared with control subjects [de Jong 2005]. To date, there have been no studies in which quantitative CT estimates of airway disease have been compared with pathological measures in CF patients. The majority of High Resolution CT (HRCT) studies in CF were carried out using semi-quantitative scoring systems. Aside from the inherent intra- and inter-observer variations, the major limitations of these scoring systems relate to the lack of consensus on which system to use and to the failure to use definitions of CT abnormalities consistently [de Jong 2005].

In this current study, it is intended to evaluate the advantages of using computer methodologies to quantify peripheral airway disease. The quantification process will display the location, severity, extent of airway dilatation, bronchial wall thickening, and the presence of mucous impacted airways.

4.3.2. CT Image of the Airway

The schematic in Figure 4.2 shows the various measurements that can be made on CT images of airways and the vessels, which frequently accompany them. Linear measurements include the following [de Jong 2005]:

- The airway perimeter (P_i)
- The long and short axes of the outer airway area (A_o)
- The lumen area (A_i)
- Wall thickness (A_{wt})
- Airway lumen diameter (ALD)
- Airway outer diameter ($A_oD = ALD + A_{wt}$)
- Arterial diameter (AD).

Ratios of various linear dimensions include: ALD/AD ; A_{wt}/AD ; A_{wt}/ALD ; as well as long to short axis ratios, which are a measure of the obliquity of the section [de Jong 2005].

The area dimensions include the following :

- A_i ; airway wall area (A_{aw})
- Outer airway area ($A_o = A_{aw} + A_i$)
- Arterial area (AA).

Ratios of various areas include: A_i/AA ; A_{aw}/AA ; and percentage wall area ($WA\% = A_{aw}/A_o \times 100\%$). The square root of A_{aw} is often derived, since it is relatively linearly related to P_i . Finally, airway dimensions can be referenced to body surface area (*e.g.* A_{aw}/BSA and A_{wt}/BSA) [de Jong 2005].

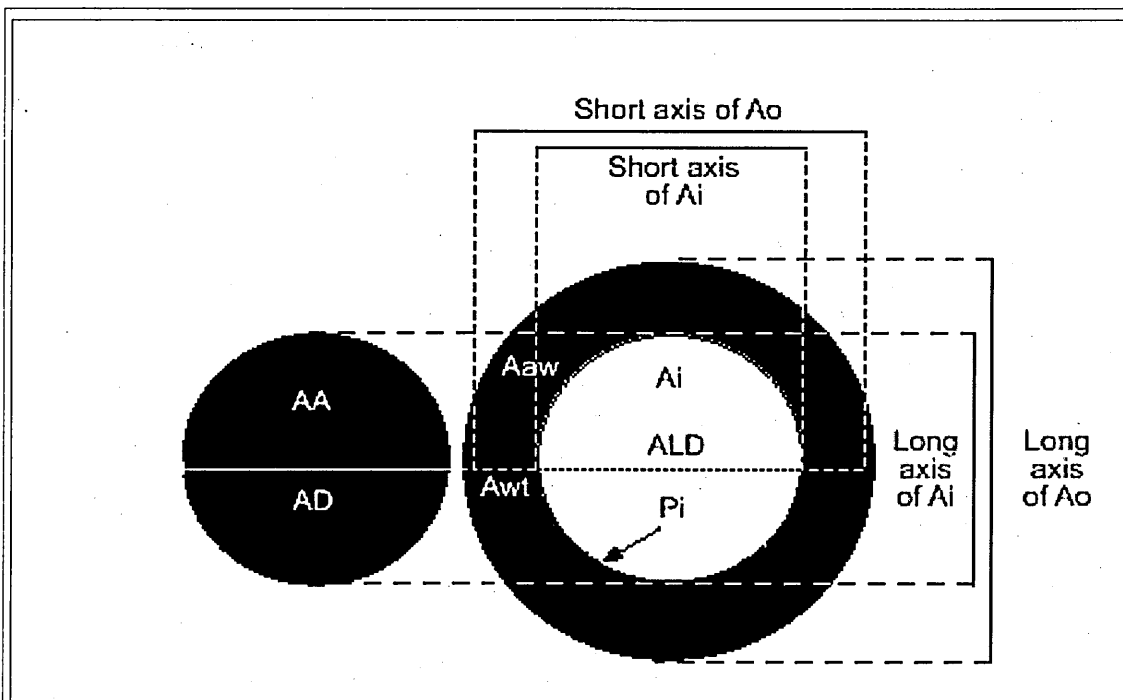


Figure 4.2 - Dimensions of the airway lumen, airway wall, and accompanying pulmonary artery (Image courtesy de Jong 2005).

However, the information that can be obtained from CT is essentially less detailed than those obtained from histological examinations. For example, CT cannot distinguish which components of the airway wall are thickened. Despite this limitation, the ability of CT to measure multiple airways relatively, non-invasive and repeatedly offers major potential advantages [de Jong 2005]

4.3.3. CT Image Data

CT imaging is based on X-ray attenuation of various tissues. Pixels in an image obtained by CT scanning are displayed in terms of relative radio-density. The digital value assigned to each pixel is according to the mean attenuation of the tissue that it corresponds to on a scale from -1000 to +1000. This scale is known as the Hounsfield Unit (HU) [Albertyn 1996]. The Hounsfield scale was invented in 1972 by Godfrey Newbold Hounsfield and is a quantitative measure of radio-density used to evaluate CT scans. In this scale, water has an attenuation of 0 Hounsfield Units (HU) while air has (-)1000 HU, bone has a value of the order of (+)1000 HU and metal objects beyond (+) 1000 HU [Albertyn 1996]. Thus, a CT image can potentially have more than 2000 different Hounsfield values stored as 16 bit data.

The Digital Imaging and Communications in Medicine (DICOM) standard was created by the National Electrical Manufacturers Association (NEMA) to aid the distribution and viewing of diagnostic image data, such as CT, MRI, and US scans. A single DICOM file contains both a header (which stores information about the patient's name, the type of scan, image dimensions, etc.), as well as all the image data. In a CT image, written in DICOM image format, the image data is not written in Hounsfield Units but rather in normal units. To convert from the normal units found in CT data (a typical data set ranges from 0 to 4000 or so) one has to apply the following linear transformation of the data. The linear transformation is:

$$HU = mx + b \quad [4.1]$$

Where

HU is Hounsfield Unit

x is Pixel_Value

m is Slope

b is Intercept

The values of the *Slope* and *Intercept* used in the above conversion can be found in the header of the DICOM image file . The tags, which are used in the header, to identify the values, are generally called the *Rescale Slope* and *Rescale Intercept*. *Rescale Slope* and *Rescale Intercept* typically have values of 1 and (-)1024, respectively. For example following tag information, corresponding to *Rescale Slope* and *Rescale Intercept*, are read from the header of the DICOM image shown in Figure 4.3.

[Ln 144] *Rescale Intercept* (0028,1052) [sbcIndexRange 1...1] DS [-1024]
[Ln 145] *Rescale Slope* (0028,1053) [sbcIndexRange 1...1] DS [1]

Making use of the above values for the *Slope* and *Intercept*, the original units, found in the CT image data, are converted to the corresponding Hounsfield units. For a set of sample locations, Figure 4.3 shows the pixel values, in their original units, read from the image data, and their corresponding values in Hounsfield units.

DFOV 252
Tilt : 0
45.75
1.25mm

Figure 4.3 - Annotated CT Image showing two locations of airway and accompanying pulmonary artery

As discussed above a CT image can potentially have more than 2000 different Hounsfield values, but a computer monitor can display only 256 different shades of grey, at any one time. The technique of windowing is an electronic manipulation of the data to enable these 256 shades of grey to represent a limited range, or window, of Hounsfield values. In the medical imaging community the windowing parameters are referred to as 'window centre' (C) and the 'window width' (W) of an image. Narrowing the window or compressing the grey scale increases contrast for the purpose of visual perception [Albertyn 1996]

For this study the facilities of a graphical user interface [Selvan, 2007] were used to visualize the CT image data and choose the appropriate windowing parameters. Figure 4.4 shows the DICOM image viewing facility that was used to view the CT images and choose the appropriate windowing parameters.

The sample annotated CT image in Figure 4.3 shows two locations of airway and close by pulmonary artery marked with the corresponding pixel values. Figure 4.5 shows the Region 1 part of the CT image (Figure 4.3) displayed using appropriate windowing parameters to highlight either only the blood vessel or the blood vessel and the airway.

Figure 4.6 shows the location of the rectangular region of interest (ROI) of size 24x16, enclosing Region 1 of Figure 4.3. The Hounsfield values within the ROI ranges from minimum (-)1024 to maximum (+)528. Although the range of the values is 1552, there are only 256 unique values. Hence, the images shown in Figures 4.3 and 4.5 were obtained by optimally mapping the 1552 range of values to the available 256 gray level values, for display purpose.

Re Scale I Re Quantise

QICOM iiiKHj! R* Quantised Fmm (l Hu Tu 4095 Hu

Figure 4.4 - Graphical user interface facility [Selvan, 2007] to view DICOM images and to choose the appropriate windowing parameters.

a

b

Figure 4.5 - Region 1 part of the CT image (Figure 4.3) displayed using appropriate windowing parameters to highlight either only the blood vessel (a) or the blood vessel and the airway (b).

Figure 4.6 also shows the colour coded four different classes of regions, namely blood-vessel (Red), airway wall (Green), lumen (Blue) and lung parenchyma (Black) as perceived by a radiologist. The colour coding was carried out manually. The manually segmented region can be seen superimposed on the original image to show the appropriateness of the manual segmentation.

u

Figure 4.6 - Manually segmented and colour coded four different classes of regions, namely Blood-Vessel (Red), airway-wall (Green), Lumen (Blue) and Lung Parenchyma at the background (Black) as perceived by a radiologist.

40

ROI
Airwall
Airway
Blood
Lung Parenchyma

oc

H 20

-1000 900 -800 -700 600 500 400 -300 -200 -100 0 100 200 300 400
Hounsfield Values

Figure 4.7 - Distribution of the Pixel Values based on the Ground Truth

Graph in Figure 4.7 shows the distribution of the pixel values in Hounsfield units within the different regions. It could be seen from the graph in Figure 4.7 that there is considerable overlap of the distribution of the pixel values amongst the different

constituent regions. Especially, the artery has similar X-ray attenuation values as the airway wall. Table-4.1 lists the pixel properties within the different regions.

<i>Region</i>	<i>Count</i>	<i>Minimum Value HU</i>	<i>Maximum Value HU</i>	<i>Average Value HU</i>	<i>Standard Deviation</i>
Within ROI	384	-1024	528	-707	385
Artery	16	-270	485	250	208
Airway wall	60	-659	528	-167	264
Airway Lumen	50	-1024	-501	101	168
Lung Parenchyma	258	-1024	36	-851	205

4.3.4. Unsupervised Segmentation of the CT Image Data of the Lungs Using HCS

Based on the earlier success of HCS, in precisely outlining regions within CT images (Figure 4.8) [Selvan, 2007], it was envisaged that it would be a straightforward usage of HCS to outline the borders of the blood vessel and airway in the CT images of the lungs. Hence to start with, HCS which was earlier used to achieve such robust segmentation as shown in Figure 4.8, was applied within the region of interest shown in Figure 4.6.

Figure 4.9 (a) shows the output of the unsupervised segmentation using HCS when there are still one hundred clusters yet to be merged. Some of the major clusters could be associated with their respective underlying anatomy. Figure 4.9 (b) shows the cluster associated with lumen (Blue) and part of the lung parenchyma misclassified as lumen (coloured Yellow). (Note : It should be noted HCS as such does not have a stopping criteria it is left for the user to choose the segmentation most appropriate. See Figure 4.13 for details).

■ t l-SI .St J W * w

b

Figure 4.8 - Segmentation of a CT image using HCS.

**CT image showing a suspected area outlined in white by a neuroradiologist (a).
HCS unsupervised segmentation of the Grey matter region (Blue), White matter region
(Green) and stroke affected region (Red) and the regions' boundaries (b) (Image courtesy
Selvan, 2007).**

Figure 4.9 - The HCS process unsupervised segmentation output.

**Segmentation output when there are one hundred clusters or regions (a).
Cluster corresponding to lumen (coloured Blue) and part of the lung parenchyma mis-
classified as airway lumen (coloured Yellow) (b).**

Table 4.2 lists the pixel values (in HU) within the cluster corresponding to airway lumen (coloured Blue) and part of the lung parenchyma mis-classified as lumen

(coloured Yellow) (Figure 4.9 (b)). Inspecting the pixel values listed in Table 4.2, it is no surprise that the HCS process has clustered part of the lung parenchyma with airway lumen, since both constitute of pixels having the same X-ray attenuation of (-)1024 HU.

Table-4.2 - X-ray attenuation of the pixels within the airway lumen region (Blue) and lung parenchyma region (Yellow), mis-classified as airway lumen (Figure 4.9 b).								
<i>Pixel Values Hounsfield Units</i>	(-)1024 HU	(-)1014 HU	(-)844 HU	(-)788 HU	(-)731 HU	(-)723 HU	(-)687 HU	(-)425 HU
Airway lumen Pixel count (Total count 32)	32	0	0	0	0	0	0	0
Lung parenchyma Pixel count (Total count 34)	27	1	1	1	1	1	1	1

4.3.4.1. Additional criteria incorporated, within the HCS process, to improve segmentation

The HCS process was specifically designed to merge regions in medical images. In medical images anatomically similar regions could occur across an image. Hence, the HCS process compares and merges regions even if the regions are not adjacent to each other. Also, while evaluating the suitability of adjacent or non-adjacent regions, for merging, the HCS process considers only the image properties of the regions, under consideration.

The following observations could be made by inspecting the segmentation results of Figure 4.9 :

- Pixel locations belonging to the airway lumen region (Blue), which are contiguous, have been clustered as a single region.
- The misclassified pixel locations (Yellow) belonging to the lung parenchyma are not contiguous with the airway lumen part of the image.

Making use of the above observations, in order to minimise the above misclassification, the following two additional criteria were considered to be incorporated into the HCS process :

- While evaluating the suitability of regions for merging, along with the regions' image properties, the HCS process should also consider the spacial distance between the constituent pixels of the regions. Hence, physically nearer regions will be favoured to be clustered together than those regions spatially further away.

Hence the dissimilarity between the regions can be estimated using the expression given in equation 4.2. Lower the value more probable the regions will be merged.

$$\text{Region_Dissimilarity_Measure} = \text{Pixel_Dissimilarity_Measure} + \text{Pixel_Spatial_Distance} \quad [4.2]$$

- Avoid clustering regions which are not adjacent and only evaluate regions which are contiguous for possible merging.

To start with the HCS process was modified to incorporate the following additional criteria, for evaluating regions for merging :

- Along with the image properties of the regions the euclidean distance between the regions was also taken into consideration to evaluate the suitability of the regions for merging.

Taking into account the euclidean distance between regions, to decide which of the regions are to be merged, did reduce the amount of misclassification at the corresponding merging stage (Figure 4.10) (Table 4.3).

Looking at how the misclassification has occurred (Figure 4.10) it was hypothesized that if the second additional criteria was considered then the misclassification could be further reduced. That is the criteria of considering only clusters which are adjacent to one another, for merging. Hence, in the HCS a relevant flag was set to trigger merging of only adjacent clusters [Selvan, 2007].

Figure 4.10 - HCS unsupervised segmentation, when the additional criteria of pixel euclidean distance factor is taken into account for merging.

The segmentation output when there are ninety nine clusters or regions (a). Major clusters associated with their respective underlying anatomy are coloured as, blood-vessel (Red), airway wall (Green), airway lumen (Blue) and lung parenchyma at the background (Black) (a). Cluster corresponding to airway lumen (coloured Blue) and part of the lung parenchyma miss-classified as airway lumen (coloured Yellow) (b).

Table-4.3 - X-ray attenuation of the pixels within the airway lumen region (Blue) and lung parenchyma region (Yellow), miss-classified as airway lumen (Figure 4.10 b).

<i>Pixel Values Hounsfield</i>	<i>(-)1024</i>	<i>(-)788</i>
<i>Units</i>	<i>HU</i>	<i>HU</i>
Airway lumen	32	0
Pixel count		
(Total count 32)		
Lung parenchyma	18	1
Pixel count		
(Total count 19)		

Figure 4.11 is the result of merging when only adjacent clusters were considered for merging. The segmentation output, shown in Figure 4.11, is when there were ninety nine clusters yet to be merged. From the Figure 4.11 it can be seen that the regions belonging to the lung parenchyma are not being merged with the region belonging to the airway lumen as was the case earlier.

However part of the airway wall has merged with the adjacent lung parenchyma. This has happened because the similar clusters within the airway wall are not contiguous. This was not an issue when HCS was merging clusters even when they were not adjacent to one another. But when HCS was made to merge only adjacent clusters the non-contiguous similar clusters in the airway wall could not merge with one another. Consequently those clusters within the airway wall merged with the next more similar regions which were the adjacent lung parenchyma clusters.

**Figure 4.11 - The HCS process unsupervised segmentation, when only adjacent clusters were merged.
The segmentation output when there are ninety nine clusters or regions.**

Hence, among the two additional criteria considered to improve the results of segmentation of the airway; the criteria of merging only adjacent regions was found to be detrimental. Taking into account the spatial distance of the regions, for evaluating their suitability for merging, was found beneficial.

4.3.4.2. Unsupervised segmentation of the remapped CT image grey scale data

As discussed earlier, in Section 4.3.3, to display the potential 2000 different Hounsfield values making use of 256 different shades of grey, it is customary to enable the 256 grey levels to represent a limited range, or window, of Hounsfield values. Narrowing the window or compressing the grey scale increases contrast for the purpose of visual perception Figure 4.12 (a) displays a range of Hounsfield values from (-) 1024 to 508 mapped to 256 level of grey levels.

Since the remapping increases the contrast (Figure 4.12 (a)) it was hypothesized that the remapped CT image data might aid the segmentation process. To verify whether this was the case, the HCS process was applied on the remapped Gray scale image data. Figure 4.12 (b) shows the output of the unsupervised segmentation using HCS when there are still fifty clusters yet to be merged. Inspecting the segmentation output it could be seen that some of the major clusters could be associated with their respective underlying anatomy namely blood-vessel (Red), airway wall (Green), airway lumen (Blue) and lung parenchyma at the background (Black). Cluster corresponding to airway lumen has part of the lung parenchyma (coloured Yellow) miss-classified as lumen as well (Figure 4.12(b)).

a

b

c

Figure 4.12 - Remapped CT image data and its segmentation by the HCS process.
CT image data, ranging from (-) 1024 to 508 Hounsfield values, mapped to 256 level of grey levels (a).

Intermediate segmentation output of fifty regions when HCS process was applied on the remapped grey scale image data (b). Major clusters, associated with their respective underlying anatomy, are coloured as blood-vessel (red), airway wall (Green), airway lumen (Blue) and lung parenchyma at the background (Black) (b). Cluster corresponding to airway lumen (coloured Blue) and part of the lung parenchyma that had been miss-classified as airway lumen (coloured Yellow) (c).

Comparing the segmentation output in Figure 4.10, when the HCS process was applied on the original CT image data with the current segmentation output in Figure 4.12 (b), when the HCS process was applied on the remapped image data, the following similarities could be observed :

in both the resulting segmentation, the major clusters are associated with their respective underlying anatomy, namely blood vessel, airway wall, airway lumen and lung parenchyma (Figures 4.10(a) and 4.12(b)).

in both the resulting segmentation, part of the lung parenchyma has been misclassified as airway lumen (Figures 4.10(b) and 4.12(c)).

The major difference between the segmentation based on the original CT image data (Figure 4.10) and the segmentation based on the remapped data (Figure 4.12) is as follows:

- the segmentation achieved by making use of the remapped data includes only fifty clusters, while the segmentation by making use of the original CT image data includes ninety nine clusters that need yet to be clustered.

The significance of the above difference is discussed below :

The HCS process as such does not have a stopping criteria. The merging process will continue until only the minimal number of clusters are remaining, which in this case is a single cluster. When the HCS process made use of the original CT image data the major clusters were associated with the underlying anatomy when there were still ninety nine clusters yet to be merged (Figure 4.13 (b)). But when the HCS process

continued merging the clusters and when there were only fifty clusters yet to be merged, the clusters, in the segmentation output, could no more be associated with the underlying anatomy (Figure 4.13 (c)).

Based upon the above discussion one may come to the conclusion that making use of remapped data, instead of the original CT image data, may lead to better segmentation results. But it was subsequently found that the feature measure based on remapped data does not have as much discriminatory power as that based on the original CT image data. Hence, it was decided that it was better to carry out the segmentation, of the boundaries of the blood vessel and airway, making use of the original CT image data rather than the remapped data. For further, discussions on this observation, refer to Section 4.3.5.3 (Section 4.3.5.3 Segmentation, of the remapped CT image grey scale data, making use of initial user tagged information).

4.3.5. Incorporating user knowledge to aid segmentation

In an earlier study [Selvan, 2007] the HCS process was successfully used in precisely outlining regions within medical images of varied modalities such as MRI, CT (Figure 4.8) and Ultrasound. But in the current application it was found that the following typical characteristics of the CT image sections, of the lungs, precluded the successful application of the HCS process to segment the airway and the adjoining blood vessel :

- The images were of very low resolution.
For example, the number of pixels that constitute the blood vessel is hardly sixteen (Table 4.1) (Figure 4.6).
- The properties (X-ray attenuation values) of the components are very similar.
For example, airway wall has got very similar Hounsfield values as that of the blood vessel. Similarly, the airway lumen has got very similar Hounsfield values as that of the lung parenchyma (in the background) (Table 4.2 and Table 4.3).

Section 4.3.4 gave the details of the unsupervised segmentation of the CT image data of the lungs using HCS. It was shown that the unsupervised segmentation of the CT image data of the lungs using HCS was not very successful in segmenting the blood vessel and the airway. It was also shown how varied measures were tried to improve the results. The adopted measures did improve the results. But the final segmentation

of the ROI into its four constituent regions namely the airway lumen, airway wall, and the adjoining blood vessel was not achieved.

At this juncture it was realised that two possible routes could be taken to design a methodology to achieve a satisfactory segmentation result. The first possibility includes designing more involved heuristic rules. The second possibility consists of incorporating some manual input from the user to aid the segmentation process. The first option was rejected for the following reasons :

- This approach had already been tried in prior studies [de Jong *et al.* 2005] with limited success.
- It was demonstrated by others that even after adopting some heuristics, human intervention cannot be avoided altogether [de Jong *et al.* 2005].

Hence, it was decided to adopt the second approach of incorporating users' preference into the segmentation process.

From the earlier discussion it could be inferred that somehow the HCS process needs to be informed which are the pixel locations that need to be considered for merging, to form a region of particular type. This is necessary because the image properties, that is the X-ray attenuation, information alone is not sufficient enough to differentiate the different regions of the anatomy. For example, part of the lung parenchyma is mis-classified as airway lumen (Figure 4.9(b) and Figure 4.10(b)) because both of them have exactly the same X-ray attenuation value of (-)1024 (Table 4.2 and Table 4.3).

To pass on the information to the HCS process, regarding the association of certain pixels to certain anatomical region, either of the following methods could be used :

- An initial unsupervised segmentation could be performed using the HCS process. From the segmentation output a suitable intermediate segmentation could be used to pass on the information regarding certain pixel locations belonging to certain anatomy.
- Right at the start of the segmentation process the user tags (marks) certain pixel locations as belonging to certain corresponding anatomical region. This information could be subsequently passed on to the HCS process to assist the process during the actual segmentation process.

Both of the above methods were explored to identify the best possible option.

4.3.5.1. Passing user knowledge, based on the HCS process initial unsupervised segmentation output

The steps involved in making use of the HCS process initial unsupervised segmentation output, to pass on user knowledge, to subsequently segment the blood vessel, airway and lung parenchyma are as follows :

- The process is initiated by applying the HCS process within a region of interest.

For example, when the HCS process was applied within the region of interest shown in Figure 4.6, a sample set of the segmentation output obtained at different stages of merging is shown in Figure 4.13.

- Since the HCS process will finally result in a single region, encompassing the whole ROI, it is left for the user to choose the most appropriate segmentation output to be made use of as the input for the subsequent segmentation.

The criteria for choosing the most appropriate segmentation output are; firstly in the segmentation output it should be possible to associate the major clusters with their respective underlying anatomy, and secondly, the misclassification at that stage should be minimal.

For example, after visually inspecting the segmentation's output, in Figure 4.13, at different stages of the unsupervised merging process it could be seen that Figure 4.13 (b) is the most appropriate output of the HCS process. Because in the segmentation output of Figure 4.13 (b) some of the major clusters, amongst the ninety nine clusters, could be associated with their respective underlying anatomy. The misclassification of part of the lung parenchyma as airway lumen is minimal (Figure 4.10) when compared to the misclassification on subsequent segmentation output (Figure 4.13 c).

- Making use of the chosen most appropriate segmentation output the user tags some of the cluster of pixels (regions) as belonging to the specific anatomy. It is not necessary that the user needs to associate all the clusters of pixels.

Figure 4.14 (b) shows the clusters tagged by the user as associated with blood-vessel (Red) airway wall (Green), airway lumen (Blue) and background lung parenchyma (Black). Those pixel locations which are not tagged by the user are shown in white.

Note that the cluster of pixels belonging to part of the lung parenchyma which was misclassified as airway lumen (Figure 4.10 b) is tagged by the

user as belonging to the lung parenchyma. This information is used of by the subsequent segmentation to ensure that those collection of pixels are classified as lung parenchyma even though the image data of those pixels are the same as that of the airway lumen (Table 4.3)

The user tagged information is passed on to the HCS process for subsequent segmentation. During this subsequent segmentation process. The HCS process makes use of the user tagged information and clusters those pixel locations which were not tagged by the user. At the end of this merging process there will be four regions or cluster of pixel locations.

Figure 4.14 (c) shows the four clusters at the end of the subsequent segmentation process which made use of the user knowledge. The clusters associated with the underlying anatomy are coloured as blood-vessel (Red) airway wall (Green), airway lumen (Blue), background lung parenchyma (Black).

a

b

c

Figure 4.13 - The segmentation output of the HCS process based unsupervised segmentation of the ROI shown in Figure 4.6

The segmentation output shown are at different stages of the merging process when there are, one hundred and ninety nine clusters or regions (a),, ninety nine regions (b) and fifty regions (c).

The most appropriate segmentation output's major clusters, associated with their respective underlying anatomy, are coloured as blood-vessel (red), airway wall (Green), airway lumen (Blue) and lung parenchyma at the background (Black) (b).

Figures 4.14 (a) and (b) illustrate the above detailed process of making use of the initial unsupervised segmentation to pass on the user knowledge for subsequent segmentation. Figure 4.17 (c) gives the final segmentation of the blood vessel, airway wall, airway lumen and lung parenchyma. Table 4.4 gives the properties of the regions corresponding to the blood vessel, airway wall and airway lumen. The very high values of the standard deviation demonstrate the inhomogeneity of the regions.

c

Figure 4.14 - Passing user knowledge based on the HCS process initial segmentation. The most appropriate segmentation output of the initial HCS process chosen to pass on the user knowledge for the subsequent process (a). The segmentation output shows ninety nine clusters (regions) (a). The major clusters, associated with their respective underlying anatomy, are coloured as blood-vessel (Red), airway wall (Green), airway lumen (Blue) and lung parenchyma at the background (Black) (a). User tagged locations (clusters), making use of the initial unsupervised intermediate segmentation, blood-vessel (Red) airway wall (Green), airway lumen (Blue), background lung parenchyma (Black) and untagged pixel locations (White) (b). Final segmentation of four regions, making use of user tagged information; blood-vessel (Red) airway wall (Green), airway (Blue), lung parenchyma (Black) (c)

Table-4.4 Properties of the different anatomical regions (Figure 4.14 c)

<i>Region</i>	<i>Area (pixel count)</i>	<i>Minimum value HU</i>	<i>Maximum value HU</i>	<i>Average value HU</i>	<i>Standard Deviation</i>
Blood vessel	43	-1012	485	-262	468
Airway Wall	75	-999	528	-305	344
Airway Lumen	39	-1024	13	-955	218

The advantage of making use of the HCS process initial segmentation, to pass on the user knowledge to the HCS process for subsequent segmentation is as follows :

The major advantage of making use of the HCS process initial segmentation is that the user needs to tag a minimal number of pixel locations as belonging to the different anatomical regions. This is the case because the other pixel locations belonging to the same cluster, as the user chosen pixel, will be automatically tagged as belonging to the same anatomical region as the user tagged location.

The disadvantages of making use of the HCS process initial segmentation output to pass on the tagged information to the HCS process subsequent segmentation are as follows:

- Firstly, the user needs to choose the most appropriate partial segmentation from the earlier unsupervised segmentation. The user is at a disadvantage if the initial segmentation is too trivial in which case the user is forced to choose many locations. Also, if the initial segmentation already includes clusters which have pixels from different anatomical regions then right at the start the subsequent segmentation will have erroneous information based on which the resulting final segmentation will be suboptimal.
- Another disadvantage of making use of the output of the initial unsupervised segmentation of HCS is that HCS need to be applied more than once to obtain the final segmentation output.

4.3.5.2. Passing user knowledge, by making use of the initial user tagged information

To avoid the disadvantages associated with making use of the HCS initial segmentation output, to pass on the user knowledge to the subsequent segmentation process, it was decided not to carry-out the initial HCS segmentation but to pass the user knowledge to the HCS process. The user could tag (mark) certain pixel locations, in the unsegmented image, as belonging to the corresponding anatomical region. The tagged information is used by the HCS segmentation process to arrive upon the final segmentation.

Figures 4.15 (a) and 4.15 (b) illustrate the process of passing on the tagged information to the HCS process. Table 4.5 gives the details of the locations tagged by the user. Figure 4.15 (c) gives the final segmentation of the blood vessel, airway wall, airway lumen and lung parenchyma. Table 4.6 gives the properties of the regions corresponding to the blood vessel, airway wall and airway lumen.

Table-4.5 – Details of the user tagged locations in Figure 4.15 b.					
<i>Tagged Anatomy</i>	Blood vessel	Airway wall	Airway lumen	Lung parenchyma	Total Tagged Locations
Tagged locations count	18 (9.091%)	61 (30.81%)	19 (9.596%)	100 (50.51%)	198 (100%)
ROI (24x16) Total 384					51.56% of ROI

Figure 4.15 - Passing user knowledge, by tagging locations within the major anatomies.
CT image data, within the ROI (24x16) shown in Figure 4.6 (a)
User tagged locations, blood-vessel (Red) airway wall (Green), airway lumen (Blue),
background lung parenchyma (Yellow) and untagged pixel locations (white) (b).
Final segmentation of four regions, making use of user tagged locations as prior knowledge,
blood-vessel (red) airway wall (Green), airway (Blue), lung parenchyma (Black) (c).

Table-4.6 Properties of the different anatomical regions (Figure 4.15 c)

<i>Region</i>	<i>Area (pixel count)</i>	<i>Minimum value HU</i>	<i>Maximum value HU</i>	<i>Average value HU</i>	<i>Standard Deviation</i>
Blood vessel	29	-882	485	-31	383
Airway wall	91	-1024	528	349	352
Airway lumen	41	-1024	-604	-981	102

Inspecting the final segmentation (Figure 4.15 (c)) one could see that one of the pixel locations within the airway wall was classified as belonging to the lung parenchyma (Black). This is the case because HCS at its core is a data-driven process and associates those locations the user had tagged with the corresponding anatomy. But to cluster the rest of the untagged locations, the HCS process complies with what the data dictates. Hence when the user gives the initial locations associated with the specific anatomy, care should be taken that those locations which are ambiguous are associated with the specific anatomy. Ambiguous locations are those locations which have the same image properties but belong to different anatomy. If the user does not tag the ambiguous locations the final segmentation will not be satisfactory.

Figure 4.16 illustrates how the segmentation process is influenced by the initial tagged information provided by the user. Table 4.7 gives the details of the locations tagged by the user. Inspecting the final segmentation (Figure 4.16 (c)) one could see a part of the lung parenchyma had been segmented as the airway lumen. The reason for this is that those pixel locations in the lung parenchyma had exactly the same image properties as those of the airway lumen (Table 4.3). Hence it is imperative that the user tags ambiguous locations or at least tag those close by.

a b c

Figure 4.16 - Images illustrating how the user initial tagging information influences the final segmentation.

CT image data, within the ROI (24x16) shown in Figure 4.6 (a)
 User tagged locations, blood-vessel (red) airway wall (Green), airway lumen (Blue),
 background lung parenchyma (Yellow) and untagged pixel locations (white) (b).
 Final segmentation of four regions, making use of user tagged locations as prior knowledge,
 blood-vessel (red) airway-wall (Green), airway (Blue), lung parenchyma (Black) (c).

Table-4.7 - Details of the user tagged locations in Figure 4.16 b.

<i>Tagged Anatomy</i>	Blood vessel	Airway wall	Airway lumen	Lung parenchyma	Total Tagged Locations
Tagged locations count	18 (13.433%)	36 (26.87%)	19 (14.179%)	61 (45.52%)	134 (100%)
ROI (24x16) Total 384					34.90% of ROI

4.3.5.3. Segmentation, of the remapped CT image grey scale data, making use of initial user tagged information

As discussed earlier, in Section 4.3.3, to display the potential 2000 different Hounsfield values making use of 256 different shades of grey, it is customary to enable the 256 grey levels to represent a limited range, or window, of Hounsfield values. Narrowing the window or compressing the grey scale increases contrast for the purpose of visual perception Figure 4.17 (a) displays a range of Hounsfield values from (-) 1024 to 508 mapped to 256 level of grey levels.

Since the remapping increases the contrast (Figure 4.17 (a)) it was hypothesized that the remapped CT image data might aid the segmentation process. In Section 4.3.4.2 it was found that the unsupervised segmentation of the remapped CT image grey scale data, resulted in fewer number of major clusters (fifty) which could be associated with the underlying anatomy (Figure 4.12(b)). While the unsupervised segmentation done on the original CT image data had a higher number of major clusters (ninety nine) which could be associated with the underlying anatomy (Figure 4.13(b)).

Based on the above observations one may conclude that in the user aided segmentation making use of the remapped data instead of the original CT image data may lead to better segmentation results. To verify whether this was the case, the HCS process was applied on the remapped grey scale image data.

Figure 4.17(a) shows the CT image data, ranging from (-) 1024 to 508 Hounsfield values, mapped to 256 level of grey levels. Figure 4.17(b) shows the locations tagged by the user associated with the corresponding anatomy. Table 4.8 gives the details of the locations tagged by the user.

Table-4.8 - Details of the user tagged locations in Figure 4.17 b.

<i>Tagged Anatomy</i>	Blood vessel	Airway wall	Airway lumen	Lung parenchyma	Total Tagged Locations
Tagged locations count	19 (11.66%)	50 (30.67%)	23 (14.11%)	71 (43.56%)	163 (100%)
ROI (23x15) Total 345					47.25% of ROI

a

b

Figure 4.17 - User tagged locations on the remapped CT image data.
CT image data, ranging from (-) 1024 to 508 Hounsfield values, mapped to 256 level of grey levels (a). User tagged locations, blood-vessel (red) airway wall (Green), airway lumen (Blue), background lung parenchyma (Yellow) and untagged pixel locations (white) (b).

Figure 4.18 (a) shows the output of the final segmentation when there are four clusters associated with their respective underlying anatomy namely blood-vessel (Red), airway wall (Green), airway lumen (Blue) and lung parenchyma at the background (Black). Cluster corresponding to airway lumen has part of the lung parenchyma (coloured Yellow) miss-classified as lumen (Figure 4.18(b)). The reasons for this misclassification could be either or both of the following reasons :

- the user tagged information was not sufficient enough.
- remapping the original CT image data ranging from (-) 1024 to 508 Hounsfield values, to 256 level of grey levels has affected the discriminating ability of the feature measure.

a

b

Figure 4.18 - Segmentation of the remapped CT image grey scale data making use of user tagged information of Figure 4.17 (b).

Segmentation output when there are four regions, associated with the underlying anatomy, namely, blood-vessel (red) airway wall (Green), airway (Blue), lung parenchyma (Black) (a)

Cluster corresponding to airway lumen (coloured Blue) and part of the lung parenchyma miss-classified as airway lumen (coloured Yellow) (b).

To establish the reason(s) behind the misclassification of part of the lung parenchyma as airway lumen, the same user tagged information was used and the HCS process was applied on the original CT image data. Figure 4.19 (a) shows the output of the final segmentation when there are four clusters associated with their respective underlying anatomy namely blood-vessel (Red), airway wall (Green), airway lumen (Blue) and lung parenchyma at the background (Black).

Even after using the original CT image data the cluster corresponding to the airway lumen has part of the lung parenchyma (coloured Yellow) mis-classified as lumen (Figure 4.18(b)). But the misclassification is less than that when using the remapped CT image gray scale data. This minor misclassification is because the user tagged information was not sufficient enough. This establishes the fact that the remapping of the original CT image data to 256 gray scale data destroys the discriminating ability of the feature measure.

Figure 4.19 - Segmentation of the original CT image data making use of user tagged information of Figure 4.17 (b).

Segmentation output when there are four regions, associated with the underlying anatomy, namely, blood-vessel (red) airway wall (Green), airway (Blue), lung parenchyma (Black) (a)

Cluster corresponding to airway lumen (coloured Blue) and part of the lung parenchyma miss-classified as airway lumen (coloured Yellow) (b).

4.3.6. Synopsis of the Different Approaches Adopted to Segment the Boundaries of the Air-Way and the Accompanying Blood Vessel

Once it was found that no amount of image data based manipulation could achieve unsupervised segmentation (Section 4.3.4) it was decided that user knowledge will be passed on to the HCS process to aid the subsequent final segmentation process (Section 4.3.5). To pass on the user knowledge to aid the segmentation process various possibilities were explored. The pros and cons of the different possible ways of passing on the user knowledge, to aid the final segmentation process, are discussed below :

Passing on the user knowledge by making use of the initial unsupervised segmentation was not found to be suitable (Section 4.3.5.1)

Passing on the user knowledge right at the very start of the segmentation process addressed all the disadvantages of the initial segmentation based tagging, because unlike as in the initial segmentation based tagging, the user had complete control on which locations need to be associated with the related anatomy (Section 4.3.5.2).

The only issue with this method of passing the users' knowledge at the very start of the segmentation, is that the final segmentation depends on the initial tagging information provided by the user (Figure 4.16). But this restriction is not a big limitation provided the user makes a conscious effort to associate ambiguous locations with the corresponding anatomy.

Making use of the remapped CT image data was found to be detrimental as demonstrated in Section 4.3.5.3.

Considering the above listed pros and cons of all the possible routes explored to attain the final segmentation one can arrive upon the following requirements to attain the best possible solution :

- For segmentation processing the original CT image data should be used.
- The user knowledge regarding the anatomical structure present in the image should be given through tagging the relevant locations and associating those locations with their corresponding anatomy in the image. This user information should be passed on to the segmentation process right at the starting of the process.
- Care should be taken, such that those locations with conflicting image properties should be associated with their corresponding anatomy.

The final segmentation attained through the different segmentation processes are not similar. But the overall segmentation output reasonably captures the difference between the size of the blood vessel and the airway. That is, based upon the segmentation output it could be decided whether the airway is dilated or not. For example, comparing the outputs of the following two segmentation processes, both of which make use of the passed on user knowledge:

- segmentation using the passed on user knowledge which (the user knowledge) is based on the output of initial unsupervised segmentation (Figure 4.14 c)
- segmentation making use of initial user tagged information (Figure 4.15 c)

The shape of the regions segmented by the above two processes are different. But looking at the properties of the segmented regions (Table 4.4 and Table 4.6) one can arrive upon the conclusion that the size of the blood vessel is smaller than the combined size of airway wall and airway lumen.

Since the results of the segmentation processes are not exact it needs to be further refined. Taking the obtained solution as an approximation the identified boundaries of the blood vessel, airway wall and airway lumen are further refined in the subsequent boundary fitting process (Section 4.3.7).

4.3.7. Improving the output of the user guided HCS process and the estimation of the properties of airways and the accompanying blood vessels (Boundary approximation)

Making use of the HCS process output, that is the segmentation of the boundaries of the airways and the accompanying blood vessels, measurements such as the cross-sectional area of the airway and the accompanying blood vessel could be made (Table 4.4 and Table 4.6). But for detailed measurements of the airways and the accompanying blood vessel, as illustrated in the schematic shown in Figure 4.2, the HCS process output alone is not enough as the user guided segmentation process output varies depending upon the user input of the tagged locations (Figure 4.14 c and Figure 4.15 c) .

Apart from the above limitation, the HCS process output is not perfect. For example, inspecting the segmentation output it could be seen that the boundaries of the segmented region are jagged and irregular (Figure 4.15 c). Hence, the HCS process's output cannot be taken to represent the underlying anatomy. The reason for these limitations, of the HCS output, is because of the sparseness of the CT image data (Table 4.1) and the associated ambiguity of the CT image data (Table 4.2 and Table 4.3).

To address the above issues subsequent processing needs to be applied on the HCS process output. The details of this additional processing and how it could be used, to make measurements of the airways and accompanying vessels, is discussed (expanded) in this section.

de Jong *et al.* [2005] made the following observation.

Start Quote..

Saba et al. [Saba 2003] have developed an alternate technique for measuring airways that are not cut in cross-section. This method involves fitting an ellipse to the airway lumen and wall, and shows great promise in correcting the errors in measurement of obliquely cut airways. These techniques claim to be more accurate than the more commonly used techniques, but have not been generally applied, presumably because of the limited availability of the complex algorithms involved.

End Quote..

In our study an approach very similar to that mentioned by de Jong *et al.* [2005] above was designed and implemented. The steps involved are as follows :

- firstly, make use of the user guided HCS process to approximately outline the boundaries of the underlying anatomy
- make use of the above segmentation output, as an approximation, and best fit an elliptical boundary around the blood vessel and the airway

4.3.7.1. Fitting an ellipse to the boundaries of the airway and the accompanying blood vessel

Some of the boundary points extracted from the user guided HCS process output could be erroneous. Hence, the method that will be used to fit an ellipse, to those boundary points, should have the following properties :

- the ellipse fitting method should be extremely robust
- it should always return an ellipse even if some of the input are bad data

Over and above the above listed basic requirements the chosen ellipse fitting method should be easy to implement and the results (ellipse) should be verifiable.

Fitzgibbon *et. al* [1996] presented a least squares fitting of ellipse. They claim that their work was efficient for fitting ellipses to scattered data. Also their method incorporates the ellipticity constraint into the normalization factor. Hence, they claim that their method has the following advantages :

- It is ellipse-specific so that even bad data will always return an ellipse
- It can be solved naturally by a generalized Eigen system
- it is extremely robust, efficient and easy to implement.

To estimate the boundaries, of the airway and the accompanying blood vessel, the ellipse fitting method formulated by Fitzgibbon *et. al* [1996] was used as follows :

- firstly, the user aided HCS process was applied within the region of interest around the identified airway and the accompanying blood vessel (Section 4.3.5.2)
- if the segmentation of the airway and the accompanying blood vessel was found reasonable (Figure 4.20(b)) then the boundary points on the constituent regions were found (Figure 4.20(c))
- the estimated boundary locations of the regions are passed on to the ellipse fitting process to fit the corresponding ellipses.
- Finally, the major axis and the minor axis of the fitted ellipses are estimated (Table 4.9) (Figures 4.21 and 4.22).

Table-4.9 - Minor and Major axis (Figure 4.22) dimensions (in pixels) of the fitted ellipse to the boundary of the Blood vessel, Airway wall and Airway lumen shown in Figure 4.20 a

	Blood vessel	Airway wall	Airway lumen
Minor Axis	4.06	9.80	5.01
Major Axis	5.45	13.79	6.70

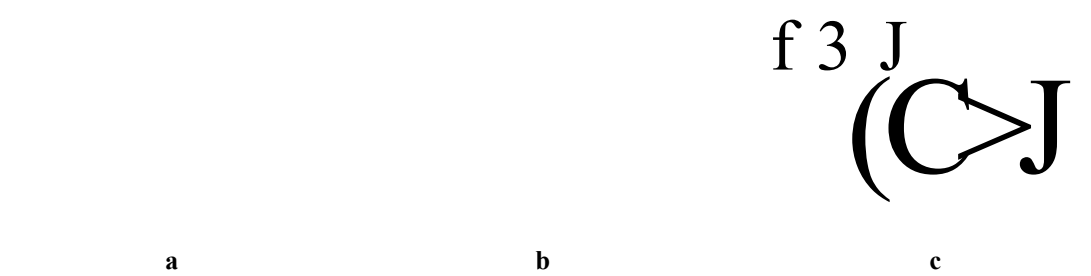


Figure 4.20 - Boundary locations of the segmented anatomies.
CT image data, ranging from (-) 1024 to 508 Hounsfield values, mapped to 256 level of grey levels (a). Segmentation of the four regions, Blood-Vessel (red) Airway Wall (Green), Airway (Blue), lung parenchyma (Black) (b). Boundary locations around the three regions, namely Blood Vessel (red), Airway Wall (Green) and Airway Lumen (Blue) (c)



Figure 4.21 Minor and Major axis of the fitted ellipse to the boundary of the Blood Vessel (a), Airway-Wall (b) and Airway Lumen(c).

Figure 4.22 Minor and Major axis of the fitted ellipse to the Blood Vessel (a), Airway-Wall (b) and Airway Lumen(c).

4.3.7.2. Quantitative Measurements of the Airways and the Accompanying Blood Vessels

Making use of the estimated short axis and long axis, through the ellipse fitting process various detailed measurements of the airway and the accompanying blood vessel could be made (Figure 4.2) [de Jong *et al.* 2005].

For the airway and the accompanying blood vessel of Figure 4.22, the linear measurements are listed in Table 4.10, the ratios of the various linear dimensions are listed in Table 4.11, the area related dimensions are listed in Table 4.12 and the ratios of the various areas are listed in Table 4.13. The square root of Aaw is often derived, since it is relatively linearly related to Pi. Finally, airway dimensions can be referenced to body surface area (e.g. (airway wall area)/BSA and (airway wall thickness)/BSA)

Table-4.10 - Linear measurements of the airway and the accompanying blood vessel of Figure 4.22.

<i>Linear Measurements</i>	<i>Value in pixels</i>
airway perimeter (Pi)	
long and short axes of the outer airway area (Ao)	13.79 and 9.80
long and short axes of the lumen area (Ai)	6.70 and 5.01
long and short axes of the artery	5.40 and 4.06
airway wall thickness (Awt)	$(9.80 - 5.01) = 4.79$
airway lumen diameter (ALD)	5.01
airway outer diameter (AoD = ALD+Awt)	$(5.01 + 4.79) = 9.80$
arterial diameter (AD)	4.06

Table-4.11 – Ratios of the various linear dimensions of the airway and the accompanying blood vessel of Figure 4.22.

<i>Ratios of the various linear dimensions</i>	<i>Value in pixels</i>
long and short axes ratio of the outer airway area	$(13.79/9.80) = 1.41$
long and short axes ratio of the lumen area	$(6.70/5.01) = 1.34$
long and short axes ratio of the artery	$(5.40/4.06) = 1.33$
(airway lumen diameter)/(arterial diameter) (ALD/AD)	$(5.01/4.06) = 1.23$
(airway wall thickness)/(arterial diameter) (Awt/AD)	$(4.79/4.06) = 1.78$
(airway wall thickness)/(airway lumen diameter) (Awt/ALD)	$(4.79/5.01) = 0.96$

Table-4.12 – Area related dimensions of the airway and the accompanying blood vessel of Figure 4.22.

<i>Area related dimensions</i>	<i>Value in pixels</i>
outer airway area ($A_o = A_{aw} + A_i$)	$(\pi \times 13.79/2 \times 9.8/2) = 106.18$
lumen area (A_i)	$(\pi \times 6.7/2 \times 5.01/2) = 26.37$
airway wall area ($A_{aw} = A_o - A_i$)	$(106.18 - 26.37) = 79.81$
arterial area (A_A)	$(\pi \times 5.4/2 \times 4.06/2) = 17.23$

Table-4.13 – Ratios of Area related dimensions of the airway and the accompanying blood vessel of Figure 4.22.

<i>Ratios of Areas related dimensions</i>	<i>Value in pixels</i>
lumen area/arterial area (A_i/A_A)	$(26.37/17.23) = 1.53$
airway wall area/arterial area (A_{aw}/A_A)	$(79.81/17.23) = 4.63$
Percentage wall area = (airway wall area/outer airway area) x 100 ($A_{aw}/A_o \times 100$)	$(79.81/106.18) \times 100 = 75\%$

4.3.8. Synopsis of the User Guided HCS process Based Estimation of the Properties of the Airways and the Accompanying Blood Vessels

Given the CT image of the cross-section of the lungs (Figure 4.3), the following are the major steps involved to estimate quantitatively the dimensions of the airway lumen and wall, and the accompanying pulmonary artery (Figure 4.2) :

- Obtain the user tagged input at the start of the HCS process based segmentation. (Section 4.3.5.2) (Figure 4.15 b)
- Perform the HCS process based segmentation (Section 4.3.5.2) (Figure 4.15 c).
- Estimate the boundary locations between the different anatomical sections (Figure 4.20 c).
- Perform a least-square fitting of ellipses making use of the estimated boundary locations (Section 4.3.7.1) (Figure 4.22).
- Estimate the quantitative measurements of the airway lumen, airway wall and the blood vessel (Section 4.3.7.2).

4.3.9. Critical Evaluation of the Implemented User Guided HCS Process Based Procedure to Estimate the Dimensions of the Air-Way and Artery

In the following aspects the implemented user guided HCS process based method differs from the earlier attempts, to measure airways dimensions :

- The HCS process based method makes use of region based measure

(distribution of the pixel values) to measure the properties of the different components (airway and artery) in an image. This is much more robust than making use of individual pixel values (X-ray attenuation) alone. Because individual pixel values may be similar (e.g. between airway wall and artery) but the distribution (or arrangement) of those values will differ between different components in an image e.g. airway and artery. This is illustrated by the success of HCS in differentiating airway wall from artery even though both airway wall and artery have very similar X-ray attenuation values.

- No heuristics are being used to obtain the segmentation of the blood vessel and the airway.
- Once the HCS process based segmentation has been initiated the process is unsupervised and no subsequent human intervention is needed.
- The HCS process based method segments and outlines both the airway as well as the adjoining blood vessel.
- The final step, in the designed solution, fits the best possible ellipses to the boundaries of the segmented anatomical regions. The ellipse fitting operation is robust enough to accommodate extraneous boundary locations.
- The operation of fitting the best possible ellipse, yields an objective measure of the dimensions, of the airway and the accompanying blood vessel.

The manual estimation of the dimensions of the airway and the accompanying blood vessel is time consuming, subjective and non-repetitive. Although the currently designed computer assisted process needs some user input. it neither needs to be very precise nor consistent. Because the HCS process and the subsequent ellipse boundary fitting process are robust and it presents a reproducible and an acceptable solution.

Fully automatic segmentation is not possible because of the following inherent issues with the source data

- The image is of very low resolution e.g. the dimensions of the blood vessels is hardly five pixels across (Table 4.9).
- The properties (X-ray attenuation values) of the components are very similar (Table 4.3).

4.3.9.1.Critical Discussion on Making Use of the User Input

The currently designed user guided segmentation process might not be a perfect alternative to a wholly manual process. Because the process needs user guidance to start the process. Expecting the user to guide the process has got an advantage as well as a disadvantage.

The advantage is :

- The user has got some control over the segmentation process.

The disadvantage is :

- expecting too much of manual intervention is neither an elegant software solution nor a comfortable one for the user.

So to improve the currently implemented user guided segmentation process one allows the user to retain control but at the same time reduce the amount of user input to the minimum. The way this can be achieved is explored below.

The main reason for the need and necessity of the user guidance is to differentiate ambiguous locations. That is to differentiate those locations which are different anatomically but have the same image properties. For example, locations in the airway lumen and locations in the lung parenchyma have exactly the same HU value (Tables 4.2 and 4.3). Similarly, some of the locations within the blood vessel have very similar HU values as that of the airway wall. To address this issue currently the segmentation process expects that the user associates (tags) those ambiguous locations with the underlying anatomy. This is done by tagging different locations within the different anatomical regions.

If one inspects the tagging information passed on by the user it could be seen that almost half of the total tagged locations are given to differentiate ambiguous locations within the lung parenchyma, from the airway (Table 4.5). Also the locations tagged within the lung parenchyma affects the final segmentation (Figure 4.16).

From the above discussion it can be concluded that if one isolates and segments only the airway wall and lumen one need not get much input from the user. Similarly, if one isolates and segments only the blood vessel on its own then the user need not give any tagging information to differentiate locations which are ambiguous between the blood vessel and the airway wall.

The anatomical regions, namely the airway (wall and lumen) and the blood vessel, can be segmented in isolation as follows :

- Prior to the HCS process based segmentation process the user draws a hand drawn boundary around the airway and the blood vessel. This will isolate those anatomical regions from each other as well from most of the lung parenchyma.
- Applying the HCS process based segmentation within the hand drawn boundary will aid the segmentation process by isolating almost all of the ambiguous locations, prior to the segmentation process.

The above possibility was further tested experimentally and validated as will be discussed in the next section (Section 4.3.10). The details of the operation of making the user input isolate the individual anatomical regions, viz. Blood-Vessel and Air-Way will be discussed in detail in Section 4.3.10.

4.3.10. Segmentation of Airway and the accompanying Blood Vessel making use of the user tagged boundary locations around the individual anatomy

From the discussion so far one can conclude that the segmentation of the boundaries of the blood vessel, airway-wall and airway (lumen) need some type of user input to aid the segmentation process. So far we have discussed how the user input can be attained through the following different ways :

- obtaining the user input through the output of an initial unsupervised segmentation (Section 4.3.5.1)
- obtaining the user input through user tagged location labelling key pixel locations as belonging to the respective anatomy (Section 4.3.5.2).

Both of the above approaches expect the user to consciously tag locations belonging to the different anatomy. Because of the precision and accuracy expected of the operation, the user may find the tagging of the locations, within the respective anatomy, tedious and time consuming. Hence, it was decided to explore the possibility of reducing the precision or accuracy required of the user while providing the tagged locations.

One of the ways of obtaining the user input without too much of precision or accuracy involved is to obtain the approximate locations around the boundaries of the two major anatomies namely the blood vessel and the air-way. In this operation

the user need not precisely tag the locations within the different anatomies, but rather only the approximate boundaries within which the two major anatomies viz. blood vessel and the air-way are located.

The reason for obtaining the locations, from the user, near the boundaries of the two major anatomies viz. blood vessel and the air-way is as follows :

- the major issue faced by the segmentation process is that the pixel locations within the airway-lumen have exactly the same Hounsfield values as the pixel locations within the lung parenchyma just outside the air-wall (Section 4.3.4, Table 4.2)..

Outlining the boundary of the airway (air-wall along with the lumen) and applying the segmentation process only within the boundary will eliminate most of the conflicting information if not all.

Obtaining from the user only the approximate locations, just outside the boundary of the air-way, will result in some of the locations belonging to the lung parenchyma included within the boundary. This inclusion of a very small part of the parenchyma will still affect the segmentation process. But this was handled by incorporating additional condition for merging. The details of what and how of the additional condition will be discussed in detail later in this section while discussing the implementation of the process.

In brief, the following are the major steps which are involved in the segmentation of the blood-vessel, the airway-wall and the lumen by just getting the approximate locations around the major anatomies viz. blood-vessel and the air-way :

- obtain the approximate locations just outside the boundaries of the blood vessel and the airway.
- connect the discrete locations given by the user, to form closed curves, by fitting cubic splines to the two set of locations.
- apply the HCS process within the two areas of the image bounded by the cubic spline curves.
- based on the segmentation yielded by the HCS process estimate the boundaries of the blood vessel, airway-wall and the airway (lumen).
- estimate the most appropriate boundaries of the anatomies by fitting the best fitting ellipses to the estimated boundary locations.

The above steps are discussed in detail in the following sections.

4.3.10.1. Marking the approximate boundaries around the Blood Vessel and the Airway-wall

The user tags (marks) locations just outside the boundaries of the blood vessel and the air-wall. This is the only input obtained from the user. The rest of the operations, to segment the boundaries of the blood vessel, airway-wall and airway lumen, are made without further intervention from the user.

Figure 4.23 shows the locations tagged by the user around the blood vessel and the air-way found in the CT image of the lungs shown in Figure 4.6. The boundary locations around the blood vessel are coloured Red and those around and just outside the airway-wall are coloured Green (Figure 4.23). The reason for assigning different colours for the different anatomies is that from here onwards the rest of the operations to segment the boundaries of the blood vessel, airway-wall and airway-lumen will be automatic.

Figure 4.23 - Locations marked by the user just outside and around the Blood Vessel (Red) and the Airway-Wall of the CT image of Figure 4.6.

4.3.10.2. Fitting cubic splines to connect the user given discrete locations and form a continuous closed curve

To reduce the manual input from the user the user is asked to mark only discrete locations around and just outside of the borders of the two major anatomies viz. blood vessel and the airway. Before the HCS process could be applied within the user tagged locations one need to identify the part of the image contained within the user tagged locations. To identify the relevant part of the image within the user tagged locations one need to first connect all the discrete user tagged locations into a contiguous curve. This is done by interpolating the discrete locations into a contiguous set of locations by a cubic spline interpolation.

The cubic spline interpolation needs to be provided with a set of three ordered adjacent locations. Hence, before one could apply the cubic spline interpolation to the set of discrete locations one needs to order the set of locations into clockwise or anti-clockwise order.

The ordering of the set of discrete user tagged locations, into an ordered set of clockwise or counter-clockwise points, is done through an algorithm known as the Graham scan. The algorithm is named after Ronald Graham, who published the original algorithm in 1972 [Graham, 1972]. Graham's algorithm finds all the vertices of a convex hull ordered along its boundary. The convex hull of n points in the plane can be found by Graham's algorithm in $O(n \log n)$ time [O'Rourke, 1998].

After ordering, the discrete set of user tagged locations, clockwise or counter-clockwise the ordered set is made contiguous by interpolating additional locations through cubic spline interpolation. Figure 4.24 shows the cubic spline interpolated locations of the non-contiguous set of points shown in Figure 4.23.

13

Figure 4.24 - Cubic spline interpolated locations of the locations marked by the user just outside and around the Blood Vessel (Red) and the Airway-Wall of the CT image of Figure 4.6.

4.3.10.3. HCS process based segmentation of the part of the image enclosed by the continuous curves

The HCS process is applied within the two regions bounded by the two contiguous curves. The output of the segmentation when there are still 20 regions yet to be merged is shown in Figure 4.25.

From the segmentation output shown in Figure 4.25 it could be seen that the major anatomies namely blood vessel (Red), airway-wall (Green) and airway-lumen (Blue) have been delineated. But some locations within the lung parenchyma have been misclassified as airway-lumen (Figure 4.25 Black).

Figure 4.25 - HCS process based segmentation of the Blood Vessel (Red), Airway-Wall and Airway-Lumen
The misclassified part of the Lumen as lung parenchyma is coloured dark (Black)

The misclassification, of some locations of lung parenchyma as airway-lumen, is due to the following reasons :

- the user tagged boundary locations, around the airway, enclose part of the lung parenchyma.

- the Hounsfield values (-1024) of the locations in the lung parenchyma, which got classified as airway-lumen, are exactly the same as that of the airway-lumen (Table 4.2).

- the HCS process compares and merges even those locations which do not border to each other (Section 4.3.4.1).

Of the three reasons listed above one do not have much control on the first two. Firstly, one cannot expect the user to precisely give the boundary locations such that the lung parenchyma is excluded. Secondly, it is either the nature of the anatomy or the limitation of the acquisition device or both that the given value of the X-ray attenuation of the lung parenchyma is very similar to that of the airway lumen.

To address the third reason, which will prevent the misclassification from occurring, one can restrict the HCS process from merging locations which are not bordering to each other. Since the airway wall lies between the lung parenchyma and the airway lumen; by restricting the HCS process to merge only bordering regions one can prevent the locations in lung parenchyma from merging with the locations in the airway lumen even if they are found similar. But restricting the HCS process to merge only bordering regions will be detrimental to the merging of the regions within the airway-wall Figure 4.11 (Section 4.3.4.1). Hence, one cannot arbitrarily disallow the HCS process from merging regions not bordering to each other. But knowing in theory what should be the Hounsfield values of the airway-lumen (-1024)

one can restrict those regions whose average pixel value is around -1024 from merging with non-bordering regions.

4.3.10.4. Reducing the misclassification by specifying pixel value range to restrict merging of regions across the Airway-Wall

As discussed above to restrict the misclassification of locations from lung parenchyma as belonging to the airway-lumen one need to disallow the regions, to which those locations belong to, from merging with the non-bordering regions of the airway-lumen.

To restrict similar regions of the lung parenchyma from merging with the similar non-bordering regions of the airway-lumen, but still allow other non bordering similar regions (e.g. within the airway-wall) to merge with one another following additional steps were incorporated :

- the user provides a range of Hounsfield values as parameters for the HCS process.
- during the merging process the HCS process will check the average pixel value of similar non-bordering regions.
- if the average pixel values of the non-bordering similar regions falls within the user provided Hounsfield value range then those non-bordering regions are not merged even if they are found similar.

Figure 4.26 shows the segmentation output when the pixel value range is given from -1024 to -974. As it can be seen from the output there are still misclassified lung parenchyma. The reason behind this misclassification is because when regions which were restricted from merging merge with adjacent regions the average value of the region get altered and thus fall out of the restricted range. The misclassification could be possibly eliminated by choosing the right pixel value range. But this will be a hit and miss process and hence not found suitable. Hence, to eliminate the misclassification altogether alternative method is proposed. The alternative proposed method will be discussed in Section 4.3.11.

Figure 4.26 - HCS process based segmentation of the Blood Vessel (Red), Airway-Wall and Airway-Lumen
The misclassified part of the Lumen as lung parenchyma is coloured dark (Black)

4.3.10.5. Estimating the dimensions of the Blood vessel, Airway-wall and Airway-lumen

As it can be seen from Figure 4.26 most of the pixel locations belonging to the blood vessel, airway wall and airway lumen have been properly segmented as their respective anatomical regions. Making use of the bordering pixel locations belonging to the respective segmented regions ellipses were fitted to approximate the boundaries of the respective anatomies (Section 4.3.7). Figure 4.27 shows the major and minor axis of the fitted ellipses to the respective anatomies. Table 4.14 lists the values of the major and minor axis of the fitted ellipses to the respective anatomies.

Table-4.14 - Minor and Major axis dimensions (in pixels) of the fitted ellipse to the boundary of the Blood vessel, Airway wall and Airway lumen (Figure 4.27)

	Blood vessel	Airway wall	Airway lumen
Minor Axis	3.50	9.21	4.52
Major Axis	4.05	12.65	7.02

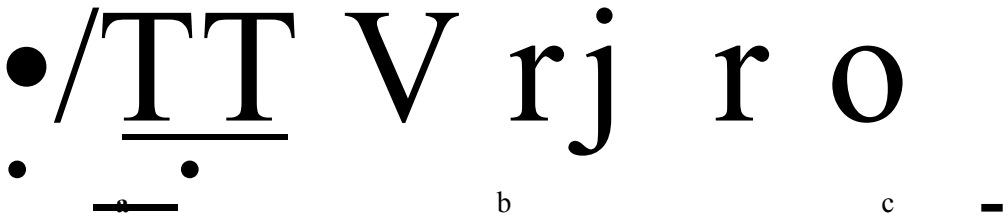


Figure 4.27 - Minor and Major axis of the fitted ellipse to the Blood Vessel (a), Airway-Wall (b) and Airway-Lumen (c).

Comparing the values listed in Table 4.14 and those listed in Table 4.9 there are minor variations (Table 4.15). But the earlier values in the Table 4.9 were obtained with the user tagging the relevant locations corresponding to the different anatomy (Section 4.3.5.2). Thus, in the earlier approach the user involvement is much more higher than the present approach.

Table-4.15 – The difference between the Minor and Major axis dimensions (in pixels) of the fitted ellipse to the boundary of the Blood vessel, Airway wall and Airway lumen (Figure 4.22) (Table 4.9) and (Figure 4.27) (Table 4.14)			
	Blood vessel	Airway wall	Airway lumen
Minor Axis	$(3.5 - 4.06) = -0.56$	$(9.21 - 9.80) = -0.59$	$(4.52 - 5.01) = -0.49$
Major Axis	$(4.05 - 5.45) = -1.4$	$(12.65 - 13.79) = -1.14$	$(7.02 - 6.70) = 0.32$

4.4. Summary

In this chapter we discussed how the user can exploit the HCS process segmentation output to incorporate his/her decision process for the objective measurements of the dimensions of the Air-Way and the accompanying Blood Vessel present in CT images of the lungs. This process of interleaving user decision seamlessly with the HCS processing of the diagnostic images augments the diagnostic information present within the image data.

Chapter Six will discuss how the above HCS aided interpretation can be subsequently used for the monitoring of physiological conditions. Specifically, the following HCS aided monitoring will be discussed in detail :

- HCS process aided monitoring of Cystic Fibrosis.

Chapter 5 HCS Process Aided Interpretation of X-ray Mammograms

5.1. Introduction

In Chapter 4 user decision incorporated processing of CT images of the lungs demonstrated one of the objectives of this study, that is user decision incorporated image processing techniques can be used for processing diagnostic images and augment the information present in those images to aid the diagnosis process.

In this chapter the following application in which user decisions were incorporated during the processing of the X-ray image data, and thus augment their diagnostic information, is discussed in detail :

- user decision incorporated processing of X-ray mammograms.

5.2. User Decision Incorporated Processing of X-ray Mammograms

The processing of X-ray mammograms was yet another application in which HCS process was used to investigate the incorporation of users' decision during the processing of the diagnostic image data. In this application the HCS process was used to incorporate the user decisions during the processing of X-ray Mammograms to design and implement an objective measure to differentiate benign from malignant abnormalities.

In this application the HCS process was applied in two stages. Each of the two stages need to be initialised by the user decision process. The user decision process involved, prior to each of the two stages, is briefly described below :

- before applying the HCS process, in the first stage, the user decides the approximate location of the abnormality. Around the approximate location, decided by the user, the HCS process was applied. This is the first stage of applying the HCS process.
- before the second stage application of the HCS process the user decides which of the different segmentations output, yielded by the first stage HCS process, defines the appropriate boundaries of the abnormality and the healthy regions. Making use of the user decided segmentation output, of the first stage HCS, the more appropriate boundaries of the abnormality and the healthy regions are delineated.

Subsequently, the second stage HCS process estimates the dissimilarity

measure between the abnormality and the healthy regions. The objective measure, to differentiate benign from malignant abnormality, is based on this dissimilarity measure estimated by the HCS process during the second stage.

In the following sections details of the above outlined methodology, which was designed and implemented to quantitatively differentiate benign from malignant abnormality, will be discussed.

5.2.1. Mammogram Image Data

The Mammographic Image Analysis Society (MIAS) is an organisation of UK research groups interested in the understanding of mammograms and has generated a database of digital mammograms. Films taken from the UK National Breast Screening Programme have been digitised to 50 micron pixel edge with a Joyce-Loebl scanning microdensitometer, a device linear in the optical density range 0-3.2 and representing each pixel with an 8-bit word. The database contains 322 digitised films. It also includes radiologist's "truth"-markings on the locations of any abnormalities that may be present.

The original MIAS Database (digitised at 50 micron pixel edge) has been reduced to a 200 micron pixel edge and padded/clipped so that all the images are 1024x1024 pixels. The reduced size Mammographic images are available via the Pilot European Image Processing Archive (PEIPA) at the University of Essex, as mini-MIAS database of mammograms. The mammogram images are available for download from the web-link <http://peipa.essex.ac.uk/info/mias.html>], (visited on August 2011)

To quantitatively evaluate the performance of HCS process, in quantitatively differentiating benign from malignant abnormalities, mammogram images from the mini-MIAS database of mammograms [Suckling *et. al.* 1994], were used.

5.2.1.1. mini-MIAS Database of Mammograms

The mini-MIAS database provides a list which gives appropriate details about the mammograms. The details are provided in a format as follows

1st column :

MIAS database reference number

2nd column :

Characteristics of the breast tissue :

F Fatty

G Fatty-glandular

D Dense-glandular

3rd column:

Class of abnormality present :

CALC Calcification

CIRC Well-defined/circumscribed masses

SPIC Spiculated masses

MISC Other, ill-defined masses

ARCH Architectural distortion

ASYM Asymmetry

NORM Normal

4th column:

Severity of abnormality :

B Benign

M Malignant

5th, 6th columns:

x,y image-coordinates of the centre of the abnormality.

7th column:

Approximate radius (in pixels) of a circle enclosing the abnormality.

As an example following is an entry in the mini-MIAS list :

mdb001 G CIRC B 535 425 197

The above entry gives the following information about the corresponding mammogram :

Mammogram image id	: mdb001
Breast tissue type (G)	: Fatty-glandular
Class of abnormality (CIRC)	: Well-defined/circumscribed mass
Severity of the abnormality (B)	: Benign
Centre of the abnormality location (x,y)	: 533, 425
Approximate radius (in pixels) of the circle enclosing the abnormality	: 197.

The mammograms image data are stored as 8 bit Gray-scale data in the Netpbm Gray-scale image format PGM (Portable Gray Map).

5.2.2. Preliminary Investigation of the HCS Process Based Analysis of the X-ray Mammograms

As a preliminary test run, the HCS process was applied on two of the mini-MIAS database mammograms. The mammograms that were chosen namely Image ID mdb097 and Image-ID mdb102 had benign and malignant abnormality respectively. The following sections will discuss the result of applying the HCS process to analyse these two mammogram image data.

5.2.2.1. HCS Process Analysis of a Benign Abnormality

Mammogram image data mdb097 (Figure 5.1) has a fatty background tissue with a abnormality of benign asymmetric density (circled in white).

To reduce the processing time, a region of interest (ROI) of size 140 x140 (shown in white) was chosen as enclosing the abnormality. The HCS process was applied within the ROI. Figures 5.2 to 5.5 illustrate the segmentation output of the HCS process when applied to the mdb097 mammogram image data, within the ROI.

Figure 5.1 - Digitised X-ray Mammogram image data, mini-MIAS mdb097.
Of fatty background tissue with benign asymmetric abnormality, (abnormality circled,
in white, based on mini-MIAS information)

During the HCS process the number of regions will decrease as the allowable dissimilarity level between the merging regions is increased (Table 5.1). Because, as the allowable dissimilarity between the merging regions is increased more and more regions having higher dissimilarity, than the earlier merged regions, will merge. Figures 5.2 to 5.5 show the hierarchy of different regions and their boundaries found during the HCS process. These segmentations are chosen by the user because in these segmentations one of the segmented region could be identified as part of the abnormality.

Table 5.1 - Details of the intermediate segmented results shown in Figures 5.2 to 5.5

Regions and Boundary Images	Number of Regions	Dissimilarity between the Regions
Figure 5.2	5	> 10%
Figure 5.3	4	> 20%
Figure 5.4	3	> 21%
Figure 5.5	2	> 25%

In the intermediate segmented image shown in Figure 5.2 it could be seen that most of the pixels of the regions having average density values between 181 to 190 (coloured in Fuschia and Red) are well within the border of the lesion (circled in white) marked by the expert. But there are also pixels belonging to the two regions (coloured in Fuschia and Red) outside the lesion border as well.

To evaluate the above results, if we adopt the criteria by Kegelmeyer *et. al.* [Kegelmeyer *et. al.* 1994] which states :

- a computer finding is considered as a true positive detection if its area is overlapped by at least 50% of a true lesion as indicated by an expert radiologist;
- a computer finding that does not so overlap a true lesion is considered as false positive; and
- a true lesion that is not overlapped by any computer finding is considered as false negative.

By the above criteria, the diagnostic accuracy performance of HCS process at this stage is 100% true positive.

Table 5.2 - Details of the five regions in the intermediate segmentation result shown in Figure 5.2

Region (shown in colour)	Minimum Density value	Maximum Density value	Average Density value	Standard Deviation of the Density values
Red	182	199	190	2.8
Fuschia	172	191	181	3.2
Yellow	165	182	174	2.5
	160	177	168	2.5
Green	145	170	162	2.7

Figure 5.2 - Intermediate segmented image showing the live regions and their boundaries

From the intermediate segmented image shown in Figure 5.3 it could be seen that still most of the pixels of the regions having average density values between 180 to 190 (coloured in Red and Fuschia) are well within the border of the lesion (circled in white) marked by the expert. But there still are pixels belonging to the two regions (coloured in Red and Fuschia) outside the lesion border as well.

To evaluate the above results, if we adopt the criteria by Kegelmeyer *et. al* [Kegelmeyer *et. al.* 1994], as mentioned earlier, the diagnostic accuracy performance of HCS process at this stage is still 100% true positive.

Table 5.3 - Details of the four regions in the intermediate segmentation result shown in Figure 5.3

Region (shown in colour)	Minimum Density value	Maximum Density value	Average Density value	Standard Deviation of the Density values
Red	182	199	190	2.8
Fuschia	171	191	180	3.3
Blue	160	182	171	3.5
Green	145	171	162	2.8

Figure 5.3 - Intermediate segmented image showing the four regions and their boundaries

In the intermediate segmented image shown in Figure 5.4 it could be seen that still most of the pixels of the region having average density value 185 (coloured in Fuschia) are well within the border of the lesion (circled in white) marked by the expert. But still there are also pixels belonging to the region (coloured in Fuschia) outside the lesion border as well.

To evaluate the segmentation output in Figure 5.4, if we adopt the criteria by Kegelmeyer *et al.* [Kegelmeyer *et. al* 1994], as mentioned earlier, the diagnostic accuracy performance of HCS process at this stage is still 100% true positive.

Table 5.4 - Details of the three regions in the intermediate segmentation result shown in Figure 5.4

Region (shown in colour)	Minimum Density value	Maximum Density value	Average Density value	Standard Deviation of the Density values
Fuschia	174	199	185	4.6
	160	184	172	4.0
Green	145	171	162	2.9

Figure 5.4 - Intermediate segmented image showing the three regions and their boundaries

In the intermediate segmented image shown in Figure 5.5 it could be seen that most of the pixels of the region, which has an average density value of 181 (coloured in Fuschia), are still well within the border of the lesion (circled in white) marked by the expert. But still there are also pixels belonging to the region (coloured in Fuschia) outside the lesion border as well.

To evaluate the above results, if we adopt the criteria by Kegelmeyer *et al.* [Kegelmeyer *et al* 1994], as mentioned earlier, the diagnostic accuracy performance of HCS process at this stage is still 100% true positive.

Table 5.5 - Details of the two regions in the intermediate segmentation result shown in Figure 5.5

Region (shown in colour)	Minimum Density value	Maximum Density value	Average Density value	Standard Deviation of the Density values
Fuschia	169	199	181	5.6
Green	145	184	167	5.1

Figure 5.5 - Intermediate segmented image showing the two regions and their boundaries

5.2.2.2. HCS process analysis of a malignant abnormality

Mammogram image data mdb102 (Figure 5.6) has a dense-glandular background tissue with a abnormality of malignant asymmetric density (circled in white).

To reduce the processing time, a region of interest (ROI) of size 100 x174 (shown in white) was chosen enclosing the abnormality. The HCS process was done within the ROI. Figure 5.7 to Figure 5.10 illustrate the segmentation output of the HCS process applied to mdb102 mammogram image data, within the ROI.

**Figure 5.6 - Digitised X-ray Mammogram image data, mini-MIAS mdb102.
Of dense-glandular background tissue with malignant asymmetric abnormality,
(abnormality circled, in white, based on an expert findings)**

Figures 5.7 to 5.10 show the hierarchy of different regions and their boundaries found during the HCS process.

The number of regions will decrease as the allowable dissimilarity level between the merging regions is increased (Table 5.6). This is because, the allowable dissimilarity between the merging regions is increased more, and more regions having higher dissimilarity, than the earlier merged regions, will merge.

Table 5.6 - Details of the intermediate segmented results shown in Figure 5.7 to 5.10

Regions and Boundary Images	Number of Regions	Dissimilarity between the Regions
Figure 5.7	6	> 24%
Figure 5.8	4	> 31%
Figure 5.9	3	> 40%
Figure 5.10	2	> 46%

In the intermediate segmented image shown in Figure 5.7 it could be seen that most of the pixels of the region having average density value of 212 (coloured in Red) is well within the border of the lesion (circled in white) marked by the expert.

Table 5.7 - Details of the six regions in the intermediate segmentation result shown in Figure 5.7

Region (shown in colour)	Minimum Density value	Maximum Density value	Average Density value	Standard Deviation of the Density values
Red	200	224	212	5.1
Fuschia	184	206	196	4.3
Yellow	171	192	182	4.2
Blue	154	178	169	4.4
Aqua	143	166	153	4.5
Green	132	150	141	3.3

Figure 5.7 - Intermediate segmented image showing the six regions and their boundaries

To evaluate the segmentation output in Figure 5.7, if we adopt the criteria by Kegelmeyer *et. al* [Kegelmeyer *et. al.* 1994], as mentioned earlier, the diagnostic accuracy performance of HCS process at this stage is still 100% true positive.

Table 5.8 - Details of the four regions in the intermediate segmentation result shown in Figure 5.8

Region (shown in colour)	Minimum Density value	Maximum Density value	Average Density value	Standard Deviation of the Density values
Red	200	224	211	5.4
Fuschia	178	206	194	5.5
Blue	154	190	174	6.1
Green	132	166	147	7.5

Figure 5.8 - Intermediate segmented image showing the four regions and their boundaries

From the intermediate segmented image shown in Figure 5.8 it could be seen that most of the pixels of the region having average density value 211 (coloured in Red) are well within the border of the lesion (circled in white) marked by the expert.

To evaluate the above results, if we adopt the criteria by Kegelmeyer *et. al.* [Kegelmeyer *et. al.* 1994], as mentioned earlier, the diagnostic accuracy performance of HCS process at this stage is still 100% true positive.

Table 5.9 - Details of the three regions in the intermediate segmentation result shown in Figure 5.9

Region (shown in colour)	Minimum Density value	Maximum Density value	Average Density value	Standard Deviation of the Density values
Fuschia				
Green				

Figure 5.9 - Intermediate segmented image showing the three regions and their boundaries

From the intermediate segmented image Figure 5.9 it could be seen that most of the pixels of the region having average density value 203 (coloured in Fuschia) reasonably overlap the border of the lesion (circled in white) marked by the expert.

To evaluate the above results, if we adopt the criteria by Kegelmeyer *et. al.* [Kegelmeyer *et. al.* 1994], as mentioned earlier, the diagnostic accuracy performance of HCS process at this stage is still 100% true positive.

Table 5.10 - Details of the two regions in the intermediate segmentation result shown in Figure 5.10

Region (shown in colour)	Minimum Density value	Maximum Density value	Average Density value	Standard Deviation of the Density values
Fuschia	159	224	198	12.3
Green	132	178	154	11.8

Figure 5.10 - Intermediate segmented image showing the two regions and their boundaries

From the intermediate segmented image shown in Figure 5.10 it could be seen that a major part of the pixels of the region having average density value 198 (coloured in Fuschia) lies outside the border of the lesion (circled in white) marked by the expert.

To evaluate the above results, if we adopt the criteria by Kegelmeyer *et. al.* [Kegelmeyer *et. al.* 1994], as mentioned earlier, the diagnostic accuracy performance of HCS process at this stage has a very low true positive. But since the standard deviation of the density values within the region (coloured Fuschia) is very high (greater than 12.0) it could be inferred that the region is highly inhomogeneous. Hence this segmentation of regions could be rejected.

The above segmentation is obtained because HCS process has got no stopping criteria and the process goes about merging regions as the allowable dissimilarity between the regions is increased. Eventually combining all the regions as one single region.

5.2.2.3. Overall Discussion of the HCS Process Analysis of the Benign and Malignant Abnormalities

From the results of segmentation of the two mammogram image data (mdb097 and mdb102) illustrated in the Figures 5.2 to 5.5 and Figure 5.7 to 5.10, respectively, the following general observations could be made :

- The number of regions decrease as the allowable dissimilarity level between the merging regions is increased.

As the allowable dissimilarity between the merging regions is increased more and more regions having higher dissimilarity, than the earlier merged regions, merge and the homogeneity within the regions decrease. This can be observed by the increase in the standard deviation of the density values within the merged regions.

- The proposed HCS based CAD system, unlike the currently existing CAD systems, does not try to detect and prompt the abnormal regions. Instead, the designed HCS process strives to highlight the subtle differences within the same image by outlining those parts of the image having similar properties, for a given allowable dissimilarity level between the regions.

The outlining of the similar part of the regions within the image might be able to draw the attention of the expert to parts of the image which are dissimilar and hence having the possibility of diseased.

5.2.3. Differentiating Benign from Malignant Abnormalities ; a Possibility

The following quantitative comparisons of the segmentation results of mammogram image data of mdb097 (Figures 5.2 to 5.5) having benign asymmetric density and of the segmentation results of mammogram image data of mdb102 (Figures 5.7 to 5.10) having malignant asymmetric density can be made :

- Comparing the dissimilarities between the different regions, during the merging process, for the mammogram image data of mdb097 (Table 5.1) and that of mammogram image data of mdb102 (Table 5.6). It could be seen that the dissimilarity between regions for the benign asymmetric density is markedly lower (10% to 25%) (Table 5.1) when compared to that of the malignant asymmetric density (24% to 46%) (Table 5.6).

Will these differences in dissimilarities between the regions for benign (Table 5.1) and malignant (Table 5.6) type of lesions provide clues to the benign or malignant nature of the lesion ?

- Comparing the average density of the regions having the highest density, during the merging process, for the mammogram image data of mdb097 (Table 5.2 to Table 5.5) and that of mammogram image data of mdb102 (Table 5.7 and Table 5.8). It could be seen that the average density of the regions having the highest density for the benign asymmetric density is markedly lower (181 to 190) (Table 5.2 to Table 5.5) when compared to that of the malignant asymmetric density (~212) (Table 5.7 and Table 5.8).

Will this marked difference in the average density values within the regions having the highest density, of benign (Table 5.2 to Table 5.5) and that of malignant (Table 5.7 and Table 5.8) type of lesions provide clues to the benign or malignant nature of the lesion ?

To explore the above raised possibilities additional routines were incorporated within HCS and additional mammograms were processed. The details of the developed programs and how the validity of the possibilities were tested will be given in Section 5.2.4.

5.2.3.1. Differentiating Benign from Malignant Abnormalities; a Hypothesis

The two mini-MIAS mammograms, mdb097 having benign asymmetry and mdb102 having malignant asymmetry, were processed by the HCS process (Sections 5.2.2.1 and 5.2.2.2). Inspecting the resulting output the following observations were made :

- comparing the dissimilarities between the different regions, as the merging process progressed; it could be seen that the dissimilarity among the regions

for the benign case (mdb097) is markedly lower (10% to 25%) (Table 5.1) when compared to that of the malignant case (mdb102) (24% to 46%) (Table 5.6).

- comparing the average density of the regions having the highest density, during the merging process, it could be seen that the average density value, of the region having the highest density, for the benign case (mdb097) is markedly lower (181 to 190) (Table 5.2 to Table 5.5) when compared to that of the malignant case (mdb102) (~212) (Table 5.7 and Table 5.8).

From the above observations it can be hypothesised that benign abnormalities have properties much closer to the healthy tissue and malignant abnormalities are markedly different from the surrounding healthy tissue.

The above hypothesis was objectively evaluated. The objective evaluation was done by the following process :

- measure the dissimilarity between the regions enclosing the abnormality and the regions enclosing the healthy tissue.
- plot the distribution of the dissimilarity measure between the abnormality regions and the healthy regions during the merging process.

It was hypothesised that the above measured and plotted dissimilarity measure will be markedly different for benign abnormalities when compared to that of malignant abnormalities, thus providing an objective measure to differentiate benign from malignant abnormalities.

5.2.4. Design and Implementation of an Objective Measure to Differentiate Benign from Malignant Abnormalities

As detailed in the earlier section the proposed objective measure is to measure the dissimilarity between the regions containing the abnormality and the regions containing healthy tissue. The measuring of the dissimilarity between the abnormality and the healthy region involves the following three steps :

- appropriate delineation of the boundary of the abnormality (Section 5.2.4.1).
- identifying the region of the image comprising the healthy part (Section 5.2.4.2).
- measuring the dissimilarity between the abnormality and the healthy region (Section 5.2.4.3)

The details of how the above three listed steps were implemented are discussed in Sections 5.2.4.1, 5.2.4.2 and 5.2.4.3.

5.2.4.1. More Appropriate Delineation of the Boundary of the Abnormalities

The success of the proposed method, to differentiate benign from malignant abnormality, squarely depends on the precision with which the boundaries, of the abnormality and the healthy part of the image, are known. Hence, the very first requirement is to know which part of the image contains the abnormality and which part of the image contains healthy tissue.

For each of the mammogram the mini-MIAS database provides an approximate radius (in pixels) of a circle enclosing the abnormality. The boundaries marked by human experts are only approximations. Hence, for the same image the abnormality marked by different experts will be of different size even though the location might be the same. This is the case because different experts generate different levels of approximations.

Figure 5.11 illustrates this fact, how a radiologist's outlining the boundary of the abnormality (Black curve) varies with that marked (red circle) by using the radius information provided by the mini-MIAS database. Comparing the approximate boundary of the abnormality as suggested by the mini-MIAS (Image ID mdb095) with the boundary drawn by another radiologist, it could be seen that there is a considerable amount of variation between the boundaries marked by the two different radiologists.

From Figure 5.11 it could be seen that even though the boundaries marked by different experts differ, in the area enclosed, they concur reasonably well with the central location of the abnormality. Hence, it could be reasonably assumed that the centre of the abnormality lies somewhere near the centre of the marked boundary. The only unknown quantity is the actual extent (i.e. the area) of the abnormality.

Since the human drawn boundaries could be taken only as approximate areas, which encloses the abnormality, one need to delineate a more appropriate boundary of an abnormality before proceeding any further. The process of delineating more appropriate boundaries of the abnormalities is discussed below.

To find a more appropriate boundary of an abnormality the following steps are followed:

- the user defines a region of interest (ROI) enclosing the approximately marked boundary of the abnormality.
- the HCS process is applied within the user defined ROI.
- the user inspects the segmentation output generated, by the HCS process, for different levels of allowable dissimilarity.
- making use of his/her expert knowledge the user chooses the segmentation where the abnormality is most appropriately defined. That is the abnormality should neither be too fragmented nor should it have merged with the healthy part within the ROI.

Figure 5.12 illustrates the above steps for the mini-MIAS mammogram (image ID mdb005). Figure 5.12 (a) shows a ROI superimposed around the lesion. The ROI is not centred to the lesion, because by doing so one will include the background rather than the breast tissue. Hence, the ROI is offset to the centre of the circle. Figure 5.12 (b and c) shows the different regions and their respective boundaries when there are still fourteen regions yet to be merged. Figure 5.12 (d and e) shows the regions and their boundaries when there are still thirteen regions yet to be merged. Figure 5.12 (f) shows the boundary of the abnormality based on the segmentation when there were still 14 regions are yet to be merged (Figure 5.12 (b and c)).

Figure 5.11 - For the mini-MIAS mammogram (Image ID mdb095) of asymmetry class of malignant abnormality in a fatty tissue, images showing the difference between the boundary of the abnormality as suggested by mini-MIAS (Red circle) and by another different radiologist (Black curve).

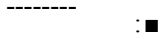


Figure 5.12 - HCS processing of the mammogram, mini-MIAS mdb095.
 Of asymmetry class of malignant abnormality in a fatty tissue.
 Mammogram mdb095 with the abnormality's approximate location circled in Red and the ROI marked in Green(a). HCS process intermediate output 14 regions (b) and 13 regions (d) and the respective region borders (c) and (e). Border of the abnormality based on user decided segmentation of 14 regions (f).

HCS will continue the merging process until there are no more regions yet to be merged, that is the whole ROI will be merged into one single region. Hence, it is left for the user to decide the most appropriate segmentation where a specific region within the segmented image will adequately represent the abnormality. The user, with his expert knowledge, will be able to make the decision of choosing the most appropriate segmentation which will have the abnormality adequately outlined. The user will be assisted, in making this crucial decision, by the boundaries, marked by the HCS process, outlining the various similar parts of the image.

In Figure 5.12 the segmented region at the centre, of the user marked location, is marked in Red. When there are fourteen regions still left to be merged (Figure 5.12 b) the regions at the centre of the user marked area has got minimal number of pixels from other part of the image. But where the number of regions, still left to be merged, have reduced to thirteen regions (Figure 5.12 d) the regions at the centre of the user marked area has got substantial number of pixels from other parts of the image. Hence, it could be seen that the region at the centre of the user marked area when there are still fourteen regions still left to be merged (Figure 5.12 b) is the most appropriate representation of the abnormality.

Figure 5.12 f shows the chosen region within the user marked area as the more appropriately delineated boundary of the abnormality. This identification of the more relevant boundary of the abnormality is done as detailed below :

Once the user has identified the segmentation that has delineated the boundary of the abnormality appropriately, the boundary of the abnormality is identified as follows :

- the part of the identified region which falls within the approximate boundary circled by the user, is considered as part of the abnormality.
- the part of the region which falls outside the user given approximate boundary and does not border (i.e not contiguous with) the part of the region within the user given approximate boundary is not considered as part of the abnormality.
- the part of the region which extends beyond the user given boundary but is contiguous with the region, within the user given approximate boundary, is considered as part of the abnormality.
- the parts of the region, which is identified as the abnormality, which are not

contiguous but are within the user given approximate boundary, are considered as part of the abnormality.

The above points are illustrated in the Figure 5.12 (mini-MIAS Image ID mdb095), Figure 5.13 (mini-MIAS Image ID mdb102) and Figure 5.14 (mini-MIAS Image ID mdb090) as described below :

- Figures 5.12 (e) and (f) illustrate how the part of the region (Red) which falls within the approximate boundary circled by the user, is considered as part of the abnormality.
- Figures 5.12 (d), (e) and (f) illustrate how the part of the region (Red) which falls outside the user given approximate boundary and does not border (i.e not contiguous with) the part of the region within the user given approximate boundary is not considered as part of the abnormality.
- Figures 5.13 (b) and (c) show where the region (Red) comprising the abnormality extends beyond the user given approximate boundary. But the region is contiguous with the part of the region, within the user given approximate boundary. Hence, that part of the region, outside the user given approximate boundary, is also considered as part of the abnormality (Figure 5.13 c).
- Figures 5.14 (b) and (c) show where the regions (Red) comprising the abnormality are not contiguous. However some of the non-contiguous regions are well within the user given approximate boundary. Hence those regions, even though they are not contiguous, are all considered as part of the abnormality (Figure 5.14 c and Figure 5.14 d).

Figure 5.13 - For the mini-MIAS image ID mdb102 of asymmetry class of malignant abnormality in a Dense-Glandular tissue (a). Figure showing the region chosen as the abnormality region (b) extending beyond the user given approximate boundary (c) (d).

b c d

Figure 5.14 - HCS processing of the mini-MIAS mdb090. Mammogram of asymmetry class of malignant abnormality in a fatty-glandular tissue For the mini-MIAS image ID mdb090 of asymmetry class of malignant abnormality in a Fatty-Glandular tissue (a). When there are 11 regions yet to be merged, figure showing the regions (Red) chosen as the abnormality region (b) are not contiguous. But since most of the chosen regions (Red) are will within the user defined approximate boundary they are chosen as part of the abnormality (c) (d).

5.2.4.2. Identifying the Region of the Image Comprising of the Healthy Part

The next step before proceeding to design a process to estimate the quantitative measure to measure the dissimilarity between the abnormality and the healthy region, is to identify which part of the image comprises of the healthy tissue.

Physiologically, a healthy tissue is all that part of the tissue which is not abnormal. But the image representation of the underlying physiology may not be exact and one need to take into account the limitation of the data acquisition mechanism.

For example, in Figures 5.12 (b) and (c), regions similar to the abnormality region (marked Red), can be found to be the present far away from the approximate boundary marked by the user. This could be because of the misrepresentation of the underlying physiology by the data acquisition system. To take into consideration the above concern, it was decided not to include the part of the image which is further from the location of the abnormality while composing the area of the healthy tissue.

The following two ways were adopted to identify the part of the image which will comprise of the healthy tissue :

- to make use of the user provided approximate boundary of the abnormality
- to make use of the HCS process output.

any one of the above two methods was used depending upon the location of the abnormality. This process is detailed in the following sections (Section 5.2.4.2.1 and Section 5.2.4.2.2).

5.2.4.2.1. Using the User Provided Approximate Boundary of the Abnormality To Identify the Healthy Part of the Image

One of the ways to ensure that only the most appropriate parts of the image are compared is to include only that part of the image, within the boundary marked by the expert. Hence, once the more appropriate boundary of the abnormality has been delineated then the rest of the image, within the user provided approximate border, is considered as the healthy region.

Figure 5.15 illustrates the above process for the mini-MIAS mammogram mdb095. Based on the HCS segmentation (Figures 5.12 b and c) the Red coloured region is considered as the more appropriately delineated abnormality and the Green coloured region is considered as the healthy part and the rest of the region (Blue coloured) within the ROI was not considered (Figure 5.15).

Figure 5.15 - Abnormal and Healthy regions considered for the mini-MIAS mdb095 Mammogram of asymmetry class of malignant abnormality in a fatty tissue. Based on the HCS segmentation (Figure 5.12) figure showing the regions considered as Abnormality (Red) and Healthy (Green). The part of the image which was considered as comprising the abnormality is shown in Red. The rest of the area, within the boundary marked by the user, which was considered as healthy is shown in Green. The part of the image within the ROI which was not considered is shown in Blue.

5.2.4.2.2. Making use of the HCS Process Output

The above detailed process, of making use of the user provided approximate boundary of the abnormality, to identify the healthy part, may not be appropriate in all conditions. For example, if the user provided approximate boundary is very close to the border of the breast tissue then that part of the image, which is closer to the border, will be influenced by the background. Hence, that part of the image may not be the exact representation of the underlying tissue type. So, to consider blindly everything within the user given approximate boundary, excluding the appropriately delineated abnormality region, as part of the healthy region will not give the required results (Refer Section 5.2.6). The inappropriateness of making use of the user given approximate boundary, to identify the healthy region, is illustrated through Figures 5.16 and 5.17 as detailed below.

Figure 5.16 (a) shows one of the mammogram images (Image ID mdb090) from the mini-MIAS database, showing the location of the abnormality circled in Red/Green. It can be seen, from Figure 5.16 (a), that the circle includes part of the image which forms part of the background at the top right hand corner.

Figure 5.16 - Abnormal and Healthy regions considered for the mini-MIAS mdb090.
Mammogram of asymmetry class of malignant abnormality in a fatty-glandular tissue.
Image showing the approximate location of the asymmetry class malignant abnormality (a). The region chosen as the abnormality area (Red) (b) and (c). Area of the image considered as healthy (Green) (d) (e).

Figures 5.16 (b) and (c) depict the intermediate segmentation output of the HCS process. The figures show the regions and their boundaries, when there are ten

regions yet to be merged. Making use of this segmentation the user selects the contiguous region (Red) as the abnormality. The healthy part is represented by the rest of the image within the user given approximate boundary (Green). The part of the image representing the abnormality (Red) and the part of the image representing the healthy area (Green) are shown in Figures 5.16 (d) and (e).

Inclusion of the rest of the image, other than the abnormality, within the approximate boundary given by the user (Figures 5.16 (d) and (e)) might include area of the image which might not be a proper representation of the healthy part. This fact is highlighted in the segmentation output in Figures 5.17 (a) to (f).

Figures 5.17 (a, b), (c, d) and (e, f) show the HCS process segmented regions and their boundaries when there were ten regions, five regions and three regions, respectively, yet to be merged. It can be seen from these segmentation output that the part of the image, coloured Yellow, is quite dissimilar from the rest of the image. This is evident from the fact that that part of the image remains as a separate region even when the rest of the regions have merged together 5.17 (e, f).

If the healthy part is considered as the rest of the image, other than the abnormality, within the approximate boundary given by the user (Figures 5.16 (d) and (e)), then that part of the, highly dissimilar area of the, image will be considered as part of the healthy region. This will result in the healthy region being inhomogeneous. Thus, the highly dissimilar part of the healthy region will give a false measure when one calculates the dissimilarity between the abnormality and the healthy region. This will result in benign abnormality being falsely categorised as malignant (Refer Section 5.2.6.1). Hence, it is crucial that one need to avoid the inclusion of the highly dissimilar region as part of the healthy region.

To address the above issue it was decided to make use of the HCS output to identify the healthy region similar to identifying the abnormality region. This process is done as follows :

- the user, via his/her expert knowledge, identifies the segmentation output which adequately represents the border of the abnormality.
- in the segmentation output identified above the user identifies the region or regions which adequately represents the healthy part, as well.

Figure 5.17 - HCS process intermediate output for mammogram image mdb090. Of asymmetry class of malignant abnormality in a fatty-glandular tissue when there were ten regions (a, b), five regions (c, d) and three regions (e, f), yet to be merged.

Figures 5.18 (a), (b) and (c) illustrate the above process of identifying the healthy region. Figure 5.18 (a) shows the intermediate segmentation output, of HCS process, when there were ten regions yet to be merged. Making use of this segmentation the user first selects the contiguous region (Red) which will represent the abnormality (Figures 5.18 (a) and (b)). Then the user selects the region (Green), which surrounds the abnormality, as the healthy part (Figures 5.18 (a) and (b)).

The above described process of selecting a specific region to represent the healthy part ensures that only relevant part of the image is considered. Consequently, the most dissimilar part of the image (Yellow) (Figure 5.18 (c)) is automatically excluded from the subsequent process to estimate the objective measure to differentiate malignant abnormality from benign abnormality.

Figure 5.18 - Abnormal and Healthy regions considered for mini-MIAS mdb090. Mammogram of asymmetry class of malignant abnormality in a fatty-glandular tissue. HCS process segmentation output when there were ten regions (a) and the border of the regions considered for being abnormality (Red) and healthy (Green) (b). The part of the image which is considered as the abnormality is shown in Red and the part of the image which is considered as the healthy region is shown in Green. Parts of the image not considered are coloured Yellow and Blue (c).

5.2.4.3. Measuring Dissimilarity Between Regions Containing the Abnormality and the Healthy Tissue

Once the more appropriate boundaries of the abnormality and the healthy parts of the image have been delineated the next step, in the implementation of the proposed objective measure, to differentiate benign from malignant abnormalities, is the measuring of the dissimilarity between the abnormality and the healthy region. The objective of this step is to quantitatively measure the dissimilarity between the regions comprising the more appropriately delineated abnormality and the regions comprising the healthy tissue. This process is carried out as detailed below.

The pixel locations, which make up the healthy and abnormality regions, are passed on to the HCS process and the merging of only those pixel locations is initiated. As the merging process proceeds the following dissimilarity measures are estimated after each merge:

Dissimilarity between clusters within the abnormality and the healthy regions (Section 5.2.4.3.1).

- Dissimilarity between the primary clusters within the abnormality region and all the clusters within the healthy region (Section 5.2.4.3.2).
- Dissimilarity between the cluster containing the user tagged location within the abnormality region and all the clusters within the healthy region (Section 5.2.4.3.3).

The details of estimating the above dissimilarity measures will be discussed in detail in Sections 5.2.4.3.1, 5.2.4.3.2 and 5.2.4.3.3.

5.2.4.3.1. Dissimilarity Between Clusters within the Abnormality and the Healthy Regions

The estimation of this measure, at the end of each merging operation, is carried out as follows :

- find the clusters within the abnormality region and the healthy region.
- estimate the dissimilarity between each of the cluster within the abnormality region and all the clusters within the healthy region.
- find the maximum, minimum and average value of the dissimilarities calculated above.

5.2.4.3.2. Dissimilarity Between the Primary Clusters within the Abnormality Region and the Clusters Within the Healthy Region

In this measure at the end of each merge first the primary cluster amongst the clusters within the abnormality region are identified. The criteria for deciding on a primary cluster are the following :

- cluster or clusters having the maximum number of pixels for that merge.
- cluster or clusters having the pixel which has got the maximum density value within it.

The process of estimating the dissimilarity between the primary cluster, within the abnormality region, and all the clusters within the healthy region is done as follows :

- identify all the primary clusters within the abnormality region
- estimate the dissimilarity between each of the primary cluster within the abnormality region and all the clusters within the healthy region.
- for each of the primary cluster find the maximum, minimum and average value of the dissimilarities calculated above.

5.2.4.3.3. Dissimilarity Between the Cluster Containing the User Tagged Location Within the Abnormality Region and the Clusters Within the Healthy Region

In estimating this measure the user's decision is made use of as follows :

- after the initial merging process within the ROI, enclosing the approximate abnormality boundary, the user identifies the relevant merge and the relevant region to delineate a more appropriate boundary of the abnormality.
- subsequently, the user inspects the clusters which eventually merged to form the more appropriately delineated abnormality and identifies the cluster which according to his/her expert opinion is the core of the abnormality.
- within the above identified core cluster the user chooses the pixel location which eventually grows to form the core of the abnormality.

The pixel location chosen by the user, as detailed above, is termed the user tagged location. It should be noted that the user could tag more than one location.

The above process of the user deciding upon a tagged location is illustrated in the Figure 5.19 (mini-MIAS Image ID mdb102), as described below :

- Figures 5.19 (a) to (h) show the intermediate segmentation output during the HCS process. The intermediate segmentation output are when there were fifty regions (a, b), twenty-six regions (c, d), ten regions (e, f) and four regions (g, h).
- When one inspects the merging process by looking at the intermediate segmentation output one can observe that the region coloured Red is the core region which eventually forms the abnormality.
- A location within the identified region at the earliest merging process is chosen as the user tagged location.

During the merging process, of the abnormality and the healthy regions, at the end of each merge the clusters to which each of the tagged pixel location belongs to is identified. These clusters are termed as user tagged clusters. The dissimilarity measure, for each of the tagged cluster, is estimated as follows :

- estimate the dissimilarity between each of the tagged cluster within the abnormality region and all the clusters within the healthy region.
- for each of the tagged cluster find the maximum, minimum and average value of the dissimilarities calculated above.
- also, for each of the tagged cluster find the maximum, minimum, average and standard deviation of the pixel values within each of the tagged cluster.

a

c

e

8

Figure 5.19 - Segmentation of mini-MIAS mammogram image mdb102. Of asymmetry class of malignant abnormality in a dense-glandular tissue. HCS process intermediate output when there were 50 regions (a, b), 26 regions (c, d), 10 regions (e, f) and 4 regions (g, h) yet to be merged.

5.2.4.3.4. The Choice of the Dissimilarity Measure Between Regions Containing the Abnormality and the Healthy Tissue

Of the above discussed different ways of measuring the dissimilarity between the abnormality region and the healthy region only the following two measures, were found to be of practical use :

- Dissimilarity between the clusters within the abnormality and the healthy regions.
- Dissimilarity between the cluster containing the user tagged location within the abnormality region and all the clusters within the healthy region.

The following measure was not found to be practical :

- Dissimilarity between the primary clusters within the abnormality region and all the clusters within the healthy region.

The reasons for the above measure being not practical are as follows :

- the way the primary cluster is identified might result in more than one cluster.
- the method might yield clusters/region that may not be the actual representation of the underlying abnormality.

For example, identifying the primary cluster based on the criteria as the cluster/region having the maximum count may not be the location of the actual core of the abnormality. The reason for this is because abnormalities might have unusual characteristics from the rest of the tissue and hence that part of the image might not have too many pixel locations to start with.

Moreover, the first two measures involve the participation of the user. Where the user chooses the regions representing the abnormality and the healthy part of the image and also chooses the part of the image which may be the core of the abnormality. In choosing the location which may form the core of the abnormality the user may make use of his/her expert knowledge may take into account other features in the image other than just the higher density values.

5.2.5. Differentiating Benign from Malignant Abnormalities by Making Use of the Objective Measure

mini-MIAS database mammograms may have any one of the following different classes of abnormality :

- Architectural distortion
- Asymmetry
- Calcification
- Spiculated masses

- Well-defined/circumscribed masses
- Other, ill-defined masses

Of the above classes of abnormalities only the asymmetry and circumscribed masses classes of abnormalities were considered to evaluate the performance of the objective measure. The reason for preferring asymmetry and circumscribed masses classes of abnormalities is discussed below.

The HCS process is a clustering process which clusters similar collections of pixels into regions of similar characteristics. The objective measure to differentiate malignant from benign abnormalities make use of HCS process's ability to collate pixels of similar properties. This is done by comparing the regions within the more appropriately delineated abnormality with the regions present within the healthy area and estimating how dissimilar are they. The higher the dissimilarity, between the regions belonging to the abnormality and the regions belonging to the healthy part, the higher the probability be that the abnormality is malignant. Hence, for a successful estimation of the objective measure the key requirement is that the abnormality and the healthy parts of the image should be made up of regions.

Only the asymmetry (Figure 5.13 and 5.16) and circumscribed masses (Figure 5.20) classes of abnormalities are spatially large enough to be able to be segmented into regions. Other classes of abnormalities like calcification are so localized that they comprise of hardly couple of pixels (Figure 5.21) and hence they cannot be segmented into regions. Moreover, without having component regions there is no way one can estimate the dissimilarity, between the regions belonging to the abnormality and the regions belonging to the healthy part.

The above issues regarding the choice of specific classes of abnormalities, for evaluating the performance of the objective measure, are demonstrated by suitable examples below.

Figure 5.19 illustrates the intermediate segmentation output of the HCS process for the mini-MIAS mammogram (Image ID mdb102). The abnormality, shown circled in Black, is of asymmetry class. The segmentation output shown in the figure illustrates how the HCS process is able to segment the abnormality into well defined regions.

Figure 5.20 illustrates the intermediate segmentation output of the HCS process for the mini-MIAS mammogram (Image ID mdb028). The abnormality, shown circled in Black, is of circumscribed mass class. The segmentation output shown in the Figure 5.20 illustrates how the HCS process is able to segment the abnormality into well defined regions.

Figure 5.21 illustrates the intermediate segmentation output of the HCS process for the mini-MIAS mammogram (Image ID mdb213). The abnormality, shown circled in Black, is of calcification class. The HCS process output shows that the precise location of the abnormality is well delineated at the early stages of the segmentation process (Figure 5.21 b and c). But the delineated area of the image is very small. Furthermore, as the merging process continues the region defining the abnormality is no more unique. Because the region comprising the abnormality has combined with the rest of the similar regions in the image (Figure 5.21 d, e, f and g).

b

Figure 5.20 - Segmentation of mini-MIAS Mammogram image mdb028.
Of circumscribed class of malignant abnormality in a fatty tissue showing the
approximate location of the circumscribed mass (a). HCS process segmented regions
and their boundaries when there were 25 (b,c), 10 (d,e) and 4 (f,g) regions.

c

e

g

Figure 5.21 - Segmentation of mini-MIAS Mammogram image mdb213. Of calcification class of malignant abnormality in a fatty-glandular tissue showing the approximate location of calcification (a). HCS process segmented regions and their boundaries when there were 39 (b,c), 8 (d,e) and 4 (f,g) regions.

In the following sections the operation of the designed objective measure, to differentiate benign from malignant abnormalities, will be discussed in detail for the breast tissue type and classes of abnormalities listed in Table 5.11.

Table 5.11 - Details of the breast tissue type, classes of abnormalities and severity of abnormality considered, for evaluating the objective measure.

Breast Tissue Types	Classes of Abnormality	Severity of Abnormality
Fatty	Asymmetry	Benign
Fatty Glandular	Well-defined/circumscribed masses	Malignant
Dense Glandular		

5.2.5.1. Classifying Malignant Abnormality Using the Objective Measure

This section will discuss in detail a sample implementation of the objective measure to classify a malignant abnormality. Figure 5.22 shows one of the mini-MIAS mammogram (Image ID mdb102). According to the information provided by the database, the mammogram is of the dense glandular breast and the abnormality belongs to an asymmetric class and is malignant.

Making use of the information provided by the database the approximate boundary of the abnormality was found which is marked as a Red circle (Figure 5.22 a). A region of interest (ROI) is centred on the abnormality, marked as a Red square (Figure 5.22 a). The HCS process was applied within the ROI. Making use of the HCS process output the user selected the region corresponding to the abnormality which is shown in Red (Figure 5.22 b, c and d). The area within the approximate circular boundary other than the abnormality was considered as healthy, which is shown Green in colour (Figure 5.22 d). Inspecting the HCS process output (Figure 5.19) the user also tagged a location which was considered as the core of the abnormality, which is shown Yellow in colour (Figure 5.22 d and e). The rest of the area within the ROI is rejected, which is shown Blue in colour (Figure 5.22 d and e).

Figure 5.22 - HCS processing of mini-MIAS mammogram (Image-ID mdb102).
Of asymmetry class of malignant abnormality in a dense-glandular tissue.
Location of the abnormality circled in Red (a). The breast tissue type is dense glandular having an asymmetric class abnormality which is malignant.
HCS process delineated four regions and their boundaries (b and c). Regions, and their boundaries, identified by the user as healthy (Green) and abnormal (Red) (d and e).

The HCS process was applied only to the pixel locations within the abnormality (Red Figure 5.22 d and e) and the healthy (Green Figure 5.22 d and e) areas of the image. As the HCS process merged similar regions within the abnormality and the healthy areas, the following measures were estimated :

- average dissimilarity amongst the regions within the abnormality area.
- average dissimilarity amongst the regions within the healthy area.
- average dissimilarity between the regions across the abnormality area and the healthy area.
- average dissimilarity between the region having the user tagged location and the rest of the regions within the abnormality area.
- average dissimilarity between the region having the user tagged location and the regions within the healthy area.

The graphs of Figures 5.23 and 5.24 show the above measures.

Making use of the above objective measures the following criteria was used to differentiate malignant from benign abnormality :

- find the maximum average dissimilarity, measured between the cluster having the user tagged location (within the abnormality) and the clusters within the healthy region.
- the criteria for differentiating malignant from benign abnormality is as follows :
 - if the value of the above estimated measure is less than fifty percent then the abnormality is benign.
 - if the value of the above estimated measure is greater than fifty percent then the abnormality is malignant.

The graph shown in Figure 5.24 demonstrates how the above measure and the criteria is able to correctly classify the abnormality, under consideration, as malignant.

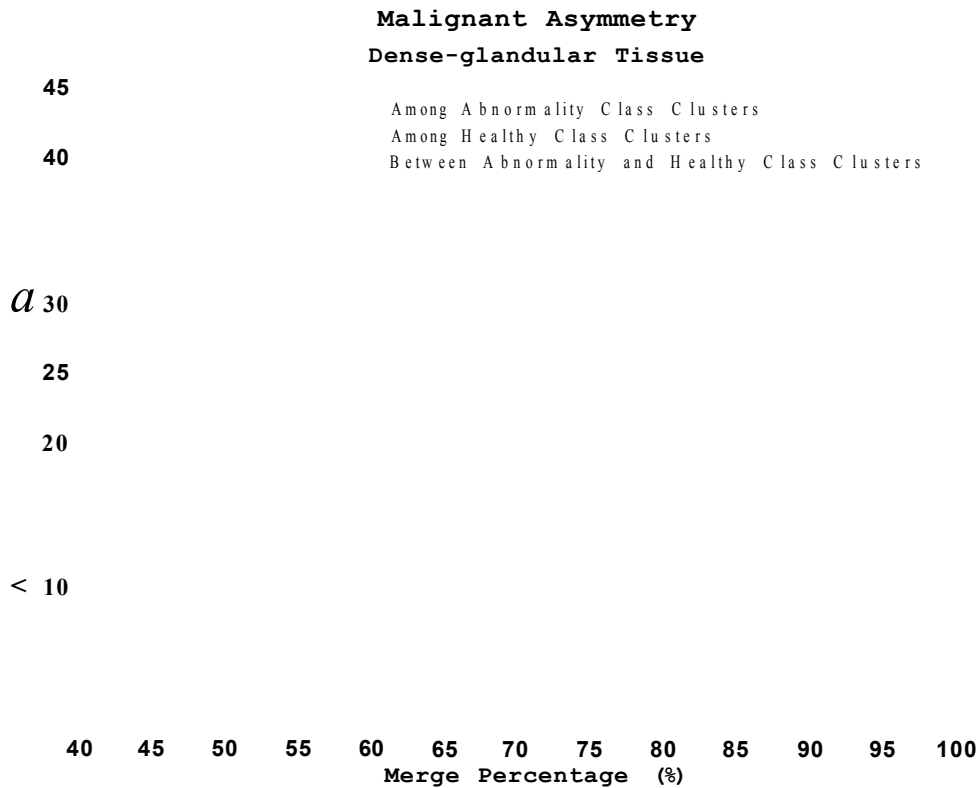


Figure 5.23 - For mini-MIAS Mammogram image (Image-ID mdb102) graph showing the dissimilarity amongst the clusters within the abnormality area and the healthy area and between the clusters within the abnormality and healthy areas.

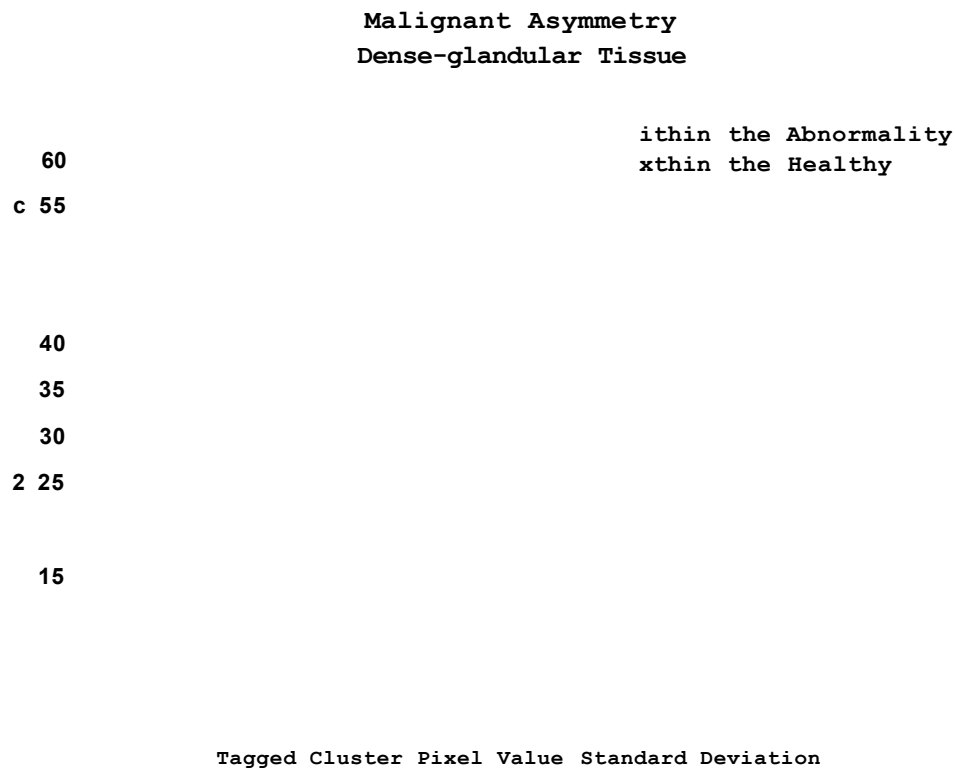


Figure 5.24 - For mini-MIAS Mammogram image (Image-ID mdb102) graph showing the dissimilarity between the cluster having the user tagged location and other clusters belonging to the abnormality area and the healthy area.

5.2.5.2. Classifying Benign Abnormality Using the Objective Measure

This section will discuss in detail a sample implementation of the objective measure to classify a benign abnormality. Figure 5.25 shows one of the mini-MIAS mammogram (Image ID mdb097). According to the information provided by the database the mammogram is of the dense fatty and the abnormality belongs to asymmetric class and was benign.

Making use of the information provided by the database the approximate boundary of the abnormality was found which is marked as a Red circle (Figure 5.25 a). A region of interest (ROI) was centred on the abnormality (marked Green in Figure 5.25 a) and HCS process was applied within the ROI. Figure 5.26 shows the regions and their boundaries of HCS process intermediate output. The intermediate segmentation output are when there were three-hundred-and-three regions (a, b), one-hundred-and-eighty regions Figure 5.26 (c, d), fifty regions Figure 5.26 (e, f) and five regions Figure 5.26 (g, h).

Making use of the HCS process output the user selected the region corresponding to the abnormality which is shown in Red (Figure 5.25 b, c and d). The area within the approximate circular boundary other than the abnormality was considered as healthy, which is shown Green in colour (Figure 5.25 d). Inspecting the HCS process output (Figure 5.26) the user also tagged a location which was considered as the core of the abnormality, which is shown Yellow in colour (Figure 5.25 d and e). Rest of the area within the ROI is not considered for further processing, shown Blue in colour (Figure 5.25 d and e).

a

c

e

Figure 5.25 - HCS processing of mini-MIAS mammogram (Image-ID mdb097).
Of asymmetry class of benign abnormality in a fatty tissue.
The breast tissue type is fatty having an asymmetric class benign abnormality
Location of the abnormality circled in Red (a).
HCS process delineated two regions and their boundaries (b and c). Regions, and their
boundaries, identified by the user as healthy (Green) and abnormal (Red) (d and e).

e

g

n

Figure 5.26 - HCS processing of mini-MIAS mammogram mdb097.
Of asymmetry class of benign abnormality in a fatty tissue.
Intermediate output when there were 303 regions (a, b), 180 regions (c, d), 50
regions (e, f) and 5 regions (g, h) yet to be merged.

The HCS process was applied only to the pixel locations within the abnormality (Red Figure 5.25 d and e) and the healthy (Green Figure 5.25 d and e) areas of the image. As the HCS process merged similar regions within the abnormality and the healthy areas, following measures were estimated :

- average dissimilarity amongst the regions within the abnormality area.
- average dissimilarity amongst the regions within the healthy area.
- average dissimilarity between the regions across the abnormality area and the healthy area.
- average dissimilarity between the region having the user tagged location and the rest of the regions within the abnormality area.
- average dissimilarity between the region having the user tagged location and the regions within the healthy area.

The graphs of Figures 5.27 and 5.28 show the above measures.

Making use of the above objective measures following criteria was used to differentiate benign from malignant abnormality :

- find the maximum average dissimilarity, measured between the cluster having the user tagged location (within the abnormality) and the clusters within the healthy region.
- the criteria for differentiating benign from malignant abnormality is as follows :
 - if the value of the above estimated measure is less than fifty percent then the abnormality is benign.
 - if the value of the above estimated measure is greater than fifty percent then the abnormality is malignant.

The graph shown in Figure 5.28 demonstrates how the above measure and the criteria is able to correctly classify the abnormality, under consideration, as benign.

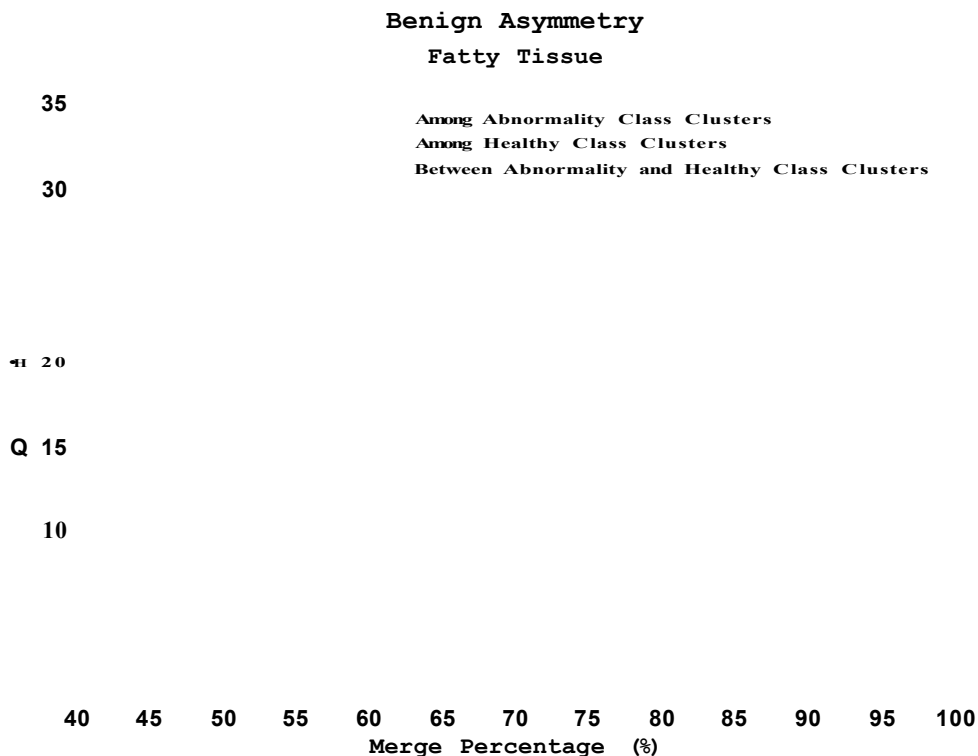


Figure 5.27 - For mini-MIAS Mammogram image (Image-ID mdb097) graph showing the dissimilarity amongst the clusters within the abnormality area and the healthy area and between the clusters within the abnormality and healthy areas.

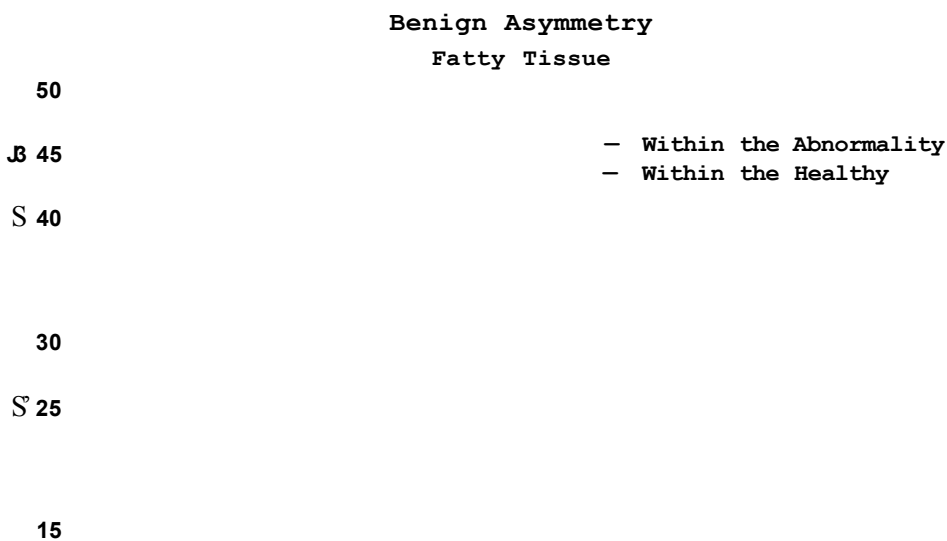


Figure 5.28 - For mini-MIAS Mammogram image (Image-ID mdb097) graph showing the dissimilarity between the cluster having the user tagged location and other clusters belonging to the abnormality area and the healthy area.

5.2.6. Necessity for the User Identified Healthy Region for the Correct Estimate of the Objective Measure

This section will discuss in detail the need and necessity for the user to select the region which will represent the healthy area around the abnormality. By means of the sample mammograms from mini-MIAS database (Image ID mdb083 and mdb090) it will be discussed how and why the performance of the objective measure, to differentiate malignant from benign abnormality, is affected by the choice of the healthy region by the user.

As it had been mentioned earlier the criteria to differentiate malignant from benign abnormalities is that the malignant abnormality will have markedly different characteristics from the surrounding healthy tissue. This difference may be due to the difference between their respective morphology. It is assumed that the image acquisition system is able to capture this difference in tissue characteristics as difference in image characteristics (image density values). Based on this assumption an objective measure was designed to measure the dissimilarity between the image characteristics of the abnormality with respect to the healthy region. This objective measure to estimate the difference in image characteristics of the abnormality from the surrounding healthy tissue was estimated as follows :

- estimate the average dissimilarity of the cluster, containing the user tagged location, within the abnormality with the clusters within the healthy region as the HCS process iterates to merge similar regions.

The above measure for a malignant case (mdb102) is plotted in Figure 5.24 and for a benign case (mdb097) is plotted in Figure 5.28. Comparing the two plots it can be seen that for the malignant case the estimated, maximum average, dissimilarity is markedly higher (above 65%). However, it should be ensured that this increase in dissimilarity is due to the abnormality being more dissimilar from the healthy tissue and not due to some extraneous data within the healthy area. One way to make sure that this is the case is to inspect the dissimilarity amongst the clusters within the healthy region. This, i.e. the dissimilarity amongst the clusters within the healthy region, should be found low. This is the case for the malignant case analysed in Section 5.2.5.1 as it can be seen from the plot in Figure 5.23. Hence, it can be inferred that the higher dissimilarity between the clusters within the abnormality and the healthy region is due to the inherent difference in characteristics of the abnormality and the healthy tissue.

In Sections 5.2.6.1 and 5.2.6.2 it will be shown that if the healthy region is not chosen adequately then the dissimilarity between the healthy region and the abnormality will not be estimated correctly.

5.2.6.1. Benign Case Getting Misclassified as Malignant

This section will discuss in detail how the inadequate choice of the healthy region of the image misclassified a benign abnormality as malignant. Further, it will be discussed how the misclassification was rectified by choosing a more appropriate healthy region to compare the abnormality region with.

Figure 5.29 (a) shows one of the mini-MIAS mammogram (Image ID mdb083). According to the information provided by the database the breast tissue type is of the fatty-glandular type and the abnormality belongs to asymmetric class and was benign. Based on the information provided the approximate boundary of the abnormality was found which is marked as a Red circle (Figure 5.29 a). A region of interest (marked Green in Figure 5.29 a) was marked circumscribing the abnormality and HCS process was applied within the ROI.

Based on the HCS process output the user selected the region corresponding to the abnormality which is shown in Red (Figure 5.29 b, c and d). The area within the approximate circular boundary other than the abnormality was considered as healthy, which is shown Green in colour (Figure 5.29 d). Rest of the area within the ROI is rejected, which is shown Blue in colour (Figure 5.29 d and e). Inspecting the HCS process output the user also tagged a location which was considered as the core of the abnormality.

c

e

Figure 5.29 - HCS processing of mini-MIAS mammogram mdb083.

The breast tissue type is fatty-glandular having an asymmetric class benign abnormality. Location of the abnormality circled in Green (a). HCS process delineated regions and their boundaries (b and c). Regions, and their boundaries, identified by the user as healthy (Green) and abnormal (Red) (d and e).

The HCS process was applied only to the pixel locations within the abnormality (Red Figure 5.29 d and e) and the healthy (Green Figure 5.29 d and e) areas of the image. As the HCS process proceeded to merge similar regions within the abnormality and the healthy areas, following measures were estimated :

- average dissimilarity amongst the regions within the abnormality area.
- average dissimilarity amongst the regions within the healthy area.
- average dissimilarity between the regions across the abnormality area and the healthy area.
- average dissimilarity between the region having the user tagged location and the rest of the regions within the abnormality area.
- average dissimilarity between the region having the user tagged location (within the abnormality) and the regions within the healthy area.

The graph plots of Figures 5.30 and 5.31 show the above measures.

Making use of the above objective measures following measure was used to identify whether the abnormality was malignant or benign :

- the maximum average dissimilarity, measured between the cluster having the user tagged location (within the abnormality) and the clusters within the healthy region was found.

Making use of the above measure following heuristic criteria was used to establish whether the abnormality was malignant or benign :

- if the value of the above estimated measure is less than fifty percent then the abnormality is benign.
- if the value of the above estimated measure is greater than fifty percent then the abnormality is malignant.

The above criteria established that the abnormality was malignant. Graph shown in Figure 5.31 demonstrates how the above measure and the criteria classified the abnormality, under consideration, as malignant.

But the abnormality was in fact benign. Thus in this case making use of the approximate boundary of the abnormality, to identify the healthy part, was not appropriate. This was the case because the approximate boundary is very close to the border of the breast tissue (Figure 5.29 a) and that part of the image, which is closer to the breast border, will be influenced by the background. One way to find out whether this is the case is to inspect the dissimilarity amongst the clusters within the

healthy region. This, i.e. the dissimilarity amongst the clusters within the healthy region, will be found high. This is the case as it can be seen from the plot in Figure 5.30. Hence it can be inferred that the higher dissimilarity between the clusters within the abnormality and the healthy region is due to the influence of the extraneous data from the background.. That is why, considering the part of the image within the approximate boundary, excluding the appropriately delineated abnormality region, as part of the healthy region (Green coloured Figure 5.29 d and e) did not give the required results.

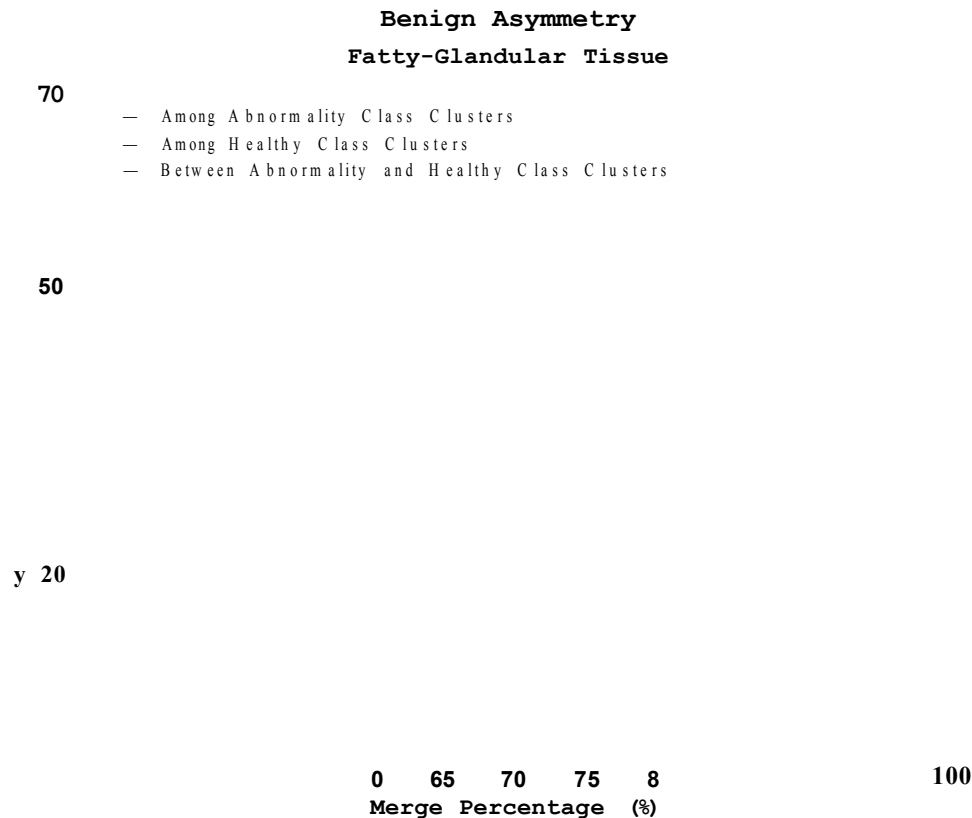


Figure 5.30 - For mini-MIAS Mammogram image (Image-ID mdb083) graph showing the dissimilarity amongst the clusters within the abnormality area and the healthy area and between the clusters within the abnormality and healthy areas.

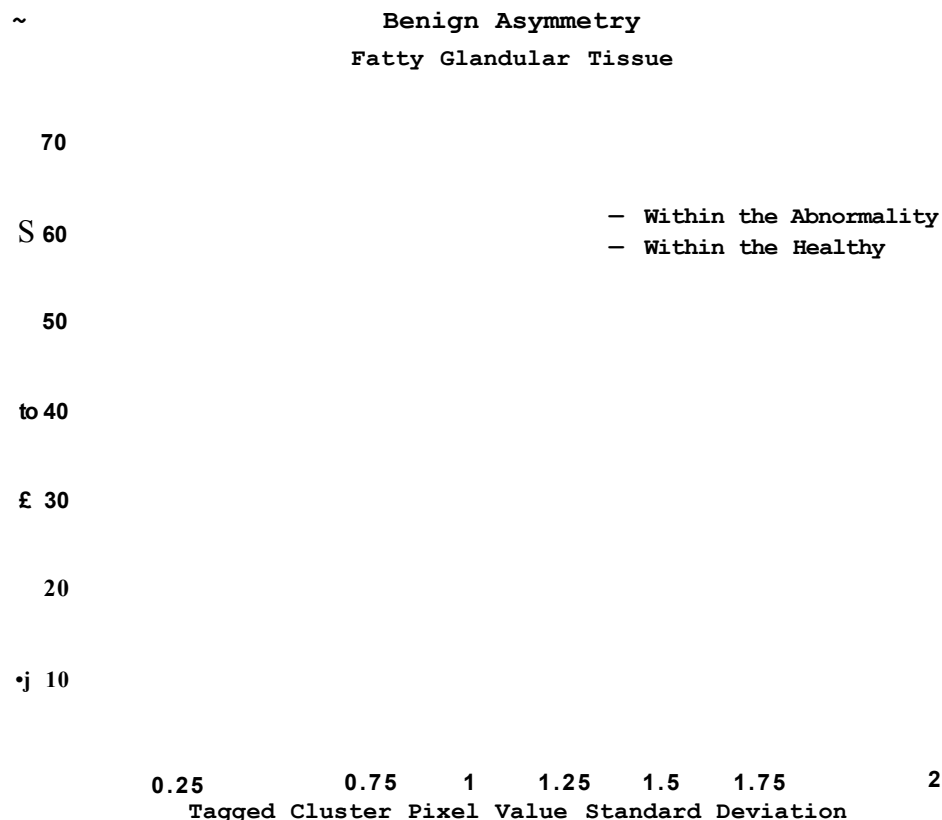


Figure 5.31 - For mini-MIAS Mammogram image (Image-ID mdb083) graph showing the dissimilarity between the cluster having the user tagged location and other clusters belonging to the abnormality area and the healthy area.

The inappropriateness of making use of the approximate boundary, to identify the healthy region, is illustrated in Figures 5.32 as detailed below.

Inclusion of the rest of the image, other than the abnormality, within the approximate boundary (Green coloured Figures 5.29 (d) and (e)) might include area of the image which might not be a proper representation of the healthy part. This fact is highlighted in the segmentation output in Figures 5.32 (a) to (f).

Figure 5.32 - HCS processing of mini-MIAS mammogram mdb083.
Of asymmetry class of benign abnormality in a fatty-glandular tissue.
HCS process intermediate output when there were 5 regions (a, b), 3 regions (c, d) and 2 regions (e, f) yet to be merged.

Figures 5.32 (a, b), (c, d) and (e, f) show the HCS process segmented regions and their boundary when there were five regions, three regions and two regions, respectively all yet to be merged. It can be seen from the segmentation output that the part of the image, coloured Yellow, is quite dissimilar from the rest of the image. This is evident from the fact that that part of the image remains as a separate region even when the rest of the regions have merged together Figure 5.32 (e, f).

Since the healthy part was considered as the rest of the image, other than the abnormality, within the approximate boundary (Green coloured Figures 5.29 (d) and (e)), the part of the highly dissimilar area of the image (Yellow coloured Figure 5.32 (e) and (f)) was also considered as part of the healthy region. This resulted in the healthy region being inhomogeneous. Thus the highly dissimilar part of the healthy region gave a false measure when the dissimilarity between the abnormality and the healthy region was calculated. This resulted in the benign abnormality being erroneously categorised as malignant.

To address the above issue it was decided to make use of the HCS output to identify the healthy region similar to identifying the abnormality region. This process is done as follows :

- the user, making use of their expert knowledge, identifies the segmentation output which adequately represents the border of the abnormality
- in the segmentation output identified above the user identifies the region or regions which adequately represent(s) the healthy part, as well.

Figures 5.33 (a), (b) and (c) illustrate the above process of identifying the healthy region. Figure 5.33 (a) shows the intermediate segmentation output, of HCS process, when there were fifteen regions yet to be merged. Making use of this segmentation the user first selects the contiguous region (Red) which will represent the abnormality (Figures 5.33 (a) and (b)). The user then selects the regions (Yellow and Green), which surround the abnormality, as the healthy part (Figures 5.33 (a) and (b)).

The above described process of selecting specific regions to represent the healthy part ensures that only relevant part of the image is considered. Consequently, the most dissimilar part of the image (Yellow) (Figure 5.32 (e) (f)) is automatically

excluded from the subsequent process to estimate the objective measure to differentiate malignant abnormality from benign abnormality.

a b c

Figure 5.33 - HCS processing of mini-MIAS mammogram mdb083.
Of asymmetry class of benign abnormality in a fatty-glandular tissue.
HCS Segmentation output when there were fifteen regions (a) and the border of the regions considered as abnormal (Red) and healthy (Yellow) (b).
The part of the image which is considered as the abnormality is shown in Red and the part of the image which is considered as the healthy region is shown in Yellow. Parts of the image not considered are coloured Green and Blue (c).

The homogeneity of the user selected healthy region could be established by inspecting the graph plotting the dissimilarity amongst the clusters within the healthy region. This, i.e. the dissimilarity amongst the clusters within the healthy region, will be found low. This is the case as it can be seen from the plot in Figure 5.34.

The graph of Figure 5.35 shows the the average dissimilarity of the cluster, containing the user tagged location, within the abnormality with the clusters within the user identified healthy region as the HCS process iterates to merge similar regions. From the plot it could be seen that the maximum average, dissimilarity is less than 50% thus correctly categorising the class of abnormality as benign.

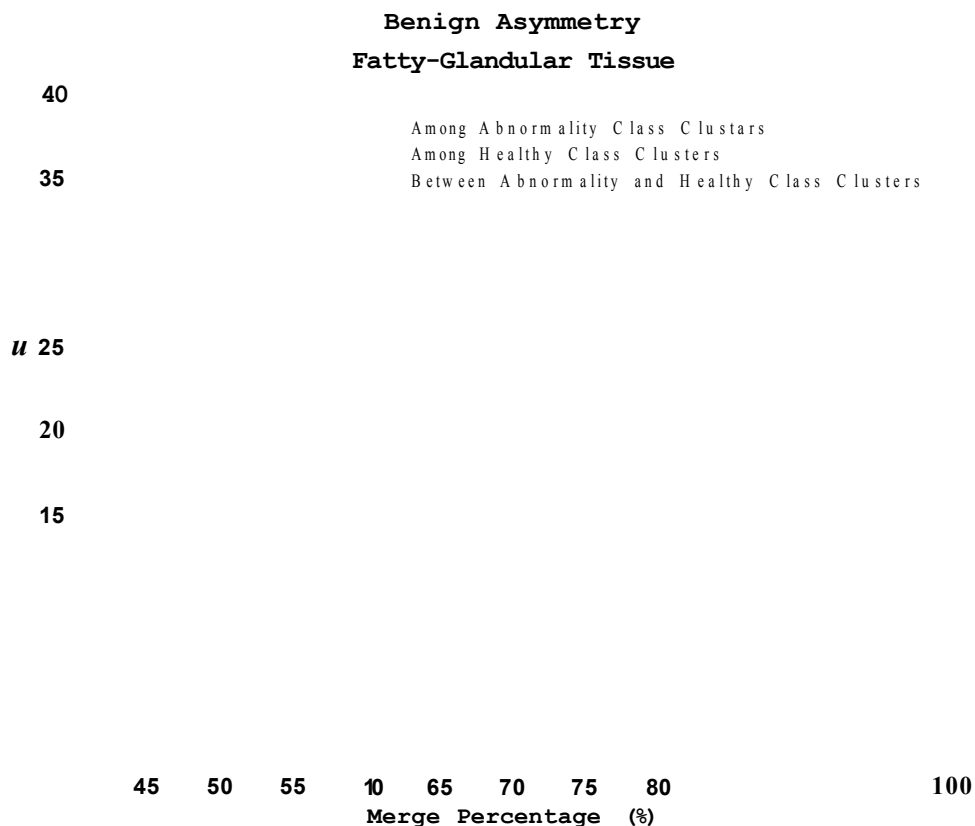


Figure 5.34 - For Image-ID mdb083 graph showing the dissimilarity amongst the clusters within the abnormality area, within the user identified healthy area and between the clusters within the abnormality and the user identified healthy areas.

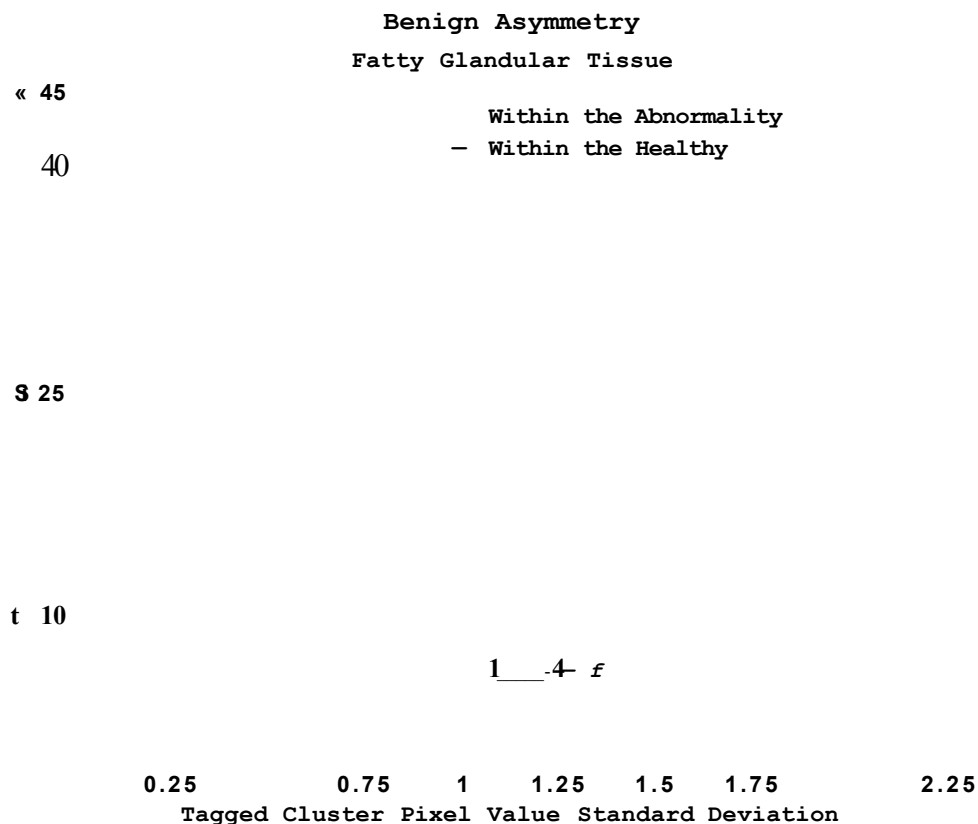


Figure 5.35 - For Image-ID mdb083 graph showing the dissimilarity between the cluster having the user tagged location and other clusters belonging to the abnormality area and the user identified healthy area.

5.2.6.2.Malignant Case Being Correctly Classified for All Wrong Reasons

As was discussed earlier, the criteria to differentiate malignant from benign abnormalities is that the malignant abnormality will have markedly different morphological characteristics from the surrounding healthy tissue. The image acquisition system should be able to represent this difference as difference in image characteristics (image density values). An objective measure was designed to make use of this dissimilarity, between the image characteristics of the abnormality with respect to the healthy region, to differentiate malignant from benign abnormalities. However, it should be ensured (made sure of) that this increase in dissimilarity is due to the abnormality being more dissimilar from the healthy tissue and not due to some extraneous data within the healthy area.

This section will discuss in detail how an inadequate choice of the healthy region of the image biased the measurement of the dissimilarity to be higher than it was actually. Furthermore, it will be discussed how the improper measurement was rectified by choosing a more appropriate healthy region to compare the abnormality region with.

Figure 5.36 (a) shows one of the mini-MIAS mammogram (Image ID mdb090). According to the information provided by the database the breast tissue type is of the fatty-glandular and the abnormality belongs to asymmetric class and was malignant. Based on the information provided the approximate boundary of the abnormality was found which is marked as a Red circle (Figure 5.36 a). A region of interest (marked Green in Figure 5.36 a) was marked circumscribing the abnormality and the HCS process was applied within the ROI.

Based on the HCS process output the user selected the region corresponding to the abnormality which is shown in Red (Figure 5.36 b, c and d). The area within the approximate circular boundary other than the abnormality was considered as healthy, which is shown Green in colour (Figure 5.36 d). The rest of the area within the ROI was rejected, which is shown Blue in colour (Figure 5.36 d and e). Inspecting the HCS process output the user also tagged a location which was considered as the core of the abnormality.

a

Figure 5.36 - HCS processing of mini-MIAS mammogram mdb090.
Of breast tissue type fatty-glandular having an asymmetric class malignant
abnormality. Location of the abnormality circled in Green (a).
HCS process delineated regions and their boundaries (b and c). Regions, and their
boundaries, identified by the user as healthy (Green) and abnormal (Red) (d and e).

The HCS process was applied only to the pixel locations within the abnormality (Red Figure 5.36 d and e) and the healthy (Green Figure 5.36 d and e) areas of the image. As the HCS process merged similar regions within the abnormality and the healthy areas, following measures were estimated :

- average dissimilarity amongst the regions within the abnormality area.
- average dissimilarity amongst the regions within the healthy area.
- average dissimilarity between the regions across the abnormality area and the healthy area.
- average dissimilarity between the region having the user tagged location (within the abnormality region) and the rest of the regions within the abnormality area.
- average dissimilarity between the region having the user tagged location and the regions within the healthy area.

The graphs of Figures 5.37 and 5.38 show the above measures.

Making use of the measure of the maximum average dissimilarity, measured between the cluster having the user tagged location (within the abnormality) and the clusters within the healthy region and the criteria that if the value of the measure is greater than fifty percent then the abnormality is malignant it can be established that the abnormality was malignant. The graph shown in Figure 5.38 demonstrates how the above measure and the criteria classified the abnormality, under consideration, as malignant.

But the issue with the above classification irrespective of the fact that the abnormality was correctly classified was that that part of the image which was identified as healthy with which the tagged location was compared was not homogeneous. This could be seen from the graph in Figure 5.37 where the average dissimilarities among the clusters within that part of the image which was considered as healthy, is above fifty percent.

Thus, in this case making use of the approximate boundary of the abnormality, to identify the healthy part, was not appropriate. This was the case because the approximate boundary is very close to the border of the breast tissue (Figure 5.36 a) and that part of the image, which is closer to the breast border, will be influenced by the background.

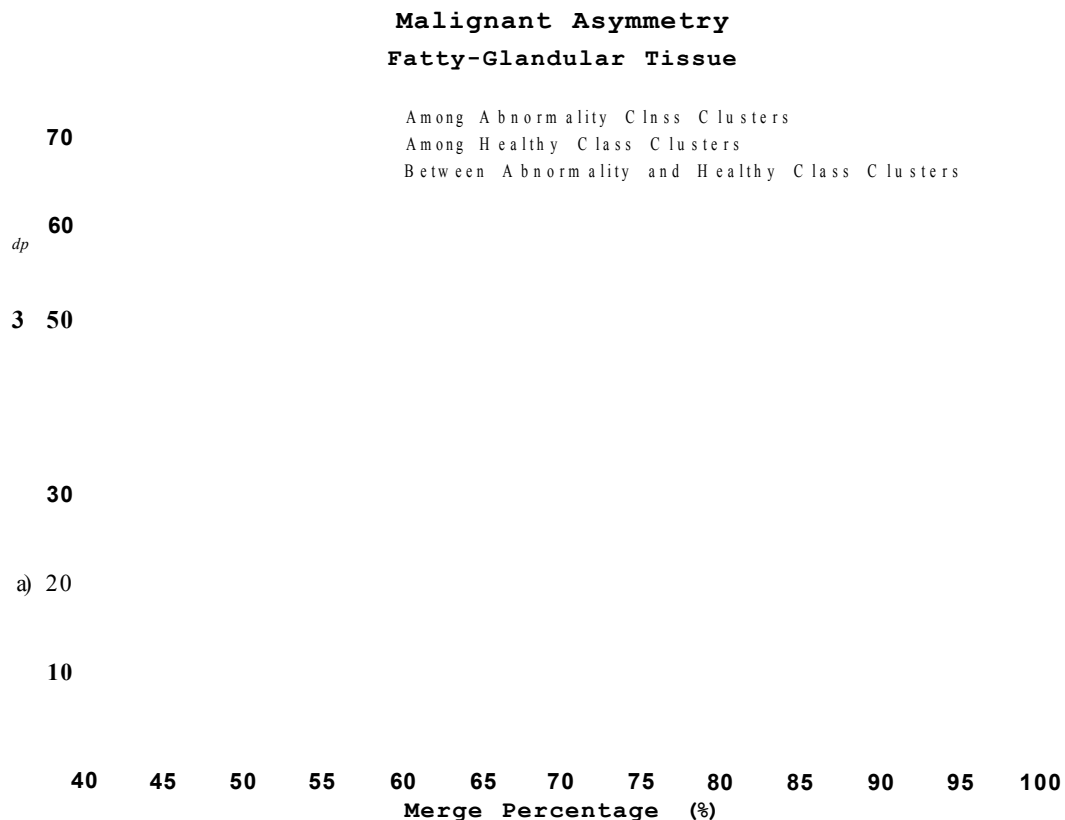


Figure 5.37 - For Image-ID mdb090 graph showing the dissimilarity amongst the clusters within the abnormality area and the user identified healthy area and between the clusters within the abnormality and the healthy areas.

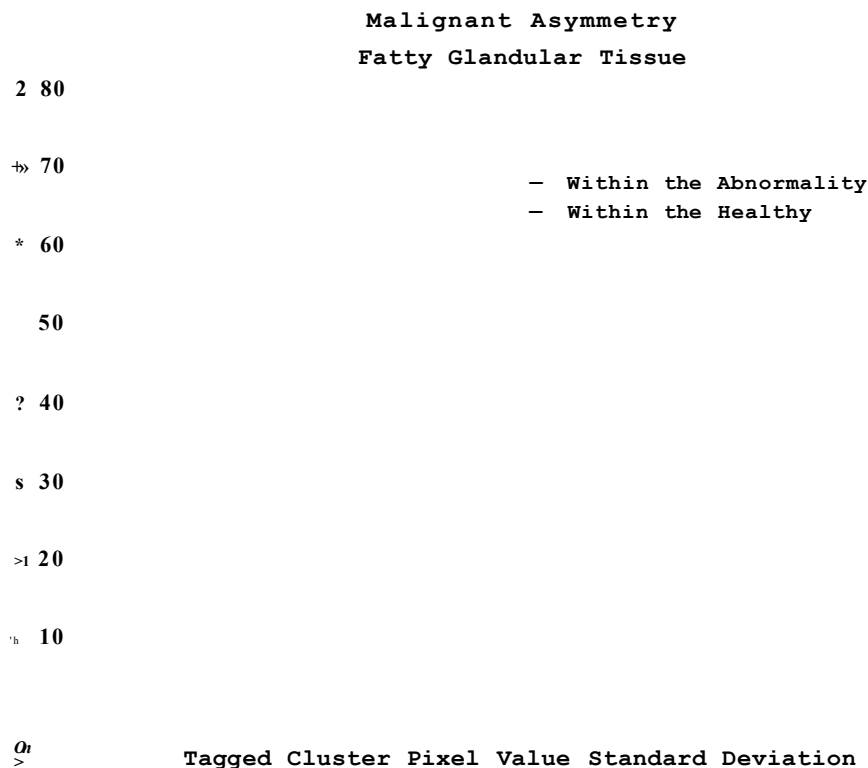


Figure 5.38 - For Image-ID mdb090 graph showing the dissimilarity between the cluster having the user tagged location and other clusters belonging to the abnormality area and the healthy area.

The inappropriateness of making use of the approximate boundary, to identify the healthy region, is illustrated in Figures 5.39. Inclusion of the rest of the image, other than the abnormality, within the approximate boundary (Figures 5.36 (d) and (e)) might include area of the image which might not be a proper representation of the healthy part. This fact is highlighted in the segmentation output in Figures 5.39 (a) to (f).

e

f

Figure 5.39 - HCS processing of mini-MIAS mammogram image mdb090.
Of asymmetry class of malignant abnormality in a fatty-glandular tissue.
Intermediate output when there were ten regions (a, b), five regions (c, d) and
three regions (e, f) yet to be merged.

Figures 5.39 (a, b), (c, d) and (e, f) show the HCS process segmented regions and their boundaries when there were ten regions, five regions and three regions respectively, yet to be merged. It can be seen from these segmentation output that the part of the image, coloured Yellow, is dissimilar from the rest of the image. This is evident from the fact that that part of the image remains as a separate region even when the rest of the regions have merged together (e, f).

Since the healthy part was considered as the rest of the image, other than the abnormality, within the approximate boundary (Figures 5.36 (d) and (e)), that part of the, highly dissimilar area of the, image was considered as part of the healthy region. This resulted in the healthy region being inhomogeneous. Thus, the highly dissimilar part of the healthy region gave a false (higher) measure, than the actual, when the dissimilarity between the abnormality and the healthy region was calculated.

To address the above issue it was decided to make use of the HCS output to identify the healthy region similar to identifying abnormality region. This process is done as follows :

- the user, via his/her expert knowledge, identifies the segmentation output which adequately represented the border of the abnormality
- in the segmentation output identified above the user identifies the region or regions which adequately represent(s) the healthy part, as well.

Figures 5.40 (a), (b) and (c) illustrate the above process of identifying the healthy region. Figure 5.40 (a) shows the intermediate segmentation output, of HCS process, when there were ten regions yet to be merged. Making use of this segmentation the user first selects the contiguous region (Red) which will represent the abnormality (Figures 5.40 (a) and (b)). The user then selects the region (Green), which surround the abnormality, as the healthy part (Figures 5.40 (a) and (b)).

The above described process of selecting specific regions to represent the healthy part ensures that only relevant part of the image is considered. Consequently the most dissimilar part of the image (Yellow) (Figure 5.39 (e) (f)) is automatically excluded from the subsequent process to estimate the objective measure to differentiate malignant abnormality from benign abnormality.

a

b

c

Figure 5.40 - Abnormal and healthy region for mini-MIAS mammogram mdb090.

Of asymmetry class of malignant abnormality in a fatty-glandular tissue.

HCS process segmentation output when there were ten regions (a) and the border of the regions considered for being abnormality (Red) and healthy (Green) (b).

The part of the image which is considered as the abnormality is shown in Red and the part of the image which is considered as the healthy region is shown in Green. Parts of the image not considered are coloured Yellow and Blue (c).

The homogeneity of the user selected healthy region could be established by inspecting graphs that show the dissimilarity amongst the clusters within the healthy region. The dissimilarity amongst the clusters within the healthy region, will be found to be low. This is the case as it can be seen from the plot in Figure 5.41.

The graph of Figure 5.42 shows the the average dissimilarity of the cluster, containing the user tagged location, within the abnormality with the clusters within the user identified healthy region as the HCS process iterates to merge similar regions. From the plot it can be seen that the maximum average, dissimilarity is still greater than 50% thus correctly categorising the class of abnormality as malignant.

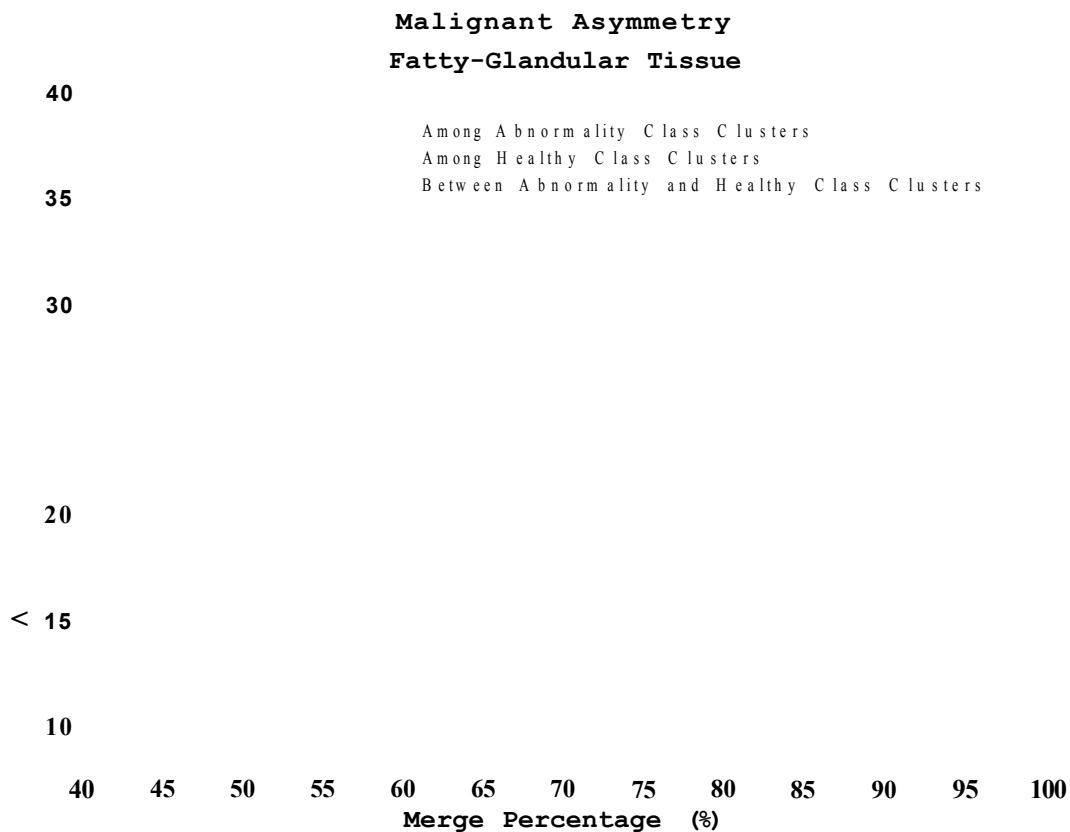


Figure 5.41 - For Image-ID mdb090 graph showing the dissimilarity amongst the clusters within the abnormality area and the user identified healthy area and between the clusters within the abnormality and the user identified healthy areas.

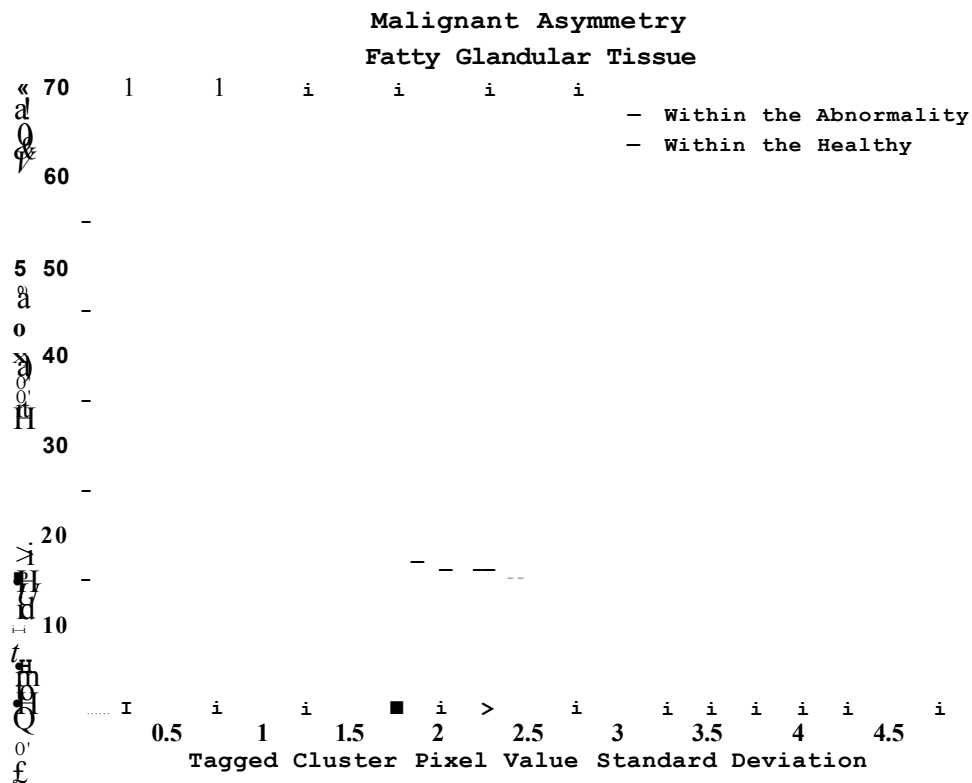


Figure 5.42 - For Image-ID mdb090 graph showing the dissimilarity between the cluster having the user tagged location and other clusters belonging to the abnormality area and the user identified healthy area.

5.3. Summary

In this chapter we discussed how the user can exploit the HCS process segmentation output to incorporate his/her decision process for the objective interpretation of the relevant information present in diagnostic images. This process of interleaving user decision seamlessly with the HCS processing of the diagnostic images to augment the diagnostic information present within the image data was demonstrated with the following application :

- HCS process aided interpretation of X-ray mammograms

Chapter Six will discuss how the above HCS aided interpretation can be subsequently used for the monitoring of physiological conditions. Specifically, the following HCS aided monitoring will be discussed in detail :

- HCS process aided monitoring of breast abnormalities.

Chapter 6 HCS Process Aided Disease Monitoring

6.1. Background

Diagnostic imaging is an invaluable tool in medicine today. Magnetic resonance imaging (MRI), computed tomography (CT), digital mammography, and other imaging modalities provide an effective means for non-invasively mapping the anatomy of a subject. These technologies have greatly increased knowledge of normal and diseased anatomy for medical research and are a critical component in diagnosis and treatment planning [Pham *et al.* 2000].

For example High-resolution computed tomography (HRCT) is the main diagnostic tool for small airways lesions. In the expiratory HRCT, there are four HRCT signs of small airways disease including limitations of air-trapping, intraluminal bronchial tree-in-bud, mosaic sign and bronchiolar lumen expansion [Vikgren *et al.* 2004]. Currently, doctors diagnose small airway disease by observing the signs and professional experience. But the lack of quantitative analysis of images made it difficult to observe objectively the signs changes of small airway disease [Xie *et al.* 2010].

But with the increasing size and number of medical images, the use of computers in facilitating their processing and analysis has become necessary [Pham *et al.* 2000]. For instance, in X-ray mammography Computer aided detection (CADe) systems address the problem that radiologists often miss signs of cancers that are retrospectively visible in mammograms. Furthermore, computer aided diagnosis (CADx) systems assist the radiologist in the classification of mammographic lesions as benign or malignant [Elter and Horsch 2009].

However, although CAD has some potential advantages it has also some important and potentially serious limitations. Philpotts based on his very recent investigation made the following suggestions to protect oneself from experiencing detrimental effects from the use of CAD in screening (mammographic) interpretation [Philpotts, 2009] :

- Never use CAD as a prescreener. The present sensitivity of CAD is not sufficient, and many cancers will be missed with this approach.
- Never use CAD as an initial step in mammogram interpretation. Again, for

the same reasons, if one concentrates primarily on areas that CAD has marked, many important findings may be missed.

- Interpret mammograms as usual, and only use CAD as a last step in a reading protocol. Do not decide not to recall a patient for a finding just because it is not marked by CAD.
- It may be worth considering that if one finds that CAD is consistently marking findings that the reader had not recognized initially and that appear important (i.e., potentially worthy of recall) that the reader should maybe step away from reading for a rest until his or her acuity has resumed.

The above discussion highlights the following observation, which has been mentioned earlier (in this Thesis report). That is, computing systems are more consistent in their perceiving (i.e. processing, outlining the image components and objectively measuring the image properties) ability but they cannot match human interpretive skills. Drawing a line so as to limit the system's interpretive function has the virtue of achieving a complementary synthesis of system and radiologists' strengths [Claridge 1997].

Hence, in this study a novel alternative system (in relevance to monitoring Cystic Fibrosis and breast abnormalities), namely computer aided monitoring (CAM) system is designed and implemented. The designed CAM system leverages the perceiving ability of the computing systems to augment the human interpretive skills.

The applicability and the performance of the designed CAM system were evaluated by using the designed CAM process in the following two medical diagnostic environment :

- Making use of the computing system to quantitatively measure the dimensions of the airway and the adjoining blood vessel, by processing the CT images of the lungs (Chapter 4 Section 4.3.10).

This is to assist the radiologists in their interpretation, of the CT images, for the presence or absence of conditions for CSF by monitoring the dilation of the airway lumen and the thickening of airway wall (Chapter 6 Section 6.2).

- Making use of the computing system to perceive the more appropriate boundaries of the abnormal and healthy regions, by processing digital X-ray mammograms (Chapter 5 Section 5.2.4.1) and to quantitatively measure the

dissimilarity between the abnormal region and the healthy region (Chapter 5 Section 5.2.5).

This is to assist the radiologists in their interpretation, of the X-ray mammograms, to differentiate malignant from benign type of breast abnormalities by monitoring suspicious locations in X-ray mammograms [Selvan *et al.* 2011] (Chapter 6 Section 6.3).

The rest of this chapter will provide the details of how the applicability and the performance of the designed CAM system were evaluated with the respect to the above listed applications, that are :

- Computer aided monitoring of the dilation of the airway lumen and the thickening of airway wall in the CT images of the lungs.
- Computer aided monitoring of the abnormalities in X-ray mammograms to differentiate malignant from benign types.

6.2. Computer Aided Monitoring of the Dimensions of the Airway and the Accompanying Blood Vessel

In Chapter 4 (Section 4.3) it was discussed in detail how HCS may be used to quantitatively measure the dimensions of the airway and the accompanying blood vessel. The performance and the probable use of that HCS based measuring process was evaluated by means of the following two approaches :

- applying the method on cases of known diagnosis
- correlating the HCS process based measure with that of an expert's.

The rest of this section will discuss in detail the above two approaches of validation of the HCS process's performance.

In Chapter 4 (Section 4.3) the different “user guided” methods developed to measure the dimensions of the airway and the accompanying blood vessel were discussed in detail. Of the different methods developed, the following are the methods which were used for each of the above two validation processes :

- for the validation method based on cases of known diagnostic
the user guided segmentation method, which made use of initial user tagged information of pixel locations as belonging to the corresponding anatomical locations (Chapter 4 Section 4.3.5.2.) was used
- for the validation method based on expert's measurement

the user guided segmentation method, which made use of user tagged boundary locations around the individual anatomy (Chapter 4 Section 4.3.10.) was the one which was used.

6.2.1. HCS Process Based Quantitative Measure of the Airway and the

Accompanying Blood Vessel Dimensions for Cases of Known Diagnosis

For this validation approach the CT image data of the same patient, for whom CT images were taken during the year 2007 and subsequently during the year 2009, were used. Based on clinical findings the patient was diagnosed healthy during the year 2007, but was diagnosed with the CF condition during the year 2009. The validation of the HCS process based measurement was carried out on the basis how the measured dimensions were in consensus with the clinically known diagnosis.

6.2.1.1. HCS Process Based Quantitative Measure of the Airway and the

Accompanying Blood Vessel Dimensions for a Healthy Case

Figure 6.1 shows the CT image of the healthy case. The image is displayed by mapping Hounsfield values from (-) 1024 to 676 to 256 levels of grey scale values. Region of interests (ROI) around two locations having a airway and an accompanying blood vessel were marked. The ROI on the left lung (Figure 6.1 a) is bound with regular boundaries. The location on the right side lung (Figure 6.1 b) has two blood vessels adjoining to the airway. Hence a hand drawn boundary was drawn around to include only one of the blood vessel and exclude the other (Figure 6.1 b) .

Figure 6.2 shows the details of the processing of the ROI on the left side lungs. Figure 6.2 (a) shows the CT image data within the ROI. The user tagged (marked) certain pixel locations, within the ROI, as belonging to the corresponding anatomical regions (Figure 6.2 b). The Red coloured pixels are the ones tagged by the user as belonging to the Blood-Vessel. Similarly, the Green ones are that of the Airway-Wall, Blue ones belong to Airway-Lumen and Yellow ones belong to lung parenchyma (tissue). The locations, within the ROI, which were left untagged by the user can be seen as White coloured (Figure 6.2 b).

Making use of the user tagged locations the HCS process segmented the part of the image within the ROI as belonging to the four different regions, namely Blood-Vessel, Airway-Wall, Airway-Lumen and lung parenchyma (Figure 6.2 c).

Figure 6.1 - CT Image data for the healthy case.
The image is displayed by mapping Hounsfield values from (-) 1024 to 676 to 256 levels of grey scale values.
Two locations having airway and adjoining blood vessel are marked.
The ROI (10x14) on the left lung (a) has regular boundaries while the ROI on the right lung (b) has a hand drawn boundary.



Figure 6.2 - Processing details of the ROI on the left lung (Figure 6.1 a).
CT image data (ROI 10x14), ranging from (-) 1024 to 676 Hounsfield values, mapped to 256 level of grey levels (a).
User tagged locations, Blood-Vessel (Red) Airway-Wall (Green), Airway-Lumen (Blue), Lung parenchyma (Yellow) and Untagged pixel location (White) (b)
Segmentation of the four regions, Blood-Vessel (Red) Airway Wall (Green), Airway-Lumen (Blue), lung parenchyma (Black) (c)

Making use of the initial segmentation (Figure 6.2 c) as an approximation, the best fitting elliptical boundaries were fitted around the Blood-Vessel, the Airway-Wall and the Airway-Lumen (Chapter 4 Section 4.3.7). Figure 6.3 and Table 6.1 show the quantitative measures of the major axis and the minor axis of the fitted ellipses for the three major anatomies, namely Blood-Vessel, Airway-Wall and Airway-Lumen, present within the regular ROI in the left lung (Figure 6.1. a).

Figure 6.3 - Minor and Major axis of the fitted ellipses to the Blood-Vessel (a), Airway-Wall (b) and Airway-Lumen (c).

Table-6.1 - Minor and Major axis dimensions (in pixels) of the fitted ellipse to the boundary of the Blood-Vessel, Airway-Wall and Airway-Lumen (Figure 6.3)

	Blood-Vessel (VD)	Airway- Wall	Airway- Lumen (ALD)	Airway-Wall Thickness (AWT)	ALD:VD
Minor Axis	5.45	6.49	2.86	3.63	0.52
Major Axis	7.64	6.99	3.58	3.41	0.47
Average	6.55	6.74	3.22	3.52	0.50

A very similar process to what was discussed above was applied to the location identified on the right lung (Figure 6.1 b). The only difference was that the boundary of the ROI, instead of being a regular shaped ROI, was a hand drawn boundary drawn around the Airway and the accompanying Blood-Vessel (Figure 6.1 b). The necessity for the hand drawn boundary was to avoid an adjoining Blood-Vessel and to isolate only one pair of Airway and the accompanying Blood-Vessel.

Figure 6.4 illustrates the details of the HCS process based segmentation processing done to objectively measure the dimensions of the Airway and the Blood-Vessel within the hand drawn boundary on the right side lungs.

Figure 6.5 and Table 6.2 show the quantitative measures of the major axis and the minor axis of the fitted ellipses for the three major anatomies, namely Blood-Vessel, Airway-Wall and Airway-Lumen, present within the hand drawn ROI in the right lung (Figure 6.1 b).

a b c

**Figure 6.4 - HCS process based segmentation details within the hand drawn boundary on the right lung (Figure 6.1 b).
CT image data (ROI 20x21), ranging from (-) 1024 to 676 Hounsfield values, mapped to 256 level of grey levels (a).
User tagged locations, Blood-Vessel (Red) Airway-Wall (Green), Airway-Lumen (Blue), lung parenchyma (Yellow) and Untagged pixel location (White) (b)
Segmentation of the four regions, Blood-Vessel (Red) Airway-Wall (Green), Airway-Lumen (Blue) and lung parenchyma (black) (c)**

a b c

Figure 6.5 - Minor and Major axis of the fitted ellipse to the Blood-Vessel (a), Airway-Wall (b) and Airway-Lumen (c).

Table-6.2 - Minor and Major axis dimensions (in pixels) of the fitted ellipse to the boundary of the Blood-Vessel, Airway-Wall and Airway-Lumen (Figure 6.4)

	Blood-Vessel (VD)	Airway- Wall	Airway- Lumen (ALD)	Airway-Wall Thickness (AWT)	ALD:VD
Minor Axis	5.87	6.11	3.45	2.66	0.59
Major Axis	8.71	7.10	5.22	1.88	0.60
Average	7.29	6.61	4.34	2.27	0.60

6.2.I.2. HCS Process Based Quantitative Measure of the Airway and the Accompanying Blood Vessel Dimensions for a CF Case

Figure 6.6 shows the CT image of the the same patient when he/she was diagnosed, after two years, as having CF. The image is displayed by mapping Hounsfield values from (-) 1024 to 77 to 256 levels of grey scale values. One region of interests (ROI)

around a location having a airway and an accompanying blood vessel was marked in the left lungs.

Figure 6.6 - CT Image data for the Cystic Fibrosis diagnosed case.
The image is displayed by mapping Hounsfield values from (-) 1024 to 77 to 256 levels of grey scale values.
One location having Airway and and accompanying Blood-Vessel is shown marked with a ROI (18x12) having regular borders.

A very similar process to what was discussed in the earlier section (Section 6.2.1.1) was applied to the location identified on the left lung (Figure 6.6). Figure 6.7 illustrates the details of the HCS process based segmentation processing done to objectively measure the dimensions of the Airway and the Blood-Vessel within the ROI on the left side lungs (Figure 6.6).

Figure 6.7 - CT image data within the ROI (18x12) marked in the left lungs of Figure 6.6.
(a) The original pixel values range from (-) 1024 to 77 Hounsfield, which are mapped to 256 level of grey levels.
(b) User tagged locations, marking Blood-Vessel (Red), Airway-Wall (Green), Airway-Lumen (Blue), lung parenchyma (Yellow) and Untagged pixel location (White).
(c) HCS process segmentation of the four regions, namely Blood-Vessel (Red) Airway-Wall (Green), Airway-Lumen (Blue), lung parenchyma (Black).

To evaluate the performance of the HCS process based measurement of the Blood-Vessel and the Airway to differentiate the healthy and the CF case one of the measures from the following set of criteria, based on the study by Long *et al.* [Long *et al.*, 2004] was made use of.

In infants with CF the mean AWT (+/-SD) was 0.58+/-0.13 mm, the ALD was 1.31+/-0.56 mm, and the VD was 1.62+/-0.58 mm. In control infants, the mean AWT was 0.49+/-0.13 mm, the ALD was 1.07+/-0.42 mm, and the VD was 1.86+/-0.64 mm. The mean AWT and ALD were greater in children with CF than in normal subjects ($P<.001$). The ALD:VD ratios increased with age in patients with CF compared with control subjects ($P=.026$). Where AWT is the Airway-Wall thickness, ALD is the Airway-Lumen diameter and VD is the Blood-Vessel diameter.

Of the above set of criteria following relative measures were considered

- Mean AWT and ALD were greater in children with CF than in normal subjects ($P<.001$).
- the ALD:VD ratios increased with age in patients with CF compared with control subjects.

The reason for choosing the above two criteria is as follows :

- the chosen criteria are not absolute measures rather they are relative measures hence one can avoid the issue of variability and standardisation and limited sample size.

Table-6.4 – The relative measures for the two cases

<i>Case Type</i>	Airway-Wall Thickness (AWT)	Airway-Lumen (ALD)	ALD:VD
Healthy	2.90	3.78	0.55
CF	4.95	2.75	0.52

Table 6.4 lists the measures for the healthy and the CF cases. Making use of the above two relative criteria following observations can be deduced :

- the Airway-Wall thickness is the only measure which has shown marked increase between the time when the patient was healthy to the time when he/she developed CF.
- the Airway-Lumen has decreased while the ratio between the Airway-Lumen and the Blood-Vessel dimensions has remained almost the same.

The above detailed process of correlating the HCS process based objective measurement, of the dimensions of the Airway and the accompanying Blood-Vessel, with that of the clinical findings was severely hampered by the lack of suitable test cases. Hence, it was decided to expand the study by comparing the HCS process based objective measurements with that of an expert's for a larger number of cases. In the next section (Section 6.22) it will be described in detail how the HCS process based objective measurements were compared with that of an expert's.

6.2.2. Correlating the HCS Process Based Objective Measurements with that of an Expert

For this validation approach CT image data of eleven patients, were used. The validation of the HCS process based measurement was done on the basis how the HCS process's objectively measured dimensions were in consensus with that of an expert's.

The following is the protocol which was followed for this part of the study :

- the radiologist chose eleven test cases for whom a High Resolution Computed Tomographic (HRCT) study had been done.
- the HRCT image data, in DICOM format, of each of the patient was written onto individual optical discs (CD) after removing the personal details which might identify the patient. That is the image data was anonymised.
- for each of the patient the location of a Airway with the accompanying Blood-Vessel in a suitable section was identified by the radiologist and conveyed to the investigator.
- the radiologist, in private, measured the dimensions of the Airway and the Blood-Vessel making use of the measuring tool (electronic calliper) provided by the CT image viewer program provided in the PACS (Picture Archiving and Communication System) workstation (Figure 6.9).
- independently the HCS process based measurement was carried out on the locations identified by the radiologist.
- the measurements carried out both by the radiologist and the HCS process were then compared.

Figure 6.9 - Screen capture of the GUI similar to one used by the radiologist to manually measure the dimensions of the Airway and the accompanying Blood-Vessel

6.2.2.I. HCS Process Based Objective Measure of the Dimensions of the Airway and the Accompanying Blood-Vessel for the Test Cases

Figures 6.10 A and B (first column) show the part of the image having an airway with the accompanying blood vessel. It can be seen that for all the eleven cases the accompanying blood vessel is attached to the airway. Also, it can be seen that for most of the cases the dimensions of the blood vessel is around five pixels. For these reasons it was found that segmentation of airway and the accompanying blood vessel making use of the tagged boundary locations just around the individual anatomy (viz. blood vessel and the airway wall) (Please see Chapter 4 Section 4.3.10) was found to be not feasible. Hence, the alternative method of making use of initial user tagged information (Please see Chapter 4 Section 4.3.5.2) was followed. Figures 6.10 A and B (second column) show the user tagged locations for each of the eleven cases. It should be noted that the tagged locations was provided by the author.

Case ID Part of the Image within the ROI User Tagged Locations

Case 01

Case 03

Case 04

IV
(

Case 05

Case 06

Case 07

Figure 6.10 (A) - Images showing the part of the image within the ROI surrounding an Airway and the adjoining Blood Vessel and the user tagged locations identifying background (Yellow) Airway Lumen (Blue), Airway Wall (Green) and Blood Vessel (Red).

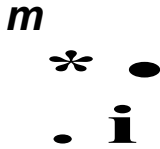



<i>Case ID</i>	<i>Part of the Image within the ROI</i>	<i>User Tagged Locations</i>
Case 08		
Case 09		
Case 11		
Case 12		
Case 13		

Figure 6.10 (B) - Images showing the part of the image within the ROI surrounding an Airway and the adjoining Blood Vessel and the user tagged locations identifying background (Yellow) Airway Lumen (Blue), Airway Wall (Green) and Blood Vessel (Red).

Making use of the user tagged information the HCS process extracted the boundaries of the blood vessel, airway wall and the airway lumen. The boundaries of the anatomies were approximated by Fitting ellipses to the respective boundary locations (Please see Chapter 4 Section 4.3.7.1). Figures 6.11 (A) and (B) show the major and minor axes of the fitted ellipses for the three anatomies for the eleven cases.





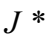

<i>Case ID</i>	<i>Dimensions of the Blood Vessel</i>	<i>Dimensions of the Airway Lumen</i>	<i>Dimensions of the Airway Wall</i>
Case 01			
	Minor = 3.6, Major = 5.2		Minor = 6.0, Major = 6.9
Case 03			
	Minor = 4.2, Major = 6.8	Minor = 1.9, Major = 2.4	Minor = 7.4, Major = 9.8
Case 04			
	Minor = 4.2, Major = 5.3	Minor = 1.0, Major = 1.6	Minor = 6.1, Major = 6.6
Case 05			
	Minor = 3.6, Major = 5.4	Minor = 3.9, Major = 6.6	Minor = 8.5, Major = 13.0
Case 06			
	Minor = 3.6, Major = 5.3		Minor = 4.8, Major = 6.3
Case 07			
	Minor = 5.5, Major = 6.6	Minor = 3.0, Major = 3.	Minor = 6.3, Major = 8.

Figure 6.11 (A) - Images showing the major and minor axes of the ellipses fitted around Blood Vessel (Red), Airway Lumen (Blue) and Airway Wall (Green).

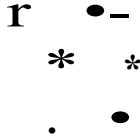


<i>Case ID</i>	<i>Dimensions of the Blood Vessel</i>	<i>Dimensions of the Airway Lumen</i>	<i>Dimensions of the Airway Wall</i>
Case 08			
	Minor = 3.6, Major = 5.2	Minor = 0, Major = 1.3	Minor = 6.0, Major = 7.9
Case 09			
	Minor = 4.3, Major = 5.0	Minor = 2.1	Minor = 6.5, Major = 7.7
Case 11			
	Minor = 6.3, Major = 7.2	Minor = 2.2, Major = 4.4	Minor = 7.2, Major = 12.0
Case 12			
	Minor = 2.3, Major = 3.5		Minor = 6.0, Major = 7.6
Case 13			
	Minor = 4.4, Major = 6.2	Minor = 3.7, Major = 5.0	Minor = 6.1, Major = 13.6

Figure 6.11 (B) - Images showing the major and minor axes of the ellipses fitted around Blood Vessel (Red), Airway Lumen (Blue) and Airway Wall (Green).

For some of the cases the axes for lumen cannot be estimated (Figure 6.11 A and B). since the region comprising the lumen had less than five pixel locations.

6.2.2.2. Comparing HCS Process Based Objective Measure with that of the Radiologist's Manual Measure

Similar to what was carried out for the earlier cases the dimensions of the major and minor axes were averaged. The cases for which the major and minor axes of the lumen were not estimated were left out. Table 6.5 lists the estimated dimensions of the anatomies in pixels. Table 6.6 lists the manual measurements, in millimetre, carried out by the expert.

Table-6.5 – HCS process based objective measure of the dimensions of the anatomies in pixels

Case ID	Airway Wall Outer Diameter	Airway-Lumen (ALD)	Airway-Wall Thickness (AWT)	Blood Vessel Diameter (VD)	ALD:VD
3	8.6	2.15	6.45	5.5	0.39
4	6.35	1.3	5.05	4.75	0.27
5	10.75	5.25	5.5	4.5	1.17
7	7.2	3.05	4.15	6.05	0.5
9	7.1	2.1	5	4.65	0.45
11	9.6	3.3	6.3	6.75	0.49
13	9.85	4.35	5.5	5.3	0.82

Table-6.6 – Measurements by the expert in millimetre

Case ID	Airway Wall Outer Diameter	Airway-Lumen (ALD)	Airway-Wall Thickness (AWT)	Blood Vessel Diameter (VD)	ALD:VD
3	4.3	2.2	2.1	2.9	0.76
4	4.0	1.8	2.2	3.1	0.58
5	5.3	2.9	2.4	2.6	1.12
7	3.6	1.8	1.8	3.2	0.56
9	3.3	2.1	2.1	2.4	0.88
11	3.5	1.6	1.6	1.6	1.0
13	4.5	2.6	2.6	3.2	0.81

For the following reasons one cannot compare directly the measurements attained through the software with that of the expert's manual measurements.

- measurements attained through the SW is in pixels, while the measurements attained by the expert in millimetre.
- one is not very sure that the locations, where the measurements are done, are exactly the same.

But since the measurements are done by both the SW and the expert for the same patient at the same image slice (section) and approximately at the same location one can compare the relative measurements.

Based on the study by Long *et al.* [Long *et al.*, 2004] Airway Wall Thickness (AWT) and Airway Lumen Diameter (ALD) were greater in children with Cystic Fibrosis (CF) than in normal subjects ($P < .001$). If VD is the Blood Vessel diameter then ALD:VD ratios increased with age in patients with CF compared with control subjects ($P = .026$). Hence one can compare the ratio ALD:VD.

Comparing the ratio ALD:VD obtained through the HCS process with that of the expert's manual measurement it can be seen that for three cases (out of seven) the measurements almost corresponds to each other.

6.2.2.3. Critical evaluation of the Results

The original plan for the study was not to compare the estimated measurements of the HCS process with those of the expert's. The original plan was to find out how well the HCS process based measures could be used to monitor the presence or absence of CF. With that as the intention originally twenty cases of known diagnosis were identified. But unfortunately the CT equipment was upgraded and those cases were no more available in anonymised form. Hence, the current set of cases of patients for whom CT images were acquired for any medical condition were collected. Since for these cases the medical conditions could be anything the study was reformulated to compare the measurements obtained by the HCS process with that of the expert.

Once again for these cases it was found that the image data had conflicting Hounsfield values which surprised the expert as well. Hence, one cannot attribute too much to these results. The only conclusion that could be confidently made was that the HCS process was robust enough to handle even noisy data.

Since three cases of known diagnosis were processed it was decided to plot the values of Airway Wall Thickness (AWT), Airway Lumen Diameter (ALD) and the ratio ALD:VD where VD is the blood vessel diameter for the earlier three cases along with the seven cases of unknown diagnosis.

Table 6.7 lists the measures for the three cases of known diagnosis estimated in the earlier sections. Table 6.8 lists the measures for the seven cases of unknown medical conditions.

Table-6.7 – The measures for the three cases of known diagnosis

Diagnosis	Airway-Wall Thickness (AWT)	Airway-Lumen (ALD)	Blood Vessel Diameter (VD)	ALD:VD
Healthy	2.90	3.78	6.92	0.55
CF	4.95	2.75	5.25	0.52
CF	5.18	5.77	3.8	1.52

Table-6.8 – The measures for the seven cases of unknown diagnosis

Case ID	Airway-Wall Thickness (AWT)	Airway-Lumen (ALD)	Blood Vessel Diameter (VD)	ALD:VD
3	6.45	2.15	5.5	0.39
4	5.05	1.3	4.75	0.27
5	5.5	5.25	4.5	1.17
7	4.15	3.05	6.05	0.5
9	5	2.1	4.65	0.45
11	6.3	3.3	6.75	0.49
13	5.5	4.35	5.3	0.82

Figure 6.12 shows the relevant plot. Inspecting the plot it can be seen that the healthy case is clearly separate from the rest. The CF cases are close to each other. The other cases are closer to CF cases but spread all over indicating that they may have some problems with their lungs.

From the above discussion it could be inferred that HCS process based CAM system has the potential to monitor the presence or absence of CF. But it is impertinent that the image data provided does not have conflicting values. With the advent of multi-detector row CT (MDCT) scanner, and given the higher resolution of the MDCT images and it's possible better sensitivity, when compared to the HRCT images used for this study, the performance of the designed CAM system in segmenting the airways and the accompanying blood vessels will improve.

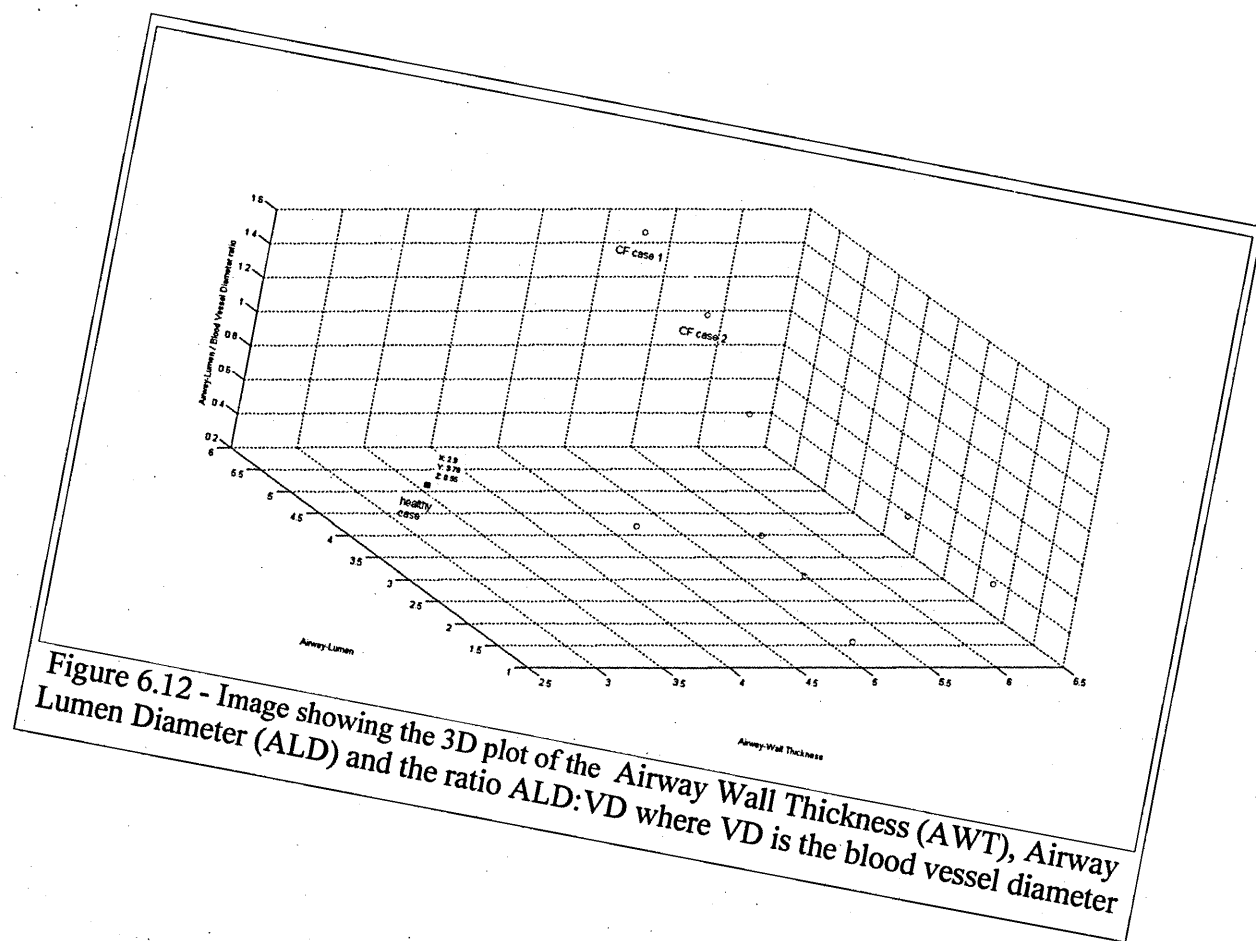


Figure 6.12 - Image showing the 3D plot of the Airway Wall Thickness (AWT), Airway Lumen Diameter (ALD) and the ratio ALD:VD where VD is the blood vessel diameter

6.3. Computer Aided Monitoring of Abnormalities in X-ray Mammograms

X-ray mammography is regarded as the most effective tool for the detection and diagnosis of breast cancer, but the interpretation of mammograms is a difficult and error prone task. Computer aided detection (CADe) systems address the problem that radiologists often miss signs of cancers that are retrospectively visible in mammograms. Furthermore, computer aided diagnosis (CADx) systems assist the radiologist in the classification of mammographic lesions as benign or malignant [Elter and Horsch 2009].

This study implements and evaluates a novel alternative system namely Computer Aided Monitoring (CAM) system. The medical professional can use the designed CAM system to objectively measure the properties of a suspected abnormal area in a mammogram. Thus it can be used to assist the medical professional to objectively monitor the abnormality. For instance, its response to treatment and consequently its prognosis.

The major limitations of the current CAD(e/x) systems are two fold, firstly the way the systems are trained and secondly the way the systems are used. The limitation of the training process is that the training samples might have had features associated with symptomatic lesions. In the actual usage environment the abnormalities might have less obvious mammographic features than symptomatic lesions. Consequently, this might lead to false negative rate of up to 25% [Bazzocchi *et al.*, 2007]. The limitation during the usage is that the thresholding, learnt by the CAdE system during the training, may not be appropriate for the actual image data under consideration. Consequently, most of the CAD prompts are false positive calls which leads to needless breast biopsies [Rossand *et al.*, 2010].

In the HCS based CAM system, designed in this study, the above issues were addressed as follows :

- The designed CAM system does not need any prior training. Since the HCS process, on which it is based, is an unsupervised segmentation process.
- The designed system does not use a fixed thresholding to differentiate the abnormalities from the healthy tissue, rather it uses an adaptive measure adapted to the actual mammogram data being analysed.

A brief description of the implementation of this CAM system is as follows : Using the approximate location and size of the abnormality, obtained from the user, the HCS process automatically identifies the more appropriate boundaries of the different regions within a region of interest (ROI), centred at the approximate location. From the set of, HCS process segmented, regions the user identifies the regions which most likely represent the abnormality and the healthy areas. Subsequently, the CAM system compares the characteristics of the user identified abnormal region with that of the healthy region; to differentiate malignant from benign abnormality.

The measuring of the dissimilarity between the abnormality and the healthy region involves the following three steps :

- appropriate delineation of the boundary of the abnormality (Chapter 5 Section 5.2.4.1).
- identifying the region of the image comprising the healthy part (Chapter 5 Section 5.2.4.2).
- measuring the dissimilarity between the abnormality and the healthy region (Chapter 5 Section 5.2.4.3)

The details of how the above three listed steps were implemented is discussed in detail in the Chapter 5 in Sections 5.2.4.1, 5.2.4.2 and 5.2.4.3, respectively. In this section the performance of the implemented CAM process, to differentiate the malignant from benign type of abnormalities, will be compared with that of a human expert.

For this validation process X-ray mammogram data of sixteen patients, from the mini-MIAS mammographic database [Suckling *et al.*, 1994], were used. The findings provided by the mammographic database for each of the case is taken as the correct one (gold standard). The evaluation of the CAM process performance was done on the following two basis

- on the basis how the CAM's diagnosis were in consensus with that of the findings given for each of the case in the mammographic database.
- comparing the CAM's performance with that of the expert in correlating with the diagnosis given by the mammographic database.

The following is the protocol which was followed to evaluate the performance of the designed CAM process when compared to a human expert :

- The designed CAM process was applied on sixteen cases from the mini-MIAS mammographic database. For each of the case the severity of the abnormality was diagnosed by, the CAM process, as described in detail in Chapter 5 (Section 5.2.4).
- Each of the sixteen cases, with the location of the abnormality marked, was shown to an expert and her diagnosis was obtained.
- For each of the case the diagnosis arrived upon by the CAM process and that by the expert was compared with that given in the mini-MIAS database.

6.3.1. Details of the Computer Aided Monitoring of the Abnormalities in X-ray Mammograms for Sixteen Test Cases

The test cases (Sixteen of them) were chosen such that, that they belong to either of the two classes of abnormality, namely Asymmetry or Well-defined/Circumscribed masses. The reason for choosing only the above mentioned two classes of abnormalities is explained in detail in Chapter 5 (Section 5.2.5).

While choosing the test cases there was no restriction on the breast tissue type. The breast tissue type could be Fatty, Fatty-Glandular or Dense-Glandular. Similarly there was no restriction on the severity of the abnormalities chosen. The severity of the abnormality could be Benign or Malignant. But the size of the abnormality was restricted such that it can be enclosed within a region of interest (ROI) of size 151x151.

The design of the CAM system is based on the premises (hypothesis) that in the X-ray mammograms, the benign abnormalities will have image properties closer to the healthy tissue and malignant abnormalities will be markedly dissimilar from the surrounding healthy tissue. Thus, it was inferred that the measured dissimilarity between the region comprising the abnormality and the region comprising the healthy tissue, will indicate whether the abnormality is benign or not. Hence if one can measure the dissimilarity between the abnormal region and the surrounding healthy region, based on that measure one should be able to decide whether the abnormality is malignant or benign.

To measure the dissimilarity between the abnormal region and the surrounding healthy region the basic requirements are as follows :

- appropriate delineation of the boundary of the abnormality
- identifying the region of the image comprising the healthy part.

In implementing the above two steps, in the designed CAM system, the human intervention (input) was used where it was found appropriate.

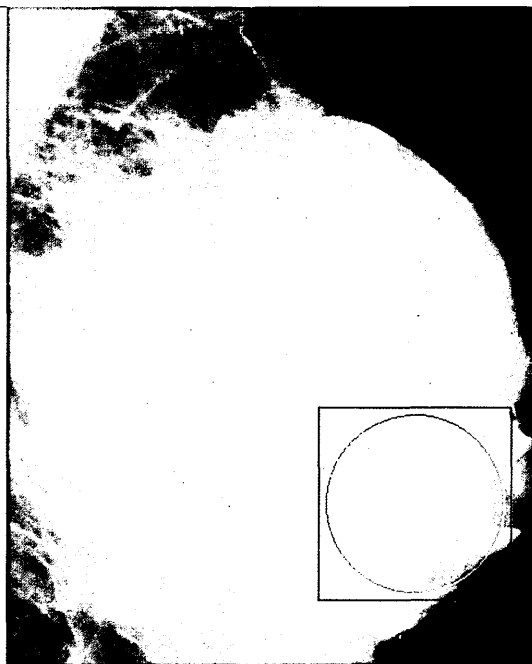
Based on the above discussion following were the steps which were followed to diagnose the sixteen cases using the designed CAM system.

For each of the sixteen cases :

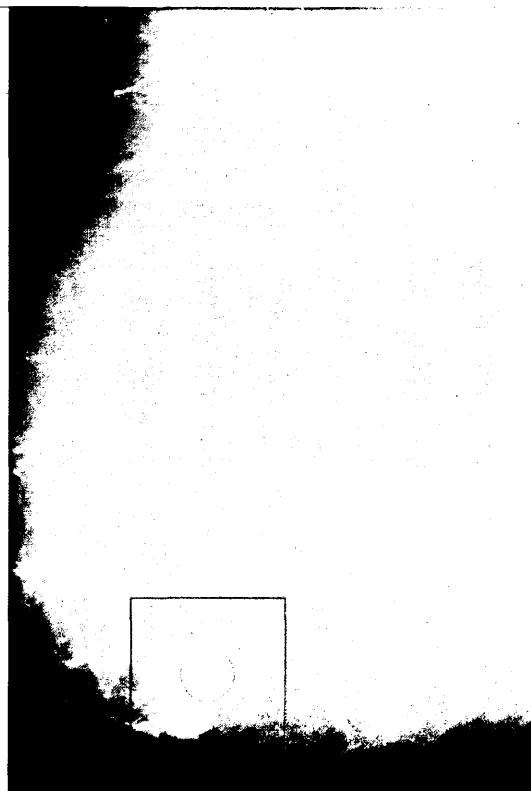
- the approximate location and the size of the abnormality was found using the information provided by the mini-MIAS database. (Expert input) (Figures 6.13 A to D)
- the HCS process was applied within a ROI of size 151x151, encompassing the abnormality. This yields a set of segmentation output.
- from the above set of HCS process segmentation output, the user identifies the most appropriate segmentation which he/she perceives as has delineated the abnormality from the surrounding healthy tissue. (user input) (Figures 6.14 A to D)
- from the above chosen specific segmentation output the user identifies the regions which he/she feels as most appropriately represent the abnormality and the healthy tissue. (user input). (Figures 6.15 A to D)
- the HCS process estimates the dissimilarity between the user chosen regions representing the abnormality and the healthy tissue.

It should be noted that in the above described process the user input was provided by a user (the author of the study) who was neither a clinician nor a radiologist but knew the severity of the abnormality (from the mini-MIAS database) for each of the cases.

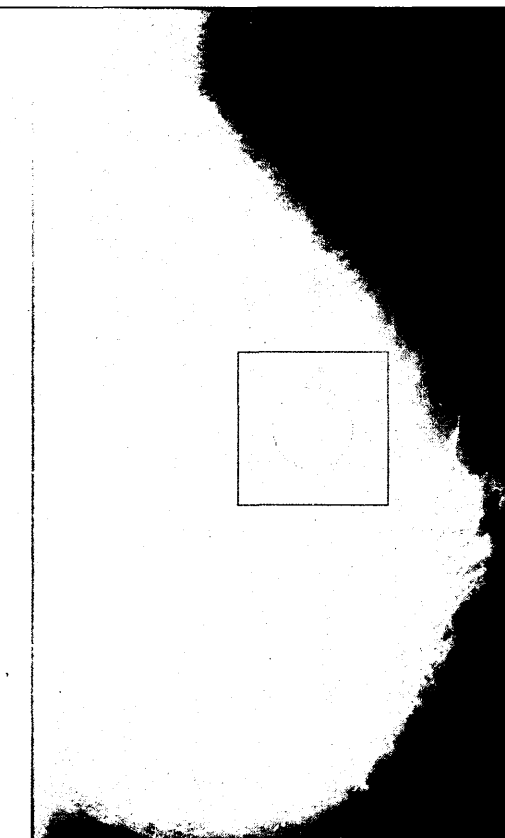
For the sixteen cases, Figure 6.13 (A to D) lists the mini-MIAS image Ids, the corresponding images, and the details of the abnormalities for each of them. Figures 6.14 and 6.15 show the images corresponding to each of the steps followed for the CAM process based diagnosis, discussed above.



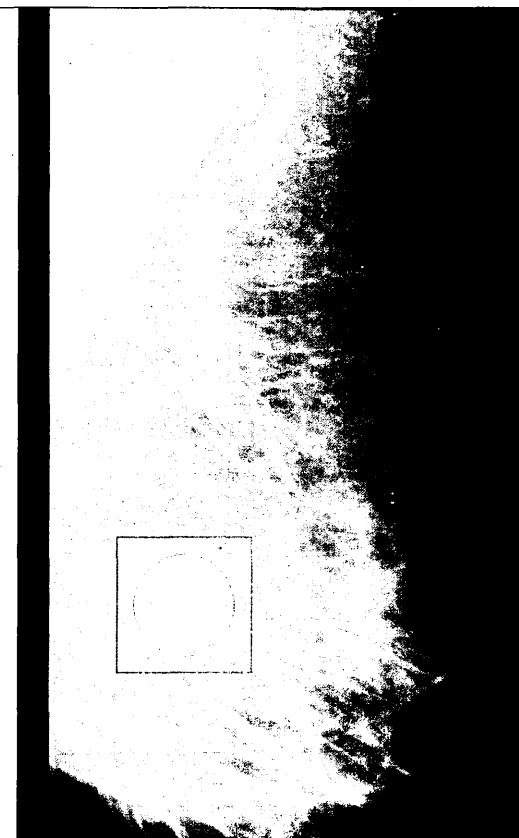
mdb002 - Fatty Glandular, Circumscribed and Benign



mdb005 – Fatty, Circumscribed and Benign



mdb012 – Fatty, Circumscribed and Benign



mdb028 – Fatty, Circumscribed and Malignant

Figure 6.13 (A) – Images showing the approximate size and location of the abnormality and the ROI surrounding it

mdb075 - Fatty, Asymmetry and Malignant. mdb083 - Fatty Glandular, Asymmetry and Benign.

mdb090 - Fatty Glandular, Asymmetry and Malignant mdb092 - Fatty, Asymmetry and Malignant

Figure 6.13 (B) - Images showing the approximate size and location of the abnormality and the ROI surrounding it

mdb095 - Fatty, Asymmetry and Malignant.

mdb097 - Fatty , Asymmetry and Benign.

mdb099 - Dense Glandular, Asymmetry and
Benign

mdb102 - Dense Glandular, Asymmetry and
Malignant

Figure 6.13 (C) - Images showing the approximate size and location of the abnormality and the ROI surrounding it

mdb104 - Dense Glandular, Asymmetry and Benign.

mdb110 - Dense Glandular, Asymmetry and Malignant.

mdb141 - Fatty, Circumscribed and Malignant

mdb270 - Fatty Glandular, Circumscribed and Malignant

Figure 6.13 (D) - Images showing the approximate size and location of the abnormality and the ROI surrounding it

<i>Image ID</i>	<i>Part of the image surrounding the abnormality within the ROI</i>	<i>For the user chosen HCS process delineated Regions</i>	<i>Segmentation HCS process delineated Region Boundaries</i>
---------------------	---	---	--

mdb002

Number of Clusters - 34

mdb005

Number of Clusters - 10

mdb012

Number of Clusters - 5

mdb028

Number of Clusters - 4

Figure 6.14 (A) - Images showing the abnormality and the ROI surrounding it (Column 2). For the HCS process segmentation, chosen by the user, the regions (Column 3) and their boundaries (Column 4)

<i>Image ID</i>	<i>Part of the image surrounding the abnormality within the ROI</i>	<i>For the user chosen HCS process delineated Regions</i>	<i>Segmentation HCS process delineated Region Boundaries</i>
---------------------	---	---	--

mdb075

Number of Clusters - 7

mdb083

Number of Clusters -15

mdb090

Number of Clusters -10

mdb092

Number of Clusters - 5

Figure 6.14 (B) - Images showing the abnormality and the ROI surrounding it (Column 2).
For the HCS process segmentation, chosen by the user, the regions (Column 3) and their boundaries (Column 4)

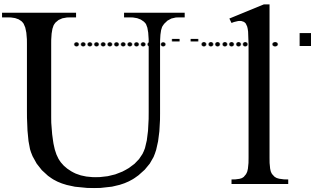


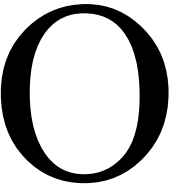

<i>Image ID</i>	<i>Part of the image surrounding the abnormality within the ROI</i>	<i>For the user chosen HCS process delineated Regions</i>	<i>Segmentation HCS process delineated Region Boundaries</i>
mdb095			
		Number of Clusters - 14	
mdb097			
		Number of Clusters - 2	
mdb099			
		Number of Clusters - 6	
mdb102			
		Number of Clusters - 4	

Figure 6.14 (C) - Images showing the abnormality and the ROI surrounding it (Column 2). For the HCS process segmentation, chosen by the user, the regions (Column 3) and their boundaries (Column 4)

<i>Image ID</i>	<i>Part of the image surrounding the abnormality within the ROI</i>	<i>For the user chosen HCS process delineated Regions</i>	<i>Segmentation HCS process delineated Region Boundaries</i>
---------------------	---	---	--

mdbl04

I

Number of Clusters - 7

mdbl10

Number of Clusters - 7

mdbl41

Number of Clusters - 8

mdbl270

Number of Clusters - 7

Figure 6.14 (D) - Images showing the abnormality and the ROI surrounding it (Column 2). For the HCS process segmentation, chosen by the user, the regions (Column 3) and their boundaries (Column 4)

For each of the sixteen cases Figure 6.14 (A to D) shows the approximate size and the ROI surrounding the abnormality. Figure 6.14 also shows the user chosen segmentation which has delineated the abnormality from the surrounding healthy tissue as perceived by the user.

From Figure 6.14 it can be seen that the level of segmentation at which the user perceives that the most appropriate boundaries of the abnormality and the healthy regions have been delineated, varies from case to case. For some cases the number of regions that need yet to be merged are higher (for example, fifteen for the case mdb002) when compared to others (for example two for the case mdb097).

Since the user is a lay person, to choose the most appropriate segmentation the user made use of the approximate boundary given by the mini-MIAS database and followed the criteria by Kegelmeyer *et. al.* [Kegelmeyer *et. al.* 1994] which states :

- a computer finding is considered as a true positive detection if its area is overlapped by at least 50% of a true lesion as indicated by an expert radiologist;
- a computer finding that does not so overlap a true lesion is considered as false positive; and
- a true lesion that is not overlapped by any computer finding is considered as false negative.

Based upon the above, the heuristics followed by the user (lay person) for choosing the segmentation which might most appropriately delineate the abnormality and the healthy regions are as follows :

- the level of segmentation should be such that the regions should be neither fragmented nor too coarse.
- the segmentation should have a region which could be visualised as belonging to the abnormality. The major part of this region should be within the approximate boundary of the abnormality given by the mini-MIAS database.
- the core of the abnormality is a location within the abnormal region, chosen above, and whose density is the highest among the pixels within the region chosen as the abnormality.

It should be noted that the location having the maximum pixel value within the Abnormality could be more than one. The additional criteria used by the user (lay person) to choose the core of the abnormality was that by inspecting the segmentation process the user (lay person) identifies that location around which the Abnormality grows as the segmentation process proceeds. For details please refer Chapter 5 (Section 5.2.4.3.3) and Figure 5.19 (Chapter 5).

- the healthy region is chosen as the region which surrounds the region which was chosen earlier as the abnormality.

For each of the sixteen cases Figure 6.15 (A to D) shows the user (lay person) identified regions and their boundaries which might most appropriately represent the abnormality and the healthy tissue as perceived by the user (lay person).

<i>mini-MIAS Image ID</i>	<i>User identified regions representing the abnormality (Red) and the healthy (Yellow) tissue.</i>	<i>Boundaries of the user identified regions representing the abnormality and the healthy tissue.</i>
mdb002		
mdb005		
mdb012		
mdb028		

Figure 6.15 (A) - Images showing the Region (Column 1) and Boundaries (Column 2) of the abnormality and the healthy region surrounding it chosen by the user.

<i>mini-MIAS Image ID</i>	<i>User identified regions representing the abnormality (Red) and the healthy (Yellow) tissue.</i>	<i>Boundaries of the user identified regions representing the abnormality and the healthy tissue.</i>
mdb075		
mdb083		
mdb090		
mdb092		

Figure 6.15 (B) - Images showing the Region (Column 1) and Boundaries (Column 2) of the abnormality and the healthy region surrounding it chosen by the user.

<i>mini-MIAS Image ID</i>	<i>User identified regions representing the abnormality (Red) and the healthy (Yellow) tissue.</i>	<i>Boundaries of the user identified regions representing the abnormality and the healthy tissue.</i>
mdb095		
mdb097		
mdb099		
mdbl02		

Figure 6.15 (C) - Images showing the Region (Column 1) and Boundaries (Column 2) of the abnormality and the healthy region surrounding it chosen by the user.

<i>mini-MIAS Image ID</i>	<i>User identified regions representing the abnormality (Red) and the healthy (Yellow) tissue.</i>	<i>Boundaries of the user identified regions representing the abnormality and the healthy tissue.</i>
mdb!04		
mdbl!O		
mdbl41		
mdb270		

Figure 6.15 (D) - Images showing the Region (Column 1) and Boundaries (Column 2) of the abnormality and the healthy region surrounding it chosen by the user.

6.3.2. Overall Results Obtained through the CAM Process

The objective measure and the classification rule adopted by the CAM process, to differentiate benign from malignant abnormality, is defined as follows :

- find the maximum average dissimilarity, measured between the cluster having the user tagged location (within the abnormality) and the clusters within the healthy region.
- if the value of the above estimated measure is less than fifty percent then the abnormality is benign.
- if the value of the above estimated measure is greater than fifty percent then the abnormality is malignant.

Table 6.9 lists the overall performance of the above defined objective measure and the corresponding classification rule, to differentiate benign (B) from malignant (M) abnormalities. The last column states "True +ve" if the classification based on the objective measure is malignant and the severity of the abnormality given, for that mammogram, by the mini-MIAS database is also malignant. Similarly the last column states "True -ve" if the classification based on the objective measure is benign and the severity of the abnormality given, for that mammogram, by the mini-MIAS database is also benign.

Table 6.9 - Performance of the CAM process in differentiating malignant from benign abnormalities

mini-MIAS Image ID	Breast Tissue Type (As per mini-MIAS)	Class of Abnormality (As per mini-MIAS)	Severity of Abnormality (As per mini-MIAS)	Maximum Average Dissimilarity Measure (Dis)	Objective Measure Based Classification B (Dis < 50%) M (Dis > 50%)
mdb002	Fatty Glandular	Circumscribed	Benign (B)	16.1%	B (True -ve)
mdb005	Fatty	Circumscribed	Benign (B)	30.5%	B (True -ve)
mdb012	Fatty	Circumscribed	Benign (B)	40.5%	B (True -ve)
mdb028	Fatty	Circumscribed	Malignant (M)	82.0%	M (True +ve)
mdb075	Fatty	Asymmetry	Malignant (M)	52.8%	M (True +ve)
mdb083	Fatty Glandular	Asymmetry	Benign (B)	43.8%	B (True -ve)
mdb090	Fatty Glandular	Asymmetry	Malignant (M)	67.4%	M (True +ve)
mdb092	Fatty	Asymmetry	Malignant (M)	53.9%	M (True +ve)
mdb095	Fatty	Asymmetry	Malignant (M)	61.5%	M (True +ve)
mdb097	Fatty	Asymmetry	Benign (B)	48.8%	B (True -ve)
mdb099	Dense Glandular	Asymmetry	Benign (B)	48.2%	B (True -ve)
mdb102	Dense Glandular	Asymmetry	Malignant (M)	65.7%	M (True +ve)
mdb104	Dense Glandular	Asymmetry	Benign (B)	32.4%	B (True -ve)
mdbl10	Dense Glandular	Asymmetry	Malignant (M)	77.9%	M (True +ve)
mdbl41	Fatty	Circumscribed	Malignant (M)	82.6%	M (True +ve)
mdb270	Fatty Glandular	Circumscribed	Malignant (M)	53.2%	M (True +ve)

6.3.3. Diagnosis of an Expert Radiologist

The opinion of an expert radiologist was got for each of the sixteen cases. The protocol followed to obtain the expert's opinion was as follows :

for each of the sixteen cases the expert was provided with the details of the location of the abnormality (as provided by the mini-MIAS), the breast tissue type and the class of the abnormalities

the expert was requested to categorise the abnormality as benign or malignant.

The following are the observations which were made on the expert's diagnosis process:

the expert found the resolution of both the image and as well as the display unit too low when compared to what she uses in her professional work.

For cases in which the expert felt that she had been handicapped by the resolution of the image she mentioned so.

- the expert used the Breast Imaging Reporting and Data System (BIRADS) score (Table 6.10) for categorising the severity of an abnormality. If the expert is not sure of the severity she categorised it as R3.

over and above the diagnosis of the severity of the abnormalities the expert also noted other structural properties found in and around the abnormalities pertaining to her diagnosis.

for some of the cases the expert wondered why another location in the image has not been marked as abnormal.

Table 6.10 - Breast Imaging Reporting and Data System (BIRADS) score.

(http://breastcancer.about.com/od/diagnosis/a/birads.htm) _____		
Category	Diagnosis	Number of Criteria
0	Incomplete	Mammogram or ultrasound didn't give the radiologist enough information to make a clear diagnosis; follow-up imaging is necessary
1	Negative	There is nothing to comment on; routine screening recommended
2	Benign	A definite benign finding; routine screening recommended
3	Probably Benign	Findings that have a high probability of being benign (>98%); six-month short interval follow-up
4	Suspicious Abnormality	Not characteristic of breast cancer, but reasonable probability of being malignant (3 to 94%); biopsy should be considered.
5	Highly Suspicious of Malignancy	Lesion that has a high probability of being malignant (>= 95%); take appropriate action.
6	Known Biopsy Proven Malignancy	Lesions known to be malignant that are being imaged prior to definitive treatment; assure that treatment is completed.

Table 6.11 lists the expert's diagnosis and the corresponding comments, if any, for the sixteen cases. (Please see Appendix 6 for the scanned image of the expert's hand written diagnosis and comments)

Table 6.11 – Performance of the expert in differentiating malignant from benign abnormalities

mini-MIAS Image ID	Breast Tissue Type (As per mini-MIAS)	Class of Abnormality (As per mini-MIAS)	Expert's diagnosis and pertaining comments B – Benign M - Malignant
mdb002	Fatty Glandular	Circumscribed	R3 Expert was not sure what to decide
mdb005	Fatty	Circumscribed	B (True -ve)
mdb012	Fatty	Circumscribed	Well defined superior, Ill defined inferior. R3, Maybe M (False +ve)
mdb028	Fatty	Circumscribed	M (True +ve)
mdb075	Fatty	Asymmetry	M (True +ve)
mdb083	Fatty Glandular	Asymmetry	M (False +ve)
mdb090	Fatty Glandular	Asymmetry	M (True +ve)
mdb092	Fatty	Asymmetry	M (True +ve)
mdb095	Fatty	Asymmetry	M (True +ve)
mdb097	Fatty	Asymmetry	R3 Expert was not sure what to decide
mdb099	Dense Glandular	Asymmetry	M (False +ve)
mdb102	Dense Glandular	Asymmetry	Low image resolution. May be M (True +ve)
mdb104	Dense Glandular	Asymmetry	R3 Probably B (True -ve)
mdb110	Dense Glandular	Asymmetry	Low image resolution M (True +ve)
mdb141	Fatty	Circumscribed	M (True +ve)
mdb270	Fatty Glandular	Circumscribed	M (True +ve)

6.3.4. Comparing HCS Process based Objective Measure with that of the Radiologist's Manual Measure

Of the sixteen cases processed the CAM process has obtained one hundred percent success rate in classifying the malignant from the benign cases. The expert had misdiagnosed two of them (False +ve) and was not sure of her diagnosis for four other cases (R3). Hence, out of sixteen cases the expert had correctly classified with confidence ten cases (63%).

However the expert was handicapped by the low resolution of the image and the display unit. The mammogram images, originally digitised at 50 microns pixel edge, had been reduced to a 200 microns pixel edge for the mini-MIAS database [Suckling *et al.*, 1994]. The display unit used to view the mammogram images was one mega-pixel resolution. In normal practice full-field digital mammograms are 70 microns resolution viewed in a display of three mega-pixels resolution.

It should also be noted that the expert did not make use of any objective measures (e.g. the pixel density values) rather she had taken into account other criteria like the structural properties of the abnormalities. For example whether the border of the abnormalities is well defined or ill defined, the presence or absence of calcification around the site etc.. Since malignant masses are often characterized by irregular tented boundaries with retraction of other fibrous structures and may be accompanied by local skin thickening or microcalcifications (Figure 6.16). Also it has been shown that isolated clusters of microcalcifications are one of the most frequent radiological features of asymptomatic breast cancer [Chan *et al.*, 1994]. A careful search for the clustered microcalcifications that may herald an early-stage cancer should be carried out on all mammograms[Kopanes, 1999]. Thus the expert had employed her expert knowledge and past experience heuristically in arriving upon a diagnosis.

Invasive Carcinoma of the Right Breast

The irregular mass with stellate borders is a strong indicator of malignancy.

Figure 6.16 - Invasive carcinoma of the right breast. The irregular mass with stellate borders is a strong indicator of malignancy. (Image courtesy <http://www.med.yale.edu/>)

6.3.5. Possible Usage of the CAM Process of Abnormalities in X-ray

Mammograms

From the preceding discussion it is seen that while human experts make use of heuristic measures the designed CAM process makes use of objective measure. From this observation one of the possible usage, that can be envisaged, for the implemented CAM process is the incorporation of the CAM's objective measure along with the expert's heuristic measure. For instance Hashimoto and Bauermeister have made the following observation about circumscribed masses :

Circumscribed masses are commonly benign. Only 1.4% of well-defined circumscribed masses are malignant. As there are many benign lesions in this category, diagnostic evaluation should be directed to excluding many of these benign lesions from being biopsied [Hashimoto and Bauermeisterhas, 2003].

They recommend the following objective measure to identify benign circumscribed masses :

(The first step is to) analyse the density of the mass. If the mass contains fat, then the abnormality is benign and does not require biopsy. If the mass has a density equal or greater than parenchyma, then further examination is necessary [Hashimoto and Bauermeisterhas, 2003]

To incorporate the above objective measure within the diagnosis pathway the CAM process designed in this study can be used. For example the HCS process can objectively measure the pixel density distribution within the more appropriately delineated abnormality (See Chapter 3 Section 3.5.1). This might assist the user to objectively evaluate whether the abnormality has fat within itself and hence benign or not.

Moreover there are problems with the subjective analysis of mammographic images by radiologist. Subjective analysis depends mainly on the experience of the human operator, but it is also affected by fatigue and other human-related factors. In addition, the interpretation is a repetitive task that requires lot of attention to minute details. Hence, it requires lot of staff time and effort, which results in slowing the diagnosis time. On the other hand, the objective analysis of mammograms, which is carried out by automated systems, provides consistent performance but its accuracy is usually lower. Due to the sensitivity of this problem, it is believed that radiologists should be involved and computers should not replace them completely [AbuBaker, 2006]. Hence the designed CAM process will be more appropriate since it incorporates the radiologists' knowledge within its objective analysis pathway.

Hartswood *et al.* [Hartswood *et al.*, 1997] in their study evaluating automated Computer Aided Mammography systems made the following observations regarding how the users of the prompting software tried to figure out the placements of the prompts :

Making sense of the(Computer Aided Mammography) system (prompts)

*The following extracts of session verbal protocols illustrate how radiologists tried to make sense of the Computer Aided Mammography system's behaviour from the evidence of the features it had prompted. In a number of instances, the transcripts show examples of misunderstanding of the extent of the system's capabilities, and confusion because of apparent inconsistencies in its behaviour. In this first set of extracts, the comments suggest radiologists were unable to accurately place the CAM system's operational scope: i.e., the types of feature it is capable of detecting. The next set of extracts focuses on radiologists' problems with understanding how the system interprets microcalcification clusters. In the final set of extracts, the radiologists indicated that they had not see (sic) anything of significance in the areas prompted.[Hartswood *et al.*, 1997]*

The above issues arise, in the usage of the existing prompting software, because of the following reasons :

- the prompting software does not give any kind of feedback to the user how and why it arrived upon the decision.
- the user is not involved in the decision process.

The user of the Computer Aided Monitoring process, developed in this study, will not face any of the above issues. The user will be quite sure how and why the CAM system classified an abnormality into either malignant or benign because the user is involved in the decision process.

6.4. Summary

In this chapter the details of the performance of the Computer Aided Monitoring (CAM) process, designed for this study, was compared with the expert's performance for the following two clinical applications

- Quantitative measure of the airway and the accompanying blood vessel dimensions
- Quantitative differentiation of malignancy from benign abnormalities.

The conclusion which could be drawn from the performance analysis done is that the designed CAM process could be used by the experts. Moreover, the designed CAM process has inbuilt provision to make use of the experts' knowledge to finalize its objective measure. Hence, the designed CAM process need not be considered as an alternative for the existing diagnostic processes in practice but rather it might be used to augment the existing processes. But to establish this possibility the CAM process need to be tried by an expert. The current evaluation of the CAM process was carried out by the observation made on how the process was used by a lay person (the author of the study). Hence, it cannot be conclusively established, at the present stage of the investigation, the exact impact of the process on the experts' performance in interpreting diagnostic images.

7.1. Introduction

Tasks such as describing a picture, for example, is simple for humans but difficult for computers. Commercial online services, such as Amazon's Mechanical Turk service [Amazon], has long facilitated access to readily available human labour, when the job is simple for humans but difficult for computers. Of late, programmers have developed toolkits, like TurKit [TurKit], that lets software engineers write algorithms to coordinate these online human workers.

One such word-processing application, which has made use of TurKit, is Soylent [Bernstein et al., 2010] [Soylent]. Soylent embed on-demand human computation within interactive systems like Microsoft Word. Microsoft Word is good at laying out a document, but poor at understanding writing and suggesting edits to it. Soylent is a word processor with a crowd inside: an add-in to Microsoft Word that uses crowd contributions to perform interactive document shortening, proofreading, and human-language macros.

Latest in this line of software tools is the MobileWorks [MobileWorks]. MobileWorks incorporates human decision process within a software, through Application Programming Interface (API). The API enables the software to delegate its toughest tasks to humans. Through the API mechanism the software program can treat humans like another piece of software with the intelligence of a human.

In the diagnostic image processing environment, Claridge contends that computing systems are more consistent in their perceiving ability but they cannot match human interpretive skills. Drawing a line so as to limit the system's interpretive function has the virtue of achieving a complementary synthesis of system and radiologists' strengths [Claridge 1997].

This thesis has presented the details of a study that has designed a diagnostic image processing process which incorporates human interpretive skill within its framework, thus, striving to achieve the synthesis of system and radiologists' strengths.

This chapter will discuss the contribution of the current study and the possible applications of the designed processes. It will also discuss the proposals to progress the work, carried out for this thesis, to the next level of making use of it in the real world environment.

The above discussion will be based on the HCS based CAM process for the following applications, which were investigated in this thesis :

- Objective measurement of the airway and the accompanying blood vessel in the CT images of the lungs.
- Objectively differentiating malignant from benign abnormalities in X-ray mammograms.

7.2. Contribution and Possible Application of the Current Study

One of the major contribution of the current study is that it has designed a CAM system which makes use of the machine's perceptual facility along with expert's interpretative skills to objectively estimate the severity of the abnormal conditions. The designed CAM system has been tested for its performance in monitoring the following medical conditions :

- monitoring of CF in children
- monitoring of breast abnormalities in women

This section will discuss the possible applications of the above CAM systems.

7.2.1. Possible Application of the Computer Aided Monitoring of CF

With the advent of multi-detector row CT (MDCT) scanner, it is possible to acquire sub-millimeter thickness images of the entire chest within a single breath-hold of 5 to 15 seconds. These new images can have the same resolution in the X, Y, and Z dimensions (isometric voxels), allowing images to be reconstructed in any orientation without loss of spatial resolution [Coxson and Lam, 2009].

Given the higher resolution of the MDCT images and its possible better sensitivity, when compared to the HRCT's images used for this study, the performance of the designed CAM system in segmenting the airways and the accompanying blood vessels will improve. Making use of the better image data the designed segmentation method can be further improved by requiring from the expert only the approximate centre marking of the airways and the blood vessels. This proposed improved method is discussed below.

To design an improvement, to the currently implemented method (Chapter 4 Section 4.3.10) the following typical anatomical properties of airway and the adjoining blood vessel could be leveraged :

- the airway lumen is always contained within the airway-wall and do not have a common boundary with the lung parenchyma..
- the airway wall Hounsfield values are markedly different from the airway lumen and its surrounding lung parenchyma.
- the blood vessel Hounsfield values are markedly different from the surrounding lung parenchyma.

Making use of the above typical anatomical properties one can improve upon the, just described, method of segmenting the blood vessel, airway wall and airway lumen which makes use of the user marked boundary locations.

The process starts, as before, by the user marking some discrete locations just outside the boundaries of the two major anatomies viz. the blood vessel and the airway wall. The discrete locations are connected together as one contiguous curve by connecting them with a cubic spline. The above two steps are the same as followed in the earlier discussed process.

The centres of the two resulting cubic spline curves will be almost at the centre of the two major anatomies viz. the blood vessel and the airway lumen (Chapter 4 Figure 4.24). Making use of these two locations, which are well within their corresponding anatomies viz. the blood vessel and the airway lumen, these two anatomies are segmented first as described below :

- first the HCS process identifies the two regions to which the central locations of the cubic splines belong to.
- as the segmentation process proceeds, the HCS process merges only those similar regions bordering the regions to which the central locations belong to.
- for additional control of the merging of the regions belonging only to the blood vessel and the airway lumen the Hounsfield value ranges of the airway lumen and the blood vessel can be made use of.

The result of the above segmentation process will be the airway lumen and the blood vessel segmented as two well defined regions.

This improvement will eliminate the requirement to give a pixel value range to restrict the pixels from lung parenchyma from merging with the airway lumen (Chapter4 Section 4.3.10.4).

Making use of the above proposed method, which requires only minimal input from the user, will allow much more rapid and efficient estimation of the dimensions of the airways and the accompanying blood vessels.

The issue of heterogeneity in airway dimensions is important both for between and within-subject comparisons [de Jong *et al.*, 2005]. King *et al.* [2004] measured heterogeneity in airway narrowing by comparing the variation within a scan to that between scans. However, this study did not address the issue of heterogeneity in baseline airway dimensions, which is important to estimate before the quantitative assessment of airway dimensions is established as an outcome measure in clinical studies [de Jong *et al.*, 2005]. Matsuoka *et al.* [2005] measured airway wall dimensions from central to peripheral airways, using contiguous 2-mm sections obtained with a MDCT scanner in normal subjects. They reported the variation in various measures of airway lumen and wall dimensions within an individual scan, and as a function of distance from the hilum to the periphery [de Jong *et al.*, 2005]. These data will prove valuable for assessing whether an observed difference or change is real or simply within the variation of the measurement [Matsuoka *et al.*, 2005].

Thus, the issue of heterogeneity in airway dimensions is important both for between and within-subject comparisons. But with the use of the currently available automated airway detection, it is only possible to make a limited number of measurements in any individual at any time [de Jong *et al.*, 2005].

Making use of the improved version of the CAM system designed in this study it may be possible to design an appropriate study methodology to measure the variation of the measurements within the same scan made at different locations

7.2.2. Possible Application of Computer Aided Monitoring of Breast

Abnormalities

The designed CAM system, to monitor the abnormal regions in X-ray mammograms, has the following facilities :

- delineate and outline more appropriate boundaries of the abnormal regions.
- objectively measure the dissimilarity between the user identified abnormal and healthy regions.

The designed CAM system having the above facilities will be most useful in application domains where more appropriate delineation of the boundaries of the abnormalities is crucial and in application domains where the dissimilarity between the abnormal regions and healthy regions need to be objectively estimated.

The following is one of the application domains where more appropriate delineation of the boundaries of the abnormalities is crucial :

Radiologists have known for years that tumour volume can indicate patient response to therapy. Until now, however, it has not been a central component in a major research design. Last year a multi-centre trial, begun at the University of California, San Francisco and slated to expand to about 20 cancer centres in the U.S., will use medical images to assess patient response to experimental drugs being tested against breast cancer. The cancer trial will gauge how well drugs work in patients before their tumours have been surgically removed so that the effect of the drug can be quantified with medical imaging [Freiherr, 2010].

"By measuring tumour volume with imaging and validating that with pathological response, we will learn more about the use of images as a marker for drug effects," said Dr. Janet Woodcock, director of the FDA centre for drug evaluation and research.

In application domains similar to the above the initial location of the abnormalities are known which is essential for the CAM system designed in this study. But what is required is the most appropriate delineation of the boundaries of the abnormalities which the designed CAM system can do far better than the human experts.

The following is one of the application domains where the dissimilarity between the abnormal regions and the healthy regions need to be objectively estimated :

To aid radiologists in earlier detection of breast cancer, Sameti [1998] conducted

a retrospective study of mammograms. In that pioneer study, screening mammograms taken prior to the detection of a malignant mass was analysed, The aim was to determine if there exists any signs of cancer development in the screening mammograms prior to the detection of a mass by the radiologist.

The conclusion of that study was that the system can be used by a radiologist to examine suspicious patterns in a mammogram. The regions which were flagged by the system have a 72% chance of developing a malignant mass by the time of next screening [Sameti, 1998].

In the application domain similar to the above the possible location which will subsequently develop into an abnormal region is known. But what is required is an objective measure which will differentiate regions which will subsequently develop into malignancy from those regions which will remain benign. The objective measure designed for the CAM system in this study will be able provide such a measure.

7.3. Further Work

The following is the synopsis of the current study :

HCS process was made use of to design CAM systems to monitor CF, by processing CT images of the lungs and monitor breast abnormalities by processing X-ray mammograms.

Based on the above synopsis one can identify the following core components of the current study :

- HCS
- CAM process to monitor CF
- CAM process to monitor breast abnormalities

This section will discuss further work that could possibly be done in future to improve or enhance the capabilities of the above components of the current study.

7.3.1. Proposed Further Work on HCS Process

The current study is more application oriented hence, much of the discussion was focused on how an operation was done rather than why it was done. The choice of a specific operation was validated if the process yielded the required or anticipated results. That is there is no theoretical validation performed on the choice of operations.

The HCS process is the core operation which was used to design the CAM process. In this study the performance of the HCS process, when compared to other segmentation algorithms, was objectively evaluated making use of the Berkeley segmentation dataset and benchmark [Arbelaez, 2007] (Please see Chapter 3 Section 3.4). Other than the above attempt to objectively measure the performance of the HCS process no other detailed analysis of the HCS process was done.

It is proposed that the theoretical analysis and validation are done for the HCS process. The HCS process is very similar to other existing clustering based segmentation algorithms like Normalized cuts [Shi and Malik, 1997] and Spectral clustering [Ng *et al.*, 2001]. Hence, the existing analytical work done on those similar methods could be taken as a guide.

Yet another aspect in which the HCS process need to be studied more closely is the process's operational optimization. By design the HCS process is processing intensive. This is because the HCS process adopts the brute force approach, where only those regions with the smallest overall dissimilarity are merged in each step. This ensures that the HCS process does not face the problem, that the resulting segmentation depends on the order in which the regions are evaluated to be merged [Thies *et al.*, 2003].

Merging only those regions with the smallest overall dissimilarity requires the comparison of all the possible combinations of the locations or regions present in a image. This is a combinatorial problem which can easily overwhelm even very powerful computing systems. But the comparison of the different pairs of regions can be done in parallel. The current parallelised implementation of the HCS process takes advantage of the availability of multi-core CPUs. But the number of CPU cores available in a reasonably priced computing systems is limited.

Recently General Purpose Graphical Processing Units (GP-GPU) with hundreds of cores are available for a very reasonable price. High performance computing can be now be achieved using a hybrid computing model where GPUs are added to a x86 CPU system. It is proposed that the HCS process software is ported to such a system so that it can take leverage GP-GPU's powerful parallel computing architecture and programming model.

7.3.2. Proposed Further Work on the CAM process to monitor CF

The CAM process designed to monitor CF was developed for and tested on HRCT data. HRCT data because of the lower resolution and lower sensitivity suffers from the partial volume effect whereby the HU values of the surrounding lung parenchyma is same as that of lumen (Please see Chapter 4 Section 4.3.4). It is proposed that the designed CAM system be evaluated and tested on the higher resolution MDCT image data.

7.3.3. Proposed Further Work on CAM process to monitor Breast Abnormalities

The HCS process based CAM system designed to monitor breast abnormalities involves the following crucial steps (Chapter 5 Section 5.2.4)

- identifying the most appropriate segmentation, amongst the HCS process output
- in the above identified segmentation,
 - marking the region which represents the abnormal tissue
 - marking the region which represents the healthy tissue
 - choosing a part of the abnormality which forms the core of the abnormality

In the current study, for validating the performance of the designed process, the above steps were performed by the author who is a lay person (Chapter 6 Section 6.3.1). It is proposed to find out whether the current results obtained by the designed CAM process can be repeated if an expert performs the above steps.

The following could be the protocol for the proposed validation process

- perform the HCS segmentation process within the ROI around the approximate location of the abnormality.
- display the segmentation output to the expert user making use of the designed GUI facility for displaying the HCS process output (Chapter 4 Section 4.2.2)
- inspecting the HCS process output the expert user does the following
 - chooses the most appropriate segmentation
 - in the above identified segmentation, the user :
 - identifies the region which represents the abnormal tissue
 - identifies the region which represents the healthy tissue
 - chooses a part of the abnormality which forms the core of the abnormality

- Making use of the above choices, made by the expert user, the designed CAM process classifies the abnormality as malignant or benign using the designed objective measure (Chapter 5 Section 5.2.5.1)

For each of the sixteen cases the choices made by the expert user and the corresponding classification of the abnormality obtained by the CAM process are compared with the one done by the lay user and the corresponding results obtained in the current study (Chapter 6 Section 6.3.1).

7.4. Conclusion

This study has developed and evaluated a novel CAM process which seamlessly combines the perceptual ability of the computer with the interpretative skill of humans. The designed CAM system can be used to monitor any conditions which require perceptual skill to interpret medical image data.

The application domains on which the designed CAM system was evaluated, viz. monitoring CF by processing CT images of the lungs and monitoring abnormalities of the breast by processing the X-ray mammograms, can be easily extended to be tested for possible clinical applications (Please see Chapter 7 Section 7.2.1 and Section 7.2.2).

It should be noted that the current results, in differentiating benign from malignant abnormalities, were obtained by processing images which are almost four times lower resolution (200 microns per pixel) when compared to the actual resolution of the digital mammogram (70 micron per pixel). Hence it is anticipated that the HCS process based CAM method will benefit from the higher resolution of the actual digital mammograms.

Also the current HCS process can handle 3-D data set by considering a neighbourhood of 3x3x3 cube around a voxel location.

Appendix 1

Following is a short critical synopsis of different medical image segmentation methods and their corresponding advantages and disadvantages, as outlined by Pham *et al.* [2000], in their survey on the methods in medical image segmentation.

Thresholding approaches segment scalar images by creating a binary partitioning of the image intensities. A thresholding procedure attempts to determine an intensity value, called the threshold, which separates the desired classes. The segmentation is then achieved by grouping all pixels with intensity greater than the threshold into one class, and all other pixels into another class.

Thresholding operation can be expressed mathematically as given by the expressions A 1.1 and A 1.2.

$$I_o = \{I(m, n) : I(m, n) > T\} \quad [A\ 1.1]$$

$$I_b = \{I(m, n) : I(m, n) \leq T\} \quad [A\ 1.2]$$

Where :

I_o : Object pixels

I_b : Background pixels

$I(m, n)$: The value of the image pixel located in the m^{th} column n^{th} row

T : Threshold value

Determination of more than one threshold value is a process called multithresholding [Sahoo et al., 1988]. Its main limitations are that in its simplest form only two classes are generated and it can not be applied to multi-channel images. In addition, thresholding typically does not take into account the spatial characteristics of an image. This causes it to be sensitive to noise and intensity inhomogeneities, which can occur in magnetic resonance images. Both these artefacts essentially corrupt the histogram of the image, making separation more difficult. For these reasons, variations on classical thresholding have been proposed for medical image segmentation that incorporate information based on local intensities [Li et al., 1995] and connectivity [Lee et al., 1998]. A survey on thresholding techniques is provided in [Sahoo et al., 1988].

Region growing is a technique for extracting a region of the image that is connected based on some predefined criteria. This criteria can be based on intensity information and/or edges in the image [Haralick and Shapiro, 1985]. Region growing can also be sensitive to noise, causing extracted regions to have holes or even become disconnected. Conversely, partial volume effects can cause separate regions to become connected. To help alleviate these problems, a homotopic region growing algorithm has been proposed that preserves the topology between an initial region and an extracted region [Mangin et al., 1995]. Fuzzy analogies to region growing have also been developed [Udupa and Samarasekera, 1996].

Classifier methods are pattern recognition techniques that seek to partition a feature space derived from the image using data with known labels [Schalkoff., 1992], [Bezdek et al., 1993]. Classifiers are known as supervised methods since they require training data that are manually segmented and then used as references for automatically segmenting new data. There are a number of ways in which training data can be applied in classifier methods. A simple classifier is the nearest-neighbor classifier, where each pixel or voxel is classified in the same class as the training datum with the closest intensity. Additional parametric and nonparametric classifiers are described in [Zijdenbos and Dawant, 1994]. A disadvantage of classifiers is that they generally do not perform any spatial modelling. This weakness has been addressed in recent work extending classifier methods to segmenting images that are corrupted by intensity inhomogeneities [Wells et al., 1996]. Neighborhood and geometric information were also incorporated into a classifier approach in [Kapur et al., 1998]. Another disadvantage is the requirement of manual interaction for obtaining training data. Training sets can be acquired for each image that requires segmenting, but this can be time consuming and laborious. On the other hand, use of the same training set for a large number of scans can lead to biased results which do not take into account anatomical and physiological variability between different subjects.

Clustering algorithms essentially perform the same function as classifier methods without the use of training data. Thus, they are termed unsupervised methods. In order to compensate for the lack of training data, clustering methods iterate between segmenting the image and characterizing the properties of the each class. In a sense, clustering methods train themselves using the available data. Three commonly used clustering algorithms are the K-means or ISODATA algorithm [Coleman and Andrews, 1979], the fuzzy c-means algorithm [Dunn, 1973], [Bezdek et al., 1993], and the expectation-maximization (EM) algorithm [Lei and Sewchand, 1992], [Liang et al., 1994]. Although clustering algorithms do not require training data, they do require an initial segmentation (or equivalently, initial parameters). The EM algorithm has demonstrated greater sensitivity to initialization than the K-means or fuzzy c-means algorithms [Davenport et al., 1988]. Like classifier methods, clustering algorithms do not directly incorporate spatial modelling and can therefore be sensitive to noise and intensity inhomogeneities. This lack of spatial modelling, however, can provide significant advantages for fast computation [Hebert, 1994]. Work on improving the robustness of clustering algorithms to intensity inhomogeneities in MR images has demonstrated excellent success [Goldszal *et al.*, 1998], [Pham and Prince, 1999].

Markov Random Fields (MRFs) are often incorporated into clustering segmentation algorithms such as the K-means algorithm under a Bayesian prior model [Pappas, 1992], [Rajapakse *et.al*, 1997], [Held *et al.*, 1997], [Goldszal *et al.*, 1998]. The segmentation is then obtained by maximizing the a posteriori probability of the segmentation given the image data using iterative methods such as iterated conditional modes [Besagal, 1986] or simulated annealing [Geman and Geman, 1984]. A difficulty associated with MRF models is proper selection of the parameters controlling the strength of spatial interactions [Li, 1995]. Too high a setting can result in an excessively smooth segmentation and a loss of important structural details. In addition, MRF methods usually require computationally intensive algorithms. Despite these disadvantages, MRFs are widely used not only to model segmentation classes, but also to model intensity inhomogeneities that can occur in MR images [Held *et al.*, 1997] and texture properties [Reed and Hans Du Buf, 1993].

Artificial Neural Networks (ANNs) are massively parallel networks of processing elements or nodes that simulate biological learning. Each node in an ANN is capable of performing elementary computations. Learning is achieved through the adaptation of weights assigned to the connections between nodes. A thorough treatment on neural networks can be found in [Clark, 1991], [Haykin, 1994]. Because of the many interconnections used in a neural network, spatial information can easily be incorporated into its classification procedures. The most widely applied use in medical imaging is as a classifier [Hall et al., 1992], [Gelenbe et al., 1996], where the weights are determined using training data, and the ANN is then used to segment new data. ANNs can also be used in an unsupervised fashion as a clustering method [Bezdek et al., 1993], [Reddick et al., 1997], as well as for deformable models [Vilarino et al., 1998].

Deformable models are physically motivated, model-based techniques for delineating region boundaries using closed parametric curves or surfaces that deform under the influence of internal and external forces. To delineate an object boundary in an image, a closed curve or surface must first be placed near the desired boundary and then allowed to undergo an iterative relaxation process. Internal forces are computed from within the curve or surface to keep it smooth throughout the deformation. External forces are usually derived from the image to drive the curve or surface towards the desired feature of interest. Mathematically, a deformable model moves according to its dynamic equations and seeks the minimum of a given energy functional [Kass et al., 1988], [Terzopoulos and Szeliski, 1992]. The main advantages of deformable models are their ability to directly generate closed parametric curves or surfaces from images and their incorporation of a smoothness constraint that provides robustness to noise and spurious edges. A disadvantage is that they require manual interaction to place an initial model and choose appropriate parameters. Reducing sensitivity to initialization has been a topic of research that has demonstrated excellent success [Cohen, 1991] [Caselles et al., 1993], [Malladi et al., 1995], [Xu and Prince, 1998]. Standard deformable models can also exhibit poor convergence to concave boundaries. This difficulty can be alleviated somewhat through the use of pressure forces [Cohen, 1991] and other modified external force models [Xu and Prince, 1998]. Another important extension of deformable models is the adaptivity of model topology using an implicit

representation rather than an explicit parameterization [Caselles et al., 1993] [Malladi et al., 1995], [McInerney and Terzopoulos, 1995]. A general review on deformable models in medical image analysis can be found in [McInerney and Terzopoulos, 1996].

Atlas-guided approaches are a powerful tool for medical image segmentation when a standard atlas or template is available. The atlas is generated by compiling information on the anatomy that requires segmenting. This atlas is then used as a reference frame for segmenting new images. Conceptually, atlas-guided approaches are similar to classifiers except they are implemented in the spatial domain of the image rather than in a feature space. The standard atlas-guided approach treats segmentation as a registration problem (see [Maintz and Viergever, 1998] for a detailed survey on registration techniques). It first finds a one-to-one transformation that maps a pre-segmented atlas image to the target image that requires segmenting. This process is often referred to as atlas warping. The warping can be performed using linear [Talairach and Tournoux, 1988], [Lancaster et al., 1997], [Andreasen et al., 1996] transformations but because of anatomical variability, a sequential application of linear and non-linear [Collins et al., 1995], [Davatzikos, 1996], [Christensen et al., 1997], [Sandor and Leahy, 1997] transformations is often used. Because the atlas is already segmented, all structural information is transferred to the target image. Atlas-guided approaches have been applied mainly in MR brain imaging. An advantage of atlas-guided approaches is that labels are transferred as well as the segmentation. They also provide a standard system for studying morphometric properties [Davatzikos et al., 1996], [Thompson and Toga, 1997], [Joshi et al., 1997]. Thus, atlas-guided approaches are generally better-suited for segmentation of structures that are stable over the population of study. One method that helps model anatomical variability is the use of probabilistic atlases [Thompson and Toga, 1997] but these require additional time and interaction to accumulate data.

Model-fitting is a segmentation method that typically fits a simple geometric shape such as an ellipse or parabola to the locations of extracted image features in an image [Pathak et al., 1998]. It is a technique which is specialized to the structure being segmented but is easily implemented and can provide good results when the model is appropriate. A more general approach is to fit spline

curves or surfaces [Bae et al., 1993] to the features. The main difficulty with model-fitting is that image features must first be extracted before the fitting can take place.

The watershed algorithm uses concepts from mathematical morphology [Gonzalez and Woods, 1992] to partition images into homogeneous regions [Vincent and Soille, 1991]. This method can suffer from over-segmentation, which occurs when the image is segmented into an unnecessarily large number of regions. Thus, watershed algorithms in medical imaging are usually followed by a post-processing step to merge separate regions that belong to the same structure [Sijbers et al., 1997].

monitor breast abnormalities.

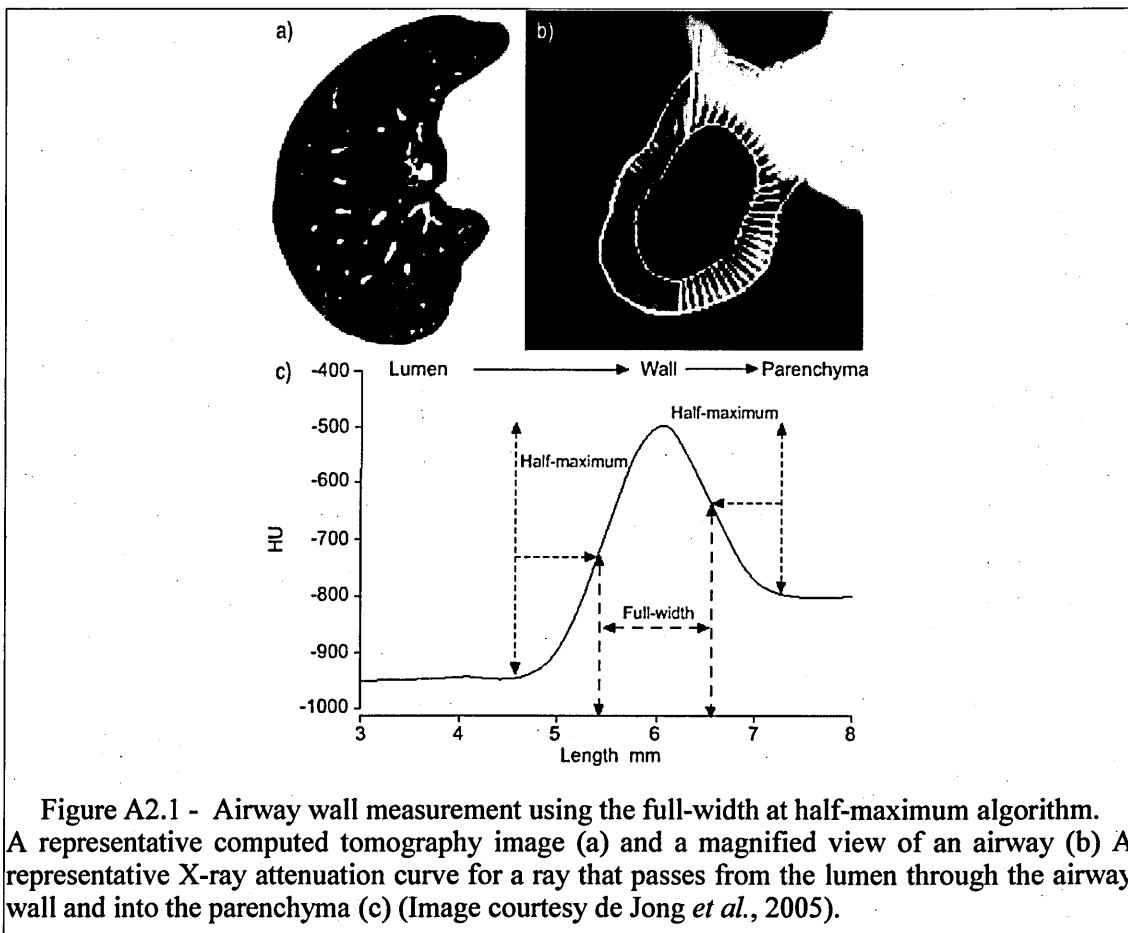
de Jong *et al.* in their publication titled "Computed tomographic imaging of the airways: relationship to structure and function" [de Jong *et al.*, 2005] have carried out a detailed review of the earlier studies which had attempted to quantitatively assess the dimensions of airways through CT images of the lungs. Following excerpt is from that publication :

Start Quote..

In the initial studies in which airway dimensions were measured using CT, the investigators relied on manual tracing of the airway images [Webb et al. 1984] [Seneterre et al., 1994] [McNamara et al., 1992] [Okazawa et al., 1996] [Bankier, et al., 1996]. These techniques are extremely time consuming and prone to error. Therefore, computer-aided and automated techniques have since been developed to measure airway lumen and wall dimensions. The first such method for measuring airway lumen used a Hounsfield unit (HU) threshold cut-off value. This technique involves identifying the airway, and measuring the X-ray attenuation values within the lumen. McNitt-Gray et al. [McNitt-Gray et al., 1997] reported that the airway lumen area could be accurately measured by including all pixels beyond a threshold cut-off of -500 HU, and King et al. [King et al., 2000] reported that a threshold of -577 HU produced the least error. However, the most commonly reported method for measuring the airway lumen and wall areas relies on the "full-width-at-half-maximum" (or "half-max") technique. This method requires that a seed point be placed in the lumen and the X-ray attenuation values measured along rays cast from this point outward toward the airway wall in all directions. As a ray enters the wall, the attenuation will increase and then decrease as it passes into the lung parenchyma. The distance between the point at which the attenuation is halfway to the maximum on the lumen side and halfway to the local minimum on the parenchymal side is considered to be the wall thickness (Figure A2.1) [Nakano et al., 2000] [Nakano et al. 2002]. Although this method provides a standardised and unbiased measurement, it has limitations. When CT scan measurements using this method are compared with phantoms and anatomical specimens [Nakano et al. 2002], the CT scans consistently overestimate airway wall area and underestimate lumen area. These systematic errors are due to a combination of factors including: the limited spatial resolution of the CT scanner; the angle of orientation of the airway within the CT slice; the ability of the scanner to detect edges (the point-spread function); the reconstruction algorithm used; the analysis technique used; and inability to visualise the folding of the epithelium. Nakano et al. [Nakano et al. 2002] have shown that the half-max method results in very large fractional errors in the measurements of small bronchi. For this reason, techniques such as the maximum likelihood method [Reinhardt et al., 1997] and score-guided erosion [King et al., 2000] have been developed. The errors due to volume averaging are particularly important

when airways are sectioned tangentially, as is the case with the majority of airways. King et al. [King et al., 2000] attempted to compensate for the obliquity of the section, by defining the angle of deviation of each airway from the perpendicular using the centroid of the same airway on the two sections on each side of the section on which the measurements are made. Saba et al. [Saba et al., 2003] have developed an alternate technique for measuring airways that are not cut in cross-section. This method involves fitting an ellipse to the airway lumen and wall, and shows great promise in correcting the errors in measurement of obliquely cut airways. These techniques claim to be more accurate than the more commonly used techniques, but have not been generally applied, presumably because of the limited availability of the complex algorithms involved.

End Quote..



Appendix 3

Coxson and Lam [2009] in their publication have critically reviewed the progression of computer techniques to qualitatively assess the Airway wall using CT. Following material is extracted from their publication :

The initial high-resolution computed tomography (HRCT) images used 1 mm slice thickness and an edge-enhancing algorithm that made it possible to visualize the airway in a manner that was similar to gross pathology. This made the technique immediately popular with investigators, and there was a flurry of publications on how to best trace the airway wall to produce the best images [McNamara *et al.* 1992], [Okazawa *et al.*, 1996], [Seneterre *et al.*, 1994]. It was quickly realized that quantitative measurements of airway structure were very dependent on the display parameters of the image [Bankier *et al.*, 1996], [Webb *et al.*, 1984], and that an automated computer approach that used the density attenuation values of the CT image was the correct method for analysis. Therefore, investigators turned their attention to developing algorithms that could measure the airway lumen and wall area on these CT scans. Some of the early approaches were very simple, using threshold techniques to find the lumen [McNitt-Gray *et al.*, 1997] and simple algorithms like the full-width at half maximum to assess the wall area [Nakano *et al.*, 2002], [Nakano *et al.*, 2002]. It was quickly decided that while these simple approaches had merit, they were not always the most accurate at determining airway dimensions. More complex algorithms using model-based approaches to provide more reliable measurements were developed [King *et al.*, 2000], [Reinhardt *et al.*, 1997], [Saba *et al.*, 2003], [San *et al.*, 2008], [Leader *et al.*, 2003]. Even though there is no consensus on the most appropriate method to measure airways, investigators have been using them to assess lung structure and function relationships in chronic obstructive pulmonary disease (COPD).

Early on, Nakano and coworkers used the full-width at half maximum method to measure the airway wall of the right apical segmental bronchus in a group of asymptomatic smokers and smokers with COPD [Nakano *et al.*, 2000]. This was an important study, even though it is well known that the major site of airflow limitation is the small airway, which a segmental bronchus clearly is not. However, these investigators were still able to show that there was a correlation between the percent of the total airway (lumen plus wall) that was airway wall

area (wall area percent [WA%]) and FEV1, FVC, and the residual volume (RV)/total lung capacity (TLC) [Nakano *et al.*, 2000]. Other investigators have shown similar findings [Berger *et al.*, 2005], [Niimi *et al.*, 2000], [Orlandi *et al.*, 2005], [Patel *et al.*, 2008], and further work from Nakano and colleagues showed that there was a correlation between airway wall measurements obtained using CT and those obtained using histology [Nakano *et al.*, 2005]. This is further backed up by other histologic data that show that in subjects with COPD, there is a thickening of the airway wall in the larger airways as well as the small airways [Tiddens *et al.*, 1995]. Other studies of large airways have shown that subjects with symptoms of chronic bronchitis have more airway wall thickening than those with airflow limitation but no symptoms [Orlandi *et al.*, 2005], [Patel *et al.*, 2008].

Because COPD is thought to be caused by airway wall remodeling, emphysema, or some combination of the two, it was hoped that CT could be used to differentiate the different COPD phenotypes. Since these phenotypes are likely to have a genetic component, Patel and coworkers used CT to quantify airway wall dimensions and emphysema in a cohort of subjects with COPD and their siblings [Patel *et al.*, 2008]. This study showed that there was a significant familial concordance of airway wall thickening such that if a subject with COPD has thickened airway walls, there is an increased odds ratio that their sibling would also have airway wall thickening [Patel *et al.*, 2008]. It has long been hypothesized that sex is responsible for differences in the airway wall dimensions. Using the NETT study, Martinez and colleagues showed that women had a higher airway wall area compared with lumen perimeter than men [Martinez *et al.*, 2007]. However, this cohort is a highly selected group of subjects chosen to be candidates for lung volume reduction surgery. Recently, using a community sample of smoking control subjects and subjects with COPD, Grydeland and coworkers showed that the airway wall area was higher in subjects with COPD and higher in men regardless of disease status [Grydeland *et al.*, 2009]. These authors also showed that airway wall thickness decreased slightly with increasing age in subjects with and without COPD, and that it increased with smoking history only in the control group. These studies indicate that there are differences in the structure of the airway wall that are very likely under some form of genetic control.

Appendix 4

Coxson and Lam [2009] in their publication have listed the limitations to the use of CT scanning to measure airways. Following material is extracted from their publication :

The first and obvious limitation is the resolution of the CT scanner. In usual clinical CT scanning, the field of view limits the pixel size to approximately 0.5 mm in the X and Y dimension. Furthermore, until the recent advent of multi-slice CT scanners that can acquire images with 0.5-mm slice thickness; the CT slice thickness has limited the Z dimension to 1 mm. This means that the airways that are responsible for airflow limitation are below the resolution of the CT scanner. A CT method that is becoming quite popular to assess small airway disease is gas trapping using expiratory CT scans (Figure A4.1). One of the first studies to look at expiratory CT was performed by Gevenois and colleagues, who reported that expiratory CT scans did not accurately quantify emphysema but probably reflect air trapping [Gevenois *et al.*, 1996]. Expiratory CT scans have been used to quantify air trapping in post-lung transplant bronchiolitis [de Jong *et al.*, 2006], [Dod *et al.*, 2008] and asthma [Busacker *et al.*, 2009], [Lee *et al.*, 2008],-[Zeidler *et al.*, 2006], but have not been used extensively in COPD research. Lee and colleagues have shown that expiratory lung density correlates the BODE index and that the CT measurement of air trapping correlates with physiologic measurements of air trapping [Lee *et al.*, 2008]. Akira and coworkers also used expiratory CT scans in subjects with COPD and found that expiratory CT scans are associated with pulmonary function in subjects with severe obstruction, but not in subjects with less severe obstruction [Akira *et al.*, 2009]. One of the drawbacks of expiratory CT scans is that they expose the subject to the extra radiation associated with a second CT scan. However, it is becoming recognized that expiratory CT scans do provide very useful information, and it is very likely that more studies using this approach will be performed in the near future [Coxson and Lam, 2009] .

A second limitation to the measurement of airways using CT scans is that there is no definitive data on the best algorithm to measure the airway wall. While a great deal of research has gone into airway wall algorithms [Reinhardt *et al.*, 1997], [Saba *et al.*, 2003], [Nakano *et al.*, 2000], [Hasegawa *et al.*, 2006], [Brown *et al.*, 2000], [King *et al.*, 1999], [Montaudon *et al.*, 2007], [Aykac *et al.*, 2003], [Tschirren *et al.*, 2005], there is no clear indication that one algorithm provides more useful data than another one [Coxson and Lam, 2009] .

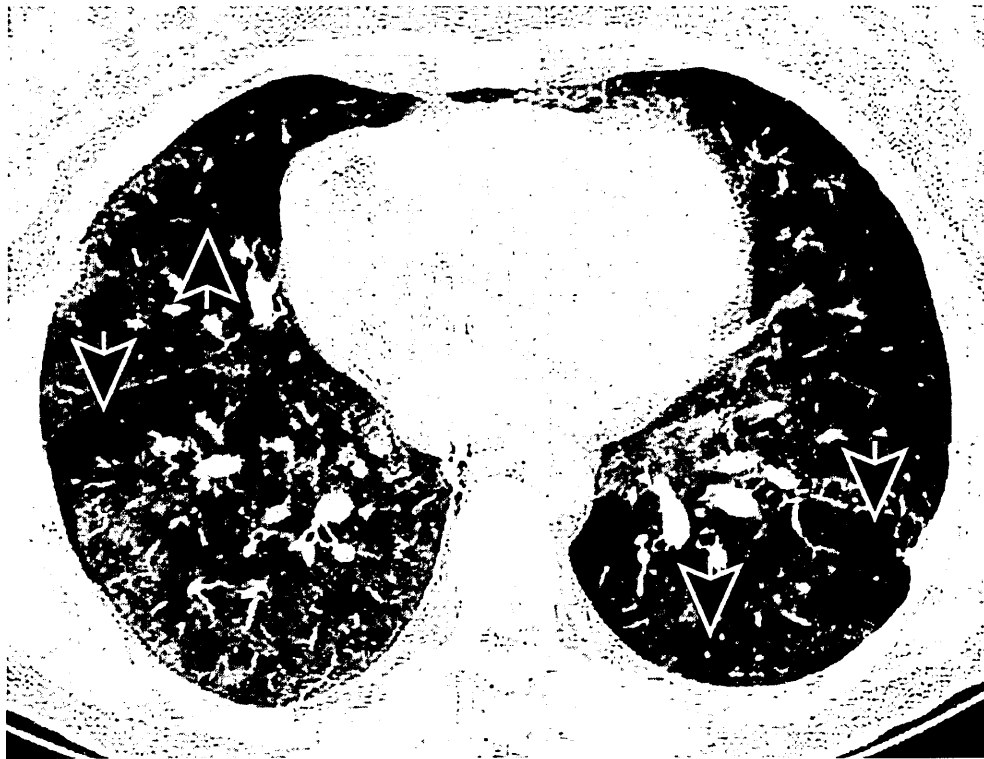


Figure A4.1 – Thin slice CT scan showing regions of gas trapping.

This figure shows a thin slice (1 mm slice thickness) CT scan acquired after expiration. Most of the lung has increased density (less dark), but parts of the lung are exhibiting signs of gas trapping (arrows) and appear darker on the image. It is thought that these regions of gas trapping are caused by small airway narrowing. (Image and caption courtesy Coxson and Lam, 2009).

Third, the analysis of airways using three-dimensional algorithms is still in its infancy, and while there is great hope that these data will provide more meaningful data than the simple sample of two-dimensional airways, the data are clearly lacking in this area. An obvious problem of the three-dimensional approach is that there are now many airways that can be "named" and measured, and because these data have never existed before, investigators do not know how many airways or how many airway paths to measure. It should also be noted that there are very few longitudinal studies of airways. Longitudinal analysis of airways is very problematic because the effect of CT image acquisition parameters such as X-ray dose, subject position, and volume of inspiration (to name a few) is completely unknown. It is very likely that the size of breath the subject takes will produce very different CT images of the airway tree, thereby affecting all of the data derived from the images. Finally, because airway measurements are still in their infancy and require specialized computer

hardware and software, these analyses have a long way to go before they become practical in the clinical setting. As such they remain in the research domain and are limited in their applicability [Coxson and Lam, 2009] .

Appendix 5

Pham *et al.* [2000] in their survey on the current methods in medical image segmentation have got the following to say regarding segmentations in digital X-ray mammograms :

Segmentation in digital mammography is typically performed for localization of tumours [Pohlman *et al.*, 1996], [Li *et al.*, 1995], micro-calcification clusters [Cheng *et al.*, 1998], [Ibrahim *et al.*, 1997], [Strickland and Hahn, 1996], or other indicators of pathology [Kallergi *et al.*, 1992]. In delineating suspicious masses for mammography, segmentation methods are typically employed in one of two ways. In the first approach, the mammogram is initially segmented into candidate regions which are then labelled as being suspicious or normal [Polakowski *et al.*, 1997], [Li *et al.*, 1995], [Ibrahim *et al.*, 1997], [Karssemeijer, 1997]. In the second approach, the image is first processed to detect for the presence of pathology and a segmentation is performed as a final step to determine its precise location [Cheng *et al.*, 1998], [Kupinski and Giger, 1998] [Gupta and Undrill, 1995], [Chen and Lee, 1995]. Thresholding and its variations are the most often used segmentation technique in X-ray mammography [Polakowski *et al.*, 1997], [Strickland and Hahn, 1996], [Cheng *et al.*, 1998], [Gupta and Undrill, 1995], [Ibrahim *et al.*, 1997], although extensions of region growing methods have also been proposed [Kupinski and Giger, 1998], [Pohlman *et al.*, 1996]. A comparison of thresholding and region growing was presented in [Kallergi *et al.*, 1992]. Because pathological areas often possess different textural properties in mammograms, Markov random field methods have also been successfully employed [Li *et al.*, 1995], [Chen and Lee, 1995].

Appendix 6

Figure A6.1 shows the hand written notes of the radiologist while she did the diagnosis of the sixteen cases. The first column has got the mini-MIAS case ID and the corresponding actual severity of the abnormality (noted after the diagnosis process).

kW v ; *T
(i-1*.

mini-MIAS Image ID	Breast Tissue Type (As specified in mini-MIAS)	Class of Abnormality (As specified in mini-MIAS)	Diagnosis and Comments
16. mdb002 6	Fatty Glandular	Circumscribed *	
8. mdb008	Fatty	Circumscribed	
14. mdb012	Fatty	Circumscribed	
7. mdb025 & I [Y]	Fatty	Circumscribed	
11. nmlb075 m	Fatty	Asymmetry	
6. mdb083	Fatty Glandular	Asymmetry	
5. mdb090 b j i FI I	Fatty Glandular	Asymmetry	
12. mdb092 m	Fatty	Asymmetry	
3. mdb093 II]	Fatty	Asymmetry	
4. mdb097 a	Fatty	Asymmetry	
2. mdb099 0	Dense Glandular	Asymmetry n	
1. mdb102 m	Dense Glandular	Asymmetry	
10. mdb104 r^L	Dense Glandular	Asymmetry	
9. nxlbl10	Dense Glandular	Asymmetry	
13. mdb141 m	Fatty	Circumscribed	
15. mdb270 YY\	Fatty Glandular	Circumscribed	

Figure A6.1 - Radiologist's diagnosis of the sixteen mini-MIAS cases.
This figure shows the handwritten notes of the Radiologist, made during diagnosing of the sixteen mini-MIAS cases.

References

1. AbuBaker,A.A, Qahwaji,R.S., Aqel,M.J., Al-Osta,H. and Saleh,M.H. "Efficient Pre-processing of USF and MIAS Mammogram Images", *Journal of Computer Science* 3 (2): 67-75, 2006.
2. Adel, M., Rassigni, M., Bourennane, S., and Juhan, V. "Statistical Segmentation of Regions of Interest on a Mammographic Image", *EURASIP Journal on Advances in Signal Processing*, Volume 2007, Article ID 49482. 2007
3. Akira M, Toyokawa K, Inoue Y, Arai T. "Quantitative CT in chronic obstructive pulmonary disease: inspiratory and expiratory assessment." *AJR American Journal of Roentgenol* 2009;192:267-272. 2009.
4. Alberdi, E., Povyakalo, A., Strigini, L. and Ayton, P. "Effects of incorrect computer-aided detection (CAD) output on human decision-making in mammography" *Academic Radiology* Volume 11, Issue 8, 2004. <http://www.dirc.org.uk/research/DIRC-Results/MammographvCitv.html> (Last visited on October 2011)
5. Alberdi, E., Povyakalo, A.A., Strigini, L., Ayton,P., Hartswood,M., Procter,R. and Slack,R. "Use of computer-aided detection (CAD) tools in screening mammography: a multidisciplinary investigation", *The British Journal of Radiology*, vol. 78, pp. 31-40. 2005.
6. Albertyn LE and Brown RV *Interpreting CT Head Scans A basic guide to image analysis*. Churchill Livingstone, Medical division of Pearson Professional Limited New York, 1996.
7. Amazon <https://www.mturk.com/mturk/welcome> (Last visited on October 2011)
8. Andreasen N.C., Rajarethinam R., Cizadlo T., Arndt S, Swayze VW 2nd, Flashman LA, O'Leary DS, Ehrhardt JC and Yuh WT. "Automatic atlas-based volume estimation of human brain regions from MR images." *Journal of Computer Assisted Tomography*, 20:98-106, 1996.
9. Andrey, P. and Tarroux, P., "Unsupervised segmentation of Markov random field modeled textured images using selectionist relaxation", *IEEE Transaction Pattern Anal. Machine Intelligence*, vol. 20, pp. 252-262.1998.
10. Arbelaez, P. "Boundary Extraction in Natural Images Using Ultrametric Contour Maps." *Proceedings 5th IEEE Workshop on Perceptual Organization in Computer Vision* (POCV'06). June 2006. New York, USA.
11. Arbelaez, P., Fowlkes, C. and Martin,.D., "The Berkeley Segmentation Dataset and Benchmark" <http://www.eecs.berkelev.edu/Research/Projects/CS/vision/bsds/> (Last updated June 2007)

12. Ayache N., Cinquin P., Cohen I., L. Cohen L., Leitner F., and Monga O. "Segmentation of complex three-dimensional medical objects: a challenge and a requirement for computer-assisted surgery planning and performance". In R.H. Taylor, S. Lavallee, G.C. Burdea, and R. Mosges, editors, *Computer-integrated surgery: technology and clinical applications*, pages 59-74. MIT Press, 1996.
13. Aykac D, Hoffman EA, McLennan G, Reinhardt JM. "Segmentation and analysis of the human airway tree from three-dimensional X-ray CT images." *IEEE Transaction on Medical Imaging* 2003;22:940-950. 2003.
14. Bae K.T., Giger M.L., Chen C., and Kahn C.E.. "Automatic segmentation of liver structure in CT images." *Medical Physics*, 20:71-78, 1993.
15. Bankier AA, Fleischmann D, Mallek R, Windisch A, Winkelbauer FW, Kontrus M, Havelec L, Herold CJ, Hiibsch P. "Bronchial wall thickness: appropriate window settings for thinsection CT and radiologic-anatomic correlation". *Radiology*, 199: 831-836. 1996.
16. Bazzocchi, M., Mazzarella, F., Del Frate, C., Girometti, R. and Zuiani, C. "CAD systems for mammography: a real opportunity? A review of the literature". *Radzo/ogy Medicine*;12(3):329 353. 2007.
17. Berger P, Perot V, Desbarats P, Tunon-de-Lara JM, Marthan R, Laurent F. "Airway wall thickness in cigarette smokers: quantitative thin-section CT assessment." *Radiology* 2005;235:1055-1064. 2005.
18. Bernstein, M., Little, G., Miller, R.C., Hartmann, B., Ackerman, M., Karger, D.R., Crowell, D., and Panovich, K. "Soylent: A Word Processor with a Crowd Inside." *In Proceedings. UIST2010. ACM Press*. 2010.
19. Besag J. "On the statistical analysis of dirty pictures". *CVGIP: Image Understand.*, 57:359-372,1986.
20. Beyer T. and Moonka R. "Normal mammography and ultrasonography in the setting of palpable breast cancer" Presented at the 89th Annual Meeting of the North Pacific Surgical Association, Seattle, Washington, November 8-9, 2002.
21. Bezdek J.C., Hall L.O., and Clarke L.P. "Review of MR image segmentation techniques using pattern recognition." *Medical Physics*, 20:1033-1048, 1993.
22. Bezdek, J.C., Hall, L.O. and Clarke, L.P. "Review of MR image segmentation techniques using pattern recognition", *Medical Physics*, vol. 20, pp. 1033-1048. 1993.
23. Bhattacharya, U., Chaudhuri, B. B. and Parui, S. K., "An MLP-based texture segmentation method without selecting a feature set" *Image and Vision Computing* 15 937-948, 1997.

24. Birdwell RL, Ikeda DM, O'Shaughnessy KF, Sickles EA. "Mammographic characteristics of 115 missed cancers later detected with screening mammography and the potential utility of computer-aided detection" *Radiology*;219(1):192-202. 2001.
25. Brem RF, Baum J, Lechner M, Kaplan S, Souders S, Naul LG, Hoffmeister J. "Improvement in sensitivity of screening mammography with computer-aided detection: a multiinstitutional trial" *AJR Am J Roentgenol*;181(3):687- 693. 2003
26. Brody AS, Klein JS, Molina PL, Quan J, Bean JA, Wilmott RW. "High-resolution computed tomography in young patients with cystic fibrosis: distribution of abnormalities and correlation with pulmonary function tests". *Journal of Paediatrics*;145:32-38. 2004.
27. Brown MS, Goldin JG, McNitt-Gray MF, Greaser LE, Sapra A, Li KT, Sayre JW, Martin K, Aberle DR. "Knowledge-based segmentation of thoracic computed tomography images for assessment of split lung function." *Medical Physics* 2000;27:592-598. 2000.
28. Busacker A, Newell JD Jr, Keefe T, Hoffman EA, Granroth JC, Castro M, Fain S, Wenzel S. "A multivariate analysis of risk factors for the air-trapping asthmatic phenotype as measured by quantitative CT nalysis." *Chest* 2009;135:48-56. 2009.
29. Caselles V., Catta F., Coll T., and Dibos F. "A geometric model for active contours." *Numerische Mathematik*, 66:1-31, 1993.
30. Caselles, V., Kimmel, R. and Sapiro, G. "Geodesic active contours", *International Journal of Computer Vision.*, vol. 22, pp. 61-79. 1997.
31. Chan HP, Doi K, Vyborny CJ, Schmidt RA, Metz CE, Lam KL, Ogura T, Wu YZ, MacMahon H. "Improvement in radiologists' detection of clustered microcalcifications on mammograms" *Radiology* 25, pp. 1102-1110; 1990.
32. Chan, H.-P., L.T. Niklason, D.M. Ikeda, K.L. Lam and D.D. Adler, "Digitizing requirements in mammography: Effects on computer aided detection of microcalcifications", *Med. Phys.*, 21:1203-1211. 1994. 2004.
33. Chaney E.L. and Pizer S.M. "Defining anatomical structures from medical images." *Seminars in Radiation Oncology*, 2:215-225, 1992.
34. Chen C.H. and Lee G.G. "On digital mammogram segmentation and microcalcification detection using multiresolution wavelet analysis". *Graphics Modelling and Image Processing.*, 59:349-364, 1997.
35. Cheng H. D and Cui M., "Mass Lesion Detection with a Fuzzy Neural Network", *Pattern Recognition*, vol. 37, pp. 1189-1200, 2004.

36. Cheng H., Lui Y.M., and Freimanis R.I. "A novel approach to microcalcification detection using fuzzy logic technique". *IEEE Transaction in Medical Imaging*, 17:442-450, 1998.
37. Cheng, H. D. and Ying Sun, "A hierarchical approach to color image segmentation using homogeneity", *IEEE Transactions on Image Processing*, VOL. 9, NO. 12, 2071-2082, 2000.
38. Christensen. G.E., Joshi S.C., and Miller M.I. "Volumetric transformation of brain anatomy." *IEEE Transactions in Medical Imaging*, 16:864-877, 1997.
39. Ciatto S, Ambrogetti D, Collini G, Cruciani A, Ercolini E, Risso G, Rosselli Del Turco M., "Computer-aided detection (CAD) of cancers detected on double reading by one reader only.", *Breast*. 2006 Aug;15(4):528-32. 2006.
40. Claridge, E., "Experts' assessment as a "gold standard" for characterisation of lesions" *In proceedings of Medical Image Analysis and Understanding Oxford* 1997.
41. Clark J.W. "Neural network modelling." *Physics in Medicine and Biology*, 36:1259-1317, 1991.
42. Clarke L.P., Velthuizen R.P., Camacho M.A., Heine J.J., Vaidyanathan M., Hall LO, Thatcher RW, Silbiger ML. "MRI segmentation: methods and applications." *Magnetic Resonance Imaging*, 13:343-368, 1995.
43. Cohen L.D., "On active contour models and balloons." *CVGIP: Image Understanding*, 53:211-218, 1991.
44. Coleman G.B. and Andrews H.C. "Image segmentation by clustering." *Proceedings IEEE*, 5:773-785, 1979.
45. Coleman G.B. and Andrews H.C., "Image segmentation by clustering", *Proc. IEEE*, vol. 5, pp. 773-785. 1979.
46. Collins D.L., Holmes C.J., Peters T.M., and Evans A.C. "Automatic 3-D model-based neuroanatomical segmentation." *Human Brain Mapping*, 3:190-208, 1995.
47. Coxson H.O. and Lam S. "Quantitative Assessment of the Airway Wall Using Computed Tomography and Optical Coherence Tomography", *The Proceedings of the American Thoracic Society* 6:439-443 2009.
48. Davatzikos C., Vaillant M., Resnick S., Prince J. L., Letovsky S., and R. N. Bryan R. N. "A computerized method for morphological analysis of the corpus callosum." *Journal Of Computer Assisted Tomography*, 20:88-97, 1996.
49. Davatzikos C. "Spatial normalization of 3D images using deformable models." *Journal Computer Assisted Tomography*, 20:656-665, 1996.

50. Davenport J.W., Bezdek J.C., and Hathaway R.J. "Parameter estimation for finite mixture distributions" *Computers and Mathematics with Applications*, 15:810-828, 1988.
51. Davies, E.R., and Plummer, A.P.N., "Thinning algorithms: A critique and a new methodology," *Pattern Recognition*, vol. 14, no. 1-6, pp. 53-63, 1981.
52. de Jong PA, Dodd JD, Coxson HO, Storne ss-Bliss C, Pare PD, Mayo JR, Levy RD. "Bronchiolitis obliterans following lung transplantation: early detection using computed tomographic scanning." *Thorax* 2006; 61:799-804. 2006.
53. de Jong PA, Müller NL, Paré PD and Coxson HO "Computed tomographic imaging of the airways: relationship to structure and function" *European Respiratory Journal*; 26:140-152. 2005.
54. de Jong PA, Nakano Y, Hop WC, Long FR, Coxson HO, Paré PD and Tiddens HA. "Changes in airway dimensions on computed tomography scans of children with cystic fibrosis.", *American Journal of Respiratory Critical Care Medicine*. 2005 Jul 15;172(2):218-24. 2005 (July).
55. de Jong PA, Nakano Y, Lequin MH, Mayo JR, Woods R, Pare PD, Tiddens HA. "Progressive damage on high resolution computed tomography despite stable lung function in cystic fibrosis". *European Respiratory Journal*;23:93-97. 2004.
56. Dodd JD, Barry SC, Barry RB, Gallagher CG, Skehan SJ and Masterson JB. "Thin-section CT in patients with cystic fibrosis: correlation with peak exercise capacity and body mass index". *Radiology* 240:236-245. 2006.
57. Dodd JD, de Jong PA, Levy RD, Coxson HO, Mayo JR. "Conventional high-resolution CT versus contiguous multidetector CT in the detection of bronchiolitis obliterans syndrome in lung transplant recipients." *Journal of Thoracic Imaging* 2008;23:235-243. 2008.
58. Dollar, P., Tu, Z. and Belongie, S. "Supervised Learning of Edges and Object Boundaries, *IEEE Computer Vision and Pattern Recognition (CVPR)*, June, 2006.
59. Dunn J.C. "A fuzzy relative of the ISODATA process and its use in detecting compact well-separated clusters." *Journal of Cybernetics*, 3:32-57, 1973.
60. Elter M, A.L. and Horsch, A., "CADx of mammographic masses and clustered microcalcifications review" *Medical Physics* 2009 Jun;36(6):2052-68. 2009.
61. Estrada, F. J. and Jepson, A. D. "Benchmarking Image Segmentation Algorithms", *International Journal of Computer Vision*, Vol. 85, No. 2, p. 167, 2009.
62. Fayad LM, Jin Y, Laine AF, Berkmen YM, Pearson GD, Freedman B, Van Heertum R. "Chest CT Window Settings with Multiscale Adaptive Histogram Equalization: Pilot Study" *Radiology* 223, pp 845-852, 2002.

63. Fitzgibbon, A.W.; Pilu, M.; Fisher, R.B. "Direct least-square fitting of Ellipses", *International Conference on Pattern Recognition*, Vienna, August 1996.
64. Freiherr, G. "Medical imaging takes key role in revolutionary new cancer protocol", *Diagnostic Imaging* March 2010 <http://www.diagnosticimaging.com/>
65. Gale, A., Krupinski, E.A., and Manning, D.J. "Medical Image Perception Society Conference XI", *The British Journal of Radiology*, 79, S109-S1101. 2006.
66. Gelenbe E., Feng Y., and Krishnan K.R.R. "Neural network methods for volumetric magnetic resonance imaging of the human brain." *Proceedings IEEE*, 84:1488-1496, 1996.
67. Geman S. and Geman D. "Stochastic relaxation, Gibbs distributions, and the Bayesian restoration of images." *IEEE Transaction on Pattern Analysis and Machine Intelligence*, PAMI-6:721-741, 1984.
68. Gevenois PA, De Vuyst P, Sy M, Scillia P, Chaminade L, de Maertelaer V, Zanen J, Yemault J-C. "Pulmonary emphysema: quantitative CT during expiration." *Radiology* 1996;199:825-829. 1996.
69. Girometri, R., Cereser, L., Bazzocchi, M. and Zuiani, C. "CAD comes under scrutiny in breast screening debate", *Diagnostic Imaging Europe*. Vol. 26 No. 7 October 29, 2010.
70. Goergen SK, Evans JE, Cohen GPB, and MacMillan JH. "Characteristics of breast carcinomas missed by screening radiologists". *Radiology*, 204:131-135 1997.
71. Goldszal A.F., Davatzikos C., Pham D.L., Yan M.X.H., Bryan R.N., and Resnick S.M. "An image processing system for qualitative and quantitative volumetric analysis of brain images." *Journal of Computer Assisted Tomography*, 22:827-837, 1998.
72. Gonzalez, R. C., Richard, E. W., "Digital Image Processing", *Addison Wesley*, 1992.
73. Gonzalez R.C. and Woods R.E. "Digital Image Processing." *Addison-Wesley*, 1992
74. Gonzalez, R.C., and Wintz, P. "Digital image processing", *Addison-Wesley*, 1987.
75. Graham, R.L. "An efficient algorithm for determining the convex hull of a finite planar set" *Information Processing Letters* 1,132-3 1972
76. Grimson W.E.L., Ettinger G.J., Kapur T., Leventon M.E., Wells W.M. and R. Kikinis R. "Utilizing segmented MRI data in image-guided surgery." *International Journal Pattern Recognition Artificial Intelligence*, 11:1367-1397, 1997.

77. Grydeland TB, Dirksen A, Coxson HO, Pillai SG, Sharma S, Eide GE, Gulsvik A, Bakke PS. "Quantitative CT: Emphysema and airway wall area by gender, age and smoking." *European Respiratory Journal* October 1, 2009 vol.34 no.4 858-865. 2009.
78. Gupta R. and Undrill P.E. . "The use of texture analysis to delineate suspicious masses in mammography". *Physics. Medicine and Biology*, 40:835-855, 1995.
79. Hall L.O., Bensaid A.M., Clarke L.P., Velthuizen R.P., Silbiger M.S., and Bezdek J.C. "A comparison of neural network and fuzzy clustering techniques in segmenting magnetic resonance images of the brain." *IEEE Transaction on Neural Networks*, 3:672-682, 1992.
80. Han D., Li W., Lu X., Wang T., and Wang Y. "Automatic Segmentation Based on AdaBoost Learning and Graph-Cuts" A. Campilho and M. Kamel (Eds.): *ICIAR 2006, LNCS 4141*, pp. 215-225, 2006 *Image Analysis and recognition: third international conference, ICIAR 2006, Povia de Varzim, Portugal, September 18-20, 2006*.
81. Haralick R.M. and Shapiro L.G. "Image segmentation techniques." *Computer Vision Graphics and Image Processing*, 29:100-132, 1985.
82. Haralick, R. M., Shanmugam, K., Dinstein, I., "Textural Features for Image Classification", *IEEE Transactions in Systems, Man, and Cybernetics*, Vol. SMC-3, No. 6, Pages 610-621. 1973.
83. Hartwood, M., Procter, R., Williams, L., Prescott, R. and Dixon, P. "Drawing the line between perception and interpretation in computer-aided mammography" *In Proceedings of the First International Conference on Allocation of Functions: Allocation of Functions*; 01 Oct 1997-03 Oct 1997; Galway. International Ergonomics Association Press; 1997. p. 275-291. 1997.
84. Hartwood, M., Procter, R., and Williams, L. "Prompting in mammography: Computer-aided Detection or Computer-aided Diagnosis" In: *Proceedings of the Second Medical Image Understanding and Analysis Conference*, Leeds, July, 1998
85. Hasegawa M, Nasuhara Y, Onodera Y, Makita H, Nagai K, Fuke S, Ito, Betsuyaku T, Nishimura M. "Air-flow limitation and airway dimensions in chronic obstructive pulmonary disease." *American Journal of Respiratory and Critical Care Medicine* 2006;173:1309-1315. 2006.
86. Hashimoto, B. and Bauermeister, D. *Breast Imaging: A correlative Atlas*, Thieme Medical Publishers 2003.
87. Haykin S. "Neural networks: a comprehensive foundation." Macmillan College, New York, 1994.
88. Hebert T.J. "Fast iterative segmentation of high resolution medical images." *IEEE Transaction on Nuclear Science*, 44:1363-1367, 1997.

89. Helbich TH, Heinz-Peer G, Eichler I, et al. "Cystic Fibrosis: CT Assessment of Lung Involvement in Children and Adults". *Radiology*. 213:537-544. 1999.
90. Held K., Kops E.R., Krause B.J., Wells W.M., Kikinis R., and Hans-Wilhelm H. "Markov random field segmentation of brain MR images." *IEEE Transaction on Medical Imaging*, 16(6), 1997.
91. Ibrahim N., Fujita H. , Hara T., and Endo T. "Automated detection of clustered microcalcifications on mammograms: CAD system application to MIAS database". *Physics Medicine and Biology*, 42:2577-2589, 1997.
92. Jain, A.K. and Dubes, R.C., "Algorithms for Clustering Data", Prentice Hall, 1988.
93. Jeon, M., Alexander, M., Pedrycz, W. and Pizzi, N. "Unsupervised hierarchical image segmentation with level set and additive operator splitting", *Pattern Recognition Letter* 26 1461-1469 2005.
94. Johnson, CD, "Hard- versus Soft-Copy Interpretation" *Radiology* 227, pp 629-630, 2003.
95. Joshi. S.C., Miller M.I. and Grenander U. "On the geometry and shape of brain sub-manifolds." *International Journal on Pattern Recognition and Artificial Intelligence*, 11:1317-1343, 1997.
96. Kallergi M., Woods K., Clarke L.P., Qian W., and Clark R.A. "Image segmentation in digital mammography: comparison of local thresholding and region growing algorithms." *Computer in Medical Imaging and Graphics*, 16:323-331, 1992.
97. Kannan, R., Vempala, S. and Vetta, A. "On Clusterings - Good, Bad and Spectral", Technical Report, Computer Science Department, Yale University. 2000.
98. Kapur T., Grimson W.E.L., Kikinis R. and. Wells W.M. "Enhanced spatial priors for segmentation of magnetic resonance imagery." In Proc. 1st Int. Conference Medical Image Computation Computer Assisted Intervention (MICCAI98), pages 457-468, 1998.
99. Karssemeijer N. "Automated classification of parenchymal patterns in mammograms". *Physics Medicine and Biology*, 43:365-389, 1998.
100. Kass M., Witkin A. and Terzopoulos D. "Snakes: Active contour models." *International Journal on Computer Vision*, 1:321-331, 1988.
101. Kegelmeyer Jr., W.P.; Pruneda, J.M.; Bourland, P.D.; A. Hillis, A.; Riggs, M.W. and Nipper, M.L.; "Computer-aided mammographic screening for spiculated lesions", *Radiology*, vol. 191, pp. 331-336, May 1994.

102. Khoo V.S., Dearnaley D.P., Finnigan D.J., Padhani A., S.F. Tanner S.F., and Leach M.O. "Magnetic resonance imaging (MRI): considerations and applications in radiotherapy treatment planning." *Radio-therapy Oncology*, 42:1-15, 1997.
103. Kim, I.Y. and Yang, H.S "A systematic way for region based image segmentation based on Markov random field model", *Pattern Recognition Letters*, vol. 15, pp. 969-976. 1994.
104. King G.G., Carroll J.D., Müller N.L., Whittall K.P., Gao M., Nakano Y. and Paré P.D., "Heterogeneity of narrowing in normal and asthmatic airways measured by HRCT". *European Respiratory Journal*; 24: 211-218. 2004.
105. King G.G., Muller N.L., Pare P.D.. "Evaluation of airways in obstructive pulmonary disease using high-resolution computed tomography." *American Journal of Respiratory and Critical Care Medicine* 1999;159:992-1004. 1999.
106. King G.G., Muller N.L., Whittall K.P., Xiang Q.S., Pare P.D. "An analysis algorithm for measuring airway lumen and wall areas from high-resolution computed tomographic data". *American Journal of Respiratory Critical Care Medicine*; 161: 574-580. 2000.
107. Kiraly, Atilla P., Odry, Benjamin L., Godoy, Myrna C. B., Geiger, Bernhard, Novak, Carol L., and Naidich, David P. "Computer-aided Diagnosis of the Airways: Beyond Nodule Detection", *Journal of Thoracic Imaging*, Volume 23 - Issue 2 - pp 105-113. May 2008.
108. Kopanes, D.B., "*Breast Imaging*." 2nd Edn. Philadelphia, PA: Lippincott-Raven. 1999.
109. Kopans, D.B. *Breast Imaging*, Lippincott Williams & Wilkins Publishers 2007.
110. Kupinski M.A. and Giger M.L. "Automated seeded lesion segmentation on digital mammograms". *IEEE Transaction on Medical Imaging*, 17:510-517, 1998.
111. Lancaster J.L., Rainey L.H., Summerlin J.L., Freitas C.S., Fox P.T., Evans A.C., Toga A.W., and Mazziotta J.C. "Automated labeling of the human brain: A preliminary report on the development and evaluation of a forward-transform method." *Human Brain Mapping*, 5:238-242, 1997.
112. Larie S.M. and S.S. Abukmeil S.S. "Brain abnormality in schizophrenia: a systematic and quantitative review of volumetric magnetic resonance imaging studies." *Journal of Psychology*, 172:110-120, 1998.
113. Leader JK, Zheng B, Rogers RM, Sciurba FC, Perez A, Chapman BE, Patel S, Fuhrman CR, Gur D. "Automated lung segmentation in X-ray computed tomography: development and evaluation of a heuristic threshold-based scheme." *Academic Radiology* 2003;10:1224-1236. 2003.

114. Lee C., Hun S., Ketter T.A., and Unser M. "Unsupervised connectivity-based thresholding segmentation of midsagittal brain MR images." *Computer in Biology and Medicine*, 28:309-338, 1998.
115. Lee KY, Park SJ, Kim SR, Min KH, Choe YH, Jin GY, Lee YC. "Low attenuation area is associated with air-ow limitation and airway hyperresponsiveness." *Journal of Asthma* 2008;45:774-779. 2008.
116. Lee YK, Oh YM, Lee JH, Kim EK, Kim N, Seo JB, Lee SD. "Quantitative assessment of emphysema, air trapping, and airway thickening on computed tomography." *Lung* 2008;186:157-165. 2008.
117. Lei T. and Sewchand W. "Statistical approach to X-Ray CT imaging and its applications in image analysis - part II: A new stochastic model-based image segmentation technique for X-Ray CT image." *IEEE Transaction on Medical Imaging*, 11(1):62-69, 1992.
118. Lev, M.H., Farkas, J., Gemmete, J.J., Hossain, S.T., Hunter, G.J., Koroshetz, W.J. and Gonzalez, R.G., "Acute Stroke: Improved Nonenhanced CT Detection-Benefits of Soft-Copy Interpretation by using variable window width and center level settings", *Radiology* 213, Pages 150-155. 1999.
119. Li H.D., Kallergi M., Clarke L.P., Jain V.K., and R.A. Clark R.A.. "Markov random field for tumor detection in digital mammagraphy." *IEEE Transaction on Medical Imaging*, 14:565-576, 1995.
120. Li H., Deklerck R., De Cuyper B., Hermanus A., Nyssen E., and Cornelis J. "Object recognition in brain CT-scans: knowledge-based fusion of data from multiple feature extractors". *IEEE Transaction on Medical Imaging*, 14:212-229, 1995.
121. Li H.D., Kallergi M., Clarke L.P., Jain V.K., and Clark R.A. "Markov random field for tumour detection in digital mammagraphy". *IEEE Transaction in Medical Imaging*, 14:565-576, 1995.
122. Li S.Z.. "Markov random field modeling in computer vision." Springer, 1995.
123. Li, S.Z. *Markov random field modelling in computer vision*. Springer, 1995.
124. Liane E. and Philpotts, "Can Computer-aided Detection Be Detrimental to Mammographic Interpretation?", *Radiology*, 253, 17-22. October 2009.
125. Liang Z., MacFall J.R., and Harrington D.P.. "Parameter estimation and tissue segmentation from multispectral MR images." *IEEE Transaction on Medical Imaging*, 13:441-449, 1994.
126. Liu S., Babbs C.F. and Delp E.J. "Multiresolution Detection of Spiculated Lesions in Digital Mammograms", *IEEE Transactions on Image Processing*, vol. 10, no. 6, June 2001.

127. Long FR, Williams RS, Castile RG. "Structural airway abnormalities in infants and young children with cystic fibrosis.", *Journal of Paediatrics* 2004 Feb;144(2):154-61. 2004.
128. Lu, Q. and Jiang, T. "Pixon-based image denoising with Markov random fields", *Pattern Recognition*, vol. 34, pp.2029-2039. 2001.
129. Maintz J.B.A. and Viergever M.A. "A survey of medical image registration." *Medical Imaging Analysis* 2:1-36 1998.
130. Malladi R., Sethian J.A., and B.C. Vemuri B.C.. "Shape modeling with front propagation: A level set approach." *IEEE Transaction on Pattern Analysis and Machine Intelligence*, 17:158-175, 1995.
131. Mangin J.F., Frouin V., Bloch I., Regis J., and Lopez-Krahe J. "From 3D magnetic resonance images to structural representations of the cortex topography using topology preserving deformations." *Journal of Mathathematical Imaging and Visualisation*, 5:297-318, 1995.
132. Martin D.R., Fowlkes C.C., and Malik J., "Learning to Detect Natural Image Boundaries Using Local Brightness, Color, and Texture Cues", *IEEE Transactions on Pattern Analysis and Machine Intelligence*, VOL. 26, NO. 1, January 2004.
133. Martin, D., Fowlkes, C., Tal, D. and Malik, J. "A database of human segmented natural images and its application to evaluating segmentation algorithms and measuring ecological statistics" *International Conference on Computer Vision*, Vancouver, Canada. 2001.
134. Martin, D.R., Fowlkes, C.C., and Malik, J. "Learning to Detect Natural Image Boundaries Using Brightness and Texture," *Computer* Volume: 15, Issue: December, Publisher: MIT Press, Pages: 1-8. 2002.
135. Martinez FJ, Curtis JL, Sciurba F, Mumford J, Giardino ND, Weinmann G, Kazerooni E, Murray S, Criner GJ, Sin DD, Hogg J, AL Ries, Hanl M, Fishman AP, Make B, Hoffman EA, Mohsenifar Z and Wise R "Sex differences in severe pulmonary emphysema." *American Journal of Respiratory and Critical Care Medicine* 2007; 176:243-252. 2007.
136. Matsuoka S, Kurihara Y, Nakajima Y, Niimi H, Ashida H and Kaneoya K. "Serial change in airway lumen and wall thickness at thin-section CT in asymptomatic subjects". *Radiology* 234: 595-603. 2005.
137. McInerney T. and Terzopoulos D. "Deformable models in medical image analysis: a survey." *Medical Image Analysis*, 1:91-108, 1996.
138. McInerney T. and Terzopoulos D. "Topologically adaptable snakes." In *Proceedings Fifth International Conference on Computer Vision*, pages 840-845, 1995.

- 139.McNamara AE, Muller NL, Okazawa M, Amtorp J, Wiggs BR, Pare PD. "Airway narrowing in excised canine lung measured by high-resolution computed tomography". *Journal of Applied Physiology*; 73: 307-316. 1992.
- 140.McNitt-Gray MF, Goldin JG, Johnson TD, Tashkin DP, Aberle DR. "Development and testing of image-processing methods for the quantitative assessment of airway hyperresponsiveness from high-resolution CT images". *Journal of Computer Assisted Tomography*, 21: 939-947. 1997.
- 141.MobileWorks <http://www.mobileworks.com/index.html> (Last visited on October 2011)
- 142.Montaudon M, Berger P, de Dietrich G, Braquelaire A, Marthan R, Tunon-de-Lara JM, Laurent F. "Assessment of airways with three-dimensional quantitative thin-section CT: in vitro and in vivo validation." *Radiology* 2007;242:563-572. 2007.
- 143.Moon, MA "Breast Density Predicts Mammography Failure". *OB/GYN News*. May 15, 2000.
- 144.Mugglestone, M., Lomax, R., Gale, A.G., Wilson ARM "The effect of prompting mammographic abnormalities on the human observer" *In Proceedings of the Third International Workshop on Digital Mammography. Chicago*, pp. 87-92 June 1996.
- 145.Muller-Gartner H.W., Links J.M., Prince JL, Bryan RN, McVeigh E, Leal JP, Davatzikos C, and Frost JJ. "Measurement of radiotracer concentration in brain gray matter using positron emission tomography: MRI-based correction for partial volume effects." *Journal of Cerebral Blood Flow and Metabolism*, 12:571-583, 1992.
- 146.Mumcuoglu EU, Prescott J, Baker BN, Clifford B, Long F, Castile R, and Gurcan MN. "Image analysis for cystic Fibrosis: automatic lung airway wall and vessel", *Conference Proceeding IEEE Engineering Medicine Biology Soc.*; 2009:3545-8. 2009.
- 147.Nadler, M. and Smith, E. P. *Pattern Recognition Engineering* John Wiley and Sons inc. 1993.
- 148.Nakano Y, Muro S, Sakai H, Hirai T, Chin K, Tsukino M, Nishimura K, Itoh H, Pare PD, Hogg JC, Mishima M. "Computed tomographic measurements of airway dimensions and emphysema in smokers. Correlation with lung function". *American Journal of Respiratory Critical Care Medicine*, 162: 1102-1108. 2000.
- 149.Nakano Y, Whittall KP, Kalloger SE, Coxson HO, Pare PD, English JC. "Development and validation of human airway analysis algorithm using multidetector row CT". *Proceedings of SPIE*; 4683: 460-469. 2002.

150. Nakano Y, Wong JC, de Jong PA, Buzatu L, Nagao T, Coxson HO, Elliott WM, Hogg JC, Pare PD. "The prediction of small airway dimensions using computed tomography. *American Journal of Respiratory and Critical Care Medicine*" 2005;171:142-146. 2005.
151. Ng, A.Y., Jordan, M.I. and Weiss Y. "On Spectral Clustering: Analysis and an algorithm", *In Advances in Neural Information Processing Systems* 14. 2001.
152. NHSBSP, "Working Party of the Radiologists Quality Assurance Coordinating Group. Computer aided detection in mammography", *NHSBSP Publication* No. 48. London, UK: NHSBSP, 2001.
153. NIH-Publication-No.-95-3650
http://www.ornl.gov/sci/techresources/Human_Genome/posters/chromosome/cf.shtml (Last visited on October 2011)
154. Niimi A, Matsumoto H, Amitani R, Nakano Y, Mishima M, Minakuchi M, Nishimura K, Itoh H, Izumi T. "Airway wall thickness in asthma assessed by computed tomography: relation to clinical indices." *American Journal of Respiratory and Critical Care Medicine* 2000;162:1518-1523. 2000.
155. Nishikawa RM. and Vybomy, CJ. "Current status and future directions of computer-aided diagnosis in mammography", *Comput Med Imaging Graph.* 2007 Jun-Jul;31(4-5):224-35. 2007.
156. O'Rourke J. *Computational Geometry in C* (page 86) Cambridge University press, 2nd Edition, 1998.
157. Ohlander, R., Price, K., and Reddy. R. "Picture segmentation by a recursive region splitting method" *Computer Graphics Image Processing*, 8:313-333, 1978.
158. Okazawa M, Muller NL, McNamara AE, Child S, Verburgt L, Pare PD. "Human airway narrowing measured using high resolution computed tomography". *American Journal of Respiratory Critical Care Medicine*; 154: 1557-1562. 1996.
159. Oliver A., Freixenet J, Marti R. and Zwiggelaar R. "A comparison of breast tissue classification techniques". *Medical Image Computer Assisted Intervention*. 2006;9(Pt 2):872-9. 2006.
160. Oliver A., Freixenet J., Marti J., Perez E., Pont J., Denton E.R. and Zwiggelaar R. "A review of automatic mass detection and segmentation in mammographic images", *Medical Image Analysis*. 2010 Apr;14(2):87-110. 2010.
161. Onega T, Aiello Bowles EJ, Miglioretti DL, Carney PA, Geller BM, Yankaskas BC, Kerlikowske K, Sickles EA, Elmore JG. "Radiologists' perceptions of computer aided detection versus double reading for mammography interpretation", *Academic Radiology*. 2010 Oct;17(10):1217-26. 2010.

- 162.Orlandi I, Moroni C, Camiciottoli G, Bartolucci M, Pistolesi M, Villari N, Mascalchi M. "Chronic obstructive pulmonary disease: thin-section CT measurement of airway wall thickness and lung attenuation". *Radiology* 2005;234:604-610. 2005.
- 163.Osanai, T., Gomi, N., Wakita, T., Yamashita, T., Ichikawa, W., Nihel, Z. and Sugihara, K. "Ultrasound-guided Core Needle Biopsy for Breast Cancer: Preliminary Report", *Japan Journal of Clinical Oncology*; 30(2)65-67. 2000.
- 164.Pappas T.N. "An adaptive clustering algorithm for image segmentation." *IEEE Transaction on Signal Processing*, 40:901-914, 1992.
- 165.Patel BD, Coxson HO, Pillai SG, Agusti AGN, Calverley PMA, Donner CF, Make BJ, Muller NL, Rennard SI, Vestbo J, Wouters, E, Hiorns, M, Nakano, Y, Camp, P, Nasute Fauerbach, P, Screaton, N, Campbell, E, Anderson, W, Silverman, E, Lomas, D "Airway wall thickening and emphysema show independent familial aggregation in COPD." *American Journal of Respiratory and Critical Care Medicine* 2008;178:500-505. 2008.
- 166.Pathak S.D., Grimm P.D., Chalana V., and Kim Y. "Pubic arch detection in transrectal ultrasound guided prostate cancer therapy." *IEEE Transaction on Medical Imaging*. 17:762-771, 1998.
- 167.Pham D.L. and Prince J.L. "An adaptive fuzzy c-means algorithm for image segmentation in the presence of intensity inhomogeneities." *Pattern Recognition Letters*, pages 57-68, 1999.
- 168.Pham D.L, Xu C.Y. and Prince J.L. "A survey of current methods in medical image segmentation", *Annual Review of Biomedical Engineering, Annual Reviews*, vol. 2, pp. 315-337, 2000. [Technical report version, JHU/ECE 99-01, Johns Hopkins University].
- 169.Philpotts, LE, "Can Computer-aided Detection Be Detrimental to Mammographic Interpretation?" *Radiology* October 2009 253, 17-22. 2009.
- 170.Pitas, I., *Digital Processing Algorithms and Applications*, John Wiley and Sons, Inc. 2000.
- 171.Pohlman S., Powell K.A., Obuchowski N.A., Chilcote W.A., and Grundfest-Broniatowski S. "Quantitative classification of breast tumors in digitized mamograms". *Medical Physics*, 23:1337-1345, 1996.
- 172.Polakowski W.E., Cournoyer D.A., Rogers SK., DeSimio M.P., Ruck D.W., Hoffmeister J.W., and Raines R.A. "Computer-aided breast cancer detection and diagnosis of masses using difference of Gaussians and derivative-based feature saliency". *IEEE Transaction in Medical Imaging*, 16:811-819, 1997.
- 173.Press, W.H., Teukolsky, S. A., Vetterling, W.T., and Flannery, B.P. *Numerical Recipes in C The Art of Scientific Computing*, Second Edition Cambridge University Press, 2002.

174. Rahbar G., Sie A.C., Hansen G.C., Prince J.S., Melany M.L., Reynolds H.E., Jackson V.P., Sayre J.W. and Bassett L.W. "Benign versus Malignant Solid Breast Masses: US Differentiation" From the 1996 RSNA scientific assembly. 1999.
175. Rajapakse J.C., Giedd J.N., and Rapoport J.L. "Statistical approach to segmentation of single-channel cerebral MR images." *IEEE Transaction in Medical Imaging*, 16:176-186, 1997.
176. Reddick W.E., Glass J.O., Cook E.N., Elkin T.D., and Deaton R.J. "Automated segmentation and classification of multispectral magnetic resonance images of brain using artificial neural networks." *IEEE Transaction on Medical Imaging*, 16:911-918, 1997.
177. Reed T.R. and Hans Du Buf J.M. "A review of recent texture segmentation and feature extraction techniques." *CVGIP: Image Understanding*, 57:359-372, 1993.
178. Reinhardt JM, D'Souza ND, Hoffman EA. "Accurate measurement of intrathoracic airways". *IEEE Transaction Medical Imaging*; 16: 820-827. 1997.
179. Rossand G., Lorenzo C., Massimo B. and Chiara Z., "CAD comes under scrutiny in breast screening debate" *Diagnostic Imaging Europe*. Vol. 26 No. 7 October 29, 2010.
180. Saba OI, Hoffman EA, Reinhardt JM. "Maximizing quantitative accuracy of lung airway lumen and wall measures obtained from X-ray CT imaging". *Journal of Applied Physiology*; 95: 1063-1075. 2003.
181. Sahoo P.K., Soltani S. and Wong A.K.C. "A survey of thresholding techniques." *Computer Vision Graphics and Image Processing*, 41:233-260, 1988.
182. Sahoo, P.K, Soltani, S. and Wong, A.K.C., "A survey of thresholding techniques", *Computer Vision Graphics and Image Processing*, vol. 41, pp. 233-260. 1988.
183. Sameti, M. "Detection of soft tissue abnormalities in mammographic images for early diagnosis of breast cancer" Doctor of Philosophy dissertation, Department of Electrical and Computer Engineering, The University of British Columbia. November 1998.
184. San Jose Estepar R, Reilly JJ, Silverman EK, Washko GR. "Three-dimensional airway measurements and algorithms." *Proceedings of American Thoracic Society* 2008;5:905-909. 2008.
185. Sandor S. and Leahy R. "Surface-based labeling of cortical anatomy using a deformable atlas." *IEEE Transacton on Medical Imaging*, 16:41-54, 1997.
186. Sarkar, A. Biswas, M.K. and Sharma, K.M.S. "A simple unsupervised MRF model based image segmentation approach", *IEEE Transaction and Image Processing*, vol. 9, pp. 801-812. 2000.

- 187.Schalkoff R.J. "Pattern recognition: statistical, structural and neural approaches." John Wiley and Sons, 1992.
- 188.Schroeter, P. and Bigun, J. "Hierarchical image segmentation by multi dimensional clustering and orientation-adaptive boundary refinement", *Pattern Recognition*, Vol. 28, No. 5, pp. 695-709. 1995.
- 189.Selvan, A.N.; Saatchi, R.; Amavasai, B.P.; Travis, J.R; "A Dissimilarity Visualisation System for CT: Pilot Study" *In The International Conference on Computer as a Tool*. EUROCON Serbia & Montenegro, Belgrade, November 22-24, 2005. Volume 2, Pages:1007 - 1010, 2005.
- 190.Selvan, A.N., "Highlighting Dissimilarity in Medical Images Using Hierarchical Clustering Based Segmentation (HCS)" *MPhil. dissertation*, Faculty of Arts Computing Engineering and Sciences, Sheffield Hallam University, Sheffield, UK, 2007.
- 191.Selvan, A.N., Saatchi, R. and Ferris, C.M. "Improving Medical Image Perception by Hierarchical Clustering based Segmentation" //?: *9th International Conference on Information Technology and Applications in Biomedicine*, Lamaka, Cyprus, 4-7 November, 2009.
- 192.Selvan, A. N., Saatchi, R. and Ferris, C. M. "Computer Aided Monitoring of Breast Abnormalities in X-ray Mammograms". *In Medical Image Understanding and Analysis Conference*, London, 14-15 July, 2011.
- 193.Selvan, A. N., "Boundary Extraction in Images Using Hierarchical Clustering-based Segmentation" *British Machine Vision Conference (Student workshop)*, Dundee, UK, Sept. 2011.
- 194.Seneterre E, Paganin F, Bruel JM, Michel FB, Bousquet J. "Measurement of the internal size of bronchi using high resolution computed tomography (HRCT)". *European Respiratory Journal*, 7: 596-600.1994.
- 195.Shi, J., and Malik, J. "Normalized Cuts and Image Segmentation",In Proceedings, of IEEE Conference on Computer Vision and Pattern Recognition, Puerto Rico. 1997.
- 196.Sijbers J., Scheunders P., M. Verhoye M., A. Van Der Linden A., Van Dyck D. and Raman E. "Watershed-based segmentation of 3D MR data for volume quantization." *Magnetic Resonance Imaging*, 15:679-688, 1997.
- 197.Sonka, M. and Fitzpatrick, J. M. *Handbook of Medical Imaging Volume 2 Medical Image Processing and Analysis*. Published by SPIE The international society for optical engineering.2000.
- 198.Soylent <http://projects.csail.mit.edu/soylent/> (Last visited on October 2011)
- 199.Strickland R.N. and Hahn H.I. "Wavelet transforms for detecting microcalcifications in mammograms". *IEEE Transaction in Medical Imaging*, 15:218-229, 1996.

200. Suckling, J., Parker, J., Dance, DR., Astley, S., Hutt, I., Boggis, C., Ricketts, I., Stamatakis, E., Cemeaz, N., Kok, SL., Taylor, P., Betal, D., and Savage, J., "The Mammographic Image Analysis Society Digital Mammogram Database" *Exerpta Medica. International Congress* Series 1069 pp375-378, 1994. [mini-MIAS <http://peipa.essex.ac.uk/info/mias.html> (Last visited on October 2011)]
201. Suetens P., Bellon E., Vandermeulen D., Smet M., Marchal G., Nuyts J., and Mortelmans L.. "Image segmentation: methods and applications in diagnostic radiology and nuclear medicine." *European Journal of Radiology*, 17:14-21, 1993.
202. Tabar L. and Dean P; *Teaching atlas of Mammography* New York: Thieme, 1985.
203. Talairach J. and Tournoux P. "Co-Planar Stereotaxic Atlas of the Human Brain. 3-Dimensional Proportional System: An Approach to Cerebral Imaging." Thieme Medical Publisher, Inc., Stuttgart, NY, 1988.
204. Taylor P. "Invited review: computer aids for decision-making in diagnostic radiology - a literature review." *British Journal of Radiology*, 68:945-957, 1995.
205. Terzopoulos D. and Szeliski R. "Tracking with Kalman snakes." In A. Blake and A. Yuille, editors, *Active Vision, Artificial Intelligence*, pages 3-20. The MIT Press, Cambridge, Massachusetts, 1992.
206. The Breast Surgeons Group of the British Association of Surgical Oncology. "Guidelines for surgeons in the management of symptomatic breast disease in the United Kingdom", *European Journal of Surgical Oncology* 1995:21. 1995.
207. Thies C, Malik A, Keysers D, Kohnen M, Fischer B, Lehmann TM: "Content-based retrieval in medical image databases by hierarchical feature clustering". *Procs SPIE* 2003; 5032: 598-608. 2003
208. Thompson P. and Toga A.W. "Detection, visualization and animation of abnormal anatomic structure with a probabilistic brain atlas based on random vector field transformations." *Medical Image Analysis* 1:271-294, 1997.
209. Tiddens HA, Pare PD, Hogg JC, Hop WC, Lambert R, de Jongste JC. "Cartilaginous airway dimensions and air-flow obstruction in human lungs." *American Journal of Respiratory and Critical Care Medicine* 1995;152:260-266. 1995.
210. Tilton JC "Method for recursive hierarchical segmentation by region growing and spectral clustering with a natural convergence criterion", *Disclosure of Invention and New Technology: NASA Case Number GSC 14, 328-1*, February 28, 2000.
211. Tilton, J.C "Hierarchical Image Segmentation" *Online Journal of Space Communication* Issue No. 3 Winter 2003 Research and Applications. 2003.

212. Tschirren J, Hoffman EA, McLennan G, Sonka M. "Intrathoracic airway trees: segmentation and airway morphology analysis from low-dose CT scans." *IEEE Trans Med Imaging* 2005;24:1529-1539. 2005.
213. TurKit <http://groups.csail.mit.edu/uid/turkit/> (Last visited on October 2011)
214. Udupa J. K. and Samarasekera S. "Fuzzy connectedness and object definition: Theory, algorithms and applications in image segmentation." *Graphical Model and Image Processing*, 58(3):246-261, 1996.
215. Udupa, J.K. and Samarasekera, S. "Fuzzy connectedness and object definition: Theory, algorithms and applications in image segmentation", *Graph. Mod. Im. Proc.*, vol, 58, pp. 246-261. 1996.
216. Unnikrishnan, R., Pantofaru, C. and Hebert, M. "Toward Objective Evaluation of Image Segmentation Algorithms", *IEEE Transactions on Pattern Analysis and Machine Intelligence*, VOL. 29, NO. 6, 29-944, June 2007.
217. Vikgren J, Boijesen M, Andelid K, Ekberg-Jansson A, Larsson S, Bake B, Tylen U. "High-resolution computed tomography in healthy smokers and never-smokers: a 6-year follow-up study of men born in 1933", *Acta Radiology* 2004 Feb;45(1):44-52. 2004.
218. Vilarino D.L., Brea V.M., Cabello D., and Pardo J.M. "Discrete-time CNN for image segmentation by active contours." *Pattern Recognition Letters*, 19:721-734, 1998.
219. Vilarino, D.L., Brea, V.M., Cabello, D. and Pardo, J.M. "Discrete-time CNN for image segmentation by active contours", *Pattern Recognition Letters*, vol. 19, pp. 721-734. 1998.
220. Vincent L. and Soille P. "Watersheds in digital spaces: an efficient algorithm based on immersion simulation." *IEEE Transaction on Pattern Analysis and Machine Intelligence*, 13:583-598, 1991.
221. Warren Burhenne LJ, Wood SA, D'Orsi CJ, Feig SA, Kopans DB, O'Shaughnessy KF, Sickles EA, Tabar L, Vybomy CJ and Castellino RA. "Potential contribution of computer-aided detection to the sensitivity of screening mammography", *Radiology*;215(2):554-562. 2000. [Published correction appears in *Radiology* 2000;216(1):306.]
222. Webb WR, Gamsu G, Wall SD, Cann CE, Proctor E. "CT of a bronchial phantom: factors affecting appearance and size measurements". *Investigative Radiology*; 19: 394-398. 1984.
223. Weiss, Y., "Segmentation using eigenvectors: a unifying view", Technical Report, Computer Science Department, UC Berkeley. 1999.
224. Wells W.M., Grimson W.E.L., Kikins R., and Jolesz F.A. "Adaptive segmentation of MRI data." *IEEE Transation on Medical Imaging*, 15:429-442, 1996.

- 225.Worth A.J., Makris N., Caviness V.S., and Kennedy D.N.. "Neuroanatomical segmentation in MRI: technological objectives." *International Journal on Pattern Recognition and Artificial Intelligence*, 11:1161-1187, 1997.
- 226.Worth, A.J., Makris, N., Meyer, J.W., Caviness, V.S. Jr. and Kennedy, D.N., "Automated Segmentation of Brain Exterior in MR Images Driven by Empirical Procedures and Anatomical Knowledge" Presented at the XVth International Conference on *Information Processing in Medical Imaging (IPMI 1997)*, Poultney, Vermont, June, 1997, vol. 1230, pp. 99-112. 1997.
- 227.Xie, G., Cao, T., Yan, C. and Wu, Z. "Texture Features Extraction of Chest HRCT Images Based on Granular Computing", *Journal of Multimedia*, Vol. 5, No. 6, December 2010.
- 228.Xu C. and Prince J.L. "Snakes, shapes, and gradient vector flow." *IEEE Transaction on Image Processing*, 7:359-369, 1998.
- 229.Yang, F. and Jiang, T. "Pixon-based Image Segmentation with Markov random fields", *ACCV2002: The 5th Asian Conference on Computer Vision*, 23--25 January 2002, Melbourne, Australia. 2002.
- 230.Yu, K., Ji, L., Wang, L., and Xue, P., "How to Optimize OCT Image", *Optics Express* Vol. 9. No. 1 July 2001.
- 231.Yu, S.X., "Segmentation Induced by Scale Invariance" *IEEE Conference on Computer Vision and Pattern Recognition*, San Diego, CA, June 20-26, 2005.
- 232.Yusof N.M., Isa N.A.M and Sakim H.A.M. "Computer-Aided Detection and Diagnosis for Microcalcifications in Mammogram", *IJCSNS International Journal of Computer Science and Network Security*, VOL.7 No.6, June 2007.
- 233.Zavalett VA, Bartholmai BJ and Robb RA "High Resolution Multidetector CT-Aided Tissue Analysis and Quantification of Lung Fibrosis". *Academic Radiology* Vol. 14, Issue 7, Pages 772-787. 2007.
- 234.Zeidler MR, Kleerup EC, Goldin JG, Kim HJ, Truong DA, Simmons MD, Sayre JW, Liu W, Elashoff R, Tashkin DP. "Montelukast improves regional air-trapping due to small airways obstruction in asthma." *European Respiratory Journal* 2006;27:307-315. 2006.
- 235.Zhang, T.Y., and Suen, C.Y., "A fast parallel algorithm for thinning digital patterns", *Communications of the ACM*, vol. 27, no. 3, pp. 236-239, 1984.
- 236.Zhao, B., Gamsu, G., Ginsberg, M.S., Jiang, Li and Schwartzn, L.H, "Automatic detection of small lung nodules on CT utilizing a local density maximum algorithm", *Journal of applied clinical medical physics*, Volume 4, Number 3, Summer 2003.

237. Zhou, H., Schaefer, G., Sadka, A. and Celebi, M.E. "Anisotropic mean shift based fuzzy C-means segmentation of dermoscopy images" *IEEE Journal of Selected Topics in Signal Processing*, Vol. 3, No. 1, 26-34, 2009.
- Nakano Y, Muller NL, King GG, Niimi A, Kalloger SE, Mishima M, Pare PD. "Quantitative assessment of airway remodeling using high-resolution CT." *Chest* 2002;122:271S-275S. 2002.
238. Zijdenbos A.P. and Dawant B.M. "Brain segmentation and white matter lesion detection in MR images." *Critical Reviews in Biomedical Engineering*, 22:401-465, 1994.